The toluene sub-mechanism was tuned from the reduced TRF-PAH mechanism [28], and it was employed as the initial mechanism based on two reasons: (1) The size of the TRF-PAH mechanism is compact, which is advantageous for three-dimensional engine combustion simulation; and (2) The mechanism has good performance in predicting species concentrations and flame speeds.

Figure 4 illustrates the principal reactions of the reduced toluene mechanism. Toluene is predominantly consumed through three pathways: the H-atom abstraction reactions leading to the production of $C_6H_4CH_3$ (R6), $C_6H_5CH_2$ (R1), and the reaction R5. Among these, the formation of $C_6H_5CH_2$ is the primary pathway for toluene consumption, while C6H5OH ranks as the second most abundant product. Through some intermediate species, such as $C_6H_5CH_2O$, C_6H_5, and C_6H_5O, the toluene molecule ultimately converts into the small molecules. Some species, such as $C_6H_5CH_2OO$, C_6H_5CO, and $OC_6H_4CH_3$, which are absent in Figure 4, were also incorporated into the toluene sub-mechanism.

The NOx and PAH sub-mechanisms of the original TRF-PAH mechanism were retained in the current mechanism. The NOx sub-mechanism includes four species and 12 reactions, and it contains thermal reactions and N_2O-intermediate reactions. The PAH mechanism is able to reproduce PAH formation up to a four-ring PAH. Herein, H-atom abstraction reactions, methyl substitution reactions, and hydrogen abstraction acetylene addition (HACA) make great contributions to PAH formation, and hence the reactions of MAHs (e.g., A_1C_2H and $A_1C_2H_3$) were considered. As reported in Ref. [28], the predictions obtained from the PAH mechanism demonstrated outstanding agreement with the measured data collected from eight different flames, which indicated that the present PAH mechanism is satisfactory to some extent.

3.3. Decalin Sub-Mechanism

The decalin mechanism was reduced from the detailed decalin oxidation mechanism proposed by Dagaut et al. [29]. As shown in Figure 4, the current decalin mechanism contains both low- and high-temperature mechanisms, and so the mechanism exhibits the capability to accurately describe decalin oxidation across a broad temperature range. The reactions framed by the dashed box (Figure 4) belong to the low-temperature mechanism.

Decalin radicals can be diverse considering the symmetrical structure of a decalin molecule. Three $C_{10}H_{17}$ radicals lumped as 'RDECALIN' were produced via decalin consumption reactions with small molecules including O_2, H, and HO_2, as shown in Figure 4 (R12–R15). In accordance with Yu et al. [30], the low-temperature and high-temperature mechanisms exhibit significant differences in their core reactions. In the low-temperature regime, the primary consumption pathway for RDECALIN involves the O_2 addition reaction (R16), while other consumption reactions are negligible. The formation of alkylperoxy radicals (RDECOO) via R16 is followed by their isomerization to hydroperoxy alkyl (QDECOOH). QDECOOH, in turn, undergoes a conversion to ZDECA (lumped $C_{10}H_{17}O_4$ isomers) through the reaction R18. ZDECA is then consumed, leading to the formation of $C_{10}H_{16}O_3$ isomers (KHDECA), and the decalin chain-branching sequence is completed by the reaction R20, which represents the KHDECA decomposition at low temperatures. Conversely, in the high-temperature regime, the decomposition of RDECALIN primarily occurs through reactions that tend to generate C_5H_8 species and cyclopentylcyclopentene (DCYC5). Then C_5H_8 decomposes to cyclopentadiene (CYC_5H_6) via the H-abstraction reaction (R23). Eventually, the big hydrocarbon molecules are converted into small C2–C4 molecules.

3.4. N-Dodecane Sub-Mechanism

The n-dodecane mechanism was reduced via our previous work [31] and was briefly introduced here. As shown in Figure 4, n-dodecane is consumed by three reactions (R29–R31) to produce dodecyl radicals ($C_{12}H_{25}$) at low temperatures. $C_{12}H_{25}$ then transforms to peroxy dodecyl radicals ($C_{12}H_{25}OO$) via the pathway reaction R32, which is significant for the formation of the negative temperature coefficient (NTC) region. Hydroperoxy dodecyl

radicals ($C_{12}H_{24}OOH$) are produced by a isomerization reaction (R33). $C_{12}H_{24}OOH$ transforms into $O_2C_{12}H_{24}OOH$ by reacting with oxygen (R34). $C_{12}KET$ radicals are produced from the reaction R35, and they further decompose into a few species, including $C_5H_{11}CO$, with the reaction R36. The small species will be generated through the decomposition reaction R37. However, at high temperatures, dodecyl radicals first convert to $C_{12}H_{24}$ by a reaction with oxygen (R38) and then decompose into C2–C4 molecules via the reaction R39 or directly produce the small hydrocarbon molecules by R40.

3.5. Isocetane Sub-Mechanism

The isocetane sub-mechanism was also taken from our previous work [32]. A short depiction of the isocetane sub-mechanism is given here. The consumption of isocetane is completed by the reactions R41–R43 at low temperatures (Figure 4). Ketohydroperoxide is produced via the reactions R44–R47, while the decomposition of ketohydroperoxide is completed by the reactions R48 and R49. At high temperatures, all reactions are represented by the three reactions R50, R51, and R52.

4. Results and Discussion

The experimental data, including IDTs, species concentrations, and laminar flame speeds determined by various devices, were used for validating the current kinetic mechanism. The mechanism was first validated for each component and then for the surrogate fuel mixture. The validation of the individual components will give a more comprehensive assessment on the accuracy and reliability of the JFS mechanism. The simulations were performed on CHEMKIN-PRO Version-19.0 software [33].

4.1. Verifications of Toluene

4.1.1. IDT

It is necessary to validate the current mechanism on IDT because the fuel autoignition behaviors characterized by IDT are important for engine combustion and emission performances [34]. Figure 5 exhibits a comparison of the measured and simulated IDTs for toluene in a shock tube under varying conditions of temperature, pressure, and equivalence ratios. The measurements were determined by Shen et al. [35], and the predicted IDT with the current mechanism and the based mechanism [28] were exhibited. Both the reduced mechanism and the based mechanism demonstrated strong agreement with the measurements. The current mechanism showed better performance under an equivalence ratio of 1.0. Compared to the based mechanism, the IDTs predicted by the current mechanism are closer to the measurements at low pressure. In addition, the predicted IDTs of toluene are compared with the determined IDTs in an RCM [36]. The corresponding results are presented in Figure 6. The toluene IDTs were slightly underestimated, but the discrepancy is acceptable.

4.1.2. Species Concentration

As emphasized by Pitz et al. [37], it is equally crucial to validate the profiles of major species concentrations alongside the validation of fuel IDT. Hence, the current mechanism was validated for the major species profiles during the oxidation process. In Figure 7, the concentration profiles of critical species in the premixed toluene flame are displayed. These species include reactants (toluene and oxygen), an inactive gas (argon), and products (such as carbon monoxide and hydrogen). Li et al. [38] experimentally investigated premixed toluene flames at three equivalence ratios (Φ = 0.75, 1.0, and 1.5) under a pressure of 10 atm. A satisfactory agreement was observed between the predicted and observed species profiles for all flames, with a notable consistency observed in the case of the stoichiometric toluene flame. The argon species concentration initially decreased and then stabilized further downstream of the burner. The model accurately predicted this trend, demonstrating its capability to replicate the mole expansion effects observed in the toluene flame, as reported in reference [38]. Additionally, the model successfully captured

the overall profiles of the final products, specifically water and carbon dioxide, and the maximum deviations between the measurements and predictions for final products are less than 10%. Carbon monoxide displayed a profile resembling that of hydrogen, gradually surpassing carbon dioxide as the predominant carbon product. Despite the discrepancies in the predicted species concentrations of toluene and oxygen compared to the corresponding measurements at equivalence ratios of 0.75 and 1.5, the model successfully represented the depletion positions of these species with accuracy.

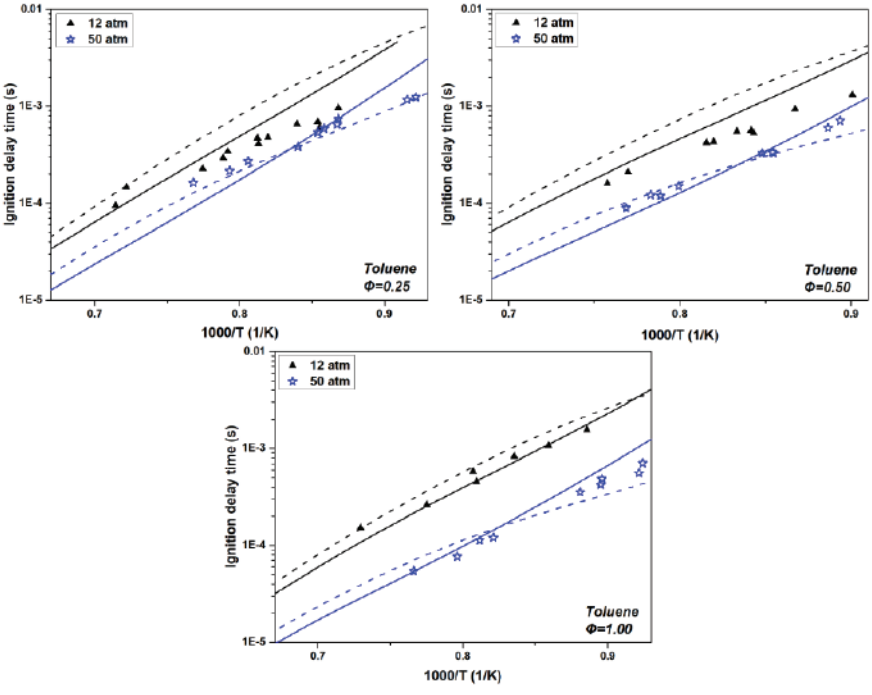

Figure 5. The measured (symbols [35]) and predicted (solid lines: current mechanism, dash lines: the based mechanism [28]) toluene IDTs determined in shock tube.

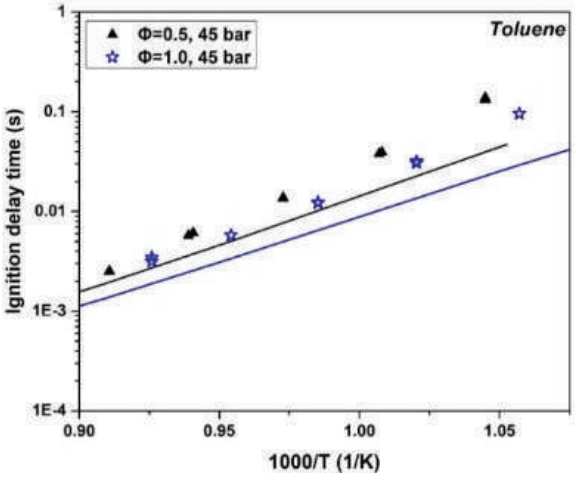

Figure 6. The measured (symbols) and simulated (lines) toluene IDTs in RCM.

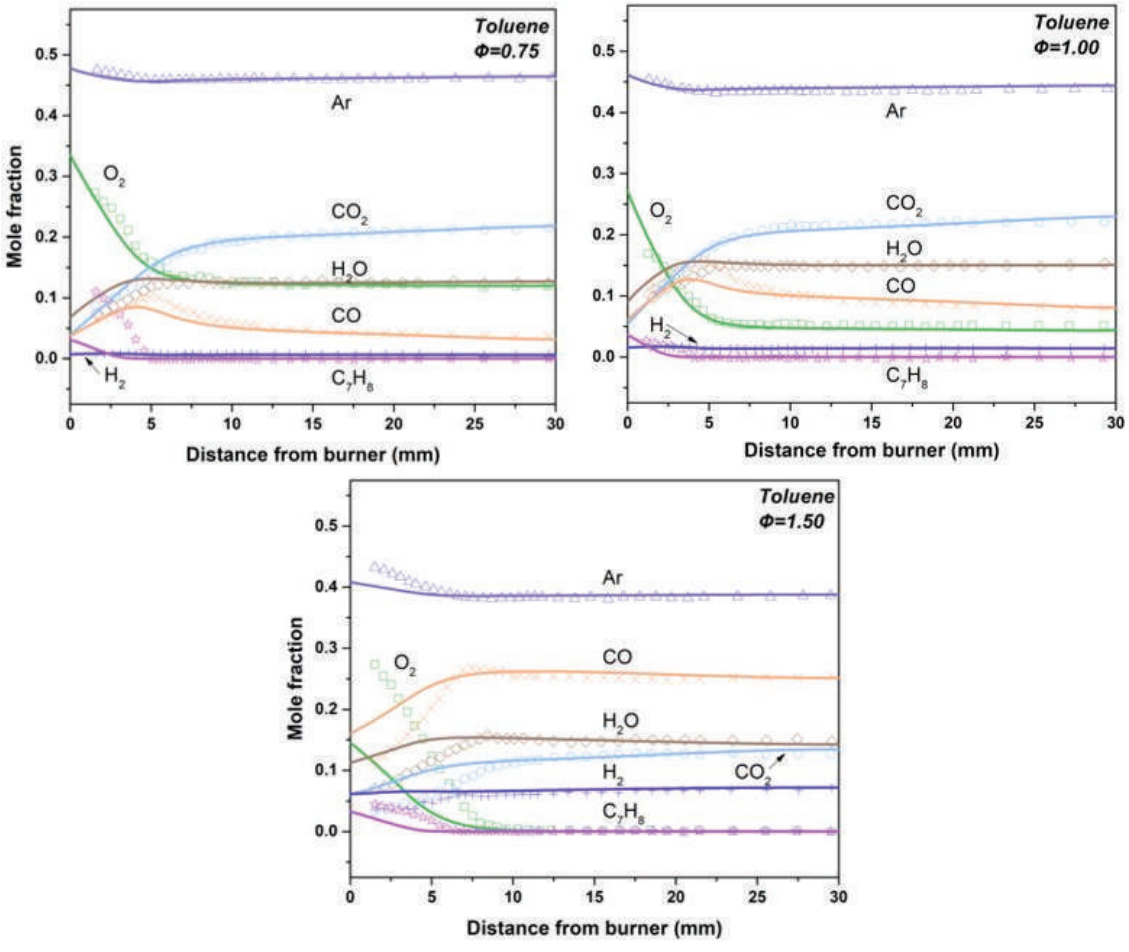

Figure 7. The major species profiles of premixed toluene flames under three equivalence ratios (0.75, 1.0, and 1.5) and a pressure of 10 atm. The determined results [38] are represented by symbols, while the simulated values from the current mechanism are depicted by lines.

Figure 8 shows the toluene oxidation process in a JSR [39] at a residence time of 0.6 s and a pressure of 10 atm. The concentration evolution of both the major species (CO, CO_2, and C_7H_8) and the minor species (C_2H_2 and C_4H_4) are presented in Figure 8. The current mechanism rendered good performance in predicting the concentration profiles of C_7H_8, CO, and CO_2. C_2H_2 is esteemed as a significant precursor of PAH and soot formation [40]. Moreover, the proposed model exhibits its capability to predict the toluene concentration evolution. Furthermore, the mechanism successfully predicted the species profiles of C_4H_4 under different conditions, except for the scenario with an equivalence ratio of 1.5.

4.1.3. Laminar Flame Speed

The laminar flame speed (LFS) is a valuable parameter that provides insights into the reactivity, heat release rate, and propagation characteristics of actual fuels. Figure 9 shows the comparison between the simulated and measured LFSs of counter-flow toluene flames. The measurements were conducted under two conditions: p = 1 atm, Tu = 298 K [41], and p = 3 atm, Tu = 450 K [42], where Tu denotes the temperature of the unburned mixture. It can be observed that the mechanism performed well in predicting the flame

behavior under atmospheric conditions. However, the discrepancy of the predictions and measurements were larger under fuel-rich conditions compared to oxygen-rich conditions. Therefore, we can conclude that the current mechanism is more suitable for modeling lean-burn engine combustion.

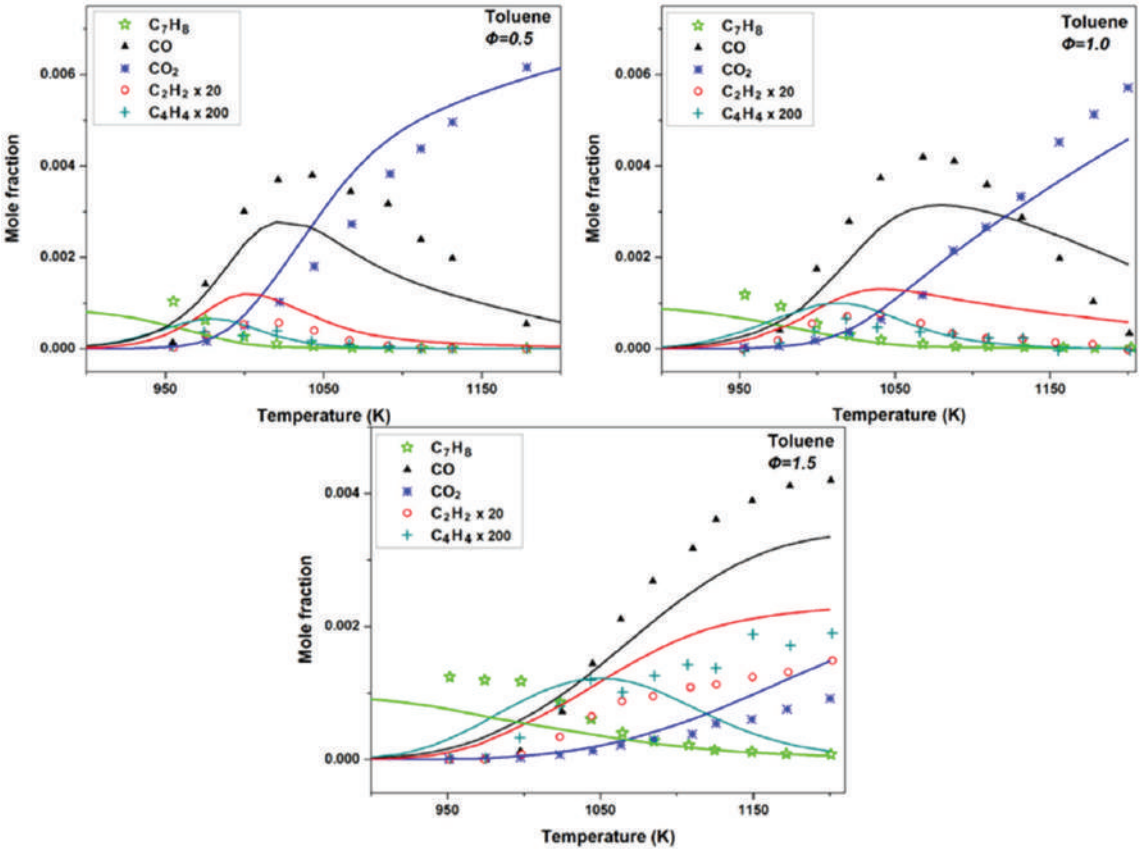

Figure 8. The concentrations of species resulting from the oxidation of toluene in the JSR are presented for various equivalence ratios at 0.6 s residence time and a pressure of 10 atm. The measured values [39] are denoted by symbols, while the simulation results obtained by the current mechanism are represented by lines.

4.2. Verifications of Decalin

4.2.1. IDT

Figure 10 displays the comparisons of the simulated and measured ignition delay times for decalin in a shock tube. The experimental data were obtained from previous studies [43,44], while the simulation results were obtained with both the present mechanism and the detailed mechanism [29]. Except for the case of $\Phi = 0.5$ and $p = 12$ atm, the current mechanism consistently outperformed the detailed mechanism across all other conditions, as demonstrated in Figure 10. However, considering the results achieved by the detailed mechanism, the level of discrepancy observed under the mentioned condition is still within an acceptable range. These results confirm that the current mechanism effectively captures the dependence of IDT on pressure and equivalence ratio, particularly at two specific conditions: (1) $p = 20$ atm, $\Phi = 0.5$; (2) $p = 40$ atm, $\Phi = 1.0$.

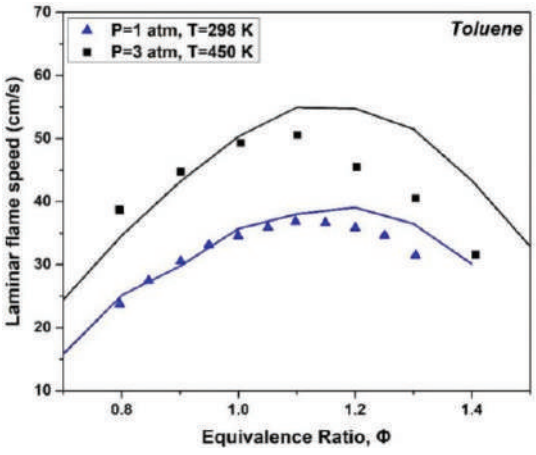

Figure 9. The simulated and measured LFSs in counter-flow toluene flames.

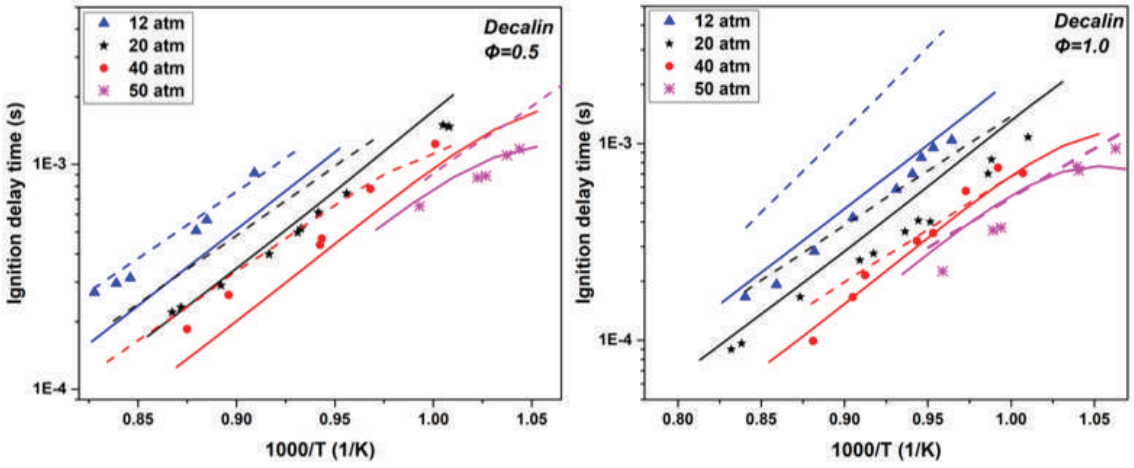

Figure 10. The measured (symbols) and predicted IDTs (solid lines: current mechanism; dash lines: the detailed mechanism) for decalin in a shock tube.

Figure 11 depicts the ignition delay time (IDT) of decalin over a temperature range of 770 K to 1250 K. Non-thermal combustion (NTC) behaviors were observed within this temperature range. At low-pressure conditions (p = 20 atm), the NTC region started at around 910 K, while at high temperatures, the NTC region initiated at a higher temperature of approximately 940 K. The shift in the NTC region suggests that pressure significantly influences the NTC behavior, which aligns with similar findings reported in Ref. [45].

In Figure 12, the decalin IDT is presented as determined in a rapid compression machine over a broad temperature range. The measurements were conducted at various equivalence ratios and a 15 atm compression pressure [30]. The results clearly demonstrate that IDTs decrease with increasing equivalence ratios. The variations in IDTs among different conditions were relatively small within the temperature range of 631 to 750 K, indicating a weak influence of equivalence ratio on IDTs at low temperatures. As the temperature increased, the differences in the ignition delay times (IDTs) became more pronounced. This can be attributed to the intensified chain-branch reactions occurring between the decalin molecules and hydroperoxyl radicals in both the negative-temperature-

coefficient and high-temperature zones. The current mechanism successfully captures these observed behaviors.

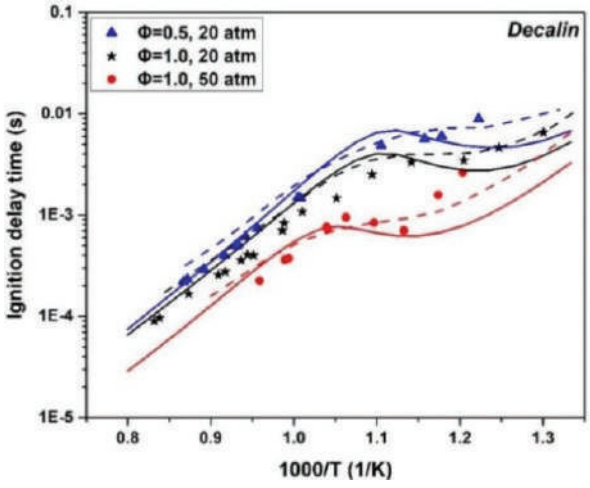

Figure 11. The decalin IDTs' NTC behaviors in a shock tube. The measured (symbols [43,44]) and predicted IDTs (solid lines: current mechanism; dash lines: the detailed mechanism [29]) for decalin.

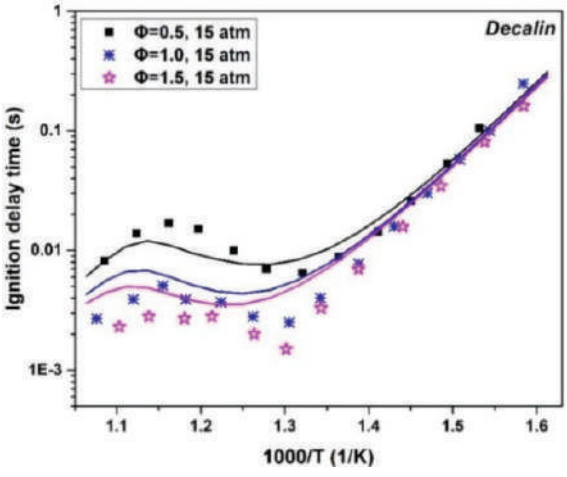

Figure 12. The measured (symbols) and predicted (lines) decalin IDTs in a RCM at three equivalence ratios under 15 atm compression pressure.

4.2.2. Species Concentration

Figure 13 exhibits the species profiles of the premixed decalin flames [46]. The predictions and measurements showed excellent agreement across various equivalence ratios. According to the ROP analysis, CO is predominantly generated through reactions involving HCO and HCCO, while its consumption occurs through its reaction with hydroxyl radicals, leading to the formation of CO_2. The formation of H_2O is notably influenced by H-atom abstraction reactions as well as the reaction between OH and H_2. H_2 is produced through a reaction between decalin and formaldehyde (CH_2O). The positions of depletion for decalin species varied with different equivalence ratios, and in the case of the stoichiometric decalin flame, the depletion position was observed to be closer to the burner surface. Similar observations were reported in the referenced study [38].

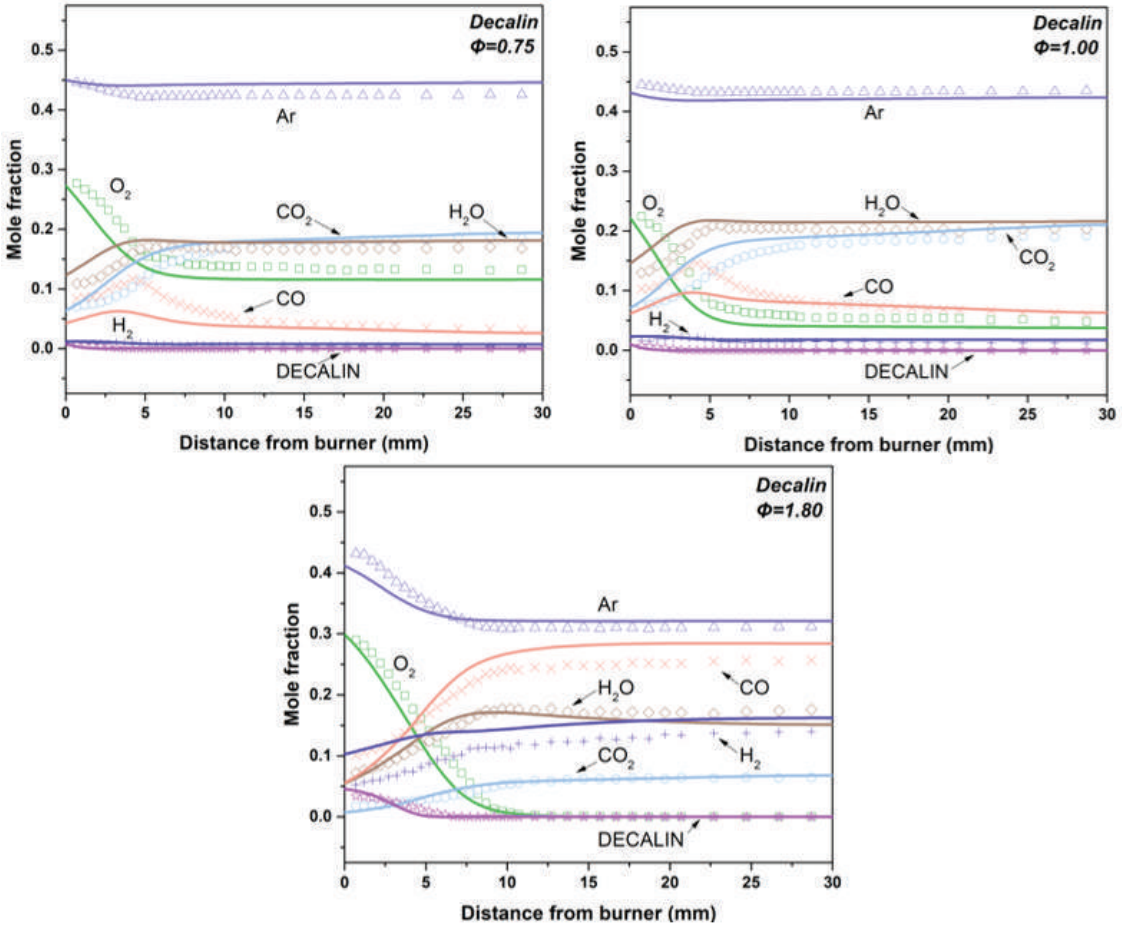

Figure 13. The premixed decalin flames species profiles at various equivalence ratios. The measured values [46] are denoted by symbols, while the simulated values from the current mechanism are represented by lines.

The species concentration profiles of decalin were also examined in the JSR [29]. C_2H_2 and CH_4 were selected for validating the accuracy of the current mechanism since they are the significant intermediate hydrocarbons produced during decalin oxidation. The current mechanism accurately predicted the concentration variations of C_2H_2 and CH_4, although it slightly overestimated the decalin concentration. It was observed that the concentration of CO initially increased and then reached a steady level above 900 K. The concentration of CO_2 exhibited a continuous increase with rising temperature. Overall, the current mechanism demonstrated good performance in reproducing these trends. Furthermore, the concentration profiles of CH_2O, a major aldehyde produced during the oxidation process of decalin, were also accurately captured by the current mechanism (Figure 14).

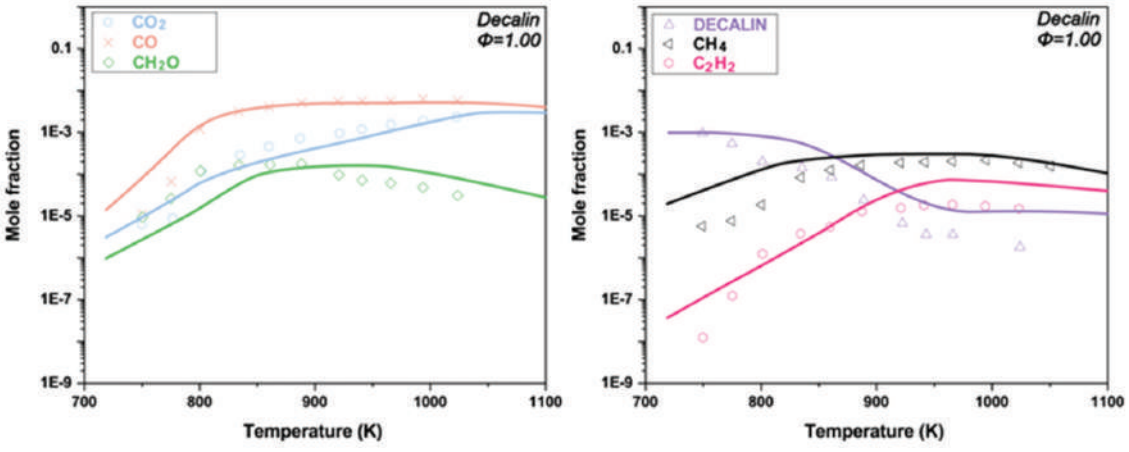

Figure 14. The measured (symbols [29]) and predicted (lines) concentration profiles of species resulting from the oxidation of decalin in the JSR at an equivalence ratio of 1.0 and a compression pressure of 10 atm.

4.2.3. Laminar Flame Speed

Figure 15 illustrates the determined and predicted LFSs for the counter-flow decalin flame at atmospheric pressure [47]. The initial mixture temperature for the flame is 443 K. It is evident that the current mechanism accurately predicts the laminar flame speed of decalin, although the deviation between measured and predicted LFSs becomes larger under high equivalence ratios.

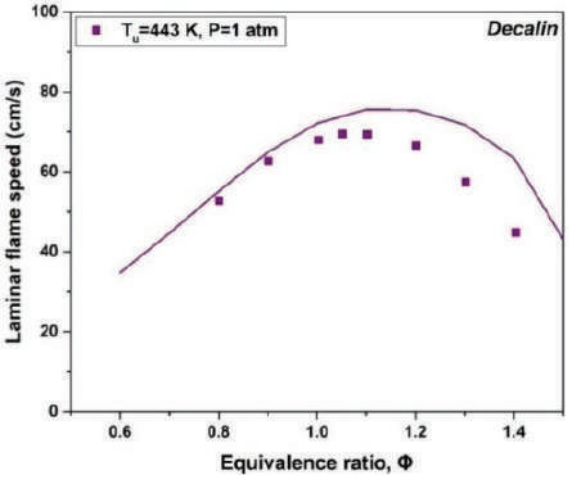

Figure 15. The laminar flame speeds of the counter-flow decalin flame. The line stands for the simulations, and dots represent the experimental data [47].

4.3. Verifications of n-Dodecane

4.3.1. IDT

Figure 16 shows the predicted and measured n-dodecane IDTs at two equivalence ratios (0.5 and 1.0) under three pressures (14 atm, 20 atm, and 40 atm). The shock tube measurements were taken from the Refs. [48–50]. The results confirmed that the current mechanism was capable of capturing the variation trends of the measured IDTs, except in

the case of p = 40 atm. The NTC behaviors observed in the temperature range from 750 K to 900 K were well reflected by the mechanism. In addition, the experimental phenomenon that IDT decreases with an increase in pressure was also captured by the mechanism.

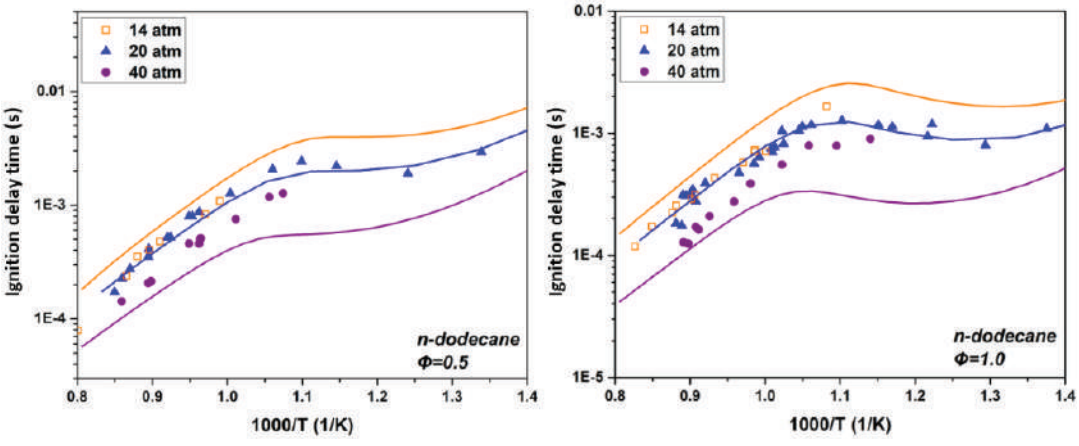

Figure 16. The measured (symbols) and predicted (lines) IDTs of n-dodecane in shock tube.

4.3.2. Species Concentration

Malewicki et al. [14] conducted JSR experiments to investigate the n-dodecane oxidation process. The experiments were carried out at a residence time of 1 s, a pressure of 10 atm, and three equivalence ratios. The comparison between the computed and measured results is shown in Figure 17. The prediction for the variation trend of O_2 and n-dodecane ($C_{12}H_{26}$) with temperature was consistent with the measurements under all conditions. H_2O was slightly underestimated, but the deviation is still at an acceptable level. There were some deviations between the simulated and determined mole fractions of C_2H_2 and CO_2; nevertheless, the overall simulated profiles of C_2H_2 and CO_2 were satisfactory.

4.3.3. Laminar Flame Speed

The measured data of the n-dodecane laminar flame speed were adopted here from the experiment conducted by Kumar et al. [51]. The measurement was performed at atmospheric pressure and unburned mixture temperatures of 400 K and 470 K. It can be easily seen from Figure 18 that the predictions showed fairly good agreement with the experimental data under all conditions.

4.4. Verifications of Isocetane

4.4.1. IDT

The IDTs of isocetane were measured in a shock tube under two pressures (10 atm and 40 atm) and three equivalence ratios (0.5, 1.0, and 1.5) by Oehlschaeger et al. [52]. Figure 19 presents the predictions and measurements of isocetane IDT, and the maximum deviations between the measured and predicted IDT appeared under the condition of p = 10 atm and Φ = 1.0, confirming the derived mechanism can accurately predict IDT. The decreasing trend of IDT with increasing pressure was perfectly captured by the mechanism. Due to the absence of experimental data, the NTC behaviors were not obviously observed at low pressure and low equivalence ratios. Therefore, it is necessary to do further IDT validations for isocetane in the future.

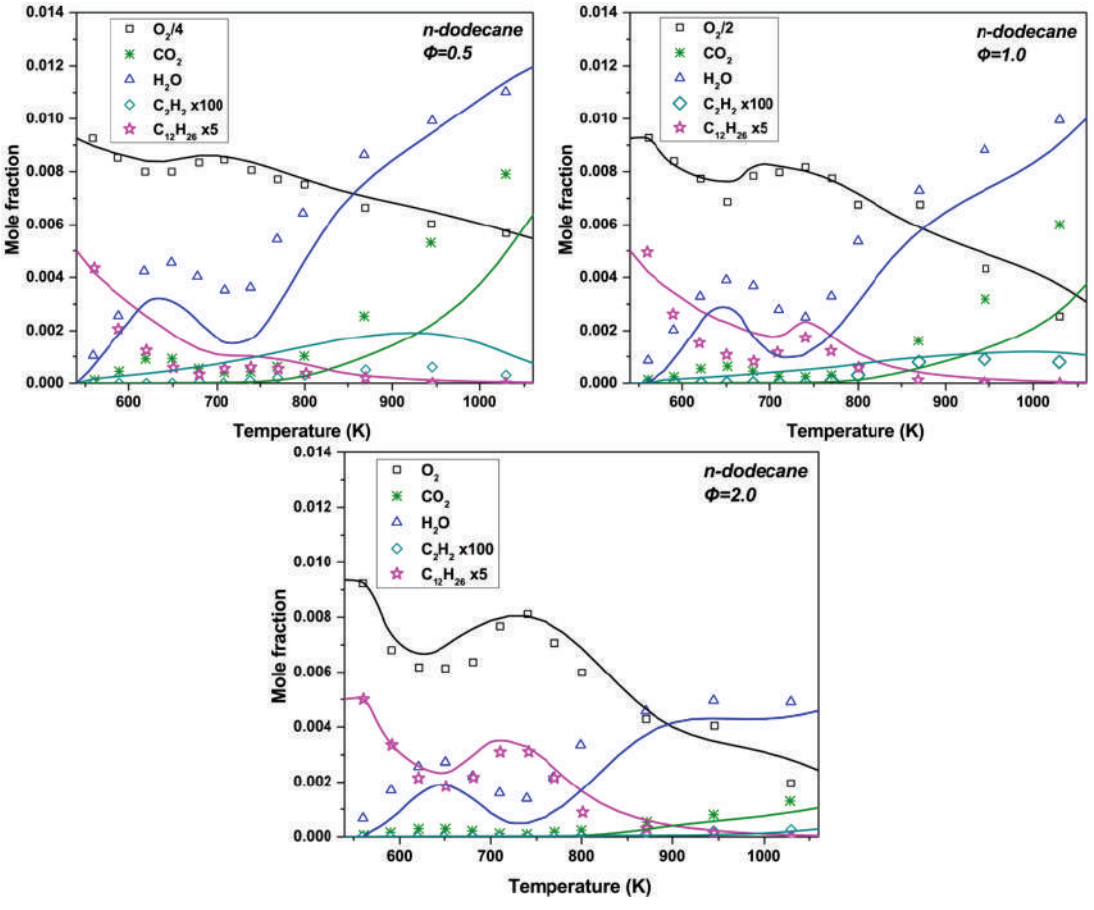

Figure 17. The measured (symbols [14]) and predicted (lines) mole fractions of the species during n-dodecane oxidation in JSR experiments at different equivalence ratios.

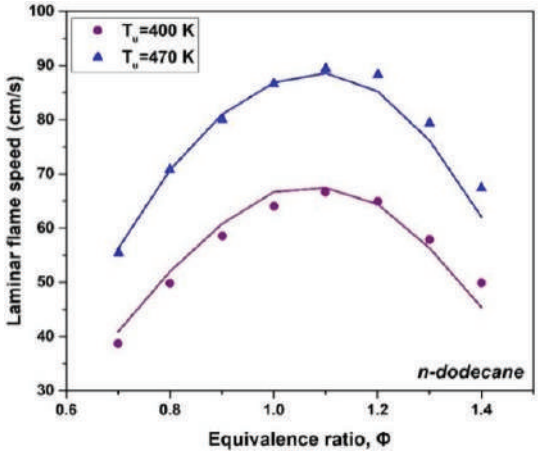

Figure 18. The laminar flame speeds of the n-dodecane flame. The line stands for the simulations, and dots represent the experimental data [51].

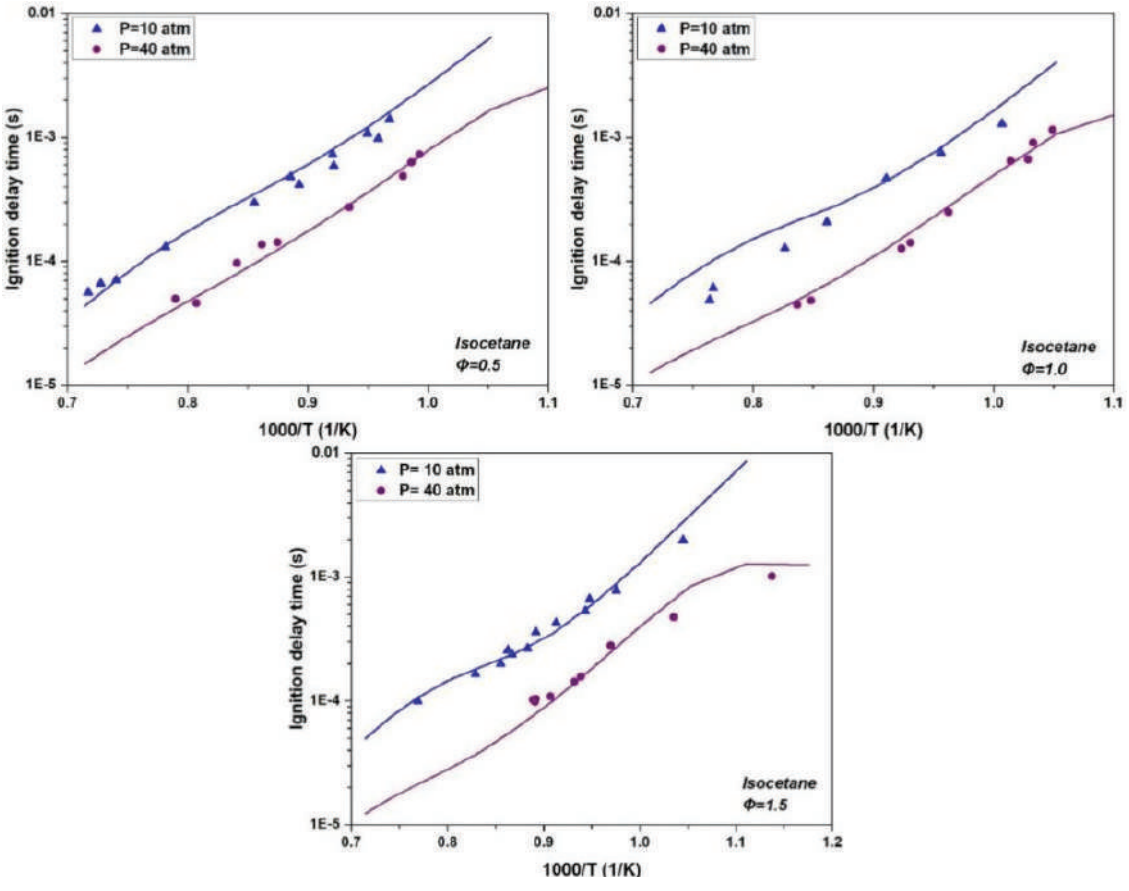

Figure 19. The measured (symbols [52]) and predicted IDTs (lines) of isocetane in the shock tube.

4.4.2. Species Concentration

Figure 20 shows the concentrations profiles of the major species produced during isocetane oxidation in a JSR [53]. The measurements were performed at a residence time of 1 s, under a pressure of 10 atm, and under three equivalence ratios (0.5, 1.0, and 2.0). It can be seen that the mechanism nicely predicts the consumption trend of isocetane under all conditions. The species mole fractions of H_2O and CO were also well predicted. The concentration of isocetane was overestimated in the high temperature range when $\Phi = 0.5$. For intermediate hydrocarbon products, the species profiles of CH_4 were not excellently reproduced by the mechanism, especially in the case of $\Phi = 1.0$.

4.5. Verifications of Jet Fuel

In this section, comparisons of ignition delay times, species mole fractions, and laminar flame speeds were further carried out for the newly developed JFS surrogate and the target jet fuel POSF-4658.

4.5.1. IDT

The shock tube experiments of jet fuel (POSF-4658) were conducted by S. Vasu et al. [8] and Wang et al. [54], as shown in Figure 21.

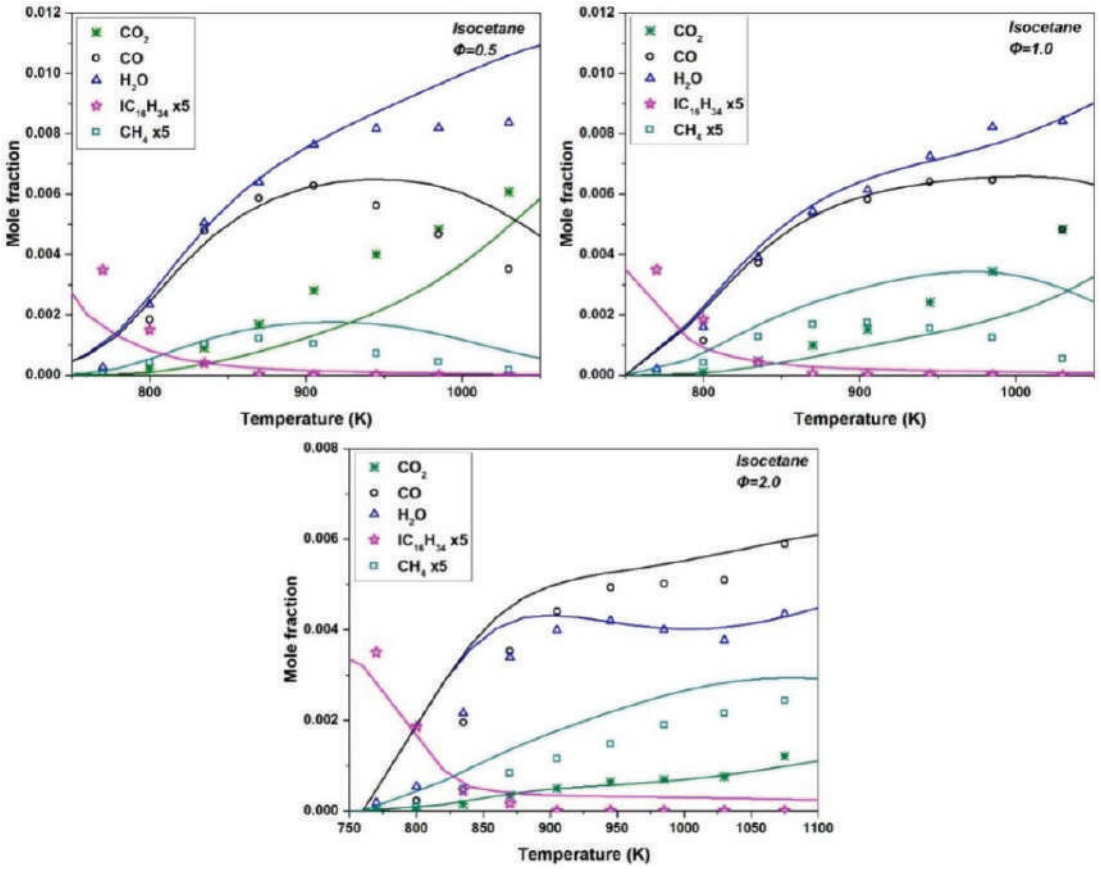

Figure 20. The measured (symbols [53])and predicted (lines) major species profiles of isocetane in JSR experiments at different equivalence ratios.

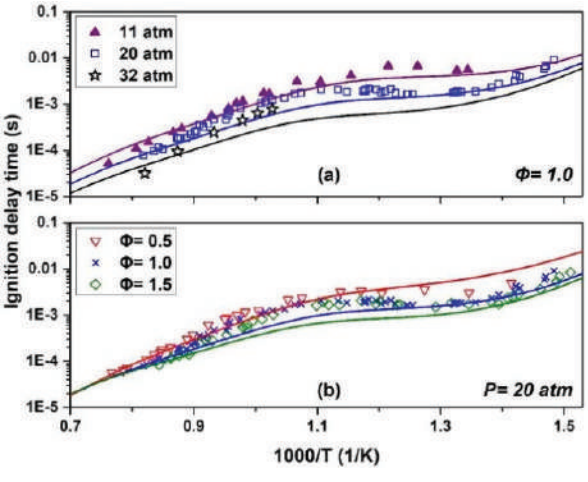

Figure 21. The comparisons between the determined and simulated IDTs of jet fuel under different (**a**) pressures and (**b**) equivalence ratios in a shock tube.

The comparisons between the determined and simulated IDTs of jet fuel at three pressures are exhibited in Figure 21a, while Figure 21b shows the results at three equivalence ratios: Φ = 0.5, 1.0, and 1.5. The overall trends of the jet fuel IDTs were well reflected by the current mechanism, especially at low pressure and low equivalence ratios, which can be attributed to the reason that the H/C, CN, and LHV of the proposed JFS surrogate are similar to those of the target fuel. Although the predicted NTC region underwent a slight shift to the left under the conditions of Φ = 1.5 and 20 atm pressure, the NTC behavior was satisfactorily captured via the developed mechanism. Furthermore, the maximum deviation between the predicted and measured IDTs is less than 0.001 s, and the small deviations between the predicted and measured IDTs can be attributed to two reasons: (1) Some reactions and species are removed from the reduced mechanism, which inevitably makes the mechanism unable to reproduce the measurements as well as the detailed mechanism. (2) There are still some differences between the properties of the JFS surrogate and the target fuel, which in turn influence the performance of the associated mechanism.

Figure 22 shows the comparison results between the measured IDTs and the IDTs predicted from the current JFS mechanism as well as the UM1 and UM2 mechanisms at Φ = 1.0 and p = 20 atm. Both the surrogates UM1 and UM2 contain four components, and the components of UM2 and the current JFS surrogate are identical. The detailed mechanisms of UM1 and UM2 were developed by Kim et al. [15]. In general, all of the mechanisms give good predictions of the measured IDTs of jet fuels. The predictions still suffer some deviations in IDT against the experimental data within the intermediate temperature range (from 855 to 1030 K), even with the detailed mechanisms, and the maximum deviation between the predicted and measured IDTs is about 0.0015 s. It is worth mentioning that the reduced JFS mechanism has a comparable emulation capability to the UM1 and UM2 mechanisms, although the UM1 and UM2 mechanisms are much more detailed compared to the current mechanism.

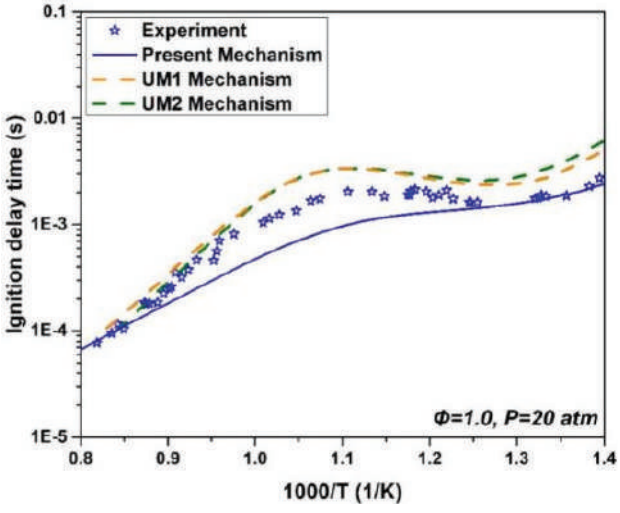

Figure 22. The comparison between the determined IDTs of jet fuel [12] and the simulated IDTs by the current mechanism, as well as the UM1 and UM2 mechanisms [15].

4.5.2. Species Concentration

Figure 23 shows the species profiles of the JFS surrogate in comparison with the experimental data determined in a shock tube at the temperature range of 890 K to 1680 K by Malewicki et al. [14].

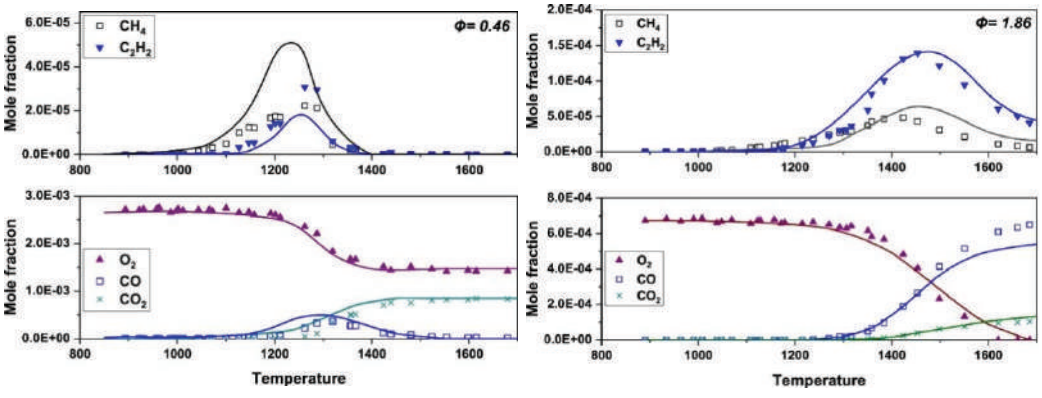

Figure 23. The measured and predicted species profiles of jet fuel. Symbols are the experimental data [14]; lines are the predictions made by the current mechanism.

The concentration profiles of CH_4 and C_2H_2 were well captured by the current mechanism, except for the slight overprediction for CH_4 at the lean condition (Φ = 0.46), which implies that the mechanism is reliable in predicting the soot and PAH formulation in engine combustion. The decaying trend of O_2 and the increasing trend of CO_2 were both greatly reflected by the mechanism. As shown in Figure 23, the current mechanism also showed good performance in predicting the CO concentration except for a slight underestimation under the rich- and high-temperature condition (Figure 22b). Overall, the current mechanism exhibited a satisfactory prediction of the major species concentrations of the JFS surrogate, although the maximum deviation between the measurements and the predictions of CH_4 was larger than the measured value. In fact, similar deviations were also observed even using a detailed mechanism, as reported by Malewicki et al. [14].

4.5.3. Laminar Flame Speed

The comparison results between the simulated and measured laminar flame speeds is shown in Figure 24. The laminar flame speeds of jet fuel were measured by Dooley et al. [13] at atmospheric pressure and the unburned mixture temperatures of 400 K and 470 K. The predicted values showed a surprising consistency with the measurements, and the maximum discrepancy between them was less than 9.4%. According to Li et al. [55], H_2, CO, and small hydrocarbons have decisive impacts on flame propagation; hence, great consistency can be attained through the adoption of a detailed C1/H_2/CO sub-mechanism in the current JFS mechanism.

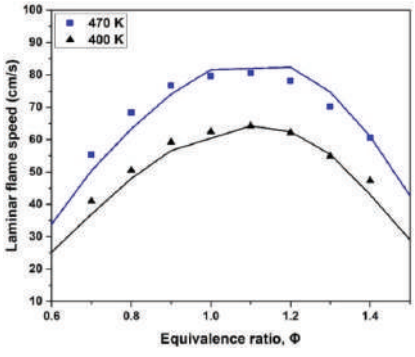

Figure 24. The comparison between the measured and predicted laminar flame speeds. Symbols represent the experimental data [13], lines are the values predicted by the current mechanism.

5. Conclusions

In this study, a new four-component jet fuel surrogate (n-dodecane/iso-octane/isocetane/decalin/toluene) was formulated with a property optimizer. The chemical and physical properties of the target jet fuel were considered during the formulation of the fuel surrogate. Compared to the previous-existing jet surrogates, the current jet fuel surrogate showed better performance in emulating the real jet fuel properties. The deviations in CN, TSI, LHV, and density are −0.35, −1.29, 0.87, and 1.84, which are extremely in a low level. The property deviations of MW (10.73%), viscosity (5.88%), and surface tension (8.71%) are slightly larger, but these remain within acceptable ranges.

A compact reduced kinetic mechanism consisting of 124 species and 590 reactions was proposed for the newly formulated surrogate. This mechanism is highly suitable for practical engine combustion simulations due to its reduced size. The mechanism is composed of four sub-mechanisms covering toluene, decalin, n-dodecane, and isocetane. It was systematically developed, starting from the C5–C16 reactions and transitioning to the C2–C4 reactions, followed by the $H_2/O_2/C1$ reactions, PAH reactions, and NOx reactions. To validate the proposed mechanism, experimental data including ignition delay time (IDT), species concentrations, and laminar flame speeds were utilized, encompassing both the surrogate mixture and its individual components. The results demonstrated a favorable concordance between the proposed mechanism and the experimental data. The current mechanism could accurately capture the variations of the ignition delay time in the negative temperature coefficient (NTC) region. Consequently, the proposed mechanism emerges as a viable choice for effective utilization in practical engine simulations.

Author Contributions: Conceptualization, G.L.; methodology, G.L.; software, B.C.; validation, B.C.; data curation, C.Z.; writing—review and editing, L.C. (Longfei Chen); supervision, L.C. (Liuyong Chang). All authors have read and agreed to the published version of the manuscript.

Funding: This work was supported by the National Natural Science Foundations of China (Grant No. 52306181 and Grant No. 52306184) and National Key Research and Development Project of China (Grant No. 2022YFB2602002).

Institutional Review Board Statement: Not applicable.

Informed Consent Statement: Not applicable.

Data Availability Statement: The data used to support the findings of this study are available from the corresponding author upon request.

Conflicts of Interest: The authors declare no conflict of interest.

References

1. Wolfowitz, P. *DoD Management Policy for Energy Commodities and Related Services*; Department of Defense: Washington, DC, USA, 2004; p. 4140.25.
2. Sarathy, S.; Farooq, A.; Kalghatgi, G.T. Recent progress in gasoline surrogate fuels. *Prog. Energy Combust. Sci.* **2018**, *65*, 67–108. [CrossRef]
3. Zhen, X.; Yang, W.; Daming, L. An overview of the chemical reaction mechanisms for gasoline surrogate fuels. *Appl. Therm. Eng.* **2017**, *124*, 1257–1268. [CrossRef]
4. Kim, D.; Violi, A. Hydrocarbons for the next generation of jet fuel surrogates. *Fuel* **2018**, *228*, 438–444. [CrossRef]
5. Yu, W.; Zhao, F.; Yang, W.; Tay, K.; Xu, H. Development of an optimization methodology for formulating both jet fuel and diesel fuel surrogates and their associated skeletal oxidation mechanisms. *Fuel* **2018**, *231*, 361–372. [CrossRef]
6. Dooley, S.; Won, S.H.; Dryer, F.L. Chapter 10—Surrogate fuels. In *Computer Aided Chemical Engineering*; Faravelli, T., Manenti, F., Ranzi, E., Eds.; Elsevier: Amsterdam, The Netherlands, 2019; pp. 513–602.
7. Violi, A.; Yan, S.; Eddings, E.G.; Sarofim, A.F.; Granata, S.; Faravelli, T.; Ranzi, E. Experimental formulation and kinetic model for JP-8 surrogate mixtures. *Combust. Sci. Technol.* **2002**, *174*, 399–417. [CrossRef]
8. Vasu, S.S.; Davidson, D.F.; Hanson, R.K. Jet fuel ignition delay times: Shock tube experiments over wide conditions and surrogate model predictions. *Combust. Flame* **2008**, *152*, 125–143. [CrossRef]
9. Dagaut, P.; El Bakali, A.; Ristori, A. The combustion of kerosene: Experimental results and kinetic modelling using 1- to 3-component surrogate model fuels. *Fuel* **2006**, *85*, 944–956. [CrossRef]

10. Gokulakrishnan, P.; Gaines, G.; Currano, J.; Klassen, M.S.; Roby, R.J. Experimental and Kinetic Modeling of Kerosene-Type Fuels at Gas Turbine Operating Conditions. *J. Eng. Gas Turbines Power* **2006**, *129*, 655–663. [CrossRef]
11. Eddings, E.G.; Yan, S.; Ciro, W.; Sarofim, A.F. Formulation of a surrogate for the simulation of jet fuel pool fires. *Combust. Sci. Technol.* **2005**, *177*, 715–739. [CrossRef]
12. Dooley, S.; Won, S.H.; Chaos, M.; Heyne, J.; Ju, Y.; Dryer, F.L.; Kumar, K.; Sung, C.-J.; Wang, H.; Oehlschlaeger, M.A.; et al. A jet fuel surrogate formulated by real fuel properties. *Combust. Flame* **2010**, *157*, 2333–2339. [CrossRef]
13. Dooley, S.; Won, S.H.; Heyne, J.; Farouk, T.I.; Ju, Y.; Dryer, F.L.; Kumar, K.; Hui, X.; Sung, C.-J.; Wang, H.; et al. The experimental evaluation of a methodology for surrogate fuel formulation to emulate gas phase combustion kinetic phenomena. *Combust. Flame* **2012**, *159*, 1444–1466. [CrossRef]
14. Malewicki, T.; Gudiyella, S.; Brezinsky, K. Experimental and modeling study on the oxidation of Jet A and the n-dodecane/iso-octane/n-propylbenzene/1, 3, 5-trimethylbenzene surrogate fuel. *Combust. Flame* **2013**, *160*, 17–30. [CrossRef]
15. Kim, D.; Martz, J.; Violi, A. A surrogate for emulating the physical and chemical properties of conventional jet fuel. *Combust. Flame* **2014**, *161*, 1489–1498. [CrossRef]
16. Verhelst, S.; Turner, J.W.; Sileghem, L.; Vancoillie, J. Methanol as a fuel for internal combustion engines. *Prog. Energy Combust. Sci.* **2019**, *70*, 43–88. [CrossRef]
17. Bae, C.; Kim, J. Alternative fuels for internal combustion engines. *Proc. Combust. Inst.* **2017**, *36*, 3389–3413. [CrossRef]
18. Yu, W.; Yang, W.; Tay, K.; Zhao, F. An optimization method for formulating model-based jet fuel surrogate by emulating physical, gas phase chemical properties and threshold sooting index (TSI) of real jet fuel under engine relevant conditions. *Combust. Flame* **2018**, *193*, 192–217. [CrossRef]
19. McDaniel, A.; Dickerson, T.; Luning-Prak, D.; Hamilton, L.; Cowart, J. *A Technical Evaluation of New Renewable Jet and Diesel Fuels Operated in Neat Form in Multiple Diesel Engines*; SAE Technical Paper; SAE International: Warrendale, PA, USA, 2016. [CrossRef]
20. Murphy, M.J.; Taylor, J.D.; McCormick, R.L. *Compendium of Experimental Cetane Number Data*; National Renewable Energy Laboratory: Golden, CO, USA, 2004.
21. *DIPPR Project 801—Full Version*; Design Institute for Physical Property Research/AIChE: New York, NY, USA, 2012.
22. Mensch, A.; Santoro, R.; Litzinger, T.; Lee, S.-Y. Sooting Characteristics of Surrogates for Jet Fuels. *Combust. Flame* **2010**, *157*, 1097–1105. [CrossRef]
23. Gill, R.J.; Olson, D.B. Estimation of Soot Thresholds for Fuel Mixtures. *Combust. Sci. Technol.* **1984**, *40*, 307–315. [CrossRef]
24. Grunberg, L.; Nissan, A.H. Mixture Law for Viscosity. *Nature* **1949**, *164*, 799–800. [CrossRef]
25. Poling, B.E.; Thomson, G.H.; Friend, D.G.; Rowley, R.L.; Wilding, W.V. *Perry's Chemical Engineers' Handbook*; McGraw-Hill Publishing: New York, NY, USA, 2008.
26. Hugill, J.; Van Welsenes, A.J. Surface tension: A simple correlation for natural gas+ conensate systems. *Fluid Phase Equilibria* **1986**, *29*, 383–390. [CrossRef]
27. Agosta, A.; Cernansky, N.; Miller, D.; Faravelli, T.; Ranzi, E. Reference components of jet fuels: Kinetic modeling and experimental results. *Exp. Therm. Fluid Sci.* **2004**, *28*, 701–708. [CrossRef]
28. Wang, H.; Yao, M.; Yue, Z.; Jia, M.; Reitz, R.D. A reduced toluene reference fuel chemical kinetic mechanism for combustion and polycyclic-aromatic hydrocarbon predictions. *Combust. Flame* **2015**, *162*, 2390–2404. [CrossRef]
29. Dagaut, P.; Ristori, A.; Frassoldati, A.; Faravelli, T.; Dayma, G.; Ranzi, E. Experimental and semi-detailed kinetic modeling study of decalin oxidation and pyrolysis over a wide range of conditions. *Proc. Combust. Inst.* **2013**, *34*, 289–296. [CrossRef]
30. Yu, L.; Wu, Z.; Qiu, Y.; Qian, Y.; Mao, Y.; Lu, X. Ignition delay times of decalin over low-to-intermediate temperature ranges: Rapid compression machine measurement and modeling study. *Combust. Flame* **2018**, *196*, 160–173. [CrossRef]
31. Chang, Y.; Jia, M.; Liu, Y.; Li, Y.; Xie, M.; Yin, H. Application of a Decoupling Methodology for Development of Skeletal Oxidation Mechanisms for Heavy n-Alkanes from n-Octane to n-Hexadecane. *Energy Fuels* **2013**, *27*, 3467–3479. [CrossRef]
32. Fan, W.; Jia, M.; Chang, Y.; Xie, M. Understanding the relationship between cetane number and the ignition delay in shock tubes for different fuels based on a skeletal primary reference fuel (n-hexadecane/iso-cetane) mechanism. *Energy Fuels* **2015**, *29*, 3413–3427. [CrossRef]
33. CHEMKIN-PRO RJI, San Diego, CA. 15112, Reaction Design. 2011. Available online: https://www.ansys.com/products/fluids/ansys-chemkin-pro (accessed on 6 July 2023).
34. Wang, L.; Wu, Z.; Ahmed, A.; Badra, J.A.; Sarathy, S.M.; Roberts, W.L.; Fang, T. Autoignition of direct injection spray of light naphtha, primary reference fuels, gasoline and gasoline surrogate. *Energy* **2019**, *170*, 375–390. [CrossRef]
35. Shen, H.-P.S.; Vanderover, J.; Oehlschlaeger, M.A. A shock tube study of the autoignition of toluene/air mixtures at high pressures. *Proc. Combust. Inst.* **2009**, *32*, 165–172. [CrossRef]
36. Kukkadapu, G.; Kang, D.; Wagnon, S.W.; Zhang, K.; Mehl, M.; Monge-Palacios, M.; Wang, H.; Goldsborough, S.S.; Westbrook, C.K.; Pitz, W.J. Kinetic modeling study of surrogate components for gasoline, jet and diesel fuels: C7-C11 methylated aromatics. *Proceeding Combust. Inst.* **2019**, *37*, 521–529. [CrossRef]
37. Pitz, W.J.; Mueller, C.J. Recent progress in the development of diesel surrogate fuels. *Prog. Energy Combust. Sci.* **2019**, *37*, 330–350. [CrossRef]
38. Li, Y.; Cai, J.; Zhang, L.; Yuan, T.; Zhang, K.; Qi, F. Investigation on chemical structures of premixed toluene flames at low pressure. *Proceeding Combust. Inst.* **2011**, *33*, 593–600. [CrossRef]

39. Yuan, W.; Li, Y.; Dagaut, P.; Yang, J.; Qi, F. Investigation on the pyrolysis and oxidation of toluene over a wide range conditions. I. Flow reactor pyrolysis and jet stirred reactor oxidation. *Combust. Flame* **2015**, *162*, 3–21. [CrossRef]
40. Zhao, F.; Yang, W.; Zhou, D.; Yu, W.; Li, J.; Tay, K.L. Numerical modelling of soot formation and oxidation using phenomenological soot modelling approach in a dual-fueled compression ignition engine. *Fuel* **2017**, *188*, 382–389. [CrossRef]
41. Davis, S.; Wang, H.; Breinsky, K.; Law, C.K. Laminar flame speeds and oxidation kinetics of benene-air and toluene-air flames. Conference Laminar flame speeds and oxidation kinetics of benene-air and toluene-air flames. *Symp. (Int.) Combust.* **1996**, *26*, 1025–1033. [CrossRef]
42. Johnston, R.; Farrell, J. Laminar burning velocities and Markstein lengths of aromatics at elevated temperature and pressure. *Proc. Combust. Inst.* **2005**, *30*, 217–224. [CrossRef]
43. Zhu, Y.; Davidson, D.; Hanson, R. Pyrolysis and oxidation of decalin at elevated pressures: A shock-tube study. *Combust. Flame* **2014**, *161*, 371–383. [CrossRef]
44. Oehlschlaeger, M.A.; Shen, H.-P.S.; Frassoldati, A.; Pierucci, S.; Ranzi, E. Experimental and Kinetic Modeling Study of the Pyrolysis and Oxidation of Decalin. *Energy Fuels* **2009**, *23*, 1464–1472. [CrossRef]
45. Curran, H.; Gaffuri, P.; Pitz, W.; Westbrook, C. A Comprehensive Modeling Study of n-Heptane Oxidation. *Combust. Flame* **1998**, *114*, 149–177. [CrossRef]
46. Zeng, M.; Li, Y.; Yuan, W.; Li, T.; Wang, Y.; Zhou, Z.; Zhang, L.; Qi, F. Experimental and kinetic modeling study of laminar premixed decalin flames. *Combust. Flame* **2017**, *36*, 1193–1202. [CrossRef]
47. Li, B.; Zhang, H.; Egolfopoulos, F.N. Laminar flame propagation of atmospheric iso-cetane/air and decalin/air mixtures. *Combust. Flame* **2014**, *161*, 154–161. [CrossRef]
48. Vasu, S.; Davidson, D.; Hong, Z.; Vasudevan, V.; Hanson, R. n-Dodecane oxidation at high-pressures: Measurements of ignition delay times and OH concentration time-histories. *Proc. Combust. Inst.* **2009**, *32*, 173–180. [CrossRef]
49. Shen, H.-P.S.; Steinberg, J.; Vanderover, J.; Oehlschlaeger, M.A. A Shock Tube Study of the Ignition of n-Heptane, n-Decane, n-Dodecane, and n-Tetradecane at Elevated Pressures. *Energy Fuels* **2009**, *23*, 2482–2489. [CrossRef]
50. Haylett, D.R.; Davidson, D.F.; Hanson, R.K. Ignition delay times of low-vapor-pressure fuels measured using an aerosol shock tube. *Combust. Flame* **2012**, *159*, 552–561. [CrossRef]
51. Kumar, K.; Sung, C.J. Laminar flame speeds and extinction limits of preheated n-decane/O2/N2 and n-dodecane/O2/N2 mix-tures. *Combust. Flame* **2007**, *151*, 209–224. [CrossRef]
52. Oehlschlaeger, M.A.; Steinberg, J.; Westbrook, C.K.; Pitz, W.J. The autoignition of iso-cetane at high to moderate temperatures and elevated pressures: Shock tube experiments and kinetic modeling. *Combust. Flame* **2009**, *156*, 2165–2172. [CrossRef]
53. Dagaut, P.; Hadj-Ali, K. Chemical Kinetic Study of the Oxidation of Isocetane (2,2,4,4,6,8,8-Heptamethylnonane) in a Jet-stirred Reactor: Experimental and Modeling. *Energy Fuels* **2009**, *23*, 2389–2395. [CrossRef]
54. Wang, H.; Oehlschlaeger, M.A. Autoignition studies of conventional and Fischer–Tropsch jet fuels. *Fuel* **2012**, *98*, 249–258. [CrossRef]
55. Li, J.; Zhao, Z.; Kazakov, A.; Chaos, M.; Dryer, F.L.; Scire, J.J., Jr. A comprehensive kinetic mechanism for CO, CH_2O, and CH3OH combustion. *Int. J. Chem. Kinet.* **2007**, *39*, 109–136. [CrossRef]

World Electric Vehicle Journal

MDPI

Article

Reasons Why Only Kuwaiti Citizens Drive Electric Vehicles despite Being Only a Quarter of the Population

Sumayya Banna [1], Andri Ottesen [2,*] and Basil Alzougool [1]

[1] LSE Middle East Centre (MEC), Arab Open University (AOU), Ardiya P.O. Box 830, Kuwait; sumayya@aou.edu.kw (S.B.); balzougool@aou.edu.kw (B.A.)
[2] LSE Middle East Centre (MEC)—Sustainability Research and Consultancy (CSRC), Australian University (AU), West Mishref P.O. Box 1411, Kuwait
* Correspondence: a.ottesen@au.edu.kw

Abstract: The adoption of fully battery-powered electric vehicles (EVs) in Kuwait is currently at less than one percent of the population, and hence Kuwait has the lowest index rank among countries around the globe. Effectively, only Kuwaiti nationals have the opportunity to own EVs, as there are no fast direct-current charging stations in Kuwait, and Kuwaiti landlords (expats cannot own real estate) do not allow the installation of EV-charging home wall boxes at their rented properties. Given these facts, this paper only focuses on the preferences of Kuwaiti nationals, even though they only constitute 25 percent of the population of Kuwait. To accomplish the present objectives, a quantitative descriptive method (closed-ended questions) was used to collect data from a sample of 227 Kuwaiti nationals who were representative of the owners of half a million internal combustion engine (ICE) cars and that were categorized as early majority consumers. The findings of the present study indicate that over 50 percent of the respondents would prefer to buy an EV in the following three years when certain criteria were satisfied, including government-controlled pricing policies and recharging point availability, high-speed roads, and free EV-dedicated parking spaces. Furthermore, over 40 percent of respondents stated that they would contemplate purchasing an electric vehicle if the price of gasoline or diesel increased by 19 to 50 percent. The findings also indicated that more than 40 percent of respondents believed that EVs are fire- and crash-safe, and roughly 50 percent of the respondents would be willing to pay between 6 and 20% more for an EV because they believe that EVs are ecofriendlier vehicles and are significantly faster than conventional petrol vehicles. Additionally, respondents rewarded those vehicles with an excellent mark because of their ecological, economical, and technological attributes and benefits.

Keywords: electric vehicles; green transport; carbon footprint; Kuwaiti national customer preference

Citation: Banna, S.; Ottesen, A.; Alzougool, B. Reasons Why Only Kuwaiti Citizens Drive Electric Vehicles despite Being Only a Quarter of the Population. *World Electr. Veh. J.* **2023**, *14*, 287. https://doi.org/10.3390/wevj14100287

Academic Editors: Wenbin Yu and Guang Zeng

Received: 27 August 2023
Revised: 21 September 2023
Accepted: 28 September 2023
Published: 10 October 2023

1. Introduction and Significance

The Pathway for the Reduction of Greenhouse Gas (GHG) Emissions in Kuwait

In 2021, Kuwait emitted 25 tons of CO_2 per capita, which was the third highest in the world after its neighbors Qatar and Bahrain (36 and 27 tons of CO_2 per capita, respectively). This made Kuwait's carbon emissions more than four times higher than the average in 28 European Union countries (6.1 tons of CO_2 per capita) [1–3]. The State of Kuwait has pledged to the United Nations to reduce GHG emissions by adopting a "low carbon equivalent emission economy". In its first NDC, submitted in April 2018, Kuwait outlined its action plan to reduce greenhouse gas emissions via launching its Shayaya Renewable Energy Park, a 3.2 GWe renewable solar and wind energy compound, and the creation of a mass transit (metro) system that has yet to be realized 5 years later. There are some issues of consistency and clarity in the Kuwaiti government's pledge to reduce greenhouse gas emissions and its action plan, as "there is no discussion of what this pledge entails or how it should be implemented" [4,5]. The largest emitting sector is electricity generation

(58 percent), which is primarily used for air cooling through the use of air conditioning and for the desalination of saline water in the world's hottest and driest climate conditions. The oil and gas sector is responsible for 11% of GHG emissions, whereas the transport segment of the economy is accountable for 18% of GHG emissions [6,7]. This paper aims to provide a viable path for GHG reduction by greening the transportation sector, and specifically, by transitioning from internal combustion engine (ICE) automobiles to electric vehicles (EVs) [8].

Currently, the total ownership of EVs is only about 400 vehicles (about 300 registered in Kuwait and about 100 that are estimated to drive there using a foreign license plate) [9]. This is extremely low, especially compared to Norway, the nation with the highest rate of EV adoption and with a similar population to Kuwait; Norway has over 650,000 of fully electric passenger cars and another about 200,000 Plug-In-Hybrids on the road, that is, more than one out of every four passenger cars [10]. Hence, Kuwaiti EV adoptions are 1500 times lower than the best-in-class. At the heart of this low adoption is the lack of DC fast-charging stations; Norway has about 22,000 public charging stations compared to 42 slow alternating current (AC) and no-fast-charging direct current (DC) stations in Kuwait [11,12]. What even further limits electromobility adoption, according to our interviews with all the EV car dealers and 12 current owners of EVs in Kuwait, is that Kuwaiti landlords will not allow installations of home wall boxes for their tenants, who are mostly expats who are prohibited by law to own real estate. A total lack of fast-charging DC stations and an effective ban on the installation of home-charging equipment effectively results in only Kuwaiti nationals who own their own house being able to own and operate EVs in Kuwait.

2. Background

2.1. Lowering GHG Emissions in the Transportation Sector

Only 0.2% of transportation in Kuwait is via public transport, primarily due to a lack of bus infrastructure, cultural conventions, and extreme climate conditions. There have been no campaigns or other government initiatives to promote or encourage the general public's use of public transportation [9]. Private automobiles are predominantly utilized by the majority of Kuwaiti citizens, and hence appear to be the most prevalent mode of transportation. Only about 600,000 of the 2.3 million vehicles registered in Kuwait belong to expats, who account for 70% of residents versus 30% being citizens [10]. In addition, approximately 90 percent of the 295 EVs registered in Kuwait between 2019 and March 2023 were owned by Kuwaitis [11]. One of the reasons why expats in Kuwait do not purchase electric vehicles is the absence of fast-charging stations and the refusal of landlords to enable tenants to install EV-charging wall boxes in rented properties. Kuwaiti citizens tend to live in their own houses as a result of various government programs, whereas expats are prohibited from owning real estate in Kuwait; as a result, most expatriates are forced to rent apartments and must obtain approval from their landlords for the installation of charging equipment, which is typically denied [12,13].

2.2. The Reason Electric Vehicles Are Optimal for Zero-Emission Transportation

In terms of vehicle efficiency, electric vehicles are the best adapted to reduce the carbon footprint and they have the lowest operating expenses. Mr. Abu Dagga, the director of Powerid Germany, believes that e-mobility is the key to sustainability and the high ground against climate change. The primary reason is that e-mobility is superior to ICE transportation, regardless of whether the fuel source is petroleum, diesel, or natural gas, particularly when energy losses are considered. Front-end well-to-tank investigations reveal that EVs lose approximately 6% of their energy compared to 45% in petroleum-powered vehicles [14,15]. Additionally, rear-end tank-wheels studies reveal an additional 17% energy loss for EVs compared to a 35% energy loss for diesel-powered vehicles, and a 39% energy loss for gasoline-powered vehicles, where the majority of that energy is lost as excess heat that is not converted into energy for the wheels. EVs are up to five times more effective than gasoline-powered internal combustion engine (ICE) vehicles, proving

their superiority in reducing greenhouse gas emissions (See Figure 1). The efficiency of EVs over ICEs is today three times more, but will be four times more efficient in 20 years, as EV batteries will become lighter and more efficient in terms of energy storage and transfer with new technologies, such as the solid-state batteries and EV batteries having a second life as energy storage for wind and solar farms [16]. Although EV batteries are generally disposed of with the car or replaced after their charging capacity goes below the warranty terms, which are usually from 70 to 75%, they present a cheap option in making up battery packs in a container system, as they are repurposed to store solar energy overnight when the sun is not shining. A good example of that is the 25 MWh grid-scale energy-storage system in California, where approximately 1300 disposed Honda and Nissan EV batteries are strung together in the B2U SEPV Sierra hybrid solar-storage facility, which uses slower charging time than the high-performance EVs [17,18]. The cost of installing such a system is USD 200 per kilowatt hour, as the batteries do not need refurbishing [19]. Lithium recycling factories are also coming fast online, such as the Li Cycle Rochester facility where the company claims to be able to recapture up to 95% of the battery resources for recycling using a closed-system water-based solution where the minerals are captured in a "black mass" that is then reseparated into battery-grade lithium, cobalt, and nickel, as well as other materials to be reused [20]. However, according to Powerid [16], hydrogen is not as suitable for smaller vehicles as it is for heavy-duty transport or construction vehicles, large sea vessels, or even aircrafts, due to its lack of energy efficiency, storage, and transportation complications, and a flame speed that is 10 times that of methane gas and thus more explosive [21,22]. This view is in stark contrast to that of Toyota and other Japanese automakers, who favor hydrogen as the primary source of zero-emission technology due to its rapid charging and long range, as they appear to be losing the EV world market [23].

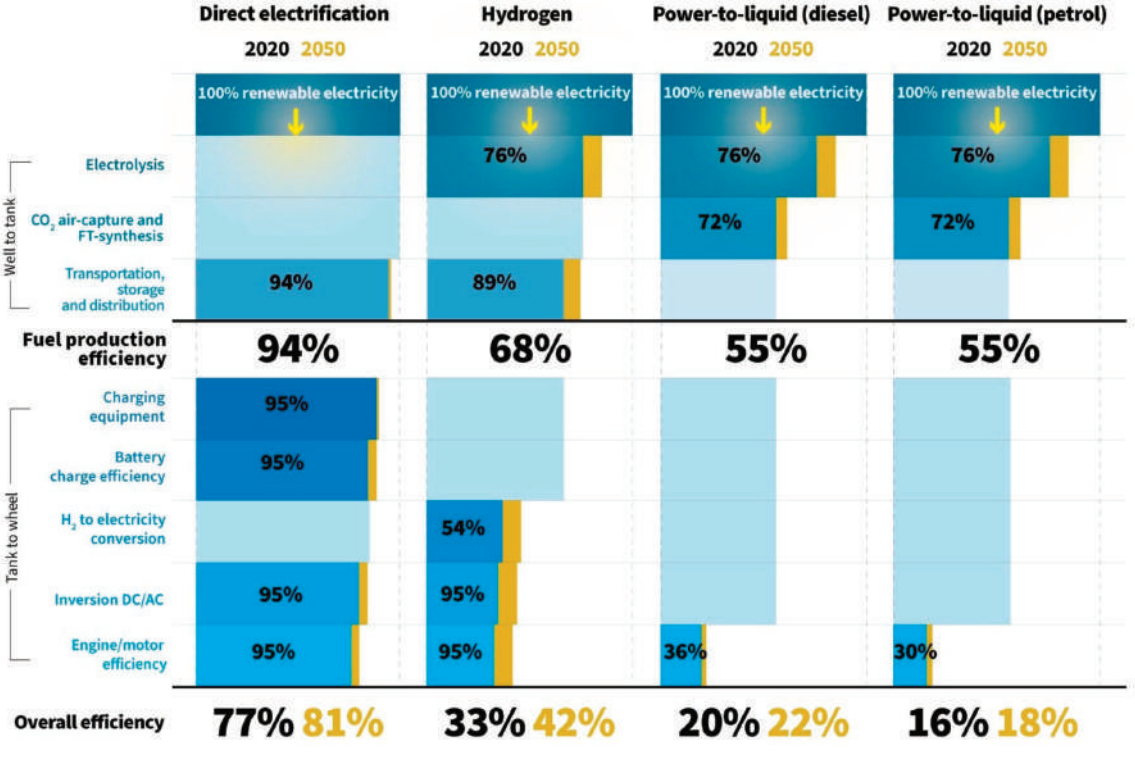

Figure 1. Vehicle fuel energy efficiency; source: Powerid. Printed with permission [16].

2.3. The Oil Savings for Each Electric Vehicle

With each transition from internal combustion engines (ICEs) to EVs, oil that would have been used for combustion is saved. This equates to approximately 10 barrels of oil equivalent (BOI) per year for a midsize car, one barrel for a motorcycle, 244 barrels for an A-class vehicle, and 274 barrels for a bus [24]. By the end of 2022, over 20 million electric vehicles will have been sold [25]. The transition from ICEs to EVs is anticipated to conserve 2.5 m petrol barrels per day by 2025, which is roughly equivalent to the everyday petrol production of Kuwait, the tenth-largest oil producer [26,27]. BloombergNEF predicts that the demand for oil will plateau in 2026, and will start to decline in 2027 as a result of the conversion from ICEs to EVs for all vehicle types. The Tesla Model-Y just took over the Toyota Corolla as the world's sales-record-breaking automobile for the first quarter for year 2023, with 267,200 vehicles sold compared to 256,400 for the Toyota Corolla [28].

2.4. Low Maintenance of Electric Vehicles

EVs have lower maintenance costs than internal combustion engine (ICE) vehicles due to the factors listed below. EVs have significantly fewer mechanical components or moving parts than ICE vehicles, with approximately 20 moving parts for EVs compared to approximately 2000 parts for ICE vehicles [29]. Fewer components translate to fewer items that can fail or wear out over time, resulting in lower maintenance costs. The US Energy Department (Office of Energy Efficiency and Renewable Energy) determined in 2021 that maintenance costs for EVs were only 6.1 cents per mile (4 cents per kilometer) compared to ICE costs of 10.1 cents per mile [30]. The following are the EERE study's explanations for this disparity: (A) Unlike ICE vehicles, EVs do not require regular lubricant replacements; (B) Electric vehicles utilize regenerative braking, which pauses the vehicle by converting the electric motor into a generator to recharge the battery. This reduces the frequency of replacing brake pads and rotors by minimizing system wear and tear. EVs lack exhaust systems, which are susceptible to corrosion and other damage in ICE vehicles. ICE vehicles require regular battery maintenance or replacement, whereas EV batteries are designed to last a very long time, often the life of the vehicle; (C) ICE vehicles require more frequent flushing of the refrigerant and other maintenance on the refrigeration system. EVs typically have less stringent cooling requirements, which further reduces their maintenance needs; (D) EVs have no gasoline pumps, fuel injectors, or fuel containers to maintain and replace; (E) Due to their simplicity and lack of moving parts, electric motors are exceptionally durable and can outlast the rest of the vehicle with minimal or no maintenance; (F) EVs have a gearless powertrain and, as a result, no (automatic) transmission (AT), which in ICE vehicles often requires costly maintenance. Altogether, these factors can save a substantial amount of money over the tenure of an EV versus an ICE vehicle.

2.5. The Durability of the EV Battery Dependence

Evidently, while routine maintenance on EVs is typically much less expensive, replacing the EV battery after the warranty expires after 8–10 years can be quite costly (Kia/Hyundai and Mercedes offer 10 years and lifetime warranties for the Hyundai Ioniq). The battery replacement cost (USD 5000–15,000) may determine the vehicle's lifespan, which is approximately 13 years for ICE vehicles [14]. EV resale value depreciation versus ICE resale value depreciation may represent the greatest operational cost if the battery does not last. Fortunately, the majority of studies indicate that EV batteries will outlive the vehicle, with over 70% of their charging capacity remaining after 13 years of use. One can anticipate a loss of 2.3% of range per charge for every year driven, which equates to approximately 13 years or 240,000 km driven before the charging capacity falls below 70% of its initial capacity [31]. According to industry sources, if the original battery is large enough, a 50% charge may suffice for the majority of usage, extending the EV's lifespan to 20 years. The Nissan Leaf has been on the market for thirteen years, and a significant number of original vehicles are still on the road. Tesla also reports empirical data of average EV utilization of 300,000 km in the United States and 244,000 km in Europe [32]. Tony Seba,

a Stanford technology forecaster, states in a recent report by RethinkX from March 2023 that the longevity and autonomy of EVs will be such that sales of new automobiles will plummet by 75% over the next 20 years, giving some hope that EV depreciation will not outweigh ICEs and that operational costs (OPEX) will be lower [33]. He also predicts that the EVs will take over the ICEs much faster than predicted based on his S-curve cost-lowering predictions for emerging technology, and that Chinese-made EVs will take over as the mainstream consumer choice in the very near future because of value for money and technology and quality improvements while lowering the cost per MW of charging capacity in production of the EV battery.

On the other hand, it is a known fact that EV batteries degrade more quickly, and the majority of studies on the durability of EV batteries were conducted in Europe or North America. The Kuwait Institute of Scientific Research (KISR), the national laboratory of Kuwait, has conducted its own research with promising results [34,35]. However, due to the lack of years that EVs have existed in Kuwait, real-world empirical data are still deficient and do not provide conclusive evidence regarding how long EV batteries will last in extreme heat conditions. The Kingdom of Saudi Arabia (KSA) recently bought a controlling stake in US Lucid Motors with the intention of producing a quarter of the production in KSA or a total of half a million vehicles by 2030 and the first car by 2025. Similarly, the Investment Promotion Agency Qatar is exploring if the country can be an EV manufacturing hub for the Middle Eastern (Arab) region in cooperation with German Volkswagen and Chinese Gaussin and Yutong, with whom the Qatari government has already partnered [36]. It is clear that the issue of EV driving with atmospheric heat reaching above 50 °C has to be dealt with both in terms of battery cooling and durability of the battery. In normal driving conditions for EVs, which are between 10 °C and 40 °C, the battery is at its nominal use capacity; at higher temperatures, the use capacity decreases, and between 60 °C and 70 °C the battery could sustain permanent damage [37].

2.6. EV Policies of the Kuwait Government as Opposed to Qatar

The Government of Kuwait will have to set goals of its transitions from conventional ICE vehicles to EVs, which in turn can offer a tremendous opportunity to reduce GHG emissions. The government of the State of Kuwait has pledged to the UN to reduce its carbon footprint as a vital share of its own national vision of 2035, which in particular contains a sustainability objective that promotes urgent actions to be implemented to fight off climate change effects [38,39]. However, conversion to EVs is not mentioned in these documents.

Qatar's national vision, much like the Kuwaiti Vision 2035, serves as a guide for the country's social, economic, environmental, and human development. However, in Qatar's vision, commitment has already been made to achieving a 25% reduction in greenhouse gas emissions by 2030. The Qataris plan to achieve this goal by converting all public transportation to electric vehicles, as well as giving significant governmental supports to various initiatives to transition to green mobility. Qatar's 'Electric Vehicle Strategy 2021' anticipates that EV sales will account for 10% of total vehicle sales in Qatar by 2030, contributing to the CO_2 reduction goals of the Paris Agreement [40].

2.7. Fast-Charging Stations in Kuwait and Qatar

Apart from the need for clear governmental goals on EV transformation, the automotive dealers in Kuwait state that the biggest hurdle for rapid mass adoption of EVs is the lack of fast-charging stations. Currently, there are no fast direct current (DC) to DC charging stations installed in Kuwait, and only 38 slow alternating current (AC) to DC charging stations spread around urban areas of Kuwait. The EV-charging facility provider ChargedKw recommends as a start to install one fast-charging station at every of the 150 gas stations in Kuwait, but due to a backlog of orders with the suppliers, the bidding process completion of this installment is likely to take 2.5 years from the initial tender, and the likely cost will be around KD 2.3 million, which is equivalent to nearly USD 8 million [41,42].

Qatar, which has half the land mass and population of Kuwait and lies 800 km south of Kuwait, is considerably father ahead in the installation of fast charging stations. As of the end of 2022, there were 100 such stations installed, and 150 installations are scheduled for 2023. Mohamed Khalid al-Sharshani, the head of the technical section at Tarsheed, which is the National Program for Conservation and Energy Efficiency, states that 600–1000 such stations will be installed by 2025 [43,44]. The rise of the fast-charging station has spurred the electrification of public transport: "We have crossed the target of converting 25 percent of the public transportation into eco-friendly mode. The public and school transportation will be completely eco-friendly by 2030", states the Minister of Transport Jassim Saif Ahmed Al Sulaiti [45,46]. Apart from aiming for 100% electric public transport by 2030, Qatar authorities still have a modest goal of transforming only 10% of all new sales in all sectors of transportation to electric, as many will be reluctant to change from their ICE vehicle given the low price of gasoline of QR 2 per liter, or about USD C 50 [47].

3. Literature Review

In general, the existing literature suggests that successful transformations and transitions are required to increase the adoption of sustainable e-mobility and surmount barriers to its adoption. While practitioners, academics, and researchers have studied the EV phenomenon on an international scale and with country-specific evidence, limited evidence has been found, however, from an emerging market of Kuwait. Apparently, there is insufficient research that has been conducted among drivers of ICE vehicles that aims to know their future stated preferences for EVs. This study had three goals: (i) to examine Kuwaiti ICE vehicle drivers' indicated perceptions of EV attitudes; (ii) to identify their preferable EV features; (iii) to determine their prospective EV purchase requirements and conditions. This research is part of a larger initiative that examines the EV landscape in Kuwait and utilizes a mixed-methods approach [48].

In summary, the recent EV literature reviews emphasized the following stated attributes for EVs:

(1) Economic: upfront purchasing prices, maintenance and repairs cost, protection and insurance cost, charging costs [49,50], and guarantees costs [51,52];
(2) Technology characteristics: battery, range, top speed, and acceleration [53–55];
(3) Infrastructure characteristics, including sluggish and rapid-charge networks, commercial and charging public infrastructures, and home-recharging infrastructures [56];
(4) Financial, nonfinancial, and social attributes: free parking spots, price reduction, government subsidy policies, health policies and safety policies [57], tax-discount policies, and penalty policies for petrol-fueled vehicles [58];
(5) Brand attributes: design, brand reputation, and credibility [59].

Interestingly, few studies were found that aimed to investigate these aforementioned attributes. In the following respects, the present study complements the current literature as follows: first, the current study applies five categories of attributes, including economic, technical, infrastructure, brand, and financial and nonfinancial policy attributes, collectively and exhaustively on a single set of options for EV preferences. Importantly, the attributes have not been investigated collectively in a single study; rather, they have been analyzed in various existing studies. Second, indeed, the present investigation focuses on conventional automobile drivers that have never been investigated. Lastly, the current research closes a void in the literature on EV trends in terms of demographics and stated preferences through a large sample survey collected in Kuwait. As the six gulf countries share similar societies, cultures, economies, government policies, climates, and geography, the present study contributes to the growing body of knowledge that can be applied to consumers in other GCC countries—Oman, the Saudi Arabian Peninsula, along with Bahrain, Qatar, and the UAE—regarding markets and stated preferences for EVs. Most studies focused on markets in developed nations such as Europe, the United States, and Australia. For instance, Guerra and Daziano analyzed a large sample of respondents' EV purchase motivations in the United States. Consumers were generally willing to pay more for longer-ranging

vehicles with shortened recharging periods, reduced operating costs due to scheduled and unscheduled maintenance, and shorter parking and charge facility search times, according to their findings [60].

By contrast, ICE vehicles continue to be perceived as more comfortable in terms of design and appearance than EVs, particularly among senior consumers. Moreover, women were discovered to be more environmentally conscious than males. Ziemba discovered that, in Poland, consumer EV acceptability is most strongly influenced by technological standards [61]. For instance, Vilchez conducted a large-scale survey among vehicle owners in a number of European nations, including Italy, France, Germany, Spain, Poland, and the UK, and found that half of the participants did not prefer EVs due to the higher initial capital cost (CAPEX)—a higher cost than conventional automobiles [62]. Fortunately, a recent study conducted by Temple found that the production of new batteries (lithium-metal batteries) could make EVs as affordable and convenient as gasoline-powered vehicles, indicating an anticipated increase in the adoption rates among car drivers worldwide as a result of technological development [63].

Kowalska-Pyzalska examined consumer preferences for alternative-fuel vehicles or electric vehicles (EVs) in Central and Eastern European nations and found that safety attributes are one of the most sought-after characteristics of EVs, followed by price, range, and brand [64]. Their findings require automakers and policymakers to actively promote electric vehicles in order to increase their adoption rates. Chao Ma analyzed the preferences of Chinese consumers for electric vehicles and found that purchase price, vehicle category, and fast-charging batteries were the most influential factors. Government policy is crucial in promoting the adoption of electric vehicles [65].

4. Methods

This study employed a quantitative descriptive approach consisting of mainly closed-ended questions to accomplish its research objectives by designing a large-scale questionnaire survey to provide a comprehensive, all-inclusive perspective on EVs in Kuwait. The first section of the extensive survey centered on respondents' demographic information, such as their gender, age, level of education, income ranges, occupation, ethnicity, and vehicle ownership. In order to measure the respondents' approach to willingness-to-buy or pay, the second section of the extensive survey consisted of exhaustive questionnaires about EV features, factors, and attributes that have been intensively discussed by the majority of the existing and updated strands of the literature. In addition, the large-scale survey was distributed to and evaluated by 50 full-time instructors and part-time educators, who provided their views and recommendations. The assessment phase comprised inquiries regarding objective, content, and layout of the questionnaire. We received 30 completed evaluations in total as part of the validation process. The overall response rate was near 60%. We subsequently incorporated the suggested modifications and revised the questionnaire's format and overall design proposed mainly by AOU instructors. To make the questionnaire easier to complete, we omitted several sections and treated it as a unit. In addition, we added the response option "I don't know" in order to collect honest responses and permit the free expression of opinions. The evaluation revealed that approximately 96% of the questionnaire's content is unambiguous, informative, and simple to understand. Similarly, 93 percent of questionnaire objectives are clearly specified, the content is relevant, and the order is logical. Of the respondents, 90 percent indicated that the content is correct and complete, and the layout is workable, and 86 percent agreed that the structure is straightforward. We developed two variants of the questionnaire; one version was written in the Arabic language and another in the English language. We used Google Forms to formulate the survey because it is one of the commonly used, validated tools for data collection. The questionnaire was then disseminated to diverse groups in Kuwait, including the general public, faculty members, students, and tutors. Participants had to be Kuwaiti citizens and 18 years of age and also hold a driver's license and a car in their own or family name in order to be eligible for the survey. We proposed this condition as many Kuwaitis use private

drivers to get around and do not possess a driving license. We believe that purchasing behavior for a car that is driven by a driver is different than purchasing behavior for a car that is driven by the owner. We started the data-collection phase from February to May of 2022. A technique of random sampling was utilized during the data-collection phase [66]. The researchers distributed the survey links by randomly selecting the target audience from diverse groups of individual nationals in Kuwait inclusive of mature students, instructors, professionals, and others. Moreover, the study sample included a few Kuwait individuals with temporary or permanent car-ownership contracts such as rental or a company car. Those were contractual employees who were provided with ICE automobiles from their employing companies with petrol paid.

Initially, we collected a large sample size (604) in order to obtain comprehensive demographic data representative of the population in Kuwait and to draw actionable conclusions about the population. Subsequently, we eliminated around 132 surveys because our aim was not to include those who never drive a car or had no driving license, and we ended up with a total of 472 questionnaires that were analyzed, and these data were used for our current analysis. However, after observing how Kuwaiti nationals had different EV purchasing behavior from the expat population, due to strict rules and restrictions expats have to adhere to in order to obtain a driver's license within the State of Kuwait, as well as expats not being allowed to own real estate and landlords not permitting installation of home charging for EVs, and as a result almost all EV buyers to date have been Kuwaiti nationals, after careful selection, we isolated the Kuwait nationals in our sample and obtained a reduced sample of 227 Kuwaiti nationals who owned and drove conventional vehicles.

At the beginning of the data-collection phase, the purpose and aims of the study were introduced to the participants and thoroughly explained. Additionally, instructions were written on the front page to prevent confusion. Then, we invited participants to complete the survey online. Finally, descriptive statistics—frequencies and percentages—were computed using SPSS 19, applying *t*-test and AVOVA tables for in-depth analysis and standard error analysis. Note that this particular endeavor has certain limitations. Because the sample was gathered from a single location, the Arab Open University in Kuwait, we are precluded from generalizing to the context of all Kuwaiti drivers. In fact, additional research with a larger sample size is required on this specific topic. For example, in-depth investigations are necessary to uncover concealed insights regarding the acceptance and preferences associated with EV use among EV owners. One of the requirements for participation in the survey was automobile ownership. In 2021, approximately 3 million vehicles were registered in the country [14]. Excluding company-owned and expat-registered vehicles, we estimate that approximately 1.6 million registered vehicles were owned by Kuwaiti citizens. Here, we examined prospective buyers and, hence, we estimated that forty percent of the population, or 6,400,000, were included in the group of prospective Kuwaiti drivers. The sample consisted of 227 Kuwaiti drivers and vehicle proprietors, or approximately 0.04 percent of the total representative population, which is modest and, if not for our resource limitations, would have ideally included at least 1000 participants. Consequently, our margin of error is approximately ± 7 percent, which translates to a 95% confidence level [67].

5. Findings

This investigation included the participation of two-hundred twenty-seven Kuwaiti ICE owners who possessed driving licenses. Table 1 provides a demographic characteristics summary. The questionnaire was completed equally by men (50.2%) and women (49.8%). More than three-quarters of the sample were between 26 years old and 39 years old (76.2%). Over one-third were unmarried (37.4%), while 25.6% were married with at least three children. Over fifty percent held bachelor's degrees. More than a fourth of respondents owned five or more automobiles (40.1%), and more than a quarter of them owned two automobiles (28.2%). More than half of the participants (53.3%), versus slightly above a

quarter (26%), were working in the public and private sectors, respectively. Over one-third of the sample (39.6%) worked in the public and government ministries sector, and a quarter (25.6%) were intermediate managers. A total of 32.6% of the participants had a monthly income of between KD 1000 and 1499.

Table 1. Demographic characteristics summary.

Variable	Categories	N = 227	%
Gender	Male	114	50.2%
	Female	113	49.8%
Age Range	26–39 years	173	76.2%
	40–49 years	42	18.5%
	50–60 years	12	5.3%
Marital Status	Single	85	37.4%
	Married without kids	24	10.6%
	Married with 1 kid	26	11.5%
	Married with 2 kids	34	15.0%
	Married with 3 kids or more	58	25.6%
Number of Cars in household	One car	12	5.3%
	Two cars	64	28.2%
	Three cars	27	11.9%
	Four cars	33	14.5%
	Five cars & more	91	40.1%
Educational Level	Less than high school	4	1.8%
	High School diploma	46	20.3%
	Trade/Commerce degree	39	17.2%
	Bachelor's degree	114	50.2%
	Master's degree	19	8.4%
	PhD	5	2.2%
Employment	Public sector	121	53.3%
	Private sector	59	26.0%
	Unemployed	21	9.3%
	Self-employed	14	6.2%
	Family-owned business	12	5.3%
Field of employments	Government & Ministries	90	39.6%
	Other private services	32	14.1%
	Educations-government & private	25	11.0%
	Oil and Gas sector	23	10.1%
	Large Kuwaiti corporation	20	8.8%
	My family business	19	8.4%
	Military or police	11	4.8%
	Health Care–government & private	7	3.1%

Table 1. *Cont.*

Variable	Categories	N = 227	%
Which of the following best describes your role in industry?	Middle Management	58	25.6%
	Administrative Staff	46	20.3%
	Upper Management	29	12.8%
	Lower Management	22	9.7%
	Support Staff	15	6.6%
	Temporary Employee	12	5.3%
	Trained Professional expert	12	5.3%
	Self-employed/Business Partner	11	4.8%
	Student-Not working	7	3.1%
	Researcher	6	2.6%
	Skilled Laborer	5	2.2%
	A Consultant	4	1.8%
Monthly Income	Less than 500 KD	22	9.7%
	500–999 KD	44	19.4%
	1000–1499 KD	74	32.6%
	1500–1999 KD	50	22.0%
	2000 and above	37	16.3%

Table 2 displays the participants' perspectives on EVs. More than forty percent of respondents (41.8%) stated that they would be willing to pay an extra 6–20%, while one-third (33.5%) stated that they would pay no more than 5% more. More than one-third of participants (37.8%) would pay 6–20% extra for EVs, which they viewed as significantly faster than a corresponding ICE vehicle (0–100 km per hour in 4 s), while approximately one-fifth (19.4%) declared that they would pay nothing extra. More than 42% of participants (42.7% to be exact) indicated that they would seriously contemplate purchasing EVs if gasoline/fuel prices would go up by 50–199%, while about 18.5% were indifferent to gasoline price changes. Over 50% (54.7%) indicated that they would contemplate purchasing an EV if and only if the government controlled the prices of EVs and offered a price reduction, making them 10–30% less expensive than gasoline vehicles, whereas roughly one-fifth (18.9%) suggested that they would change their minds if the prices were comparable to gasoline vehicles. A third of participants (29.1%) would consider purchasing EVs under the condition of the availability of rapid-charging points every 10–25 km, and a quarter (24.2%) would consider purchasing EVs if there were fast-charging stations every 26–50 km.

More than half of respondents (57.7%) responded that they would reconsider purchasing an electric vehicle under the condition of the availability of a dedicated express lane located on major highways. More than 50% (53.3%) indicated that they would reconsider purchasing an EV under the condition of the availability of free public parking spaces for EVs in an amount comparable to handicapped spaces. Also, 56% said they would purchase an EV within the next three years. Of these, 14.1% suggested that they would definitely purchase an EV, while 41.9% said that they would likely do so. A total of 46.2 percent cared about the security of EVs regarding fire and accidents; 43.2% were concerned about being able to recharge their EVs around their residential areas; however, 30.8 percent stated that they would not be able to charge their EVs in their residential areas.

Table 2. Attitudes and preferences.

Question	Categories	N = 227	%
Preferred price increases for EV	0%	42	18.5%
	1–5%	34	15.0%
	6–10%	55	24.2%
	11–20%	40	17.6%
	21–29%	22	9.7%
	30% and more	34	15.0%
Preferred speed range (0–100 kmh in 4 s)?	0%	44	19.4%
	1–5%	40	17.6%
	6–10%	43	18.9%
	11–20%	43	18.9%
	21–29%	29	12.8%
	30% and more	28	12.3%
Preferred price increase brackets for gasoline cars that would push you to think of buying an EV.	500% and above	8	3.5%
	400–499%	8	3.5%
	300–399%	12	5.3%
	200–299%	22	9.7%
	100–199%	53	23.3%
	50–99%	44	19.4%
	Less than 50%	38	16.7%
	Indifferent	42	18.5%
Prefer that the government regulates and controls the purchasing costs of EVs to be _____.	30% cheaper costs than ICE cars	78	34.4%
	10% cheaper costs than ICE cars	46	20.3%
	The same costs as ICE cars	43	18.9%
	10% higher costs than ICE cars	26	11.5%
	Indifferent	34	15.0%
Preferred fast charging stations every _____.	Less than 10 km	35	15.4%
	10–25 km	66	29.1%
	26–50 km	55	24.2%
	51–75 km	28	12.3%
	76 km and more	11	4.8%
	Indifferent	32	14.1%
Prefer a fast lane dedicated to EVs on major highways (such as on highways *30* and *40*)	No	45	19.8%
	Yes	131	57.7%
	Indifferent	51	22.5%
Preferred public and free parking spaces almost at the same capacity as handicapped spaces.	No	57	25.1%
	Yes	121	53.3%
	Indifferent	49	21.6%
Are you interested on purchasing an EV in the future?	Of course, not	34	15.0%
	Unlikely	66	29.1%
	Very likely	95	41.9%
	Certainly	32	14.1%

Table 2. *Cont.*

Question	Categories	N = 227	%
Level of safety concerns regarding EVs in Kuwait, in terms of fire and car crashes	Hazardous	18	7.9%
	Unsafe	22	9.7%
	Neutral	82	36.1%
	Safe	48	21.1%
	Very Safe	57	25.1%
The possibility of charging your EVs in residential areas in Kuwait	Very impossible	38	16.7%
	Impossible	32	14.1%
	Neutral	59	26.0%
	Possible	31	13.7%
	Very possible	67	29.5%

The following scale shows:

- High agreement: with a calculated mean (M) $\geq$ 2.33;
- Medium agreement: with a calculated mean of 1.67 $\leq$ M < 2.33;
- Low agreement: with a calculated mean < 1.67.

The highest agreement among contributors (Table 3) was regarding three EV-related issues: the environmental friendliness and lower CO_2 emissions of EVs, which leads to improved quality of breathable air (M = 2.43); significantly low fuel price (M = 2.35); and a silent engine (M = 2.33). Features with moderate agreement included improved fire and collision safety (M = 2.31), quicker and better A/C conditioning (M = 2.30), significantly faster acceleration (0–100 km/h) (M = 2.20), and notably reduced maintenance costs (M = 2.19).

Table 3. The most preferred features.

Types of Attributes	The Most Preferred Features	Mean	Std
Environmental	EVs are ecofriendly with low CO_2 emissions, leading to better air quality	2.43	0.780
Financial	Lower price than petrol	2.35	0.797
Technological	Quiet engine	2.33	0.810
Technological	Raised safety concerns—crash and fire	2.31	0.788
Technological	Faster and more powerful air conditioning	2.30	0.781
Technological	Fastest acceleration (0–100 kmh)	2.20	0.804
Financial	Lower maintenance and repair costs	2.19	0.856

Regarding the perceptions of EV purchasing, as indicated in Table 4, the sample highly agreed on the following five conditions: the preferred range of fully charged EVs should be at least 400 km (M = 2.40), the preferred battery guarantee should remain 10 years at least or after 150,000 km (M = 2.39), fast-charging stations must be located within a 5 km radius (M = 2.38), and preference of the coolness and uniqueness of EV designs (M = 2.38); the remaining preferred requirements had moderate agreement, such as spotting a change in air quality once people started to drive EVs (M = 2.32); preferred price ranges should be similar or equivalent to a gasoline car (M = 2.31); purchasing an EV if gasoline prices would increase threefold (M = 2.28); distinct lanes dedicated to EVs on motorways (M = 2.26); that a majority of respondents' friends or family would purchase an EV (M = 2.02).

Table 4. Perceptions regarding EV purchase (N = 227).

Attributes	The Preferred Criteria for Purchasing an EV	Mean	SD
Technological	The driving range of a fully charged EV should be min. 400 km	2.40	0.759
Financial	Battery guarantee should remain 10 years at least or after 150,000 km	2.39	0.770
Infrastructure	Fast-charging stations should be located within a 5 km radius	2.38	0.751
Brand	Coolness and uniqueness of design	2.34	0.767
Financial	Resale value should be on par with or higher than an ICE car	2.33	0.770
Social attributes—pro-environmental	Improvement in air quality	2.32	0.779
Financial	Price should be the same or lower than a gasoline car	2.31	0.832
Financial	Gasoline prices would increase three-fold	2.28	0.809
Infrastructure	Distinct EV lanes located on motorways	2.26	0.790
Social acceptance	Family and friends would buy an EV	2.02	0.801

6. Discussion

The proposed study investigated the attitudes, preferences, and needs of fuel-vehicle drivers regarding EVs. Intriguingly, the study discovered that more than half suggested that they preferred to purchase an electric vehicle over the period of the next three years. Respondents provided the following four conditions: (i) the policymakers and government should regulate and mitigate the cost of electric vehicles by 10 to 30 percent to make them more affordable than gasoline vehicles; (ii) public fast recharging points and facilities should be accessible and spread out at least within a 10 to 50 km radius everywhere in Kuwait; (iii) specific EV fast lanes should be available on the most congested freeways.

Consequently, these findings suggest that potential EVs drivers viewed Kuwaiti regulators as playing a crucial role in promoting EVs' reputation and recognition by planning appropriate EV transportation infrastructure and establishing policies for regulating prices. Intriguingly, our results largely mirror the results of prior research conducted for various nations. In addition, nearly 40 percent of respondents suggested that they contemplated purchasing EVs if gasoline prices increased by 50 to 199 percent in the future, recognizing that EVs are still safer during fires and accidents.

Furthermore, more than a third of respondents suggested that they were willing to pay 6 to 20 percent more for EVs than for petroleum vehicles, believing that EVs are more environmentally friendly and speedier than gasoline vehicles. This intriguing finding suggests that people in Kuwait prefer EVs to petroleum vehicles because EVs offer greater environmental, economic, and technological benefits. Similar results have been found in various countries. However, about a third of residents (mainly expats) in Kuwait's residential locations are unable to charge electric vehicles. This implies that infrastructure for charging EVs must be nearby and readily available in all Kuwaiti inhabited zones. In addition, drivers favored three distinct types of EV attributes, including environmental attributes (i.e., ecological; low CO_2 emissions, which improves air quality), financial or economic attributes (i.e., much cheaper fuel price than gasoline), and technological attributes (i.e., soundless engine), which concurs with this intriguing finding.

By contrast, the current Kuwaiti ICE drivers' sample would apparently be willing to acquire EVs within the near future because they believe that EVs' technological attributes (i.e., driving range might be at least 400 km), financial or economic attributes (i.e., battery guarantee lasts 10 years or more or 150,000 km; resale EV value should be similar to or higher than fueled vehicles), and infrastructure attributes (rapid-recharging points within 5 km) could justify it. This finding suggested that the current Kuwaiti ICE drivers' sample may acquire EVs in the near future if four criteria were met: the batteries' affordability and resale value, the infrastructure's proximity of fast-charging stations, the technological features' range, and the brands with cool and attractive designs. These findings are consistent with previous cases from various nations.

While the current study provides a broader perspective on the EV phenomenon in Kuwait, it does have some limitations. Because it lacks emphasis on empirical testing to

provide clearer conclusions about the population, the findings are primarily descriptive and furthermore based on stated (rather than revealed) preferences. Therefore, future research should employ hypothesis testing to reach a definitive general inference in Kuwait. Second, additional research must employ in-depth investigations with existing EV possessors to investigate any obstacles, identify any future opportunities, and identify favorable EV characteristics and preferred designs. One suggestion is to use a focus group to obtain a more complete image of the desired features and services, as well as to determine the most effective incentives for purchasing EVs in Kuwait and the MENA region. In addition, comparative studies from various GCC regions may be of interest because the regions operate under a similar legal and economic umbrella. Lastly, additional research should investigate the management perspectives of car dealerships in Kuwait in order to examine the obstacles that are delaying the adoption and sustained mobility models for electric vehicles (EVs), clarify ambiguity surrounding EV adoptions in Kuwait, and provide a better explanation and rationale for the reluctance to replace conventional vehicles.

7. Conclusions and Implications

Other than eliminating all government subsidies for water, electricity, and petroleum, the mass transition from ICEs to EVs is the most effective strategy for reducing Kuwait's carbon footprint if EVs are charged with electricity from renewable energy sources. However, due to a total lack of rapid-charging EV stations (direct current to direction current, DC2DC) and Kuwaiti landlords not permitting the installation of EV charging-wall receptacles, ICE to EV transition is only an option for Kuwaiti citizens who own their homes. Due to a backlog of orders and formal tendering processes in Kuwait, it will take up to four years to construct an effective fast-charging station network. This study has therefore focused predominantly on Kuwaiti nationals' stated preferences and attitudes toward electric vehicles. The current study presented substantial evidence and diversified stakeholder perspectives for the emerging market of Kuwait. The main goal here is to investigate the sustainability of EVs. The outcome showed that potential Kuwaiti customers anticipate purchasing an EV within the near future—three years—but only under specified criteria, such as the availability and readiness of appropriate infrastructure such as recharging facilities, rapid roads, and free public parking. In addition, they were willing to purchase EVs and strongly preferred EVs for their ecological, economical, and technological attributes, but only under four conditions: battery cost and resale value, accessible fast-recharging facilities (infrastructure), technological features in terms of range per full charge, and brand value and appealing design.

In light of the preceding findings, the existing investigation has both theoretical and practical implications. Theoretically, the present research supports the scant literature on sustainable mobility in developing nations, particularly MENA-GCC and Kuwait. The findings could facilitate broader comparisons and more accurate assessments for developing nations, including those in the MENA-GCC region. In practice, the results of this study indicate that Kuwaitis prefer EVs over petroleum vehicles because EVs offer environmental advantages, economic benefits, and technological advantages. Consequently, vehicle dealership marketing campaigns should emphasize the utility of electric vehicles (EVs) when promoting EVs to their target markets, vehicle commuters and vehicle proprietors. In addition, the results indicate that Kuwaitis may be prepared to purchase EVs if and only if infrastructure related to the availability of rapid recharging stations and facilities, fast traffic lanes, and free parking spaces is in place. Hence, policymakers and government regulators are encouraged to initiate the construction of infrastructure to facilitate the rapid acceptance of electric vehicles in the country.

EVs offer substantial environmental benefits that contribute to promoting the use of renewable energy, reducing both urban air pollution and greenhouse gas (GHG) emissions, and thereby reducing human health hazards associated with GHG exposure. Therefore, we propose that the government execute knowledge policies to promote knowledge plan to better teach the people of Kuwait about preservation of the environment and sustainability

issues. In addition, we propose for the policymakers in Kuwait to provide sponsorship and funding programs along with other financial assistance to EV purchasers to prevent the high price of EVs. Moreover, the government should construct accessible and appropriate infrastructure, including a wide network of recharging facilities. Thus, consumers could refuel their EVs from renewable sources of energy and prevent their EVs from running out of electricity. Additionally, highways should be enhanced and better developed for EV drivers than previously.

The study results indicate that Kuwaitis might purchase EVs in the future if infrastructure regarding rapid recharging stations were readily available and easily accessible. Therefore, policymakers must construct and provide these stations to promote the adoption of electric vehicles. Kuwaitis would apparently purchase EVs for economic reasons, particularly regarding battery life and resale value. Therefore, manufacturers of electric vehicles should develop heat-tolerant longer-lasting batteries. As Kuwaitis would apparently purchase EVs due to technological attributes relating to range per complete charge and brand attributes, manufacturers should attempt to design EVs with these characteristics. As EVs are very efficient in generating energy from the source to the wheels and efficient as a tool to reduce greenhouse gas emissions as well as other forms of air pollution, the automobile industry should gradually shift toward their implementation.

Author Contributions: A.O. is the project's Principal Investor (PI) and is responsible for its conception, methodology, and editing, as well as the acquisition and administration of funds. S.B. and B.A. were accountable for the literature review, conceptualization, synthesis, methodology, validation, formal analysis, data curation, writing preparation of the original document, and editing. All authors have read and agreed to the published version of the manuscript.

Funding: This paper is a part of wider study called "Breaking the ICE reign: mixed method study of attitudes towards buying and using EVs in Kuwait". The study was funded by the Kuwait Foundation for the Advancement of Sciences and administrated by the London School of Economics and Political Science—Middle East Center (Grant number KFAS-MEC LSE 2021 001), and received an LSE Research Ethics Committee approval.

Institutional Review Board Statement: This study has been approved by the London School of Economics and Political Science Ethics Committee (00558000004KJE9AAO, dated 24 November 2021). Consent Form Statement: As directed by the LSE Ethics Committee, an informed statement about the utilization and purpose of the study was included in the questionnaire.

Data Availability Statement: Not applicable.

Conflicts of Interest: The authors declare no conflict of interest.

References

1. Ottesen, A.; Toglaw, S.; AlQuaoud, F.; Simovic, V. How to Sell Zero Emission Vehicles when the Petrol is almost for Free: Case of Kuwait. *J. Manag. Sci.* **2022**, *9*, 1–20. [CrossRef]
2. Ottesen, A.; Banna, S.; Alzougool, B.; Damrah, S. *A Greener Kuwait—How Electric Vehicles Can Lower CO_2 Emissions*; LSE Middle East Center Kuwait Programme Paper Series 18; LSE Middle East Centre: London, UK, 2023; pp. 1–21. Available online: http://chrome-extension://efaidnbmnnnibpcajpcglclefindmkaj/https://eprints.lse.ac.uk/120091/1/A_greener_Kuwait_paper_series_18.pdf (accessed on 10 August 2013).
3. Ottesen, A.; Thom, D.; Bhagat, R.; Mourdaa, R. Learning from the Future of Kuwait: Scenarios as a Learning Tool to Build Consensus for Actions Needed to Realize Vision 2035. *Sustainability* **2023**, *15*, 7054. [CrossRef]
4. Djoundourian, S.S. Response of the Arab world to climate change challenges and the Paris agreement. *Int. Environ. Agreem. Politics Law Econ.* **2021**, *21*, 469–491. [CrossRef]
5. Sharp, D.S.; Alshamari, A.; Hameed, K. *The Quiet Emergency: Experiences and Understandings of Climate Change in Kuwait*; LSE Middle East Center Kuwait Programme Paper Series 13; LSE Middle East Centre: London, UK, 2021; Available online: http://eprints.lse.ac.uk/112491/3/The_Quiet_Emergency.pdf (accessed on 6 June 2023).
6. New Kuwait. Kuwait National Development Plant 2020–2025. 2019. Available online: https://media.gov.kw/assets/img/Ommah22_Awareness/PDF/NewKuwait/Revised%20KNDP%20-%20EN.pdf (accessed on 26 August 2023).
7. Energy Strategy: Technical Paper Summary. In *4th Kuwait Master Plan: 2040 Toward A Smart State*; Municipality of Kuwait: Kuwait City, Kuwait, 2021; p. 65.
8. Ottesen, A.; Banna, S. Why so few EVs are in Kuwait and how to amend it. *Int. J. Eng. Technol.* **2021**, *10*, 181–189. [CrossRef]

9. Navfal, M. (KIA Kuwait, Kuwait City, Kuwait). Personal communication, 2023.
10. InsideEV Norway. Plug-In Car Sales Exceeded 90% Share in June 2023. Available online: https://insideevs.com/news/675163/norway-plugin-car-sales-june2023/#:~:text=New%20passenger%20plug%2Din%20car,more%20substantial%20growth%20over%202022 (accessed on 11 September 2023).
11. Norway Electric Vehicle Association. EV Norway. 2023. Available online: https://elbil.no/english/about-norwegian-ev-association/ (accessed on 11 September 2023).
12. ChargedKW. Charging Station Location. 2023. Available online: https://www.chargedkw.com/where-to-charge (accessed on 11 September 2023).
13. Ottesen, A.; Banna, S.; Alzougool, B. Attitudes of Drivers towards Electric Vehicles in Kuwait. *Sustainability* **2022**, *14*, 12163. [CrossRef]
14. Central Statistical Bureau. Kuwait Number of Register Vehicles in Use. 2021. Available online: https://www.ceicdata.com/en/kuwait/number-of-registered-vehicles/no-of-registered-vehicles-in-use#:~:text=The%20data%20reached%20an%20all,Global%20Database\T1\textquoterights%20Kuwait%20%E2%80%93%20Table%20KW (accessed on 6 June 2023).
15. Ottesen, A.; Banna, S.; Alzougool, B. How to Cross the Chasm for the Electric Vehicle World's Laggards—A Case Study in Kuwait. *World Electr. Veh. J.* **2023**, *14*, 45. [CrossRef]
16. Abu Dagga, N. E-Mobility—Electric Vehicles Technology and Innovation. In Proceedings of the Presentation at Australian University, Technology Leading to Sustainability—The Future of Mobility, West Misref, Kuwait, 8 May 2023.
17. Anagnostopoulou, E.; Bothos, E.; Magoutas, B.; Schrammel, J.; Mentzas, G. Persuasive technologies for sustainable mobility: State of the art and emerging trends. *Sustainability* **2018**, *10*, 2128. [CrossRef]
18. Apostolaki-Iosifidou, E.; Codani, P.; Kempton, W. Measurement of power loss during electric vehicle charging and discharging. *Energy* **2017**, *127*, 730–742. [CrossRef]
19. Geng, J.; Gao, S.; Sun, S.; Liu, Z.; Zhao, F.; Hao, H. Potential of electric vehicle batteries second use in energy storage systems: The case of China. *Energy* **2022**, *253*, 124159. [CrossRef]
20. Electrek. This Solar + Storage System is Made Up of 1300 Second Life EV Batteries. 2023. Available online: https://electrek.co/2023/02/07/this-solar-storage-system-is-made-up-of-1300-second-life-ev-batteries/ (accessed on 26 August 2023).
21. McKinsey & Company. ESG Report—Creating a More Sustainable, Inclusive and Growing Future for All. 2022. Available online: https://www.mckinsey.com/about-us/social-responsibility/esg-report-overview (accessed on 26 August 2023).
22. Cole, W.; Frazier, A.W.; Augustine, C. *Cost Projections for Utility-Scale Battery Storage: 2021 Update*; National Renewable Energy Laboratory: Golden, CO, USA, 2021. Available online: https://www.nrel.gov/docs/fy21osti/79236.pdf (accessed on 26 August 2023).
23. Li-Cycle Company. A Unique and Dependable Approach to Solving the Global Battery Cycling Problem. 2023. Available online: https://li-cycle.com/technology/ (accessed on 26 August 2023).
24. Koestner, J. 6 Thing to Remember about Hydrogen vs Natural Gas. Power Engineers. Available online: https://www.powereng.com/library/6-things-to-remember-about-hydrogen-vs-natural-gas (accessed on 7 June 2023).
25. Conti, M.; Kotter, R.; Putrus, G. Energy Efficiency in Electric and Plug-in Hybrid Electric Vehicles and Its Impact on Total Cost of Ownership. In *Electric Vehicle Business Models*; Beeton, D., Meyer, G., Eds.; Lecture Notes in Mobility; Springer: Cham, Switzerland, 2015. [CrossRef]
26. Economist. How the Japan Is Losing the Global Electric-Vehicle Race. 2023. Available online: https://www.economist.com/asia/2023/04/16/how-japan-is-losing-the-global-electric-vehicle-race (accessed on 8 June 2023).
27. American Public Transportation. Public Transportation Fact Book. 2022. Available online: https://www.apta.com/research-technical-resources/transit-statistics/public-transportation-fact-book/ (accessed on 7 June 2023).
28. IEA. Global EV Outlook 2023. 2023. Available online: https://www.iea.org/reports/global-ev-outlook-2023 (accessed on 8 June 2023).
29. BloombergNEF. Electric Vehicle Outlook 2022. 2022. Available online: https://bnef.turtl.co/story/evo-2022/page/7/1 (accessed on 6 June 2023).
30. Munoz, J.F. Tesla Model Y World Best-Selling Car for Q1 2023. 2023. Available online: https://www.motor1.com/news/669135/tesla-model-y-worlds-best-selling-car-q1-2023/ (accessed on 27 August 2023).
31. Poornesh, K.; Nivya, K.P.; Sireesha, K. A Comparative study on Electric Vehicle and Internal Combustion Engine Vehicles. In Proceedings of the 2020 International Conference on Smart Electronics and Communication (ICOSEC), Trichy, India, 10–12 September 2020; pp. 1179–1183. [CrossRef]
32. Office of Energy Efficiency and Renewable Energy. Battery Electric Vehicles Have Lower Scheduled Maintenance Cost than Other Light-Duty Vehicles. 2021. Available online: https://www.energy.gov/eere/vehicles/articles/fotw-1190-june-14-2021-battery-electric-vehicles-have-lower-scheduled (accessed on 27 August 2023).
33. Forbes. By The Numbers: Comparing Electric Car Warranties. 2022. Available online: https://www.forbes.com/sites/jimgorzelany/2022/10/31/by-the-numbers-comparing-electric-car-warranties/?sh=4c832c553fd7 (accessed on 14 February 2023).
34. J.D. Power. How Long Do Electric Battery Last? 2022. Available online: https://www.jdpower.com/cars/shopping-guides/how-long-do-electric-car-batteries-last#:~:text=Generally%2C%20electric%20vehicle%20batteries%20last,not%20pair%20well%20with%20EVs (accessed on 17 June 2023).
35. EVBox. How Long Do Electric Car Battery Last? 2022. Available online: https://blog.evbox.com/uk-en/ev-battery-longevity#:~:text=According%20to%20current%20industry%20expectations,is%20nearly%20imperceptible%20to%20drivers (accessed on 17 June 2023).

36. Monta. See How Temperature Affects the Range of Your EV. 2023. Available online: https://monta.com/uk/blog/how-temperature-affects-ev-range/#:~:text=On%20average%2C%2021.5%20degree%20celsius,used%20to%20move%20the%20car (accessed on 11 September 2023).
37. RethinkX. Rethinking Transportation—Cost and Speed of Adoption. 2023. Available online: https://www.rethinkx.com/fullsummary (accessed on 17 June 2023).
38. Hamwi, H.; Alasseri, R.; Aldei, S.; Al-Kandari, M. A Pilot Study of Electrical Vehicle Performance, Efficiency, and Limitation in Kuwait's Harsh Weather and Environment. *Energies* **2022**, *15*, 7466. [CrossRef]
39. Hamwi, H.; Rushby, T.; Mahdy, M.; Bahaj, A.S. Effects of High Ambient Temperature on Electric Vehicle Efficiency and Range: Case Study of Kuwait. *Energies* **2022**, *15*, 3178. [CrossRef]
40. United States Official Website of the International Trade Administration. Qatar Electric Vehicles Challenges and Opportunities. 2022. Available online: https://www.trade.gov/market-intelligence/qatar-electric-vehicles-challenges-and-opportunities#:~:text=Qatar\T1\textquoterights%20EV%20strategy%20aims%20to,in%20motion%20in%20September%202021 (accessed on 24 April 2023).
41. Central Statistical Bureau. Kuwait Voluntary National Review. 2019 Report on the Implementation of 2030 High Level Political Forum on Sustainable Development. Available online: https://www.arabdevelopmentportal.com/publication/kuwait-voluntary-national-review (accessed on 20 August 2022).
42. Gulf Times. Kahramaa to Set Up 150 Electric Charging Stations in 2023—EV Charging Station Network to Be Expanded to about 1000 by 2025. January 2023. Available online: https://www.gulf-times.com/article/653048/qatar/kahramaa-to-set-up-150-electric-charging-stations-in-2023 (accessed on 25 April 2023).
43. Ottesen, A.; Banna, S.; Alzougool, B. Women Will Drive the Demand for EVs in the Middle East over the Next 10 Years. *Energies* **2023**, *16*, 3756. [CrossRef]
44. The Peninsula. Qatar Converts 25% Public Transit Fleet to Eco-Friendly Mode. 19 September 2022. Available online: https://thepeninsulaqatar.com/article/19/09/2022/qatar-converts-25-public-transit-fleet-to-eco-friendly-mode (accessed on 25 April 2023).
45. The Peninsula. QatarEnergy Announces Petrol and Diesel Prices for March 2023. 28 February 2023. Available online: https://thepeninsulaqatar.com/article/28/02/2023/qatarenergy-announces-petrol-and-diesel-prices-for-march-2023#:~:text=Premium%20petrol%20will%20cost%20QR,and%20diesel%20will%20cost%20QR2 (accessed on 25 April 2023).
46. Alrajhi, J.M.; Alardhi, M.; Alhaifi, K.K.; Alkhulaifi, K.; Khalfan, A.; Alhaifi, N.A.; Alazemi, J. Prediction of Electric Vehicle Charging Stations Distribution in Kuwait. *Int. J. Traffic Transp. Eng.* **2023**, *12*, 5–9. [CrossRef]
47. Kuwait Voluntary National Review. Report on the Implementation of the 2030 Agenda to the UN High-Level Political Forum on Sustainable Development, Retrieved 12.24.2021 [Online]. 2019. Available online: https://sustainabledevelopment.un.org/content/documents/23384Kuwait_VNR_FINAL.PDF (accessed on 25 April 2023).
48. Ottesen, A.; Banna, S.; Alzougool, B.; Simovic, V. Driving factors for women's switch to electric vehicles in conservative Kuwait. *J. Women's Entrep. Educ.* **2022**, *3*, 1–21. [CrossRef]
49. Contestabile, M.; Turrentine, T. Introduction: Understanding the Development of the Market for Electric Vehicles. In *Who's Driving Electric Cars: Understanding Consumer Adoption and Use of Plug-in Electric Cars*; Springer: Cham, Switzerland, 2020; pp. 1–8.
50. Zhang, Q.; Li, H.; Zhu, L.; Campana, P.E.; Lu, H.; Wallin, F.; Sun, Q. Factors influencing the economics of public charging infrastructures for EV—A review. *Renew. Sustain. Energy Rev.* **2018**, *94*, 500–509. [CrossRef]
51. Zhang, X.; Bai, X.; Shang, J. Is subsidized electric vehicles adoption sustainable: Consumers' perceptions and motivation toward incentive policies, environmental benefits, and risks. *J. Clean. Prod.* **2018**, *192*, 71–79. [CrossRef]
52. Colak, M.; Kaya, I. providing the spark: Impact of financial incentives on battery electric vehicle adoption. *J. Environ. Econ. Manag.* **2020**, *98*, 102255.
53. Li, W.; Long, R.; Chen, H.; Geng, J. A review of factors influencing consumer intentions to adopt battery electric vehicles. *Renew. Sustain. Energy Rev.* **2017**, *78*, 318–328. [CrossRef]
54. Lia, F.; Molina ETimmermans, H.; Wee, B.V. Consumer preferences for business models in electric vehicle adoption. *Transp. Policy* **2019**, *73*, 12–24. [CrossRef]
55. Liao, F.; Molin, E.; Wee, B.V. Consumer preferences for electric vehicles: A literature review. *Transp. Rev.* **2017**, *37*, 252–275. [CrossRef]
56. Lin, B.; Wu, W. Why people want to buy electric vehicle: An empirical study in first-tier cities of China. *Energy Policy* **2018**, *112*, 233–241. [CrossRef]
57. Archsmith, J.; Muehlegger, E.; Rapson, D. Future Paths of Electric Vehicle Adoption in the United States: Predictable Determinants, Obstacles and Opportunities. *Environ. Energy Policy Econ.* **2022**, *3*, 71–110. [CrossRef]
58. Kongklaew, C.; Phoungthong, K.; Prabpayak, C.; Chowdhury, M.S.; Khan, I.; Yuangyai, N.; Yuanngyai, C.; Techato, K. Barriers to electric vehicle adoption in Thailand. *Sustainability* **2021**, *13*, 12839. [CrossRef]
59. Haider, S.W.; Zhuang, G.; Ali, S. Identifying and bridging the attitude behavior gap in sustainable transportation adoption. *J. Ambient. Intell. Humaniz. Comput.* **2019**, *10*, 3723–3738. [CrossRef]
60. Kim, S.; Choi, J.; Yi, Y.; Kim, H. Analysis of Influencing Factors in Purchasing Electric Vehicles Using a Structural Equation Model: Focused on Suwon City. *Sustainability* **2022**, *14*, 4744. [CrossRef]
61. Ziemba, P. Multi-criteria approach to stochastic and fuzzy uncertainty in the selection of electric vehicles with high social acceptance. *Expert Syst. Appl.* **2021**, *173*, 114686. [CrossRef]

62. Vilchez, J.; Harrison, G.; Kelleher, L.; Smyth, A.; Thiel, C. *Quantifying the Factors Influencing People's Car Type Choices in Europe*; Publications Office of the European Union: Luxembourg, 2017; p. 18. Available online: ec.europa.eu/jrc/en/publication/eur-scientific-and-technical-research-reports/quantifyingfactors-influencing-people-s-car-type-choices-europe-results-stated-preference (accessed on 8 June 2023).
63. Temple, J. Lithium-Metal Batteries for Electric Vehicles. MIT Technology Review. 2021. Available online: www.technologyreview.com/2021/02/24/1018102/lithium-metal-batteries-electric-vehicle-car/ (accessed on 8 June 2023).
64. Kowalska-Pyzalska, A.; Michalski, R.; Kott, M.; Skowrońska-Szmer, A. Consumer preferences towards alternative fuel vehicles. Results from the conjoint analysis. *Renew. Sustain. Energy Rev.* **2022**, *155*, 111776. [CrossRef]
65. Chao Ma, S.; Fan, Y.; Guo, J.F.; Xu, J.H.; Zhu, J. Analysing online behaviour to determine Chinese consumers' preferences for electric vehicles. *J. Clean. Prod.* **2019**, *229*, 244–255.
66. Bell, E.; Bryman, A.; Harley, B. *Business Research Methods*; Oxford University Press: Oxfor, UK, 2018.
67. Hunter, Pamila, Margin of Error and Confidence Levels Made Simple. 2010. Available online: https://www.isixsigma.com/sampling-data/margin-error-and-confidence-levels-made-simple/ (accessed on 7 July 2023).

World Electric Vehicle Journal

MDPI

Article

Waste from Electric Vehicle: A Bibliometric Analysis from 1995 to 2023

Arief Nurdini [1,2], Rahmat Nurcahyo [1,*] and Anton Satria Prabuwono [3]

[1] Industrial Engineering Department, Faculty of Engineering, Universitas Indonesia, Depok 16424, Indonesia; arief.nurdini11@ui.ac.id
[2] Industrial Engineering Department, Faculty of Industrial Technology, Gunadarma University, Depok 16424, Indonesia
[3] Faculty of Computing and Information Technology in Rabigh, King Abdulaziz University, Rabigh 21911, Saudi Arabia; aprabuwono@kau.edu.sa
* Correspondence: rahmat@eng.ui.ac.id

Abstract: The introduction of electric vehicles (EVs) represents a promising solution for addressing urban air pollution, particularly CO_2 emissions in the transportation sector. Numerous countries are actively promoting EV adoption and the electrification of transportation systems, leading to a surge in research on EV-related topics. This study employs bibliometrics as a valuable tool to investigate the research landscape in electric vehicle waste management. Drawing from a dataset of 593 documents retrieved from SCOPUS from 1995 to 20 September 2023, this research employs descriptive analysis and bibliometric mapping techniques. Notably, China stands out as the leading contributor to publications, with Tsinghua University being a prominent research institution in this field. An examination of keyword trends reveals dynamic shifts in research focus. In 2023, the most frequently occurring topic is "closed loop". "Recycling" is the dominant keyword, appearing 681 times. Additionally, TreeMaps and VOSviewer results indicate that the most commonly used keywords are "electronic waste" and "recycling". Projections suggest that "recycling materials" will gain prominence in mid-2023, further highlighting the evolving nature of this research field. Researchers in recycling materials disciplines can leverage these insights to explore new research avenues and contribute to sustainable waste management practices in the context of electric vehicles.

Keywords: electric vehicle; electronic waste; e-waste; bibliometric; R tools; VOSviewer

Citation: Nurdini, A.; Nurcahyo, R.; Prabuwono, A.S. Waste from Electric Vehicle: A Bibliometric Analysis from 1995 to 2023. *World Electr. Veh. J.* **2023**, *14*, 300. https://doi.org/10.3390/wevj14110300

Academic Editors: Wenbin Yu and Guang Zeng

Received: 25 September 2023
Revised: 19 October 2023
Accepted: 24 October 2023
Published: 27 October 2023

1. Introduction

Over the last few decades, there has been a steady increase in the amount of carbon dioxide (CO_2) released into the atmosphere, and people's use of fossil fuels is directly related to global warming [1]. Based on the Environmental Protection Agency (EPA) report, CO_2 is the main gas content in global greenhouse gas emissions and is produced by fossil fuels in industrial activities, which account for up to 65% of the total global greenhouse gases [2]. In addition, the transportation sector contributed 22% of total CO_2 emissions in 2020 [3].

Introducing electric vehicles has been seen as an excellent opportunity to reduce urban air pollution, especially CO_2, from the transportation sector. Promoting electric vehicles to quickly replace internal combustion engine (ICE) vehicles is an essential strategy for countries worldwide [4]. Therefore, many countries are actively promoting the electrification of the transportation sector and encouraging the use of electric vehicles [5]. In addition to the desire to reduce CO_2 emissions, psychological factors also play a role in influencing people to use electric vehicles [6]. Based on data from the International Energy Agency (IEA) contained in the Global E.V. Outlook 2022, more than 16.5 million electric vehicles were sold in 2021, an increase of 6.6 million units from the previous year. However, the

largest electric car market in the world is still dominated by China, followed by Europe and America.

Sales of electric vehicles will rise along with the number of waste parts from these vehicles that will be recycled, including car bodywork, tires, plastics, traction batteries, electric motors, power electronics, electronic components, etc. [7,8]. Furthermore, electric car electrical component waste is also dangerous but highly valuable [9].

Review papers and bibliometric research analysis are two ways to summarize research publications [10]. Bibliometric analysis has gained immense popularity in business research in recent years. Its popularity can be attributed to the development, accessibility, and availability of bibliometric tools like Gephi, Leximancer, and VOSviewer, as well as to the scientific databases Scopus and Web of Science. The cross-disciplinary pollination of the bibliometric methodology from information science to business research. More importantly, the popularity of bibliometric analysis in business research is not a fad but rather a reflection of its utility for (1) handling large volumes of scientific data and (2) producing high research impact [11]. By rigorously interpreting vast amounts of unstructured data, bibliometric analysis aids in deciphering and mapping the cumulative scientific knowledge and evolutionary nuances of established areas. Therefore, bibliometric studies promote innovation and create a strong foundation for meaningfully advancing research. Researchers can use bibliometric analysis to their advantage by having a single point of access to information, looking into knowledge gaps, coming up with creative research ideas, and positioning their intended contributions to the field [10]. The method used is based on keywords in the Scopus database, which will be further analyzed using R-Tools and VOSviewer. This study aimed to explore the following key questions:

1. Which publications, institutions, countries, and authors have made the most significant contributions to research on electric vehicles and the waste they produce?
2. How are the authors, organizations, and nations related to one another and work together in academic research?
3. What are the current prominent research topics in this field, how are they evolving, and what will capture attention in the future?

2. Materials and Methods

2.1. Data Collection

SCOPUS, a database of content from the esteemed journal, was used in this study. Since it contains more articles than other databases, such as Web of Science [12], the Scopus database was chosen for this study's bibliometric analysis. This study did not assess Google Scholar because there were no reliable results [13]. Five hundred ninety-three documents related to electric vehicles and electronic waste were published between 1995 and September 2023. The papers will be used for further data analysis.

2.2. Bibliometric: VOSviewer and R Tools

A study method known as "bibliometrics" uses the library and information science to provide data and analysis in various formats, including statistical and quantitative methods [14]. An essential research area is bibliometrics since it offers detailed historical data that can be used to predict future research trends [15]. In addition, a range of crucial indicators, including h-index, impact factors, citations, and current status, can be used by universities, instructors, researchers, and professors to evaluate the quality of a study. There are many bibliometric tools, like VOSviewer and R Tools. VOSviewer is a free program for creating and displaying bibliometric networks, which can be based on citations, bibliographic coupling, co-citations, or author relationships. These networks can contain journals, researchers, or individual publications. The entire bibliographic dataset was acquired in .csv format from the Scopus database. Initially, we installed and loaded the Bibliometrix R package using R Studio. We then initiated the Biblioshiny application by typing "Biblioshiny()" in the R console. Biblioshiny serves as a web-based tool that offers non-programmers access to the Bibliometrix package within R [16]. Numerous tools

provided by Bibliometrix enable scholars to undertake in-depth bibliometric analyses [17]. In this paper, the tools of bibliometric VOSviewer 1.6.18 developed by Nees Jan van Eck and Ludo Waltman at Leiden University and R-Tool version 4.2.2 are combined to get a better result.

2.3. Literature Search

A comprehensive scientific literature search on the SCOPUS database. The search was further modified to include other terms, such as "electric vehicle" OR "electric vehicles" OR "EV" AND "electronic waste" OR "e-waste". The established period covered data from 2015 to 2023, and to improve the efficiency of the search process, the search was limited to specific terms. On 20 September 2023, the last web page visit occurred. The methodology flowchart is depicted in Figure 1.

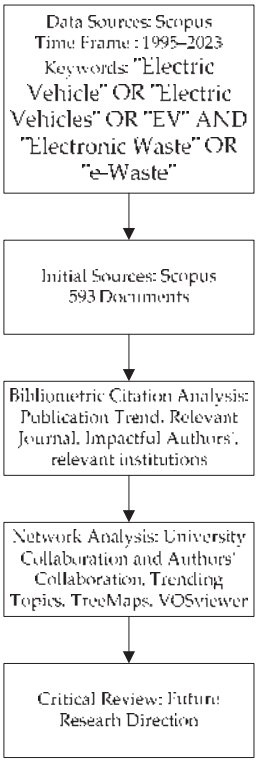

Figure 1. Methodological Flowchart for Bibliometric.

3. Results

This section may be divided into subheadings. It should provide a concise and precise description of the experimental results, their interpretation, and the experimental conclusions that can be drawn.

3.1. Data Analysis

The documents are from 1995 to 20 September 2023, and have 234 sources. A brief description can be seen in Table 1. A total of 593 documents were discovered, of which 363 are articles. During the time of the study, a total of 1944 authors contributed to the topic. The average age of the documents is 2.89, with the average number of citations per doc being 32.86. And then, 20,626 references are found in 593 documents. KeyWords Plus reached 4191, compared to the author's 1351 keywords. Only 17 documents with a single

author's name were found. We found one book, 14 book chapters, 116 conference papers, three conference reviews, 1 note, and 95 reviews.

Table 1. Main Information about the Data.

Description	Results
MAIN INFORMATION ABOUT DATA	
Timespan	1995:2023
Sources (Journals, Books, etc.)	234
Documents	593
Annual Growth Rate %	17.71
Document Average Age	2.89
Average citations per doc	32.86
References	20,626
DOCUMENT CONTENTS	
Keywords Plus (ID)	4191
Author's Keywords (DE)	1351
AUTHORS	
Authors	1944
Authors of single-authored docs	15
AUTHORS COLLABORATION	
Single-authored docs	17
Co-Authors per Doc	4.67
International co-authorships %	23.95
DOCUMENT TYPES	
Article	363
Book	1
book chapter	14
conference paper	116
conference review	3
Note	1
Review	95

3.2. Annual Publications

The fundamental details about the publications are extracted using the Bibliometrix sub-tool Biblioshiny. We could see a significant annual growth rate of 17.71 percent in the number of publications. Only one document was published in 1995. The article describes the energy and environmental impacts of electric vehicle battery production and recycling. Based on Scopus, there are 11 citations in this paper. The topic of electronic waste increased from 2010 to 2015, then decreased in 2016. Then, there was a significant increase from 2017, with 27 articles, until 2021 and 2022, with 117 and 118 articles. For more details, see Figure 2.

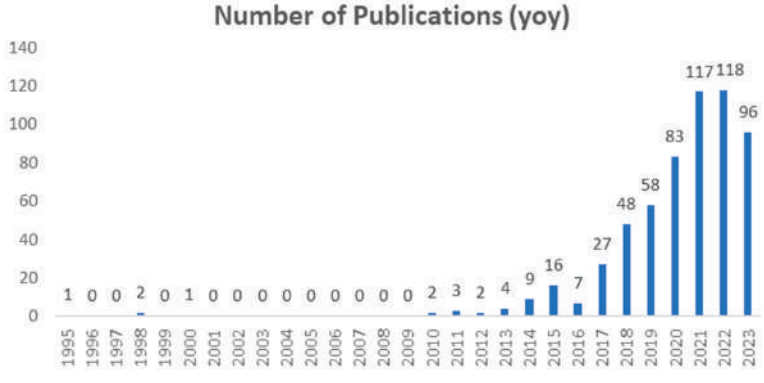

Figure 2. Number of Publications.

3.3. Annual Citations

The number of articles' citations increased as more research was conducted. Based on Figure 3, there are 11 citations for publication in 1995. Moreover, there are no citations from 1996 and 1997, 1999, and 2001 to 2009 because researchers carried out no publications. The average per doc, the citation from 1995 to 20 September 2023, is 32.86. The citations increased from 2017 with 871 citations, 2018 with 3030 citations, 2019 with 3546 citations, and 2020 with 4166 citations. We can observe that, from 1995 through early 2023, there has been a wide variety of citations per year, increasing in some and declining in others.

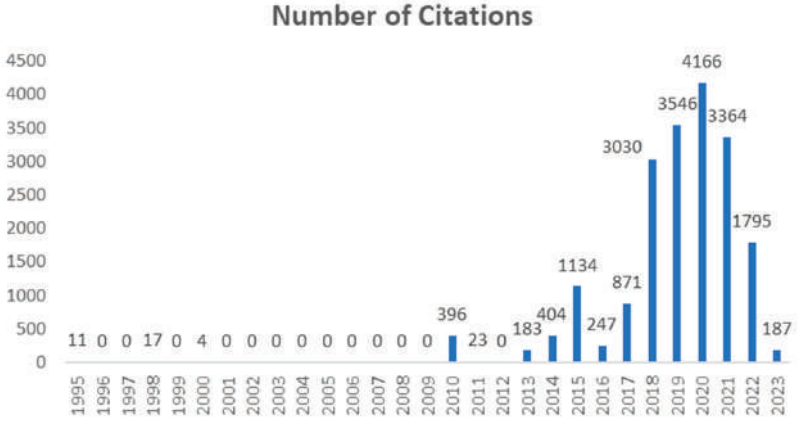

Figure 3. Number of Citations.

3.4. Highly Cited Papers

We found the most cited paper in "Lithium-ion Battery Supply Chain Considerations: Analysis of Potential Bottlenecks in Critical Metals" article by [18]. The paper was published in the Journal Joule with Cell Press Publisher. The top 30 highly cited papers can be found in Table 2.

Table 2. Top 30 Highly Cited papers.

No.	Document Title	Journal	Publisher	Year	Citation	Authors
1	Lithium-Ion Battery Supply Chain Considerations: Analysis of Potential Bottlenecks in Critical Metals	Joule	Cell Press	2017	782	[18]
2	Sustainable Recycling Technology for Li-Ion Batteries and Beyond: Challenges and Future Prospects	Chemical Reviews	American Chemical Society	2020	718	[19]
3	State-of-the-Art and Energy Management System of Lithium-Ion Batteries in Electric Vehicle Applications: Issues and Recommendations	IEEE Access	Institute of Electrical and Electronics Engineers Inc.	2018	493	[20]
4	Recycling End-of-Life Electric Vehicle Lithium-Ion Batteries	Joule	Cell Press	2019	431	[21]
5	A Mini-Review on Metal Recycling from Spent Lithium-Ion Batteries	Engineering	Elsevier Ltd.	2018	408	[22]
6	Life cycle assessment of lithium-ion batteries for plug-in hybrid electric vehicles-Critical issues	Journal of Cleaner Production	Elsevier Ltd.	2010	393	[23]

Table 2. *Cont.*

No.	Document Title	Journal	Publisher	Year	Citation	Authors
7	Recycling of spent lithium-ion batteries in view of lithium recovery: A critical review	Journal of Cleaner Production	Elsevier Ltd.	2019	392	[24]
8	Current li-ion battery technologies in electric vehicles and opportunities for advancements	Energies	MDPI AG	2019	388	[25]
9	Novel approach to recover cobalt and lithium from spent lithium-ion battery using oxalic acid	Journal of Hazardous Materials	Elsevier	2015	368	[26]
10	Examining different recycling processes for lithium-ion batteries	Nature Sustainability	Nature Publishing Group	2019	360	[27]
11	Lithium-ion batteries—Current state of the art and anticipated developments	Journal of Power Sources	Elsevier B.V.	2020	322	[28]
12	A review on the growing concern and potential management strategies of waste lithium-ion batteries	Resources, Conservation and Recycling	Elsevier B.V.	2018	287	[29]
13	A future perspective on lithium-ion battery waste flows from electric vehicles	Resources, Conservation and Recycling		2014	285	[30]
14	Pyrometallurgical options for recycling spent lithium-ion batteries: A comprehensive review	Journal of Power Sources	Elsevier B.V.	2021	254	[31]
15	Solving spent lithium-ion battery problems in China: Opportunities and challenges	Renewable and Sustainable Energy Reviews	Elsevier Ltd.	2015	247	[32]
16	Future material demand for automotive lithium-based batteries	Communications Materials	Springer Nature	2020	246	[33]
17	A critical review of lithium-ion battery recycling processes from a circular economy perspective	Batteries	MDPI	2019	227	[34]
18	Circular economy strategies for electric vehicle batteries reduce reliance on raw materials	Nature Sustainability	Nature Research	2021	180	[35]
19	Biotechnological strategies for the recovery of valuable and critical raw materials from waste electrical and electronic equipment (WEEE)—A review	Journal of Hazardous Materials	Elsevier B.V.	2019	174	[36]
20	Recent progress on the recycling technology of Li-ion batteries	Journal of Energy Chemistry	Elsevier B.V.	2020	166	[37]
21	Metallurgical and mechanical methods for recycling of lithium-ion battery pack for electric vehicles	Resources, Conservation and Recycling	Elsevier B.V.	2018	162	[38]
22	Energy and environmental assessment of a traction lithium-ion battery pack for plug-in hybrid electric vehicles	Journal of Cleaner Production	Elsevier Ltd.	2019	158	[39]
23	The Recycling of Spent Lithium-Ion Batteries: a Review of Current Processes and Technologies	Electrochemical Energy Reviews		2018	156	[40]
24	An overview of recycling and treatment of spent LiFePO4 batteries in China	Resources, Conservation and Recycling	Elsevier B.V.	2017	147	[41]
25	Progress and status of hydrometallurgical and direct recycling of Li-Ion batteries and beyond	Materials	MDPI	2020	146	[42]

Table 2. *Cont.*

No.	Document Title	Journal	Publisher	Year	Citation	Authors
26	Comparative environmental life cycle assessment of conventional vehicles with different fuel options, plug-in hybrid and electric vehicles for a sustainable transportation system in Brazil	Journal of Cleaner Production	Elsevier Ltd.	2018	146	[43]
27	Recycling and environmental issues of lithium-ion batteries: Advances, challenges and opportunities	Energy Storage Materials	Elsevier	2021	143	[44]
28	The importance of design in lithium-ion battery recycling-a critical review	Green Chemistry	Royal Society of Chemistry	2020	124	[45]
29	Eco-Efficiency Analysis of a Lithium-Ion Battery Waste Hierarchy Inspired by Circular Economy	Journal of Industrial Ecology	Blackwell Publishing	2017	137	[46]
30	Graphite Recycling from Spent Lithium-Ion Batteries	ChemSusChem	Wiley-VCH Verlag	2016	136	[47]

3.5. Most Relevant Sources

Resources are identified to determine the performance of the sources used. Based on Table 3, Resources, Conversation, and Recycling from the Netherlands are at the top, with 45 documents and an impact factor of 13.716. The Journal of Cleaner Production is a second, with a total of 30 documents and an impact factor of 11.072, and the third is the Journal of Energy Storage, with 23 documents and an impact factor of 8.907. The three prominent journals are from the Netherlands. For more details regarding the most relevant resources, see Figure 4.

Table 3. Most Relevant Sources with Impact Factor.

No.	Name of Journal	Number of Publications	Impact Factor	Rate (%)
1	Resources Conservation and Recycling	45	13.716	7.63%
2	Journal of Cleaner Production	30	11.072	5.08%
3	Journal of Energy Storage	23	8.907	3.90%
4	Energies	17	3.2	2.88%
5	Procedia CIRP	16	2.17	2.71%
6	Waste Management	14	8.816	2.37%
7	SAE Technical Papers	13	0.638	2.20%
8	ACS Sustainable Chemistry and Engineering	12	9.224	2.03%
9	Others	420		71.19%

3.6. Corresponding Author's Countries

Corresponding authors are divided into two categories: multi-country publication (MCP), which includes authors from several nations and such publications show cross-national or international collaboration; and single-country publication (SCP), where all writers are from the same country and the publication is an example of intra-national cooperation. Based on Figure 5, China has the most corresponding author documents, with 39 MCP documents and 147 SCP documents. The second country, the United States, has five MCP documents and 49 SCP documents. The third country is Germany, with eight MCP documents and 57 SCP documents.

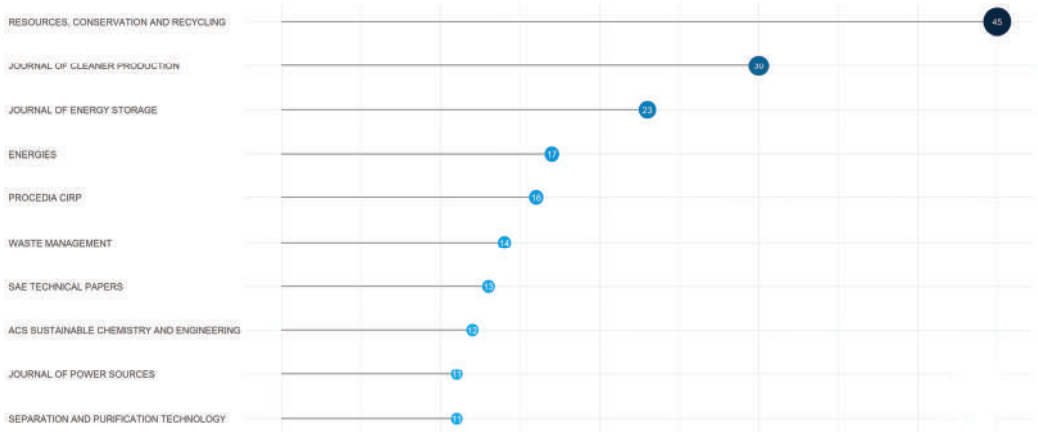

Figure 4. Most Relevant Sources.

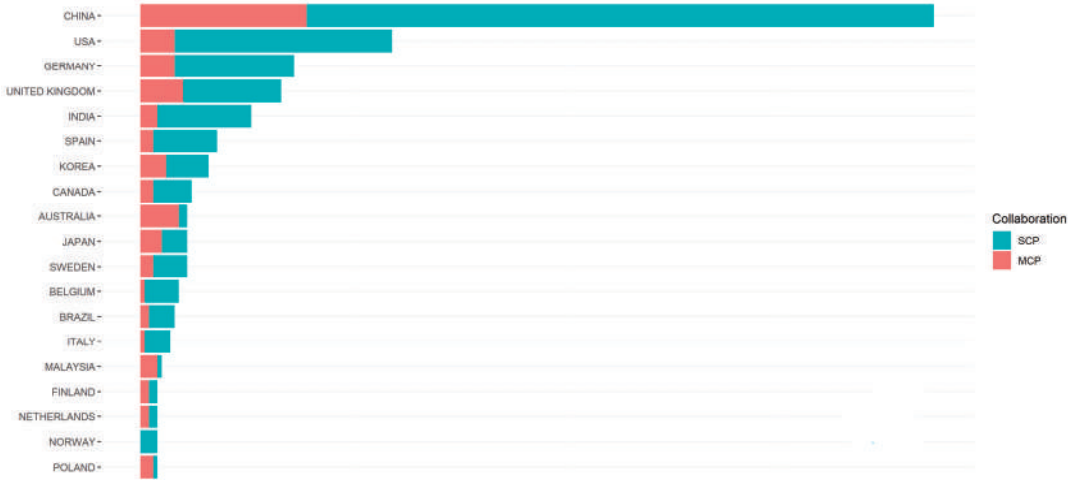

Figure 5. Corresponding Author's Countries.

3.7. Most Relevant Affiliations

The most relevant affiliations were identified to determine which university has produced the most publications on electric vehicles and electronic waste. Tsinghua University and Central South University in China are first and second, with 79 and 51 articles, respectively. The third place is Chalmers University of Technology, with 37 articles. For more details regarding the most relevant affiliations, refer to Figure 6.

3.8. Subject Categories

Subject areas are examined to determine which topics are most popular with researchers. For example, according to Figure 7, we can see that the top three research areas are engineering 22%, environmental science 19%, and energy 18%.

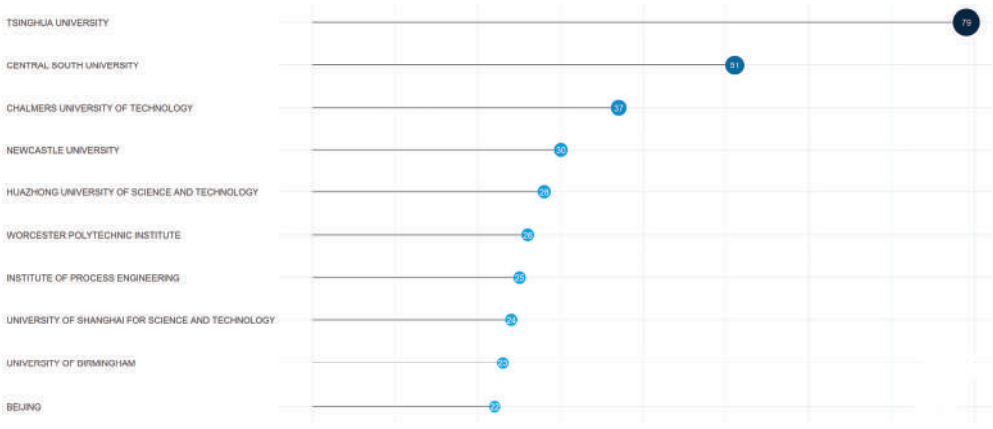

Figure 6. Most Relevant Affiliations.

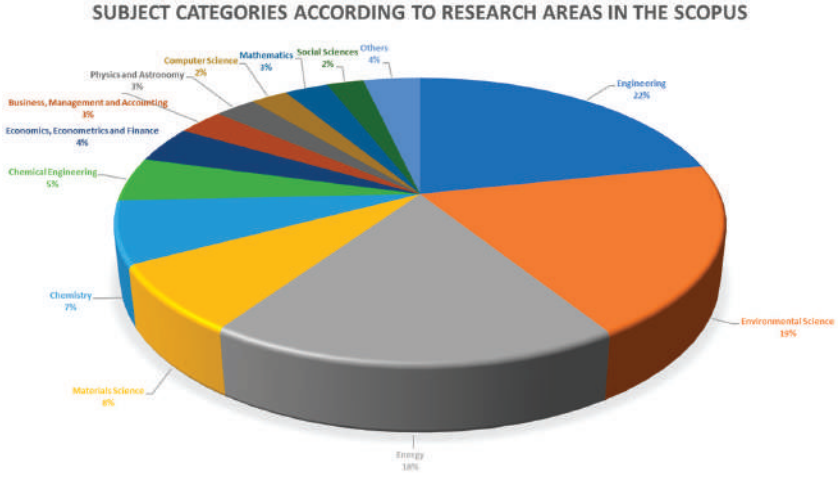

Figure 7. Subject Categories according to the Research Area.

3.9. Object Categories

The object categories explain the electronic components of electric vehicles that have been researched. In this paper, these categories are divided into four parts: batteries, charging stations, power electronics, and permanent magnets. The discussion of batteries is the most researched, as seen in [18,19,23,26,48–63]. In global electronic component waste research, there is still a dominant focus on battery waste, while research concerning electronic power component waste remains limited. For more details, please refer to Table 4.

Table 4. Object Categories.

No	Battery	Charging	Power Electronics	Permanent Magnet	Authors
1	✔				[18,19,23,26,48–63]
2	✔		✔		[63]
3			✔		[64]
4				✔	[65]
5		✔			[66,67]

3.10. Most Relevant Authors' and Production over Time

The data were analyzed to determine the most relevant authors. Based on Figure 8, Wang Y, with 18 documents, is the leading author, followed by Li J and Li Y, with 17 and 13 documents. The data were examined to determine the authors' output over time.

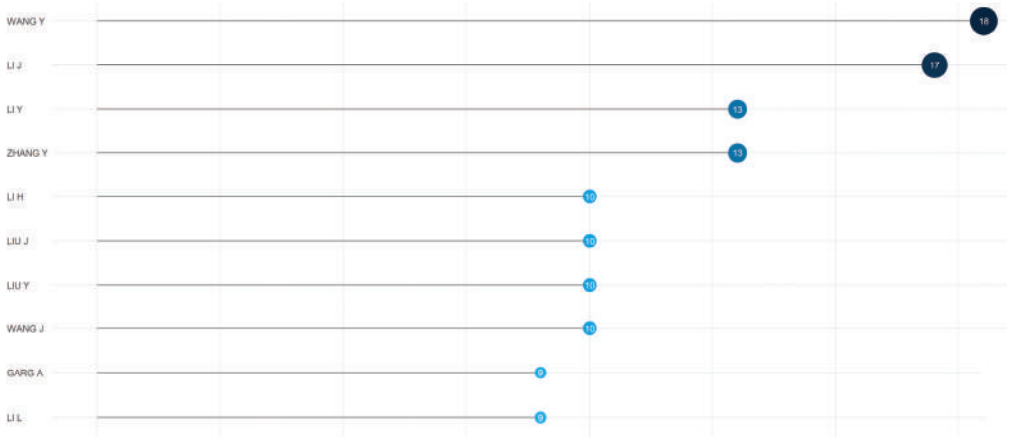

Figure 8. Most Relevant Authors'.

Wang Y published one article in 2016, 2017, and 2018—two in 2019 and 2021. There were three articles in 2020 and four in 2022 and 2023 (Figure 9). The dot color in Figure 9 shows the number of publications. The paper from Wang Y with the most citations is titled "Recent Progress on the Recycling Technology of Li-ion Batteries" in 2021, with 169 citations. The total citations from 18 documents are 856 citations.

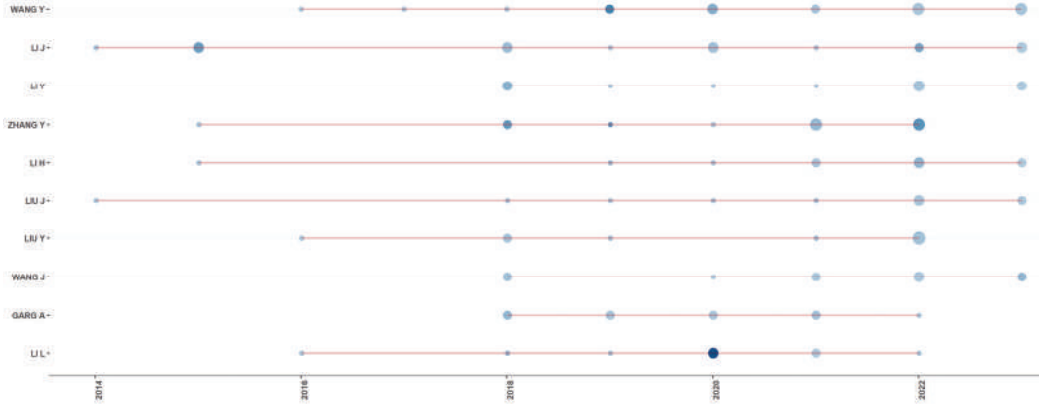

Figure 9. Author's Production over Time.

3.11. Most Frequent Words

The frequent words evolve as research advances. According to Bibliometrix, the most frequently occurring words in 1995 were "lead acid", "metal hydride electrode", and "cadmium electrode". In 2023, the most frequently used word in the literature was "recycling", totaling 678 occurrences, followed by "electronic waste", which had 603 occurrences, and "lithium-ion batteries", with 381 occurrences. The darker the color of the dot, the more citations obtained. The total number indicates that research on recycling and e-waste is evolving. For more details regarding the most relevant affiliations, see Figure 10.

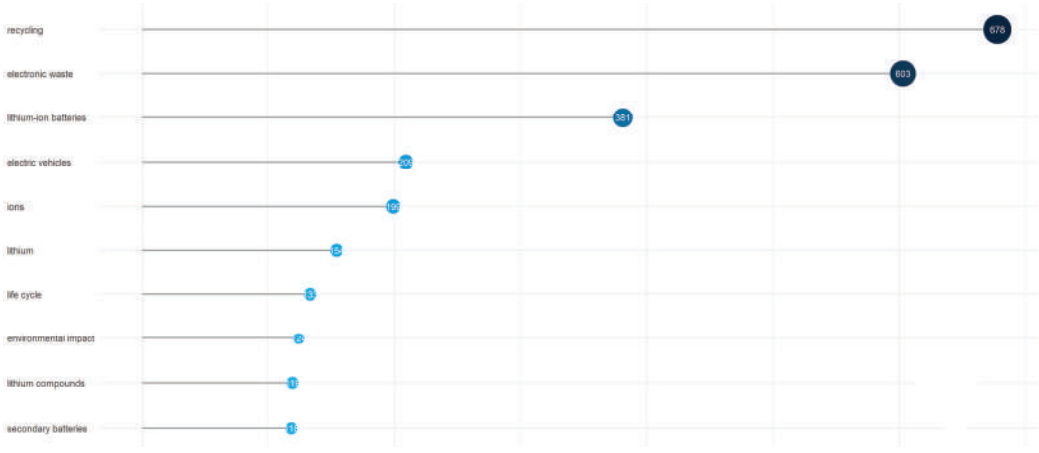

Figure 10. Most Frequent Words.

3.12. Trending Topics

Trending topics are analyzed based on the authors' keyword frequency. Frequency refers to the count of keyword usage in papers for a particular year. Based on Table 5, in 2010, the keyword "Vehicle Technology" became trending with a total frequency of 4. In 2014, the keywords "Integrated Approach", "Regenerative Braking", and "Recycling Rate" became trending with frequencies 4, 4, and 5. In 2015, the keyword "lithium alloys" became a trending topic with a total frequency of 7. In 2018, the keywords "vehicle", "hybrid vehicles", and "nickel metal hydride batteries". Each frequency of 28, 23, and 12 becomes a trending topic. Keywords "secondary batteries", "electric vehicles", and "electrodes" with frequencies 118, 45, and 29 became a trending topic in 2019. In 2020, the keywords "automotive batteries", "waste management", and "battery management systems". Each frequency of 63, 54, and 46 became a trending topic. Keywords "recycling", "electronic waste", and "lithium-ion batteries" became a trending topic in 2021, with a total frequency of 678, 603, and 381. And in 2022, the keywords "battery recycling", "cathodes", and "leaching". With a total frequency of 113, 104, and 90, they became trending topics. Furthermore, in mid of 2023, the keywords "industrial ecology", "recycled materials", and "closed loop". With a total frequency of 6, 6, and 7, they became trending topics. For more details see Figure 11.

Table 5. Trending Topic Based on Authors' Keyword.

Years	Frequent Word	Term Frequency
2010	Vehicle Technology	4
2014	Integrated Approach	4
	Regenerative Braking	4
	Recycling Rate	5
2015	Hybrid Energy Storage Systems (Hess)	3
	Leaching Solution	3
	Lithium Alloys	7
2016	Nickel Metal Hydride	4
	Policy Makers	4
2017	Plug-in Hybrid Vehicles	15
	Recovery	18
	Electric Batteries	32

Table 5. *Cont.*

Years	Frequent Word	Term Frequency
2018	Nickel Metal Hydride Batteries	12
	Hybrid Vehicles	23
	Vehicles	28
2019	Electrodes	29
	Electric Vehicles (EVS)	45
	Secondary Batteries	118
2020	Battery Management Systems	46
	Waste Management	54
	Automotive Batteries	63
2021	Lithium-ion Batteries	381
	Electronic Waste	603
	Recycling	678
2022	Spent Lithium-ion Batteries	90
	Cathodes	104
	Battery Recycling	113
2023	Industrial Ecology	6
	Recycled Materials	6
	Closed-Loop	7

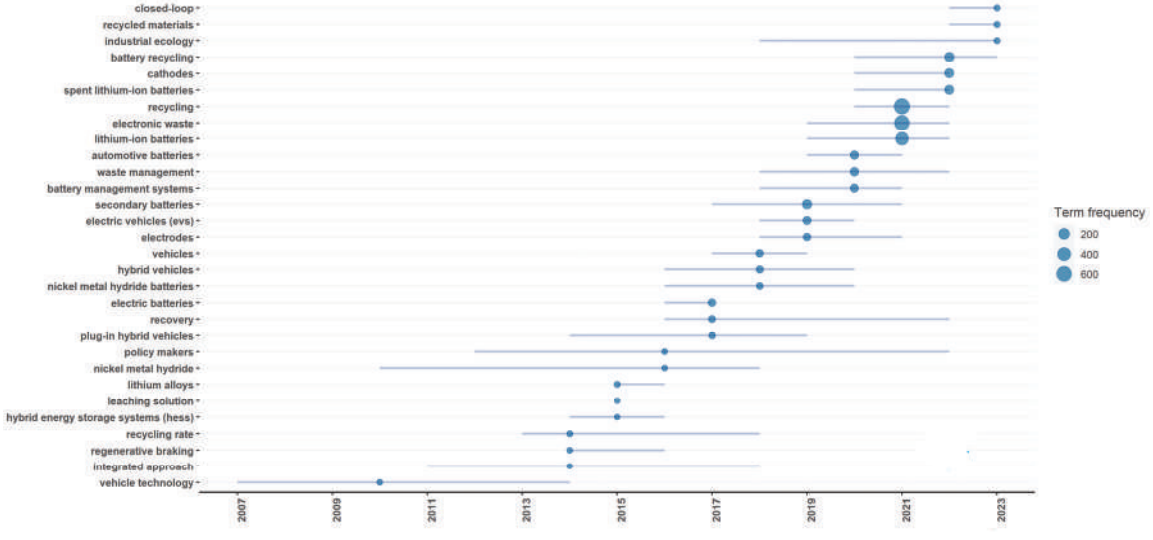

Figure 11. Trending Topics based on Authors' Keywords.

3.13. TreeMaps

The treemap depicts words frequently used as keywords in research on electric vehicles and electronic waste. For example, the graph shows that recycling ranks first at 14% with 681 occurrences, electronic waste second at 12% with 603 occurrences, lithium-ion batteries at 8% with 381 occurrences, and electric vehicles and ions at 4% each with 209 and 199 occurrences. TreeMaps can be observed in greater detail in Figure 12.

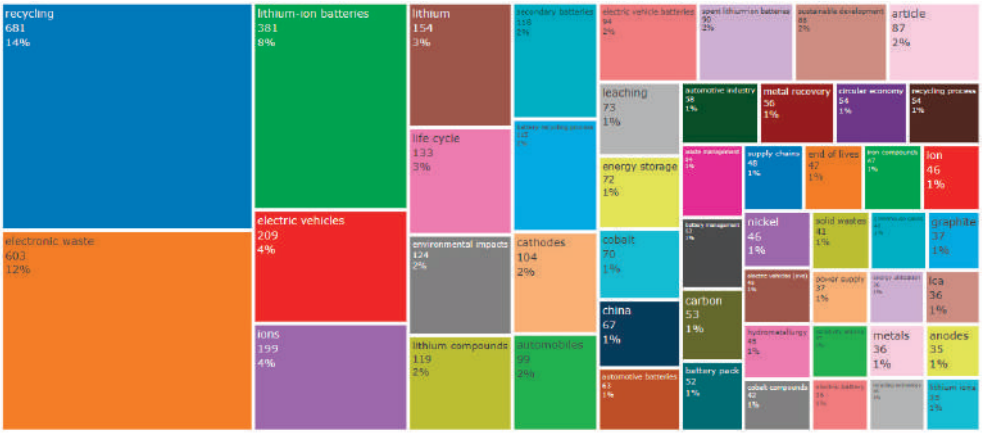

Figure 12. TreeMap Words.

3.14. Bibliometric VOSviewer

The result is divided into seven clusters. Cluster 1 (red) contains 136 keywords: lithium-ion batteries, lithium compounds, recycle, leaching, and hydrometallurgy. Cluster 2 (green) includes 131 keywords, such as lithium, nickel, metal recovery, and renewable energies. Cluster 3 (blue) contains 120 keywords: electric vehicles, energy storage, energy efficiency, economic analysis, and end-of-life batteries. Cluster 4 (yellow) includes 112 keywords: battery recycling, secondary batteries, sustainable development, and solid waste. Cluster 5 (Violet) contains 80 keywords: life cycle, life cycle analysis, life cycle assessment, environmental impact, and sensitivity analysis. Cluster 6 (green turquoise) has 73 keywords: electronic waste, recycling process, battery pack, and charging batteries. Finally, cluster 7 (orange) contains 72 keywords: waste management, electronic equipment, circular economy, and sustainability. According to Figure 13, the terms with the highest frequency include electronic waste, electric vehicles, recycling, lithium-ion batteries, battery recycling, and others.

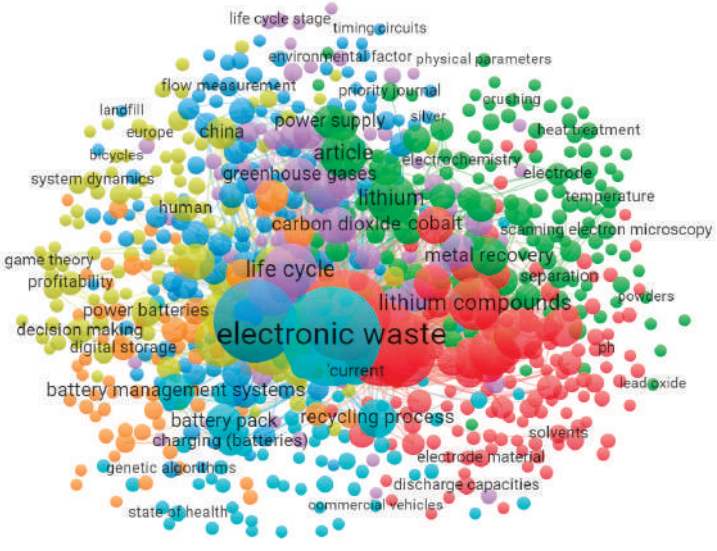

Figure 13. Bibliometric VOSviewer.

4. Discussion

Research in many diverse disciplines has begun adopting bibliometric analysis [68–70]. This study technique can show how articles published in databases are distributed throughout various topics, industries, organizations, and nations. Moreover, many databases, like Scopus, Web of Science, etc., can be utilized to retrieve the raw data for the bibliometric study. We took the source information for this research out of the Scopus Core Collection. The documents were published between 1995 and 20 September 2023, and came from 234 sources (books, journals, etc.).

There were 593 documents overall, of which 363 were articles. A total of 1944 authors have contributed to this field of study. The fundamental data about the documents were extracted using the Biblioshiny Bibliometrix sub-tool and VOSviewer. We observed a significant annual growth rate of 17.71% in the number of articles. Based on the Scopus database, the first publication related to waste electronic components for electric vehicles was found in 1995, with one document published. None of the documents from 1996, 1997, or 1999 were published. Two documents were contributed to the literature in 1998, and one was added in 2000. Throughout the following nine years, not a single new document was released. In 2010, there were two contributing documents. In 2011 and 2012, there were 3 and 2 documents, respectively. Subsequently, there was a consistent increase in the number of documents in the following years. In 2013, there were 4 documents. In 2014, there were 9 documents. In 2015, there were 16 documents. In 2016, there was a decrease to 7 documents. In 2017, there was a significant rise to 27 documents. In 2018, there were 48 documents. In 2019, there were 58 documents, and in 2020, there were 83 documents. The number of documents added to the literature increased in 2022 with a total of 118, then in 2021 with 117. Each year, the number of documents published has been steadily rising. A total of 593 documents were released in 2023.

Few publications were published at the start of the research period, and the research literature was declining. Only 11 citations were provided in 1995; from 2001 to 2009, none were accessible. There were exponential growth in the number of citations in 2013. Citations significantly increased in the year 2020. The most prolific university overall, Tsinghua University, has published 79 publications. China is the leading country regarding corresponding authors, with 37 papers published in multiple countries (MCP) and 147 documents published in a single country (SCP). The USA ranks second, with five MCP documents and 49 SCP documents. With 822 citations, Wang Y. was the author with the most significant influence. From 1998 until now, the word "recycling" has been used the most frequently in the literature, leading to a total count of 678.

Trending topics are analyzed based on the author's keywords. From the last three years in 2020, the keywords "automotive batteries", "waste management", and "battery management systems". Each frequency of 63, 54, and 46 became a trending topic. Keywords "recycling", "electronic waste", and "lithium-ion batteries" became trending topics in 2021, with a total frequency of 678, 603, and 381. And in 2022, the keywords "battery recycling", "cathodes", and "leaching". With a total frequency of 113, 104, and 90, they became trending topics. Furthermore, in mid-2023, the keywords "industrial ecology", "recycled materials", and "closed loop".

5. Conclusions

Municipal electronic waste issues are gaining momentum, and several studies have thoroughly studied the field of connected subjects. This paper used the open-source R language and the bibliometrix package to do a bibliometric analysis based on the data from 593 scientific publications received from Scopus.

An analysis of scientific output reveals that the research area of recycling electronic waste from electric vehicles is still experiencing annual sales growth that is accelerating rapidly. The findings indicate that China and the United States have the most publications, whereas Tsinghua University and Central South University produce the most work. However, when using the number of citations to indicate academic influence, China, with

6177 citations, surpasses the United States's 3334 citations and the United Kingdom's 1415 citations. With 856 citations and 18 published documents, Wang Y was the author with the most significant influence. Additionally, over the past three years, in 2021, the keywords "recycling", "electronic waste", and "lithium-ion batteries" all attained a frequency of 678, 603, and 381, respectively. "Battery recycling", "cathodes", and "leaching" are other significant terms for 2022. The subjects with the highest frequency were 113, 104, and 90. The keywords "industrial ecology", "recycled materials", and "closed loop" will also be used in the middle of 2023. Each issue becomes a trending topic six times in total. We can determine the terms frequently used in studying electric vehicles and electronic trash using TreeMaps. Recycling is mentioned 681 times (14% of all usage), electronic waste 603 times (12%), lithium-ion batteries 381 times (8%), electric vehicles 209 times (4%), ions 199 times (4%), etc. It should be mentioned that this research has significant limitations despite the in-depth investigation. For instance, this analysis is based on data from Scopus, which is unquestionably one of the most reliable and accurate sources of information; however, the trend may be different when other search engines or databases are added, as well as when manuscripts from outside core collections are taken into account. Therefore, more in-depth research in this area is required.

Author Contributions: Writing—original draft, A.N., R.N. and A.S.P. All authors contributed substantially and equally to the writing and original draft preparation. All authors have read and agreed to the published version of the manuscript.

Funding: This research received funding from Hibah Publikasi Terindeks Internasional (PUTI) Q2 Tahun Anggaran 2022-2023, Nomor NKB-707/UN2.RST/HKP.05.00/2022.

Data Availability Statement: As this paper has the character of a bibliometric, no new data were created or analyzed in this study. Data sharing is not applicable to this article.

Conflicts of Interest: The authors declare no conflict of interest.

References

1. Siqi, Z.; Guangming, L.; Wenzhi, H.; Juwen, H.; Haochen, Z. Recovery methods and regulation status of waste lithium-ion batteries in China: A mini review. *Waste Manag. Res.* **2019**, *37*, 1142–1152. [CrossRef] [PubMed]
2. EPA. *Global Greenhouse Gas Emissions Data*; EPA: Washington, DC, USA, 2022.
3. Giannakis, E.; Serghides, D.; Dimitriou, S.; Zittis, G. Land transport CO_2 emissions and climate change: Evidence from Cyprus. *Int. J. Sustain. Energy* **2020**, *39*, 634–647. [CrossRef]
4. Chen, Y.; Wu, G.; Sun, R.; Dubey, A.; Laszka, A.; Pugliese, P. A review and outlook of energy consumption estimation models for electric vehicles. *arXiv* **2020**, arXiv:2003.12873.
5. Verma, S.; Dwivedi, G.; Verma, P. Life cycle assessment of electric vehicles in comparison to combustion engine vehicles: A review. *Mater. Today Proc.* **2021**, *49*, 217–222. [CrossRef]
6. Viola, F. Electric vehicles and psychology. *Sustainability* **2021**, *13*, 719. [CrossRef]
7. Elwert, T.; Goldmann, D.; Römer, F.; Buchert, M.; Merz, C.; Schueler, D.; Sutter, J. Current developments and challenges in the recycling of key components of (hybrid) electric vehicles. *Recycling* **2015**, *1*, 25–60. [CrossRef]
8. Li, H.; Wang, Y.; Fan, F.; Yu, H.; Chu, J. Sustainable Plant Layout Design for End of Life Vehicle Recycling and Disassembly Industry Based on SLP Method, a Typical Case in China. *IEEE Access* **2021**, *9*, 81913–81925. [CrossRef]
9. Blömeke, S.; Scheller, C.; Cerdas, F.; Thies, C.; Hachenberger, R.; Gonter, M.; Herrmann, C.; Spengler, T.S. Material and energy flow analysis for environmental and economic impact assessment of industrial recycling routes for lithium-ion traction batteries. *J. Clean. Prod.* **2022**, *377*, 134344. [CrossRef]
10. Halepoto, H.; Gong, T.; Noor, S.; Memon, H. Bibliometric Analysis of Artificial Intelligence in Textiles. *Materials* **2022**, *15*, 2910. [CrossRef]
11. Donthu, N.; Kumar, S.; Mukherjee, D.; Pandey, N.; Lim, W.M. How to conduct a bibliometric analysis: An overview and guidelines. *J. Bus. Res.* **2021**, *133*, 285–296. [CrossRef]
12. Cabeza, L.F.; Chàfer, M.; Mata, É. Comparative analysis of web of science and scopus on the energy efficiency and climate impact of buildings. *Energies* **2020**, *13*, 409. [CrossRef]
13. Borri, E.; Tafone, A.; Zsembinszki, G.; Comodi, G.; Romagnoli, A.; Cabeza, L.F. Recent trends on liquid air energy storage: A bibliometric analysis. *Appl. Sci.* **2020**, *10*, 2773. [CrossRef]

14. Choi, W.; Kim, J.; Lee, S.; Park, E. Smart home and internet of things: A bibliometric study. *J. Clean. Prod.* **2021**, *301*, 126908. [CrossRef]
15. Tseng, M.-L.; Chang, C.-H.; Lin, C.-W.R.; Wu, K.-J.; Chen, Q.; Xia, L.; Xue, B. Future trends and guidance for the triple bottom line and sustainability: A data driven bibliometric analysis. *Environ. Sci. Pollut. Res.* **2020**, *27*, 33543–33567. [CrossRef] [PubMed]
16. Ejaz, H.; Zeeshan, H.M.; Ahmad, F.; Bukhari, S.N.A.; Anwar, N.; Alanazi, A.; Sadiq, A.; Junaid, K.; Atif, M.; Abosalif, K.O.A. Bibliometric analysis of publications on the omicron variant from 2020 to 2022 in the Scopus database using R and VOSviewer. *Int. J. Environ. Res. Public Health* **2022**, *19*, 12407. [CrossRef]
17. Aria, M.; Cuccurullo, C. Bibliometrix: An R-tool for comprehensive science mapping analysis. *J. Informetr.* **2017**, *11*, 959–975. [CrossRef]
18. Olivetti, E.A.; Ceder, G.; Gaustad, G.G.; Fu, X. Lithium-ion battery supply chain considerations: Analysis of potential bottlenecks in critical metals. *Joule* **2017**, *1*, 229–243. [CrossRef]
19. Fan, E.; Li, L.; Wang, Z.; Lin, J.; Huang, Y.; Yao, Y.; Chen, R.; Wu, F. Sustainable recycling technology for Li-ion batteries and beyond: Challenges and future prospects. *Chem. Rev.* **2020**, *120*, 7020–7063. [CrossRef]
20. Hannan, M.A.; Hoque, M.M.; Hussain, A.; Yusof, Y.; Ker, P.J. State-of-the-art and energy management system of lithium-ion batteries in electric vehicle applications: Issues and recommendations. *IEEE Access* **2018**, *6*, 19362–19378. [CrossRef]
21. Chen, M.; Ma, X.; Chen, B.; Arsenault, R.; Karlson, P.; Simon, N.; Wang, Y. Recycling end-of-life electric vehicle lithium-ion batteries. *Joule* **2019**, *3*, 2622–2646. [CrossRef]
22. Zheng, X.; Zhu, Z.; Lin, X.; Zhang, Y.; He, Y.; Cao, H.; Sun, Z. A mini-review on metal recycling from spent lithium ion batteries. *Engineering* **2018**, *4*, 361–370. [CrossRef]
23. Zackrisson, M.; Avellán, L.; Orlenius, J. Life cycle assessment of lithium-ion batteries for plug-in hybrid electric vehicles—Critical issues. *J. Clean. Prod.* **2010**, *18*, 1519–1529. [CrossRef]
24. Liu, C.; Lin, J.; Cao, H.; Zhang, Y.; Sun, Z. Recycling of spent lithium-ion batteries in view of lithium recovery: A critical review. *J. Clean. Prod.* **2019**, *228*, 801–813. [CrossRef]
25. Miao, Y.; Hynan, P.; Von Jouanne, A.; Yokochi, A. Current Li-ion battery technologies in electric vehicles and opportunities for advancements. *Energies* **2019**, *12*, 1074. [CrossRef]
26. Zeng, X.; Li, J.; Shen, B. Novel approach to recover cobalt and lithium from spent lithium-ion battery using oxalic acid. *J. Hazard. Mater.* **2015**, *295*, 112–118. [CrossRef]
27. Ciez, R.E.; Whitacre, J. Examining different recycling processes for lithium-ion batteries. *Nat. Sustain.* **2019**, *2*, 148–156. [CrossRef]
28. Armand, M.; Axmann, P.; Bresser, D.; Copley, M.; Edström, K.; Ekberg, C.; Guyomard, D.; Lestriez, B.; Novák, P.; Petranikova, M. Lithium-ion batteries—Current state of the art and anticipated developments. *J. Power Sources* **2020**, *479*, 228708. [CrossRef]
29. Winslow, K.M.; Laux, S.J.; Townsend, T.G. A review on the growing concern and potential management strategies of waste lithium-ion batteries. *Resour. Conserv. Recycl.* **2018**, *129*, 263–277. [CrossRef]
30. Richa, K.; Babbitt, C.W.; Gaustad, G.; Wang, X. A future perspective on lithium-ion battery waste flows from electric vehicles. *Resour. Conserv. Recycl.* **2014**, *83*, 63–76. [CrossRef]
31. Makuza, B.; Tian, Q.; Guo, X.; Chattopadhyay, K.; Yu, D. Pyrometallurgical options for recycling spent lithium-ion batteries: A comprehensive review. *J. Power Sources* **2021**, *491*, 229622. [CrossRef]
32. Zeng, X.; Li, J.; Liu, L. Solving spent lithium-ion battery problems in China: Opportunities and challenges. *Renew. Sustain. Energy Rev.* **2015**, *52*, 1759–1767. [CrossRef]
33. Xu, C.; Dai, Q.; Gaines, L.; Hu, M.; Tukker, A.; Steubing, B. Future material demand for automotive lithium-based batteries. *Commun. Mater.* **2020**, *1*, 99. [CrossRef]
34. Velázquez-Martínez, O.; Valio, J.; Santasalo-Aarnio, A.; Reuter, M.; Serna-Guerrero, R. A critical review of lithium-ion battery recycling processes from a circular economy perspective. *Batteries* **2019**, *5*, 68. [CrossRef]
35. Baars, J.; Domenech, T.; Bleischwitz, R.; Melin, H.E.; Heidrich, O. Circular economy strategies for electric vehicle batteries reduce reliance on raw materials. *Nat. Sustain.* **2021**, *4*, 71–79. [CrossRef]
36. Işıldar, A.; van Hullebusch, E.D.; Lenz, M.; Du Laing, G.; Marra, A.; Cesaro, A.; Panda, S.; Akcil, A.; Kucuker, M.A.; Kuchta, K. Biotechnological strategies for the recovery of valuable and critical raw materials from waste electrical and electronic equipment (WEEE)—A review. *J. Hazard. Mater.* **2019**, *362*, 467–481. [CrossRef]
37. Wang, Y.; An, N.; Wen, L.; Wang, L.; Jiang, X.; Hou, F.; Yin, Y.; Liang, J. Recent progress on the recycling technology of Li-ion batteries. *J. Energy Chem.* **2021**, *55*, 391–419. [CrossRef]
38. Yun, L.; Linh, D.; Shui, L.; Peng, X.; Garg, A.; Le, M.L.P.; Asghari, S.; Sandoval, J. Metallurgical and mechanical methods for recycling of lithium-ion battery pack for electric vehicles. *Resour. Conserv. Recycl.* **2018**, *136*, 198–208. [CrossRef]
39. Cusenza, M.A.; Bobba, S.; Ardente, F.; Cellura, M.; Di Persio, F. Energy and environmental assessment of a traction lithium-ion battery pack for plug-in hybrid electric vehicles. *J. Clean. Prod.* **2019**, *215*, 634–649. [CrossRef]
40. Li, L.; Zhang, X.; Li, M.; Chen, R.; Wu, F.; Amine, K.; Lu, J. The recycling of spent lithium-ion batteries: A review of current processes and technologies. *Electrochem. Energy Rev.* **2018**, *1*, 461–482. [CrossRef]
41. Wang, W.; Wu, Y. An overview of recycling and treatment of spent $LiFePO_4$ batteries in China. *Resour. Conserv. Recycl.* **2017**, *127*, 233–243. [CrossRef]

42. Larouche, F.; Tedjar, F.; Amouzegar, K.; Houlachi, G.; Bouchard, P.; Demopoulos, G.P.; Zaghib, K. Progress and status of hydrometallurgical and direct recycling of Li-ion batteries and beyond. *Materials* **2020**, *13*, 801. [CrossRef] [PubMed]
43. De Souza, L.L.P.; Lora, E.E.S.; Palacio, J.C.E.; Rocha, M.H.; Renó, M.L.G.; Venturini, O.J. Comparative environmental life cycle assessment of conventional vehicles with different fuel options, plug-in hybrid and electric vehicles for a sustainable transportation system in Brazil. *J. Clean. Prod.* **2018**, *203*, 444–468. [CrossRef]
44. Costa, C.M.; Barbosa, J.C.; Gonçalves, R.; Castro, H.; Del Campo, F.; Lanceros-Méndez, S. Recycling and environmental issues of lithium-ion batteries: Advances, challenges and opportunities. *Energy Storage Mater.* **2021**, *37*, 433–465. [CrossRef]
45. Thompson, D.L.; Hartley, J.M.; Lambert, S.M.; Shiref, M.; Harper, G.D.; Kendrick, E.; Anderson, P.; Ryder, K.S.; Gaines, L.; Abbott, A.P. The importance of design in lithium ion battery recycling—A critical review. *Green Chem.* **2020**, *22*, 7585–7603. [CrossRef]
46. Richa, K.; Babbitt, C.W.; Gaustad, G. Eco-efficiency analysis of a lithium-ion battery waste hierarchy inspired by circular economy. *J. Ind. Ecol.* **2017**, *21*, 715–730. [CrossRef]
47. Rothermel, S.; Evertz, M.; Kasnatscheew, J.; Qi, X.; Grützke, M.; Winter, M.; Nowak, S. Graphite recycling from spent lithium-ion batteries. *ChemSusChem* **2016**, *9*, 3473–3484. [CrossRef]
48. Gaines, L.; Singh, M. *Energy and Environmental Impacts of Electric Vehicle Battery Production and Recycling*; Argonne National Lab. (ANL): Argonne, IL, USA, 1995.
49. Biradar, S.; Patil, R.; Ullegaddi, M. Energy storage system in electric vehicle. In Proceedings of the Power Quality '98, Hyderabad, India, 18–18 June 1998; pp. 247–255.
50. Gaines, L.; Cuenca, R. Life-cycle costs of lithium-ion vehicle batteries. *J. Passeng. Cars Mech. Syst. J.* **2000**, *109*, 1920–1931.
51. Messagie, M.; Boureima, F.; Matheys, J.; Sergeant, N.; Timmermans, J.-M.; Macharis, C.; Van Mierlo, J. Environmental performance of a battery electric vehicle: A descriptive Life Cycle Assessment approach. *World Electr. Veh. J.* **2010**, *4*, 782–786. [CrossRef]
52. Hoyer, C.; Kieckhäfer, K.; Spengler, T.S. A strategic framework for the design of recycling networks for lithium-ion batteries from electric vehicles. In *Glocalized Solutions for Sustainability in Manufacturing, Proceedings of the 18th CIRP International Conference on Life Cycle Engineering, Braunschweig, Germany, 2–4 May 2011*; Technische Universität Braunschweig: Braunschweig, Germany, 2011; pp. 79–84.
53. Howes, J. Battery Recycling Interaction with Washington. *SAE Int. J. Mater. Manuf.* **2012**, *5*, 150–159. [CrossRef]
54. Tytgat, J. The Recycling Efficiency of Li-ion EV batteries according to the European Commission Regulation, and the relation with the End-of-Life Vehicles Directive recycling rate. In Proceedings of the 2013 World Electric Vehicle Symposium and Exhibition (EVS27), Barcelona, Spain, 17–20 November 2013; pp. 1–9.
55. Hoyer, C.; Kieckhäfer, K.; Spengler, T.S. Impact of mandatory rates on the recycling of lithium-ion batteries from electric vehicles in Germany. In *Re-Engineering Manufacturing for Sustainability, Proceedings of the 20th CIRP International Conference on Life Cycle Engineering, Singapore, 17–19 April 2013*; Springer Science & Business Media: Berlin, Germany, 2013; pp. 543–548.
56. Ramoni, M.O.; Zhang, H.-C. End-of-life (EOL) issues and options for electric vehicle batteries. *Clean Technol. Environ. Policy* **2013**, *15*, 881–891. [CrossRef]
57. Miedema, J.H.; Moll, H.C. Lithium availability in the EU27 for battery-driven vehicles: The impact of recycling and substitution on the confrontation between supply and demand until 2050. *Resour. Policy* **2013**, *38*, 204–211. [CrossRef]
58. Zeng, X.; Li, J. Spent rechargeable lithium batteries in e-waste: Composition and its implications. *Front. Environ. Sci. Eng.* **2014**, *8*, 792–796. [CrossRef]
59. Hendrickson, T.P.; Kavvada, O.; Shah, N.; Sathre, R.; Scown, C.D. Life-cycle implications and supply chain logistics of electric vehicle battery recycling in California. *Environ. Res. Lett.* **2015**, *10*, 014011. [CrossRef]
60. Träger, T.; Friedrich, B.; Weyhe, R. Recovery concept of value metals from automotive lithium-ion batteries. *Chem. Ing. Tech.* **2015**, *87*, 1550–1557. [CrossRef]
61. Oliveira, L.; Messagie, M.; Rangaraju, S.; Sanfelix, J.; Rivas, M.H.; Van Mierlo, J. Key issues of lithium-ion batteries–from resource depletion to environmental performance indicators. *J. Clean. Prod.* **2015**, *108*, 354–362. [CrossRef]
62. Qiao, Q.; Zhao, F.; Liu, Z.; Jiang, S.; Hao, H. Cradle-to-gate greenhouse gas emissions of battery electric and internal combustion engine vehicles in China. *Appl. Energy* **2017**, *204*, 1399–1411. [CrossRef]
63. Li, J.; Barwood, M.; Rahimifard, S. Robotic disassembly for increased recovery of strategically important materials from electrical vehicles. *Robot. Comput. Integr. Manuf.* **2018**, *50*, 203–212. [CrossRef]
64. Bulach, W.; Schüler, D.; Sellin, G.; Elwert, T.; Schmid, D.; Goldmann, D.; Buchert, M.; Kammer, U. Electric vehicle recycling 2020: Key component power electronics. *Waste Manag. Res.* **2018**, *36*, 311–320. [CrossRef] [PubMed]
65. Diehl, O.; Schönfeldt, M.; Brouwer, E.; Dirks, A.; Rachut, K.; Gassmann, J.; Güth, K.; Buckow, A.; Gauß, R.; Stauber, R. Towards an alloy recycling of Nd–Fe–B permanent magnets in a circular economy. *J. Sustain. Metall.* **2018**, *4*, 163–175. [CrossRef]
66. Han, X.; Liang, Y.; Ai, Y.; Li, J. Economic evaluation of a PV combined energy storage charging station based on cost estimation of second-use batteries. *Energy* **2018**, *165*, 326–339. [CrossRef]
67. Lai, C.-M.; Li, Y.-H.; Cheng, Y.-H.; Teh, J. A high-gain reflex-based bidirectional DC charger with efficient energy recycling for low-voltage battery charging-discharging power control. *Energies* **2018**, *11*, 623. [CrossRef]
68. Borregan-Alvarado, J.; Alvarez-Meaza, I.; Cilleruelo-Carrasco, E.; Garechana-Anacabe, G. A bibliometric analysis in industry 4.0 and advanced manufacturing: What about the sustainable supply chain? *Sustainability* **2020**, *12*, 7840. [CrossRef]

69. Khan, M.A.; Pattnaik, D.; Ashraf, R.; Ali, I.; Kumar, S.; Donthu, N. Value of special issues in the journal of business research: A bibliometric analysis. *J. Bus. Res.* **2021**, *125*, 295–313. [CrossRef]
70. Yu, Y.; Li, Y.; Zhang, Z.; Gu, Z.; Zhong, H.; Zha, Q.; Yang, L.; Zhu, C.; Chen, E. A bibliometric analysis using VOSviewer of publications on COVID-19. *Ann. Transl. Med.* **2020**, *8*, 816. [CrossRef]

World Electric Vehicle Journal

MDPI

Article

Vehicle-Integrated Photovoltaics—A Case Study for Berlin

Philipp Hoth, Ludger Heide *, Alexander Grahle and Dietmar Göhlich

Methods of Product Development and Mechatronics, Technische Universität Berlin, Straße des 17. Juni 135, 10623 Berlin, Germany; philipp.hoth@campus.tu-berlin.de (P.H.); alexander.grahle@tu-berlin.de (A.G.); dietmar.goehlich@tu-berlin.de (D.G.)

* Correspondence: ludger.heide@tu-berlin.de

Abstract: Recent developments in vehicle-integrated photovoltaics (VIPV) offer prospects for enhancing electric vehicle range, lowering operating costs, and supporting carbon-neutral transport, particularly in urban settings. This study evaluates the solar energy potential of parking spaces in Berlin, considering challenges like building and tree shading using digital surface models and weather data for solar simulations. Utilizing open datasets and software, the analysis covered 48,827 parking spaces, revealing that VIPV could extend vehicle range by 7 to 14 km per day, equating to a median annual increase of 2527 km. The findings suggest median yearly cost savings of 164 euros from reduced grid charging. However, the environmental benefits of solar vehicle charging were found to be less than those of traditional grid-connected photovoltaic systems. The study introduces a method to pinpoint parking spaces that are most suitable for solar charging.

Keywords: vehicle-integrated photovoltaics; VIPV; urban environment; solar simulation; trees; GIS; open source; open data

Citation: Hoth, P.; Heide, L.; Grahle, A.; Göhlich, D. Vehicl-Integrated Photovoltaics—A Case Study for Berlin. *World Electr. Veh. J.* **2024**, *13*, 113. https://doi.org/10.3390/wevj15030113

Academic Editors: Wenbin Yu and Guang Zeng

Received: 20 February 2024
Revised: 11 March 2024
Accepted: 12 March 2024
Published: 15 March 2024

1. Introduction

With climate change being a monumental challenge of the 21st century, the European Union (EU) has been implementing policies to reduce greenhouse gas (GHG) emissions. In the 2030 Climate Target plan, the European Commission proposed to cut GHG emissions by at least 55% until 2030—compared to 1990—and pursue climate neutrality by 2050 [1]. The transport sector, responsible for about 25% of GHG emissions in Europe, is a primary contributor in reaching those climate goals.

In the 2022 "REPower EU" plan, the EU adopted a solar energy strategy that aims to accelerate the deployment of solar energy to reduce GHG emissions and the dependence on fossil fuels [2]. Besides stationary applications of photovoltaics (PV), new approaches on utilizing PV in the transport sector can become beneficial in helping reduce carbon emissions.

The market share of Electric Vehicles (EV) has been on the rise over the last decade, and 17 countries have already set targets to phase out the internal combustion engine within the next few decades ([3], p. 15f). For the city of Berlin, the electrification of all private cars would lead to an additional daily electricity demand of more than 6000 MWh [4]. To reduce this demand, producing energy onboard with the use of solar panels has been suggested.

Recently, new developments of vehicle-integrated photovoltaics have appeared. A small number of Original Equipment Manufacturers (OEMs) already offer an optional solar roof with modest energy outputs, and there have been promising developments with fully solar-oriented concepts that are trying to enter the market.

This study will focus on the solar potential of vehicles with integrated photovoltaics in the urban environment of Berlin-Neukölln, Germany, which represents a densely populated urban center in Germany well and has a dataset of all parking spots available (Section 3.1). A digital surface model-based solar simulation was conducted. The model factored in the effect of shading in urban surroundings throughout the day in a year. This model was then

evaluated using a dataset of 48,827 parking sites to identify the suitability for the solar charging of parked photvoltaic-equipped EVs.

Additionally, this research will generate a methodological approach to assess solar irradiation at an urban street level, taking seasonal vegetation influence into account. A distinct feature of the method is the open data approach that enables reproducibility for any desired location, with freely available data and free, open-source software.

2. State of the Art

This section provides a literature review of research on vehicle-integrated photovoltaics (VIPV), with a focus on studies that assess vehicle PV potentials in urban environments. Further, the scope of this work is defined, and potential research gaps are identified. In the end of Section 2.5, the research gap is identified and research questions are formulated.

2.1. Commercial Availability of the Technology

A review of current VIPV products, lightweight PV cells, and module technologies was conducted by Commault et al. [5]. It was concluded that VIPV products and developments for various applications are on a steady rise, especially car-based vehicle integration.

Currently available car models with integrated solar roofs are the Toyota Prius PHV [6], the Hyundai Sonata [7], and the Hyundai Ioniq 5. Meanwhile, there are current developments to integrate PV into mass-produced private passenger cars: Sono Motors Sion [8], Lightyear, Mercedes EQXX Concept, Fisker Ocean Fisker, Inc., Manhattan Beach, CA, USA [9], Squad Solar City, Breda, The Nederland [10], and Aptera Sol Aptera Motors Corp., Carlsbad, CA, USA [11].

2.2. Previous Studies on Achievable Energy

Earlier studies about VIPV have mainly focused on supplying additional power to auxiliary systems in applications such as refrigerating, heating, or air conditioning in commercial trucks [12], buses [13], or ambulances [14]. These systems are heavily reliant on battery power when the internal combustion engine is not running. The extra energy supplied from solar panels can extend the capabilities of the onboard batteries and save fuel when the internal combustion engine is running. In the context of this study, PV systems on vehicles are exclusively used to charge the high-voltage (HV) battery of EVs and therefore contribute to the driving energy, which would typically be obtained by charging from the electricity grid.

Yamaguchi et al. [15] assumed a relatively high solar module efficiency of 35%, which enables over 30 km/day of solar driving under an average irradiance of 4 kWh/$\left(\mathrm{m}^2 \cdot \mathrm{day}\right)$. This study provides cost targets for different module efficiencies and highlights the importance of low costs for the solar panels.

Lee and Park [16] analyzed electrical scooters in India and found that using a foldable 40 Wp solar panel, up to 45% of the energy demand could be satisfied using solar energy. They did not include building shading in their considerations.

Numerous studies that focus on PV potentials do not include shading characteristics of a real-world environment or set rather simple assumptions about the influence of shading. These studies focus primarily on vehicle parameters, including the PV systems, vehicle geometry, as well as battery and charging management systems. Heinrich et al. [17] have shown that with PV on a typical sedan car roof (1.7–2 m^2; 20% panel efficiency), an additional annual driving distance of 1900–3400 km can be achieved in Freiburg, southern Germany. This amounts to 13–23% of the yearly mean driving distance of cars in Germany (15,000 km). This would also result in approximately one fewer charging stop per month in the summer and an increased range on sunny days. This scenario did not account for losses due to shading. In a second 'at work charging' scenario, a car parked in the sun from 9 a.m. to 5 p.m. from Monday to Friday (assuming no sun exposure the rest of the time) resulted in an annual solar range of 1100–2030 km, which is ~60% of the range

from the first 'always unshaded' scenario. The main challenges stated are transformation losses from the panel to the HV battery, as well as possible battery self-consumption. Another issue addressed is the curvature of car roofs, which can lead to a significant irradiance mismatch, resulting in decreased panel efficiency. Open parking/driving during the day is crucial to generate substantial energy yields. Also, the panel technology must be durable and provide an aesthetic appearance for customers. For an improvement of energy yields, other surfaces, such as the hood and/or sides, could also be equipped with solar modules.

Kutter et al. [18] have assessed the yield potential of VIPV on commercial trucks and vans. One of the five scenarios across Stockholm, Freiburg, and Seville was the use-case of a parcel delivery van, which can achieve an annual solar range of 6637 to 11,450 km, which covers 35% to 60% of the annual energy demand. The panel efficiency was assumed at 21%, and shading was not considered in this study. They also found that self-consumption can be a critical factor in the feasibility of VIPV and that it needs to be minimized. The study conducted a break-even analysis, mainly determined by irradiation, electricity prices, and vehicle charging efficiency.

2.3. Weather and Shading

To analyze the real-world potential of VIPV, it is essential to assess the influence of environmental shading. Shadowing is more prominent in urban areas where a high building and vegetation density reduce solar energy yields. There are several studies that used test vehicles to measure shadow cast in real street environments.

Carr et al. [19] measured the solar irradiance on a test vehicle in the Netherlands over a time span of 20 weeks. With extrapolated driving patterns and shadowing events, the authors showed that in good conditions, VIPV could provide up to 41% of the required driving energy and up to 5617 km/year for the reference vehicle. Another study that measured irradiance in a real-world scenario with a test vehicle is the work of Araki et al. [20]. Onboard pyranometer data measurements in Japan showed that shading impacts and a curved car roof decreased the practical solar resources by 25%. It is of note that the vehicle measurements in the Netherlands and Japan were acquired in a mainly non-urban environment. An overview of various case studies and solar irradiance measurements was composed by Araki et al. [21] that showed how different research vehicles perform in different regions. For PHEVs (Plug-in Hybrid Electric Vehicle) an average power generation of 2.1 kWh/day over 100 days was achieved on a Toyota Prius equipped with 800 Wp solar panels [22]. Under the real environment conditions in Japan, they achieved a GHG reduction of 63%. Further measurements under real driving conditions were conducted by Oh et al. [23], Ota et al. [24] in South Korea and Japan. Ota et al. [24] concluded that the PV performance under intermittent shading conditions in an urban setting still achieves a relatively high performance ratio of 0.87. Oh et al. [23] combined irradiance measurements on a solar bus route with irradiance modeling and concluded that there is little economic feasibility with the current technology used in the study. But with better utilization of roof space, it has high potential in the future. Another study of a bus route in New Zealand found that installed solar panels can offset ~8.5% of the electricity demand [25].

Many studies have assessed the solar potential of VIPV with solar irradiance datasets that provide an accurate estimation, considering weather conditions. Most solar simulations in an urban environment assess the solar potentials of rooftops. However, real-world street-level urban shading influences based on digital surface model (DSM) data have been sparsely investigated. DSM-based solar simulations are an attractive tool to assess solar yields with complex shading characteristics over a larger urban area.

The study most closely related to the approach and methodology of this article is the work of Brito et al. [26], who have assessed solar potential in the urban area of Lisbon, Portugal. It is based on the irradiance modeling methodology by Santos et al. [27]. The authors used a Digital Surface Model on which a solar simulation was conducted to include the effect of shadowing in the urban environment. They measured the solar irradiation on parking sites and roads to estimate the solar yield for

VIPV. The results showed that the annual loss due to shadowing can reach 25% for roads and over 50% for urban parking spaces. Despite the shading losses, the average solar range extension was between 10 and 18 km/(day), assuming that there is the installation of a photovoltaics system of 1 kW peak power (kWp), which can significantly reduce charging needs in the summer, especially. Since the study performed by Brito et al. [26] was found to have a very similar approach to this study, it is further discussed in the methodology, Section 3. A further study by Said-Romdhane et al. [28] investigated shading losses by city obstacles and concluded that urban shading is a serious problem for maximizing the photovoltaic potential.

2.4. Life Cycle Assessment

Kanz et al. [29] presented a life cycle assessment (LCA) of a VIPV system on a light utility electric vehicle, the StreetScooter Work L. The study compared the on-board PV electricity generation with grid charging by calculating the CO_2 equivalents per kWh for the location of Cologne, Germany. With a PV array of 930 Wp, an operation time of 8 years, and an average shadowing factor of 30%, an emission factor of 0.357 kg CO_2-eq/kWh could be achieved. The average grid charging emissions amount to 0.435 kg CO_2-eq/kWh. However, if the shadowing factor exceeds 40%, the VIPV emissions would surpass the grid charging emissions. Kanz et al. further consider scenarios of a longer vehicle lifetime of 12 years and a "green" electricity manufacturing process, both of which decrease the emissions of the VIPV solution. On the other hand, the grid charging emissions are also expected to decrease in the future with the further deployment of renewable energies in Germany.

2.5. Research Gap and Research Questions

The current literature review on the potential of VIPV has shown that there are opportunities for further research on spatial solar simulations that take shadowing into account. Specifically, a gap was identified in the research of irradiance modeling for VIPV potentials that accounts for the influence of vegetation. In previous studies, tree shading was assumed to be constant throughout the year, affecting results by up to 50% (see Section 3.4). Furthermore, there are no published studies that have assessed the street-level solar potential in Central Europe and no approaches utilizing only open data and free software.

The scope of this work includes a solar assessment for VIPV at the street level, while considering the influences of building and vegetation shading. The focus lies on the characteristics of urban solar irradiation and the resulting potentials of parked SEVs, assuming a flat horizontal solar panel on the car roof. It is summarized in the following three research questions:

- What solar yield can be achieved by using VIPV on parked vehicles in urban areas, taking into account shading and partial shading of vegetation and buildings?
- What are the potential solar range benefits and charging cost savings for private parked cars with the use of VIPV?
- From an environmental perspective, how does the implementation of VIPV on parked vehicles compare to traditional grid-connected PV systems?

The result quantifies the desired irradiance, solar yield, and range values, while identifying parking site locations that can maximize the solar potential of VIPV. This includes a novel consideration of the impact of seasonally varying vegetation.

3. Methodology

The approach to calculate the solar yield potential of Solar Electric Vehicles (SEVs) is based on a Digital Surface Model (DSM), to which a monthly solar radiation simulation is applied. The solar simulation is enriched by long-term weather data as well as vegetation influence. A detailed database of the parking points enables the assessment of received solar energy on vehicles parked in the study area of Berlin-Neukölln.

All datasets used in this study are publicly available as open data to enable reproducibility. The free geographic information systems QGIS 3.22.1 [30] and GRASS (Geographic Resources Analysis Support System) 7.8 [31] were used to develop the solar yield model and visualizations. OpenStreetMap (OSM) [32] was used as the geographic database.

DSMs are elevation raster maps generated by aerial LiDAR (Light Detection And Ranging) measurements or image-based digital surface models. They provide highly detailed altimetry datasets of cities or other desired regions. DSMs are the foundation for conducting solar simulations to generate solar irradiation maps that provide spatial information about solar energy potential, as well as shading influence by buildings, terrain, and vegetation throughout the day and year [33].

The methodology chosen in this study was found to closely resemble the works of Brito et al. [26], who assessed the "Urban solar potential for vehicle integrated photovoltaics" for the city of Lisbon. Their main concept also consisted of conducting solar simulation models based on DSMs to analyze the solar potential of vehicles in an urban area. Aside from the main idea of the solar assessment, there are also differences in the approaches, as seen in Table 1. A comparison of the study results follows in Section 5.

Table 1. Methodology comparison to Brito et al., 2021 [26].

Topic	Centeno Brito et al. [26]	This Study
Location	Lisbon	Berlin
GIS and Simulation tool	ArcGIS/Area Solar Radiation numeric model	QGIS/GRASS r.sun
Vegetation	Parking sites under trees are assumed to be totally shaded at all times	Tree shading and transmittance of trees is taken into account
Street area	Parking Sites and road network	Parking Sites only
Ground inclination (incline/tilt of roads)	Ground inclination is considered	Ground inclination is neglected (i.e., vehicles are leveled)
Vehicle heights	Vehicle heights are neglected	Vehicle height assumed at 2 m
Life Cycle CO_2 emissions	Out of scope	Considered

One of the major differences of this study compared to Brito et al. [26] is that the Lisbon study assumed that parking spots under trees were being shaded at all times. In this study, parking points under trees are also treated differently. However, the seasonal vegetation transmittance is being taken into account to be able to make accurate solar yield predications about all of the available public parking sites of the study area.

The methodology of this study is presented in the following subchapters, starting from the input parking point data (Section 3.1), the development of the custom Digital Surface Model (Section 3.2), the solar simulation and solar maps (Section 3.3), integration of vegetation (Section 3.4), and the assumptions about the solar yield model and vehicle solar system (Section 3.5). A condensed overview of the methodology is shown in Figure 1.

3.1. Parking Sites in Berlin-Neukölln

In the district (in this case, 'district' refers to the German definition of 'Ortsteil' instead of the 'Bezirk' Neukölln) of Berlin-Neukölln, the location of 48,827 individual public parking sites have been catalogued by the "OpenStreetMap Parking Space Project" by Seidel [34]. Currently, this dataset is the only publicly available high-detail dataset of parking sites in Berlin. The parking sites are represented by a point, their respective map coordinates, and other useful information, such as street name. The dataset extends over the district limits of Neukölln.

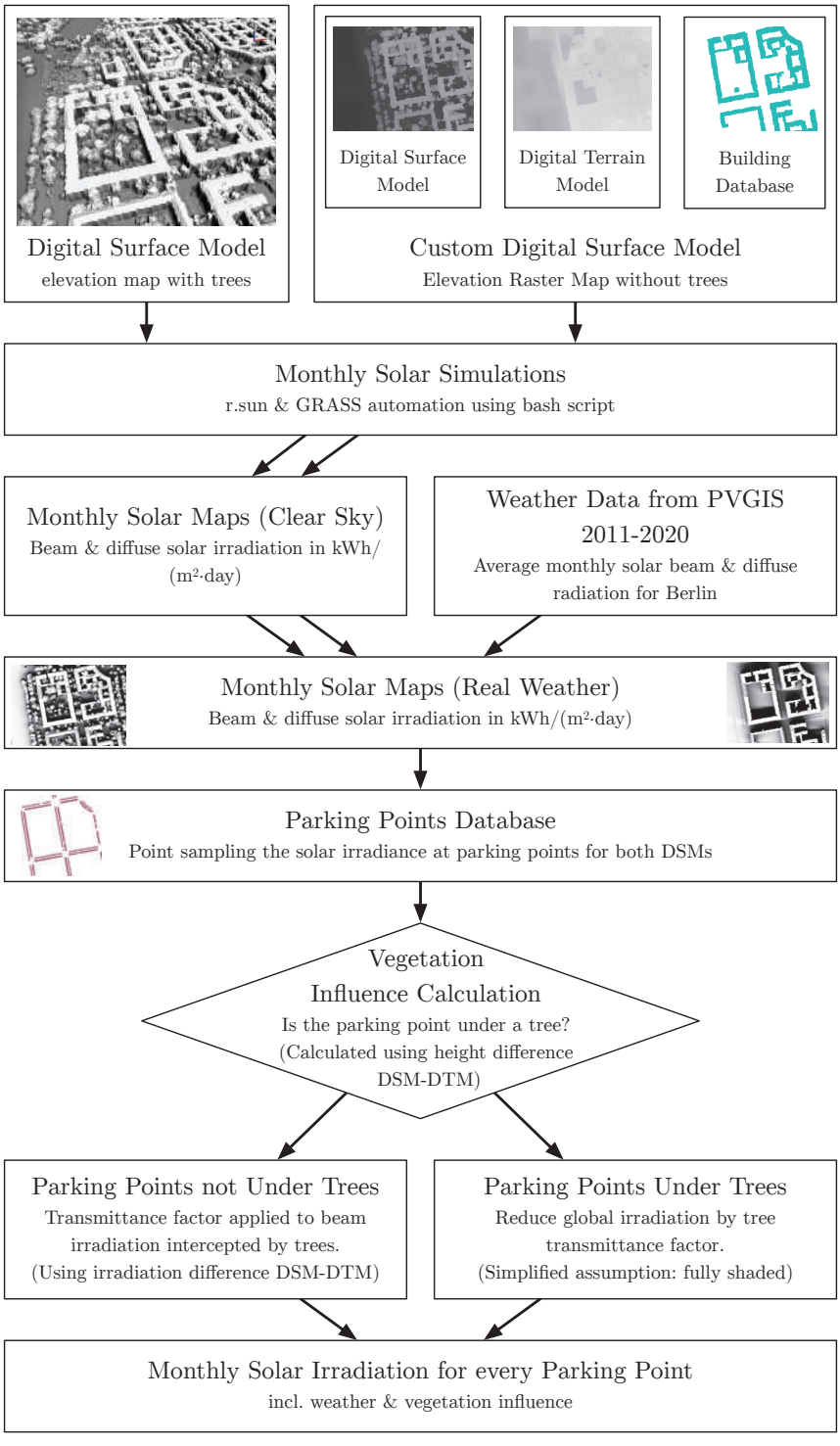

Figure 1. Methodology of the solar irradiation assessment on parking sites.

On average, private vehicles in Germany are parked 23 h of the day [35]; hence, the solar energy received while driving is not taken into account in this study. Therefore, the resulting data are representative of vehicles being parked outside the whole day. While driving, the solar energy yield can vary greatly, depending on the amount of direct solar exposure, time of day, cloudiness, etc.

This study assesses outdoor public parking areas only. According to Seidel et al. in the study area, about 19% of parking spaces are in enclosed or underground parking garages, which will not be considered in this study [34]. Also, the original parking point dataset was purged of 37 unsuitable points (19 of which had no coordinates, and 18 points were located under over-street buildings).

3.2. Development of the Custom Digital Surface Model

In order to calculate the solar potential of vehicles in a dense urban environment, a high-resolution DSM (Digital Surface Model) is needed to simulate sun shading caused by buildings, terrain, and vegetation throughout the day. In 2020, new image-based DSMs of Berlin were published by the Berlin Senate Administration of Urban Development, Construction and Living [36]. In this study, three datasets were used to develop a Custom DSM (from now on called DSM-nt, with nt meaning 'no trees') that enabled the integration of vegetation influence in the solar yield model.

The first dataset is an image-based DSM (bDOM—"Digitales bildbasiertes Oberflächenmodell") that contains the surface elevation of the entire city, including buildings and vegetation. The measurements were taken in the summer, when tree crowns are fully developed. This DSM will be used for the solar simulation, while it also provides the building elevation footprints for the custom DSM-nt, which is purged of trees.

To generate the custom DSM-nt, a second dataset in the form of a DTM (Digital Terrain Model; (DGM—"Digitales Geländemodell")) was used. This DTM contains information about the ground elevation. Buildings, vegetation, and other objects are not displayed. Both raster map datasets have a resolution of 1 m.

The third dataset, the WFS ALKIS Berlin building database supplied in QGIS, was used to crop the building footprints from the DSM to place them on top of the DTM ground. This 'building footprint' approach has been explained and used by Santos et al. [27] to analyze the potential of roof photovoltaics.

The DSM-nt along with the original DSM was then used to conduct the solar simulations discussed in Section 3.3. By simulating both DSMs, the shading influence of trees can be analyzed, as described in Section 3.4.

The DSM elevation models of the study area measure 8×6 km and therefore cover 48 km^2 of Berlin's urban area. The final step prior to the solar simulation was the integration of vehicle heights. To properly reflect the car roof's elevation, a vehicle height of 2 m was implemented into the DSM-nt raster map for each parking point.

3.3. Solar Simulation to Generate Monthly Solar Maps

For this study the *r.sun* GIS-based solar radiation model of Hofierka and Šúri [37] was chosen. It calculates the solar irradiance $\left(W/m^2\right)$ of elevation raster maps, in this case the DSM with trees and the custom DSM-nt of the study area Berlin-Neukölln. The proposed model simulates the sun position and radiation values for any given location, time, and date of the year. It casts shadows caused by elevation, such as terrain, buildings, and vegetation. The solar radiation is being split up into the beam component (direct sunlight) and the diffuse component (scattered light by the atmosphere). The *r.sun* solar radiation model is embedded in the open-source environment GRASS.

The *r.sun* model computes the solar irradiance $\left(W/m^2\right)$ over a given raster height map for a certain point in time. To simulate an entire day the *r.sun* simulation was done in 15-min steps. These solar irradiance snapshots were then summed up to calculate the solar irradiation values for the day $\left(Wh/\left(m^2 \cdot day\right)\right)$. The resulting daily solar irradiation maps

are called solar maps which contain the irradiation values for every 1 × 1 m pixel of the raster map.

The automation was accomplished by programming a *bash* script that automatically simulates each timestep and sums up the values for an entire day. To overcome computing time limitations only the representative day for each month was simulated. The representative day of a month in this context is the day with the mean daylength of the respective month. The solar irradiation values of the representative day were then assumed be present for the whole month.

The r.sun radiation model in its basic configuration calculates the solar irradiance under clear-sky conditions. To account for weather influences, in this case cloud coverage, the historical meteorological data from 2011 to 2020 of the European Photovoltaic Geographical Information System (PVGIS) was used to calculate the mean direct and diffuse solar irradiation for each month [38]. The data provided originate from the SARAH2 database, which is derived from satellite images and is validated from measurements of commercial PV modules at the European Joint Research Center.

The clear-sky solar maps were then scaled with the real solar radiation data from the weather database to create solar maps that include real-world weather influences. In this process, the weather station elevation of 39 m was also accounted for since higher elevations result in higher solar irradiation values. Ground albedo as well as diffuse reflections from buildings were not taken into account. Ground albedo can be neglected since it is mainly notable in snow-covered regions. Diffuse or direct reflections from buildings are not within the capabilities of the r.sun solar radiation model.

The solar simulation generated 12 solar maps (one for each month) that contain the spatial distribution of solar irradiation $\left(\mathrm{Wh}/\left(\mathrm{m}^2 \cdot \mathrm{day}\right)\right)$, including weather influences as well as shading areas caused by buildings. A solar map for the whole year was generated as well by combining the monthly solar maps. To extract the solar irradiation values from the solar maps, the QGIS *Point Sampling Tool* was used for the dataset of the 48,827 parking points. The result generated vector point layers (GeoPackages) that contain values of the beam and diffuse solar irradiation for each parking point for every month. The geopackages were exported as .csv/.xslx files to conduct the further vegetation influence and solar yield calculations.

Since the r.sun radiation model calculates the diffuse fraction of the solar irradiation for a flat horizontal plane, the sky view factor (SVF) was integrated into the model. The SVF is important in determining the surface radiation balance in obstructed areas [39]. The SVF is defined as the proportion of visible sky above. In an urban environment, a significant proportion of the visible sky is blocked by buildings and trees, which reduces the diffuse irradiation. The diffuse irradiation is therefore multiplied with the sky view factor (a value between 0 and 1, while 1 represents an unobstructed sky) [40,41]. In this study, the SVF was calculated with the QGIS-integrated SAGA Tool *saga:skyviewfactor* with the cell size method and 16 sectors. The operation was performed on the custom DSM-nt, which means that the SVF for this study is representative for buildings only. A sky view analysis on the DSM with trees was not performed because the resulting values very close to objects (in this case, trees, vehicles, and other objects) were highly inaccurate.

3.4. Integration of Shading by Urban Vegetation

The resulting solar maps of the custom DSM-nt do not contain any information about vegetation, which was purged from the DSM with trees earlier. In this step, the vegetation is reintegrated into the model to simulate the real-world shading effect of urban trees. To evaluate the influence of trees on the solar yield of parked vehicles directly underneath trees, there were three attributes assessed:

The first was whether a parking point is located under a tree or not. This is determined by calculating the difference between the original Digital Surface Model (DSM) and the Digital Terrain Model (DTM). Since the DSM includes trees and the DTM does not, it can be measured if there is a tree above a certain parking point. In this study, it was assumed

that if the difference of the DSM and DTM at a parking point is higher than 4 m, then this parking point is under a tree. Since the maximum height for trucks in Germany is 4 m, it is assumed that objects in the DSM that are lower than 4 m are trucks or other vehicles.

The second attribute to evaluate solar yield directly underneath trees is to quantify the transmittance (also referred to as transmissivity) of tree crowns. This topic was investigated by Konarska et al. [42] in the study "Transmissivity of solar radiation through crowns of single urban trees". The transmittance factor for several deciduous tree species was measured both in the summer, when trees are foliated, and winter, when trees are defoliated. Since the majority of trees in the study area of Neukölln are *Tilia* (Linden) and *Acer* (Maple) [43], which shed their leaves in winter, the transmittance factors by Konarska et al. [42] were applied. The mean transmittance factor of tree crowns was found to be 54% in winter and 10% in summer. This transmittance factor affects the received global irradiation (sum of the direct and beam components) under a tree. Similar transmittance factors were found by Oshio and Asawa [44], who measured an average transmittance of 0.1 during a summer afternoon on a tree-shaded sidewalk.

The third attribute required to calculate the shading influence of trees is the vegetation periods throughout the year. From the study on tree shadowing by Rosskopf et al. [45], it has been derived that deciduous trees are leafless from November until March. April to June exhibits the growth period, from July to September the tree crowns are fully developed, and in October, the leaves are shed. The transitions of the vegetation seasons were assumed to be linear. These attributes form the basis of a monthly transmittance factor, as shown in Table 2.

Table 2. Monthly transmittance factor of deciduous trees for global and direct solar irradiation.

Month	**Jan.**	**Feb.**	**Mar.**	**Apr.**	**May**	**June**	**July**	**Aug.**	**Sept.**	**Oct.**	**Nov.**	**Dec.**
Condition	leafless			growing			full crown			shed	leafless	
Transmittance global	54%			43%	32%	21%	10%			32%	54%	
Transmittance direct	48%			36%	25%	14%	3%			25%	48%	

Parking points that are not vertically located under a tree can still receive shading from trees nearby. In this model, the shading influence of trees for parking points not located under trees will only affect the beam component. (As explained in Section 3.3, the diffuse component in this model is only reduced by the sky view factor of the buildings.) To quantify the beam irradiation through tree crowns, the tree transmittance factor for direct irradiation also measured by Konarska et al. was applied (see Table 2).

The transmittance factors were then applied to the solar irradiation values of the affected parking points. The resulting solar irradiation values with weather and tree shading influence are presented in the following chapter.

A limitation of this method can be observed when the sun is at a lower angle in the sky and the irradiance hits locations under a tree. This limitation cannot be avoided when using raster maps. Shadow cast or sunshine under a tree cannot be simulated since the DSM only contains the maximum measured elevation for each 1 m $\times$ 1 m pixel. Therefore, in this study, the influence of trees was simplified and categorized in parking points under trees and parking points not under trees.

Even given these limitations, our approach improves on the state of the art in considering tree shading influence in an urban street environment. Other publications have mostly excluded the influence of vegetation in their research.

3.5. Solar Yield Calculation and Vehicle Assumptions

The final step to assess the solar potential of parked vehicles is to calculate the solar yield. The solar yield is the energy of the incoming Global Horizontal Irradiation that is being converted into electrical energy, which is stored in the vehicle battery.

For this study, it is assumed that a Solar Electric Vehicle can hold 1 kWp of installed photovoltaic power, for comparability with Commault et al. [5]. This would be achieved by

a panel size of approximately 5 m^2 and a 20% panel efficiency (also, other combinations are possible, such as a panel with 25% efficiency on a 4 m^2 surface or a future high efficiency panel with 33.3% efficiency on a 3 m^2 surface). The solar panel is assumed to be a flat horizontal surface.

The energy conversion efficiency from the solar panels into the battery is assumed at a conservative 75%. The 25% of conversion losses are caused by the DC–DC converter, ohmic losses in cables, and other conversion losses, such as the mismatch of modules (partial shading), temperature influence, and soiling [18]. The average energy consumption of state-of-the-art electric vehicles is 13 kWh/100 km [17].

The electricity price for public AC charging was assumed at a moderate 0.50 €/kWh after comparing several charging energy suppliers from Germany [46]. A monthly base fee was not comprised in the pricing. It is expected that charging prices will increase in the future, which will improve the cost savings of onboard solar panels.

As stated in Section 3.1, the mean private car in Germany is parked for 23 h of the day; hence, the energy yields are calculated for a car being parked the whole day. The full battery effect (solar power not being utilized because the battery is already full) is not taken into account within this study. The assumptions to calculate the solar yield and extended driving range were also chosen to match with the works of Brito et al. [26] to enable a comparison of the study results.

4. Results

4.1. Solar Irradiation in the Urban Environment

The mean yearly solar irradiation in Berlin from 2011 to 2020 is 1132 kWh/m^2 on a free-standing horizontal plane [38]. The diffuse and the direct sunlight components each contribute to about half of the yearly energy amount. Throughout the year, there are big differences, with December having the lowest irradiation at 17.5 kWh/m^2 and June having the highest irradiation at 171.5 kWh/m^2. On the street level, in a dense urban environment like Berlin, these values are often significantly reduced due to shading, especially in winter, as seen in Figure 2. The solar maps shown are the sum of the solar irradiance in time intervals of 15 min throughout the representative day of the month. The dark areas receive the lowest amount of irradiation, while the bright areas receive the highest amount of irradiation, with high proportions of direct sunlight throughout the day. However, even in the shade and under cloudy weather conditions, solar panels can still produce energy via diffuse light from the atmosphere.

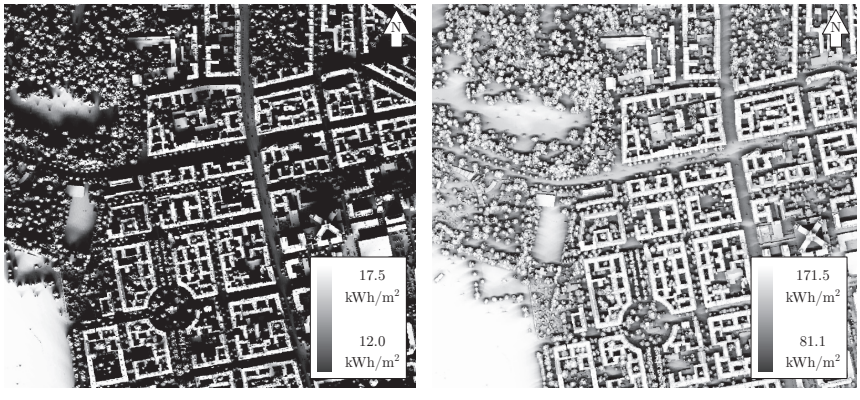

Figure 2. Solar maps for the months of December (**left**) and June (**right**). Exemplary cutout of Schillerkiez. The dark regions correspond to shaded areas. The white areas receive the highest amount of solar irradiation.

It must be pointed out that the minimum values (fully shaded areas) correspond to the diffuse fraction of the solar irradiation. In the r.sun simulation, the diffuse irradiation is

assumed to be uniform across the examined area. Therefore, when calculating the solar irradiation at the parking points, the sky view factor (SVF) was taken into account in order to improve the accuracy of the diffuse irradiation component, as described in Section 3.3. Additionally, the influence of trees was thoroughly examined in Section 3.4. The solar simulation was performed for each month and then integrated into the solar yield model to quantify the solar energy being received at each parking point.

4.2. Solar Irradiation at Parking Locations

The results of the solar assessment of parked vehicles over a complete year in Berlin-Neukölln are shown in Figure 3. It can be concluded that the urban environment causes substantial solar energy losses at the street level due to building and vegetation shading. Across the city and throughout the year, there is high variability in solar irradiation. While the best (unshaded) parking point of the dataset receives a yearly irradiation of 1120 kWh/m^2, the mean parking point receives 493 kWh/m^2. A favorable parking point above the 90th percentile still receives 871 kWh/m^2 per year; the median parking point only receives 438 kWh/m^2 per year. On average, more than half of the solar irradiation is lost due to shading.

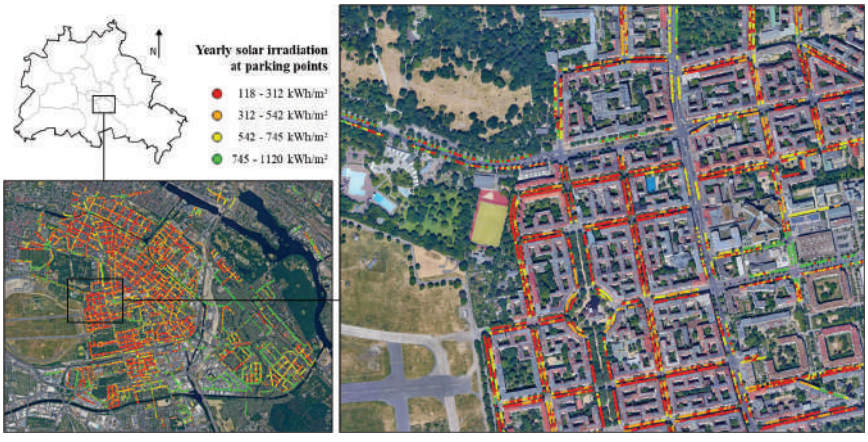

Figure 3. Yearly solar irradiation at parking points in the study area Berlin-Neukölln (**left**). A clos-eup shows the Schillerkiez area (**right**). For visualization purposes, the red points symbolize the lower 40% of parking points, while the other colors represent 20% of parking points each, according to the legend.

The model used in this study confirms that the influence of trees on solar irradiation is very high. In the summer, parking points directly under trees only receive 10% of the solar irradiation compared to unshaded parking points. Also, it becomes apparent that higher buildings south of parking areas significantly decrease the solar irradiation due to shading.

Dense residential areas like Schillerkiez encounter high amounts of shading, while commercial and industrial regions like Grenzallee have more open parking areas. These locations are more suitable for vehicle photovoltaics because people that work in the area park their car here during the day.

Figure 4 shows a histogram of the parking points by their yearly received irradiation. It is noticeable that there is a high concentration of data below 350 kWh/m^2. Nearly all of these rather unfavorable parking points are located directly under a tree and/or are heavily shaded throughout the year.

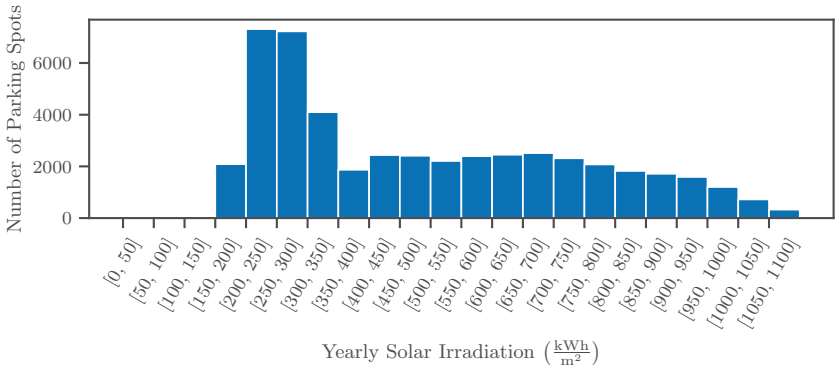

Figure 4. Histogram of the yearly solar irradiation for all parking points.

In Figure 5, a detailed image shows how the developed model can accurately distinguish irradiation values influenced by buildings and trees. Out of the 48,827 parking points, there are 18,223 located vertically under the radius of a tree crown, which amounts to 37% of the parking points. These parking points show a significant shading loss in this model because of the tree transmittance factor described in Section 3.4, especially in the summer months.

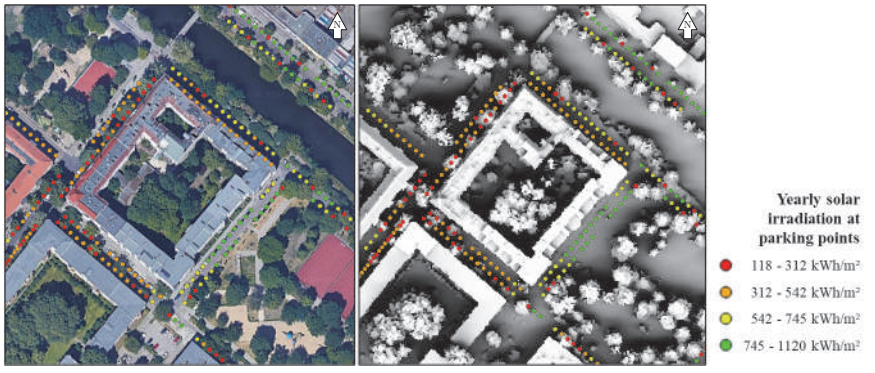

Figure 5. Detailed visualization displaying the influence of buildings and trees on the yearly solar irradiation. On the left, a GoogleMaps image is underlaid, while the right image shows the solar map of the full year. Location: Trusepark.

In Figure 6, the monthly solar irradiation is shown with the characteristic Northern Hemisphere irradiation peak in the summer months. It should be pointed out that there are very few parking points that are unshaded throughout the year. The upper quartile (75th percentile) is subjected to 38% of shading losses, while the median receives 61% of shading losses. The lower quartile (25th percentile) losses amount to a substantial 76%, which is also caused by a heavy dip of irradiation during the vegetation period from June to September, when tree crowns are fully developed.

The beam component of sunlight is crucial for maximizing solar energy yields. Since there is a high amount of shading present in cities, the diffuse fraction of solar irradiance provides a higher proportion of the solar energy yield compared to unshaded conditions. When comparing solar panels on parked vehicles in the study area with unshaded horizontal panels, the irradiation losses can be split up in beam and diffuse irradiation losses, as seen in Figure 7. While the diffuse losses stay relatively constant throughout the year, the beam losses are significantly higher in the summer months due to tree foliage.

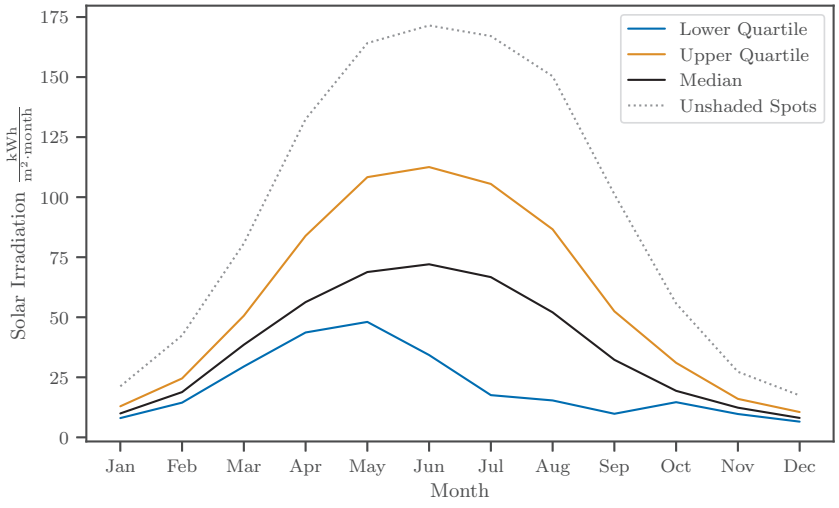

Figure 6. Monthly solar irradiation at parking points throughout the year.

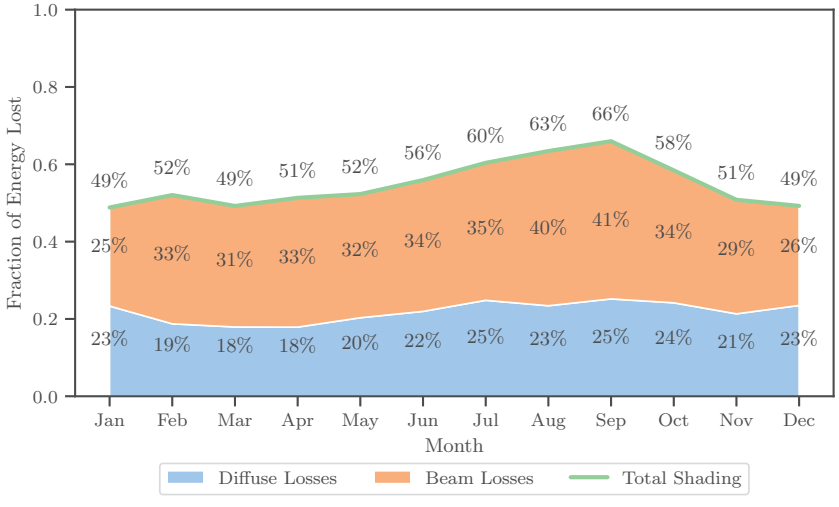

Figure 7. Monthly beam and diffuse irradiation losses as percentages of the Global Horizontal Irradiation.

4.3. Solar Yield Potential, Extended Driving Range, and Cost Savings

With the results of the solar irradiation assessment, the solar yield per vehicle on parking points is now calculated. As discussed in Section 3.5, the solar panel is assumed at 5 m^2, with 20% panel efficiency and further 25% losses between the panel and the battery.

For the analyzed parking points, the median energy capture is about 0.90 kWh/day. For a favorable parking spot (90th percentile) it is 1.79 kWh/day. Meanwhile, an unshaded parking spot provides 2.30 kWh/day.

The seasonal differences of the captured energy between winter (December to February) and summer (June to August) is quite pronounced. The median energy in winter is only 0.31 kWh/day, while in summer, it is 1.57 kWh/day. The difference of these values when compared to a favorable parking point at the 90th percentile is quite high. In a favorable location in winter, 0.51 kWh/day can be captured, while in summer, a value of

3.13 kWh/day can be achieved. An unshaded parking point in the summer provides a benchmark of 3.95 kWh/day.

In Figure 8, the energy captured per month is shown. In winter, the energy is low for all of the parking points, while in summer, there is a wide spread between favorable sunny parking points and heavily shaded points. This correlates to a greater variability of irradiation throughout the city in the summer.

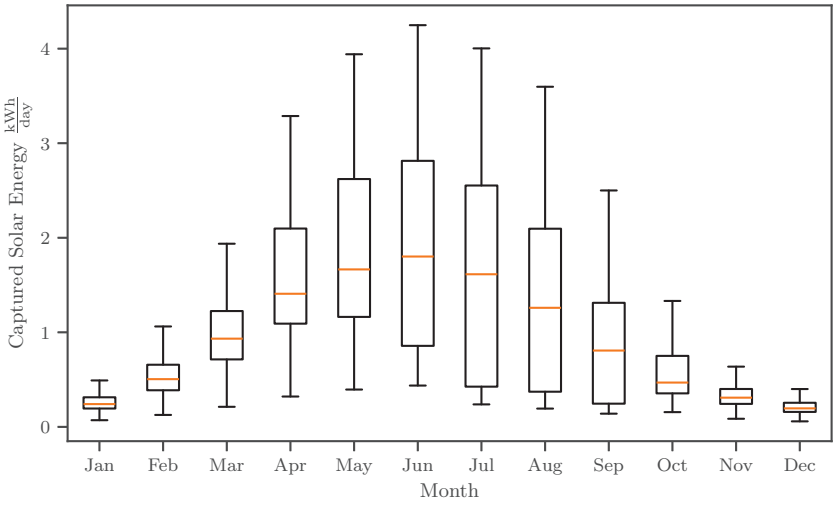

Figure 8. Captured solar energy for a 1 kWp solar array at 75% solar panel-to-battery conversion efficiency.

Assuming an energy consumption of 13 kWh/100 km (an optimistic assumption about the vehicle's efficiency, according to Heinrich et al. [17]; kept by us for compatibility with Brito et al. [26]), the extended driving range (EDR) per day and month can be calculated. Table 3 shows the daily and monthly driving range gained by the solar panels for the median and favorable parking point at the 90th percentile. Additionally, potential cost savings from reduced grid charging were calculated with an assumed electricity price of 0.50 €/kWh.

The average vehicle kilometers traveled (VKT) in Berlin is 25.5 km/day [47]. This implies that at a median parking point, about 27% of the annual kilometers traveled could be powered by energy that is generated from the solar panels. For a favorable parking point, this fraction can be as high as 54%, which can lead to a significant reduction of charging needs. Solar charging a vehicle on a summer day at a favorable parking point could cover 100% of the average daily VKT. However, since the energy delivery from VIPV varies seasonally, the charging infrastructure must be sized to fulfill the worst case charging demand, so the infrastructure savings are limited by the energy savings in the darkest months.

With an assumed PV system price of 2500 € (2.5 €/Wp), the break-even point for a median parking point would be reached after 15.2 years, which exceeds the average lifetime of private vehicles. At a favorable parking point, the break-even point would be reached after 7.7 years. With a lower proposed system cost of 1 €/Wp [18], the break-even point for a median parking point is reached after 6.1 years, and for a favorable parking point, it is reached after 3.1 years.

Table 3. Added solar range and cost savings for the median and favorable parking point.

	Median Parking Point			Favorable Point (90th Percentile)		
Month	**Daily Added Range (EDR)**	**Monthly Added Range (EMR)**	**Monthly Cost Savings**	**Daily Added Range (EDR)**	**Monthly Added Range (EMR)**	**Monthly Cost Savings**
All	6.9 km	2527 km	164.29 €	13.8 km	5027 km	326.74 €
January	1.9 km	57 km	3.73 €	3.0 km	94 km	6.11 €
February	3.9 km	109 km	7.07 €	6.5 km	182 km	11.83 €
March	7.2 km	222 km	14.46 €	11.8 km	367 km	23.83 €
April	10.8 km	325 km	21.12 €	20.4 km	611 km	39.71 €
May	12.8 km	397 km	25.81 €	24.9 km	771 km	50.10 €
June	13.9 km	416 km	27.02 €	26.6 km	799 km	51.92 €
July	12.4 km	385 km	25.02 €	24.6 km	763 km	49.58 €
August	9.7 km	300 km	19.52 €	21.2 km	657 km	42.71 €
September	6.2 km	186 km	12.11 €	13.8 km	413 km	26.82 €
October	3.6 km	112 km	7.26 €	7.3 km	227 km	14.74 €
November	2.4 km	71 km	4.63 €	3.9 km	118 km	7.69 €
December	1.5 km	47 km	3.03 €	2.5 km	76 km	4.96 €

5. Discussion

The results presented in the previous chapter show that significant shading losses are inevitable in an urban environment. Yet, the yearly added range of over 5000 km for a favorable parking location of the 90th percentile should not be neglected. It can be concluded that significant range increases—or charging energy decreases—are possible for vehicles at favorable parking spots under favorable conditions. However, the fixed parts of the transportation system, such as power grid infrastructure, charging infrastructure, and vehicle battery size, can only be reduced by a very small amount (less than 5%) when VIPV is widely implemented, as these components need to be designed for unfavorable times and places, where the energy gain is minimal. Another positive impact of VIPV could be the occurrence of fewer deep discharge events of vehicle batteries [48]. Fewer deep discharging events can result in higher battery lifetime and therefore less battery waste.

5.1. Comparison to Previous Research

When comparing the results to the findings of Brito et al. [26], the outcomes are similar. While Brito et al. estimated an annual average EDR for the median parking location to be about 10 $\mathrm{km}/(\mathrm{day} \cdot \mathrm{kWp})$, this study found an annual median EDR of 6.9 $\mathrm{km}/(\mathrm{day} \cdot \mathrm{kWp})$. This difference is most likely attributed to Lisbon being located further south and having more favorable weather conditions with lower cloud cover. The yearly unshaded solar irradiation in Berlin is 1117 $\mathrm{kWh}/\mathrm{m}^2$, whereas in Lisbon, it amounts to 1764 $\mathrm{kWh}/\mathrm{m}^2$ [38], which is 1.58 times higher than in Berlin. Brito et al. [26] also concluded that the solar potential on roads is higher than on parking sites because the distance to buildings and trees is higher in the middle of the road. This can also be applied to the results of this research, whereas it can presumed as well that the solar yield while driving in Berlin is higher on average than in a parking location. This obviously depends greatly on the choice of the parking location.

Further, Brito et al. stated that for the median urban parking space, about 33% of the annual typical driving distance could be supplied by energy generated by PV. In Berlin, this value was estimated to be 27%. It is worth mentioning that the typical driving distance used by Brito et al. [26] was 11,000 km/a, while in Berlin, a lower distance of 9323 km/a [47] was assumed, which increases the relative annual solar added range. A notable difference between the studies are the monthly irradiation losses. Brito et al. [26] found irradiation losses in winter to be much higher than in the summer, while in the study of Berlin, irradiation losses were relatively constant throughout the year. This is most likely

due to the integration of seasonal vegetation shading in this study. Since trees are blocking about 90% of the solar irradiance in the summer, the expected irradiation gains due to higher insolation angles of the sun might be mitigated by the tree foliage. Even though the results of the studies of Lisbon and Berlin are comparable, they are yet to be verified with experimental measurement data.

5.2. Limitations and Methodological Implications

The model assumptions and methodological implications have various impacts on the model results. The vehicle assumptions were chosen to match the assumptions by Brito et al. Whether a PV car roof panel with 1 kWp is feasible with current car geometries and state-of-the-art technology could be argued. Also, the assumption of the roof being flat and horizontal is a simplification since car roofs are usually curved surfaces. However, this aspect was taken into account by assuming conservative 25% conversion losses from the panel into the vehicle battery.

Another aspect that was not considered (congruent with Brito et al. [26]) is the battery saturation effect. There might be instances when the vehicle battery is fully charged and therefore cannot receive any more energy. This leads to a potential overestimation of solar energy yields within this study [49,50]. Other neglected aspects (for comparability purposes) were temperature influences and battery self-consumption [17].

Further, the energy output of VIPV on a daily or even hourly basis is highly dependent on the actual weather. In this study, weather data were averaged over time; hence, the daily solar yield and resulting added ranges can vary greatly from day to day, depending on the weather conditions and solar irradiance. The solar simulation time step interval of 15-min steps could also be decreased to increase the model's precision.

Another limitation is the assumption of the parking spots/vehicles being points. This implies that a location is either in direct sunlight or not. In a real-world scenario, there are frequent instances where the solar panels would be partially shaded, which entails a technological challenge for module manufacturers to utilize partial shading conditions [51].

The solar simulation also incorporates several limitations. One is that albedo and direct/diffuse reflections by buildings are not considered. Also, the diffuse irradiation was reduced by a sky view factor of the DSM-nt (without trees), as described in Section 3.3. This leads to an overestimation of the diffuse component of the sunlight for vehicles not parked under trees but near trees. The introduced tree transmittance factors also introduce inaccuracies because they do not distinguish the exact location of a vehicle under a tree. A tree is a highly complex and partially transmittant 3D object that alters the solar irradiance. Regarding this problem, raster DSM elevation maps are subjected to limitations. Even though DSMs are excellent tools for spatial analyses, they also induce certain constraints regarding the 3D nature of objects, especially trees. An example of this problem is a vehicle under a tree receiving sunshine from an angle. Hence, the approach of vertical shading was used in this study to approximate the shadow influence by trees at parking points directly underneath. This could lead to an underestimation of solar yields under trees.

The parking point classification (whether the point is located under a tree or not) highly depends on the accuracy of the DSM and DTM. The tree threshold of 4 m can lead to errors, i.e., smaller trees, trucks, or objects that are taller than 4 m can lead to an incorrect classification. Also, parking points under bridges or buildings can be misinterpreted (manual purging required).

5.3. Sustainability

When applying the assumptions of Kanz et al. [29] to the results within this study, it becomes apparent that the shadowing factor (shading losses) for the average parking point exceeds 50%. Therefore, VIPV would not be more sustainable than grid charging when taking all parking points into account. This means that to make VIPV a more sustainable option than grid charging, the consistent use of favorable unshaded parking locations is necessary. Kanz et al. [29] also conclude that the outcomes of VIPV LCA studies strongly

depend on the location of use of the vehicle, the annual irradiation, and the carbon footprint of the grid-mix in that location.

A different approach in evaluating the sustainability of VIPV is the comparison to stationary photovoltaics, such as a rooftop or utility-scale PV. The combined annual solar yield of all 48,827 parking points in the study area is a hypothetical 18 GWh. If this photovoltaic capacity was installed in an unshaded place like a roof, it could produce 41 GWh. These roof panels could also be sloped at a 40° angle and advantageous azimuth to generate an even greater energy yield of 48.6 GWh [38]. While VIPV can improve the charging autonomy of vehicles, they are subjected to higher shading and an unfavorable orientation compared to stationary solar panels.

In an unshaded scenario, the efficiency of VIPV onboard charging is higher than the efficiency of PV grid charging. The VIPV system only requires a DC–DC voltage conversion to charge the battery, while PV grid charging undergoes a DC–AC conversion, grid transmission losses, and, finally, AC–DC conversion within the onboard charger. The conversion losses of grid PV charging, therefore, are greater than VIPV onboard charging. However, in shaded conditions, the efficiency advantage of VIPV rapidly disappears, and it becomes more efficient to charge the vehicle via grid PV.

When comparing VIPV to rooftop solar installations from an environmental perspective, the lifetime of each system plays a very important role, as most negative environmental consequences are caused by the manufacturing process, which can be "amortized" by the energy produced during the service life. For rooftop PV installations, a lifetime of 25 years is usually assumed [52]. For the lifetime of electric vehicles, no good data set exists yet, as the wide adoption of electric vehicles is still in progress. The average fleet age in Germany is 11.3 years [53]. However, due to vehicles leaving the fleet both through scrapping and export, as well as political and economical factors affecting fleet composition, the lifetime of future VIPV-equipped cars is uncertain. A higher lifetime or highly efficient recycling program for VIPV equipment can significantly improve their ecological footprint.

6. Conclusions and Outlook

Photovoltaics are one of the future pillars of sustainable energy generation. Next to stationary PV on roofs or dedicated PV farms, VIPV could be used in scenarios where available space for stationary PV is limited and unshaded parking is an option.

The results of this study imply that VIPV will not solve the energy supply challenges for urban electric vehicles. VIPV, rather, can unfold its potential in certain use-cases, where it is assured that the solar yield is being maximized by avoiding shaded areas. Only then can VIPV become a sustainable contributor to future transportation. However, in higher latitudes, this potential is mainly restricted to the spring and summer months.

Our research shows that up to 5000 km annually can be generated using VIPV on passenger cars in ideal unshaded parking locations in Berlin, Germany. However, this applies to 10% of the observed parking locations in the study area.

The utilization of solar energy in stationary applications is more favorable because it (ideally) is unshaded, the panels can be aligned at an ideal angle and azimuth, and the conditions of use are less challenging than PV integration into a vehicle.

Photovoltaics in world regions south of Berlin (51° latitude) could significantly improve solar performance. Heinrich et al. concluded that in an unshaded scenario, the yearly solar range could be increased by 50% in Spain or even 60% in California, USA, due to higher irradiation levels [17].

Urban areas are the most challenging environments for VIPV. In rural regions and road networks, the solar yields are expected to be significantly higher. To ensure a better utilization of VIPV, designated solar parking areas could be established by communities. Mobile map applications could provide valuable information to inform drivers about favorable parking locations for solar charging. Conversely, the results of our study could also be used to identify well-shaded parking spots, where vehicles without solar panels heat up the least.

A further assessment of the potential of commercial vehicles and trucks is highly suggested. Large flat roof areas are suitable for PV, and the driving profiles are often located outside of urban areas.

The approach of this study is exclusively based on open data and free software to enable a barrier-free reproducibility for other world regions. Our methodology can be applied to different cities in a further study, analyzing the solar potential for different kinds of buildings and road layouts, tree coverage, and parking strategies and developing a generic prediction for the feasibility of VIPV in different types of cities. Further research can also be conducted on solar irradiance modeling of VIPV potential while driving. The consideration of trees can be further improved by using 3D photogrammetry.

Author Contributions: Conceptualization: L.H.; Data curation: L.H.; Funding acquisition: D.G.; Investigation: P.H., L.H. and A.G.; Methodology: P.H., L.H. and A.G.; Project administration: D.G.; Software: P.H. and L.H.; Supervision: L.H. and A.G.; Validation: L.H. and A.G.; Visualization: P.H. and L.H.; Writing—original draft: P.H.; Writing—review and editing: P.H., L.H., A.G. and D.G. All authors have read and agreed to the published version of the manuscript.

Funding: This work was supported by the German Federal Ministry for Education and Research (BMBF) as part of the "Research Campus Mobility2Grid" project, under grant number 03SF0674A. The authors acknowledge the financial support and resources provided for the development of the code and research findings reported in this paper. We acknowledge support by the German Research Foundation and the Open Access Publication Fund of TU Berlin.

Data Availability Statement: These data were derived from the following resources available in the public domain:ALKIS Berlin (https://daten.berlin.de/datensaetze/alkis-berlin-geb%C3%A4ude-wfs); DGM Berlin (https://www.berlin.de/sen/sbw/stadtdaten/geoportal/landesvermessung/geotopographie-atkis/dgm-digitale-gelaendemodelle/); bDOM Berlin (https://www.berlin.de/sen/sbw/stadtdaten/geoportal/landesvermessung/geotopographie-atkis/bdom-digitales-bildbasiertes-oberflaechenmodell/) as well as the Neukölln Parking Space Dataset (https://parkraum.osm-verkehrswende.org/project-prototype-neukoelln/report/, all accessed on 25 September 2023).

Conflicts of Interest: The authors declare no conflicts of interest.

References

1. European Commission. Delivering the European Green Deal. Available online: https://commission.europa.eu/strategy-and-policy/priorities-2019-2024/european-green-deal/delivering-european-green-deal_en (accessed on 25 September 2023).
2. European Commission. Solar Energy. Available online: https://energy.ec.europa.eu/topics/renewable-energy/solar-energy_en (accessed on 25 September 2023).
3. International Energy Agency. Global EV Outlook 2020. Available online: https://iea.blob.core.windows.net/assets/af46e012-18c2-44d6-becd-bad21fa844fd/Global_EV_Outlook_2020.pdf (accessed on 16 November 2023).
4. Straub, F.; Göhlich, D. Modelling and Simulation of a fully Electrified Urban Private Transport—A case Study for Berlin, Germany. In Proceedings of the 2023 IEEE Transportation Electrification Conference & Expo (ITEC), Detroit, MI, USA, 21–23 June 2023; pp. 1–8. [CrossRef]
5. Commault, B.; Duigou, T.; Maneval, V.; Gaume, J.; Chabuel, F.; Voroshazi, E. Overview and Perspectives for Vehicle-Integrated Photovoltaics. *Appl. Sci.* **2021**, *11*, 11598. [CrossRef]
6. Miyoshi, T. Solar Charging System for Prius PHV. *J. Jpn. Soc. Appl. Electromagn. Mech.* **2017**, *25*, 379–382. [CrossRef]
7. Hyundai Motor Group. Everything About the Sonata Hybrid's Solar Roof. Available online: https://www.hyundaimotorgroup.com/story/CONT0000000000091508 (accessed on 25 September 2023).
8. Sono Motors. Sion. Available online: https://web.archive.org/web/20221113201804/https://sonomotors.com/en/sion/ (accessed on 25 September 2023).
9. Fisker, Inc. Fisker Ocean. Available online: https://www.fiskerinc.com/ocean (accessed on 25 September 2023).
10. Squad Mobility BV. Squad Soar City Car. Available online: https://www.squadmobility.com/squad#specs (accessed on 25 September 2023).
11. Aptera Motors Corp. Driven by the Sun. Available online: https://aptera.us/ (accessed on 25 September 2023).
12. Kühnel, M.; Hanke, B.; Geißendörfer, S.; von Maydell, K.; Agert, C. Energy forecast for mobile photovoltaic systems with focus on trucks for cooling applications. *Prog. Photovoltaics Res. Appl.* **2017**, *25*, 525–532. [CrossRef]
13. Wendeker, M.; Gęca, M.J.; Grabowski, Ł.; Pietrykowski, K.; Kasianantham, N. Measurements and analysis of a solar-assisted city bus with a diesel engine. *Appl. Energy* **2022**, *309*, 118439. [CrossRef]

14. Almonacid, G.; Muñoz, F.J.; de la Casa, J.; Aguilar, J.D. Integration of PV systems on health emergency vehicles. The FIVE project. *Prog. Photovoltaics Res. Appl.* **2004**, *12*, 609–621. [CrossRef]
15. Yamaguchi, M.; Nakamura, K.; Ozaki, R.; Kojima, N.; Ohshita, Y.; Masuda, T.; Okumura, K.; Satou, A.; Nakado, T.; Yamada, K.; et al. Analysis for the Potential of High-Efficiency and Low-Cost Vehicle-Integrated Photovoltaics. *Solar RRL* **2022**, *7*, 2200556. [CrossRef]
16. Lee, K.Y.; Park, S. Reducing Charging Burden of Light Electric Vehicles by Integrated Photovoltaic Modules. In Proceedings of the 2022 IEEE Vehicle Power and Propulsion Conference (VPPC), Merced, CA, USA, 1–4 November 2022; pp. 1–6. [CrossRef]
17. Heinrich, M.; Kutter, C.; Basler, F.; Mittag, M.; Alanis, L.; Eberlein, D.; Schmid, A.; Reise, C.; Kroyer, T.; Neuhaus, D.; et al. Potential and Challenges of Vehicle Integrated Photovoltaics for Passenger Cars. In Proceedings of the 37th European Photovoltaic Solar Energy Conference and Exhibition, Virtual, 7–11 September 2020; pp. 1695–1700. [CrossRef]
18. Kutter, C.; Alanis, L.E.; Neuhaus, D.H.; Heinrich, M. Yield potential of vehicle integrated photovoltaics on commercial trucks and vans. In Proceedings of the 38th European PV Solar Energy Conference and Exhibition, Virtual, 6–10 September 2021.
19. Carr, A.; van den Tillaart, E.; Burgers, A.; Köhler, T.; Newman, B. Vehicle integrated photovoltaics: Evaluation of the energy yield potential through monitoring and modelling. In Proceedings of the 37th EUPVSEC European PV Solar Energy Conference and Exhibition, Lisbon, Portugal, 7–11 September 2020; WIP GmbH & Co Planungs-KG: München, Germany, 2020.
20. Araki, K.; Ota, Y.; Yamaguchi, M. Measurement and Modeling of 3D Solar Irradiance for Vehicle-Integrated Photovoltaic. *Appl. Sci.* **2020**, *10*, 872. [CrossRef]
21. Araki, K.; Carr, A.; Chabuel, F.; Commault, B.; Derks, R.; Ding, K.; Duigou, T.; Ekins-Daukes, N.; Gaume, J.; Hirota, T.; et al. State-of-the-Art and Expected Benefits of PV-Powered Vehicles. Available online: https://iea-pvps.org/wp-content/uploads/2021/07/IEA_PVPS_T17_State-of-theart-and-expected-benefits-of-VIPV_report.pdf (accessed on 11 March 2024).
22. Masuda, T.; Araki, K.; Okumura, K.; Urabe, S.; Kudo, Y.; Kimura, K.; Nakado, T.; Sato, A.; Yamaguchi, M. Next environment-friendly cars: Application of solar power as automobile energy source. In Proceedings of the 2016 IEEE 43rd Photovoltaic Specialists Conference (PVSC), Portland, OR, USA, 5–10 June 2016; IEEE: Piscataway, NJ, USA, 2016. [CrossRef]
23. Oh, M.; Kim, S.M.; Park, H.D. Estimation of photovoltaic potential of solar bus in an urban area: Case study in Gwanak, Seoul, Korea. *Renew. Energy* **2020**, *160*, 1335–1348. [CrossRef]
24. Ota, Y.; Araki, K.; Nagaoka, A.; Nishioka, K. Evaluating the Output of a Car-Mounted Photovoltaic Module Under Driving Conditions. *IEEE J. Photovoltaics* **2021**, *11*, 1299–1304. [CrossRef]
25. ur Rehman, N.; Hijazi, M.; Uzair, M. Solar potential assessment of public bus routes for solar buses. *Renew. Energy* **2020**, *156*, 193–200. [CrossRef]
26. Brito, M.C.; Santos, T.; Moura, F.; Pera, D.; Rocha, J. Urban solar potential for vehicle integrated photovoltaics. *Transp. Res. Part D Transp. Environ.* **2021**, *94*, 102810. [CrossRef]
27. Santos, T.; Gomes, N.; Freire, S.; Brito, M.; Santos, L.; Tenedório, J. Applications of solar mapping in the urban environment. *Appl. Geogr.* **2014**, *51*, 48–57. [CrossRef]
28. Said-Romdhane, M.B.; Skander-Mustapha, S.; Slama-Belkhodja, I. Analysis study of city obstacles shading impact on solar PV vehicle. In Proceedings of the 2021 4th International Symposium on Advanced Electrical and Communication Technologies (ISAECT), Alkhobar, Saudi Arabia, 6–8 December 2021; pp. 1–6. [CrossRef]
29. Kanz, O.; Reinders, A.; May, J.; Ding, K. Environmental Impacts of Integrated Photovoltaic Modules in Light Utility Electric Vehicles. *Energies* **2020**, *13*, 5120. [CrossRef]
30. QGIS Association. QGIS Geographic Information System. Available online: http://www.qgis.org (accessed on 11 March 2024).
31. GRASS Development Team. *Geographic Resources Analysis Support System (GRASS GIS) Software, Version 8.2*; Open Source Geospatial Foundation: Dover, DE, USA, 2022. [CrossRef]
32. OpenStreetMap Contributors. OpenStreeMap Dataset. Available online: https://www.openstreetmap.org (accessed on March 13 2024).
33. Freitas, S.; Catita, C.; Redweik, P.; Brito, M. Modelling solar potential in the urban environment: State-of-the-art review. *Renew. Sustain. Energy Rev.* **2015**, *41*, 915–931. [CrossRef]
34. Seidel, A. Parkraumanalyse für den Berliner Ortsteil Neukölln—Methoden- und Ergebnisbericht. Available online: https://parkraum.osm-verkehrswende.org/project-prototype-neukoelln/report (accessed on March 13 2024).
35. Kuhnimhof, T.; Nobis, C. Ergebnisbericht. Available online: https://bmdv.bund.de/SharedDocs/DE/Anlage/G/mid-ergebnisbericht.pdf?__blob=publicationFile (accessed on March 13 2024).
36. Senatsverwaltung für Stadtentwicklung, Bauen und Wohnen. Geotopographie/ATKIS. Available online: https://www.berlin.de/sen/sbw/stadtdaten/geoportal/landesvermessung/geotopographie-atkis/ (accessed on 25 September 2023).
37. Hofierka, J.; Šúri, M. The solar radiation model for Open source GIS: Implementation and applications. In Proceedings of the Open Source GIS—GRASS Users Conference 2002, Trento, Italy, 11–13 September 2002.
38. European Commission, Joint Research Centre Energy Efficiency and Renewables Unit. PVGIS-5 Geo-Temporal Irradiation Database. Available online: https://re.jrc.ec.europa.eu/pvg_tools/en/ (accessed on March 13 2024).
39. Dirksen, M.; Ronda, R.; Theeuwes, N.; Pagani, G. Sky view factor calculations and its application in urban heat island studies. *Urban Clim.* **2019**, *30*, 100498. [CrossRef]
40. Böhner, J.; Antonić, O. Chapter 8 Land-Surface Parameters Specific to Topo-Climatology. In *Developments in Soil Science*; Elsevier: Amsterdam, The Netherlands, 2009; pp. 195–226. [CrossRef]

41. Häntzschel, J.; Goldberg, V.; Bernhofer, C. GIS-based regionalisation of radiation, temperature and coupling measures in complex terrain for low mountain ranges. *Meteorol. Appl.* **2005**, *12*, 33–42. [CrossRef]
42. Konarska, J.; Lindberg, F.; Larsson, A.; Thorsson, S.; Holmer, B. Transmissivity of solar radiation through crowns of single urban trees—Application for outdoor thermal comfort modelling. *Theor. Appl. Climatol.* **2013**, *117*, 363–376. [CrossRef]
43. Referat Freiraumplanung und Stadtgrün. Straßenbäume in Berlin. Available online: https://www.berlin.de/sen/uvk/natur-und-gruen/stadtgruen/daten-und-fakten/stadtbaeume/ (accessed on March 13 2024).
44. Oshio, H.; Asawa, T. Estimating the Solar Transmittance of Urban Trees Using Airborne LiDAR and Radiative Transfer Simulation. *IEEE Trans. Geosci. Remote Sens.* **2016**, *54*, 5483–5492. [CrossRef]
45. Rosskopf, E.; Morhart, C.; Nahm, M. Modelling Shadow Using 3D Tree Models in High Spatial and Temporal Resolution. *Remote Sens.* **2017**, *9*, 719. [CrossRef]
46. Verivox GmbH. Ladetarife für E-Autos. Übersicht Ladetarife: Anbieter und Kosten. Available online: https://www.verivox.de/elektromobilitaet/ladetarife/ (accessed on 3 February 2023).
47. Kirk, E. In Deutschland sind Kfz-Halter*innen im Schnitt 11.085 Kilometer p. a. Unterwegs. Available online: https://www.check24.de/unternehmen/presse/pressemitteilungen/in-deutschland-sind-kfz-halter*innen-im-schnitt-11.085-kilometer-p.-a.-unterwegs-2059/ (accessed on March 13 2024).
48. Kouzelis, A. Model-Based Impact Analysis of Vehicle-Integrated Photovoltaics and Vehicle-to-Grid on Electric Vehicle Battery Life. Available online: http://resolver.tudelft.nl/uuid:f3f716b3-f57e-486b-b5b9-8d5edf643d41 (accessed on 25 October 2023).
49. Lodi, C.; Gil-Sayas, S.; Currò, D.; Serra, S.; Drossinos, Y. Full-battery effect during on-board solar charging of conventional vehicles. *Transp. Res. Part D Transp. Environ.* **2021**, *96*, 102862. [CrossRef]
50. Birnie, D.P. Analysis of energy capture by vehicle solar roofs in conjunction with workplace plug-in charging. *Sol. Energy* **2016**, *125*, 219–226. [CrossRef]
51. Götz, D.; Hahn, D.; Gottschalg, R.; Dassler, D.; Schindler, S.; Hanifi, H. Evaluation of shading tolerance of PV modules with different module designs for mobile applications by simulation, indoor and outdoor measurements. In Proceedings of the 36th European Photovoltaic Solar Energy Conference and Exhibition, Marseille, France, 9–13 September 2019; pp. 1–6.
52. Martinopoulos, G. Are rooftop photovoltaic systems a sustainable solution for Europe? A life cycle impact assessment and cost analysis. *Appl. Energy* **2020**, *257*, 114035. [CrossRef]
53. Kraftfahrt-Bundesamt. Durchschnittsalter der Personenkraftwagen Wächst. Available online: https://www.kba.de/DE/Statistik/Fahrzeuge/Bestand/Fahrzeugalter/2021/2021_b_kurzbericht_fz_alter_pdf.pdf;jsessionid=A280D8FA3BFB96F7C153FA41124F3002.live11292?__blob=publicationFile&v=2 (accessed on 18 November 2023).

energies

MDPI

Article

Investigation on Traffic Carbon Emission Factor Based on Sensitivity and Uncertainty Analysis

Jianan Chen [1], Hao Yu [2], Haocheng Xu [2], Qiang Lv [2], Zongqiang Zhu [2], Hao Chen [1], Feiyang Zhao [1,*] and Wenbin Yu [1,*]

[1] School of Energy and Power Engineering, Shandong University, Jinan 250061, China; chenjianan@mail.sdu.edu.cn (J.C.); 202314499@mail.sdu.edu.cn (H.C.)
[2] China Automotive Engineering Research Institute Co., Ltd., Chongqing 401122, China; yuhao1@caeri.com.cn (H.Y.); xuhaocheng@caeri.com.cn (H.X.); lvqiang@caeri.com.cn (Q.L.); zhuzongqiang@caeri.com.cn (Z.Z.)
* Correspondence: fyzhao@sdu.edu.cn (F.Z.); wbyu@sdu.edu.cn (W.Y.)

Abstract: The premise for formulating effective emission control strategies is to accurately and reasonably evaluate the actual emission level of vehicles. Firstly, the active subspace method is applied to set up a low-dimensional model of the relationship between CO_2 emission and multivariate vehicle driving data, in which the vehicle specific power (*VSP*) is identified as the most significant factor on the CO_2 emission factor, followed by speed. Additionally, acceleration and exhaust temperature had the least impact. It is inferred that the changes in data sampling transform the establishment of subspace matrices, affecting the calculation of eigenvector components and the fitting of the final quadratic response surface, so that the emission sensitivity and final fitting accuracy are impressionable by the data distribution form. For the *VSP*, the best fitting result can be obtained when the *VSP* conforms to a uniform distribution. Moreover, the Bayesian linear regression method accounts for fitting parameters between the *VSP* and CO_2 emission factor with uncertainties derived from heteroscedastic measurement errors, and the values and distributions of the intercept and slope α and β are obtained. In general, the high-resolution inventory of the carbon emission factor of the tested vehicle is set up via systematically analyzing it, which brings a bright view of data processing in further counting the carbon footprint.

Keywords: CO_2 emission; vehicle specific power; active subspaces; multivariate analysis; uncertainty analysis

Citation: Chen, J.; Yu, H.; Xu, H.; Lv, Q.; Zhu, Z.; Chen, H.; Zhao, F.; Yu, W. Investigation on Traffic Carbon Emission Factor Based on Sensitivity and Uncertainty Analysis. *Energies* **2024**, *17*, 1774. https://doi.org/10.3390/en17071774

Academic Editor: Anastassios M. Stamatelos

Received: 13 March 2024
Revised: 5 April 2024
Accepted: 6 April 2024
Published: 8 April 2024

1. Introduction

The transportation sector is the third largest CO_2 emission source after power and industry. Carbon emissions from transportation can cause significant harm to the climate and environment [1]. Therefore, how to reduce vehicle exhaust pollution and greenhouse gas emissions has become an undeniable challenge [2]. Roughly, China emitted 35% of the world's total CO_2 emissions in 2023 [3]. Road transportation contributes to 70~80% of the CO_2 emissions in the transportation sector of China, which still dominates as one of the largest parts of total carbon emissions [4,5]. An action plan of decarbonizing China's road transport is becoming among the stated national policies [6]; meanwhile, the technology roadmap for energy saving and new energy vehicles is being undertaken by many researchers and institutes, with the aim to achieve carbon neutrality by 2060.

How to accurately and reasonably evaluate the actual emission level of vehicles is a prerequisite for formulating effective emission control strategies. Many scholars have conducted research on this issue. When characterizing the emission characteristics of different operating conditions, instantaneous operating parameters such as speed [7,8], acceleration [9,10], fuel consumption [11,12], and driving distance [13] are used while the vehicle specific power (*VSP*) is a newly proposed alternative parameter in correlation with

speed and acceleration. Jimenez et al. [14] found that the *VSP* could capture the majority of the dependence of light vehicle emissions on driving conditions when combined with traffic flow data, thus improving the accuracy of the predicted emissions. Song et al. [15] compared the estimated fuel consumption with actual data and demonstrated that the *VSP* bin distribution model is reliable and accurate in estimating fuel consumption. When the real-time speed data are available, the speed-specific *VSP* bin distribution model may help monitor dynamic transportation, to facilitate quantifying the relationship between *VSP* distributions and vehicle fuel consumption or emissions. Forcetto et al. [16] applied the *VSP* as an additional parameter for improving the evaluation of the vehicle dynamics, which can add a better comprehension of the real drive emission (RDE) dynamic, complementing the regulatory parameters. By combining fuel consumption rates with *VSP* distributions, Zhang, L. et al. [17] proposed an improved method for evaluating eco-driving behavior depending on the *VSP* distribution at a specific speed, providing a potential way to evaluate fuel consumption and emission combined with traffic conditions.

Vehicle CO_2 emission is typically influenced by a combination of multiple factors, so it is necessary to reveal the impacts of simultaneous multi-factor variables on emission factors, in order to summarize the methods for constructing a high-resolution database of the carbon emission factor. At present, existing multi-factor variable analysis models, such as COPERT [18,19], MOBILE [20,21], IVE [22], etc., are all based on static factors such as vehicle type, vehicle mileage, fuel quality, and fuel volatility to study the vehicle emission factors of motor vehicles. The traditional one-at-a-time (OAT) sensitivity analysis applied in the sensitivity analysis can only predict the relative sensitivity of a single input parameter at a time, so that it precludes the synergistic effects between multiple input parameters. A multivariate analysis is able to reflect the combined effects of multiple variables on output, which displays a more accurate and flexible performance than an OAT sensitivity analysis. However, a multi-factor analysis of emission factors based on dynamic driving conditions is rarely reported.

The active subspace (AS) is an emerging dimensionality reduction method for multivariate analysis, which can obtain the low-dimensional structure of the multivariate function by transforming the high-dimensional space [23,24]. At the same time, the component values of the active direction vector can provide global sensitivity information of the target quantity relative to the input parameters [25]. In the field of engineering, the active subspace method has been applied in sensitivity analysis studies of turbomachinery [26,27] and combustion [28–30], but, up to now, few reports of AS application in transportation emissions analysis had been presented.

Moreover, as the data size increases, the uncertainties driven by the error distribution from the sampling data play an important role in the accounting accuracy of carbon emissions under varied transportation scenarios. Thus, uncertainty quantification is necessary when formulating emission factor models based on real-driving cycles.

Bayesian inference methods have been used widely for model calibration and uncertainty analysis [31,32]. The goal of the Bayesian regression method is to characterize the parameter distribution consistent with the given experimental dataset, instead of finding the best fit for regression model parameters [33,34]. Li et al. [35] used Bayesian approaches to explicitly accommodate the uncertainty of the model predictions. Mudgal, A. et al. [36] modeled the speed profiles of drivers by using a Bayesian inference methodology, and then estimated the vehicular emissions using past experimental data. Martin et al. [37] presented a new Bayesian methodology called the Cambridge Automotive Research Modelling Application (CARma), which was able to categorize the sources of uncertainty and calibrate uncertain parameters to present the results as probability distribution functions.

The active subspace method and Bayesian linear fitting method are used in this study to combine multivariate analysis with uncertainty analysis, explore the sensitivity of vehicle emissions to operating parameters, and improve the accuracy of emission prediction by considering the distribution of operating points. This method comprehensively studies the impact of vehicle driving parameters on emission factors, laying the foundation for con-

structing a high-resolution database of the carbon emission factor. The study is structured as follows: In Section 2, the methodologies of this study are introduced, including the data processing and the principles of data analysis methods, such as multivariate analysis and uncertainty analysis. Then, Section 3 describes the details analysis of the sensitivity and the uncertainty of the carbon emission factor. Finally, some concluding remarks are given in Section 4.

2. Materials and Methods

2.1. Data Source

In China, light gasoline vehicles account for a large proportion of road traffic. Meanwhile, China has fully implemented the national VI motor vehicle emission standards. Therefore, in this study, the multi-purpose gasoline passenger vehicle that meets the national VI motor vehicle emission standards was chosen. The source of data used in this study is the RDE test conducted by China Automotive Engineering Research Institute Co., Ltd. (Chongqing, China).

The RDE test was conducted once and employed by using on-board emission measurement system OBS-ONE GS Unit from Japan's HORIBA company to measure the vehicle's emissions per second. The test route is shown in Figure 1. The test route is located in Chongqing, China. The total length of this route is 82.096 km, and the maximum altitude and minimum altitude are 499.4 m and 240.9 m, respectively. The test data are divided into three working conditions based on the vehicle's driving speed, urban ($v \leq 60$ km/h), suburban (60 km/h $< v \leq 90$ km/h), and highway ($v > 90$ km/h), as shown in Figure 2, and the distribution of driving conditions is shown in Table 1.

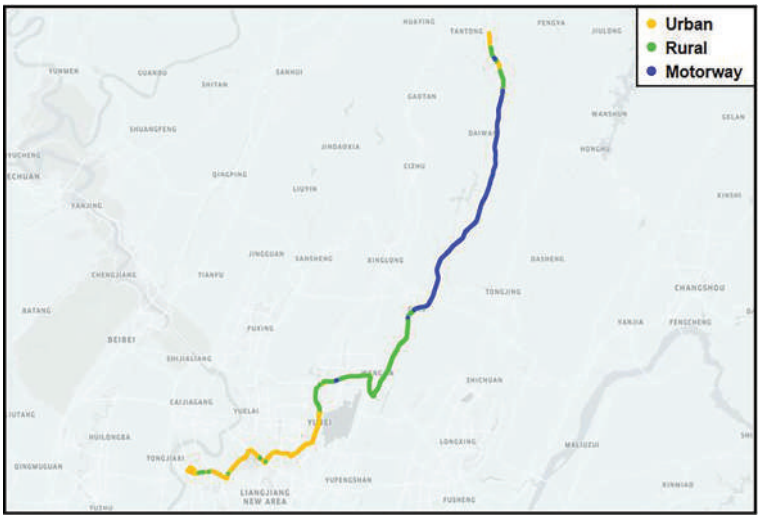

Figure 1. Testing route.

Table 1. Distribution of vehicle driving conditions.

	Urban	Rural	Motorway	Total
Average Speed (km/h)	28.2	77.6	106.0	
Distance (km)	27.2	26.7	28.3	82.096
Duration (h:min:s)	0:57:52	0:20:36	0:16:00	1:34:28

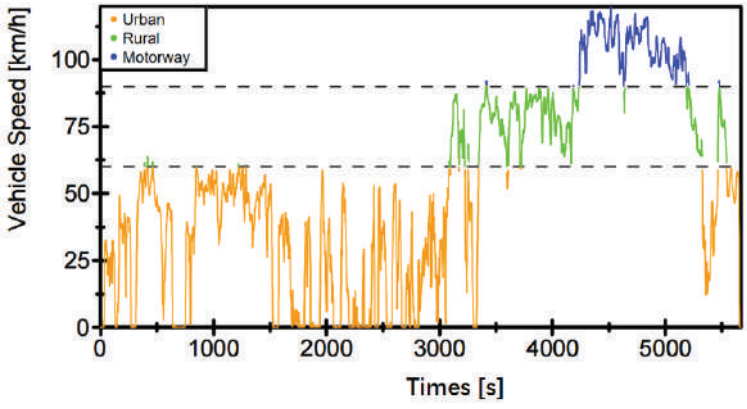

Figure 2. The speed structure of vehicle driving.

2.2. VSP Binning Method

VSP is a dynamic proxy variable of the vehicle with vector nature, defined as the power output per unit mass of motor vehicle towed by the engine (kw/t) or m^2/s^3 [14]. For light gasoline vehicles, the formula for *VSP* is computed as [38]:

$$VSP = v \times (1.1a + 0.132) + 0000302 \times v^3 \quad (1)$$

where v is the driving speed of the tested vehicle in a unit of m/s, and a is the driving acceleration of the tested vehicle in a unit of m/s^2.

The values of *VSP* can be one-to-one corresponded and classified with cluster bins, thus using the overall *VSP* distribution as a function of average vehicle speed for statistical analysis. Since there is a certain degree of discreteness in RDE data, this study conducted cluster analysis on *VSP* [38], when *VSP* bin = k, and $VSP \in [k - 0.5, k + 0.5]$. The data are mainly concentrated in *VSP* bin $\in [-20, 20]$, accounting for 96.93%. Therefore, this study mainly focuses on the data in this range, and the *VSP* bin distribution is shown in Figure 3.

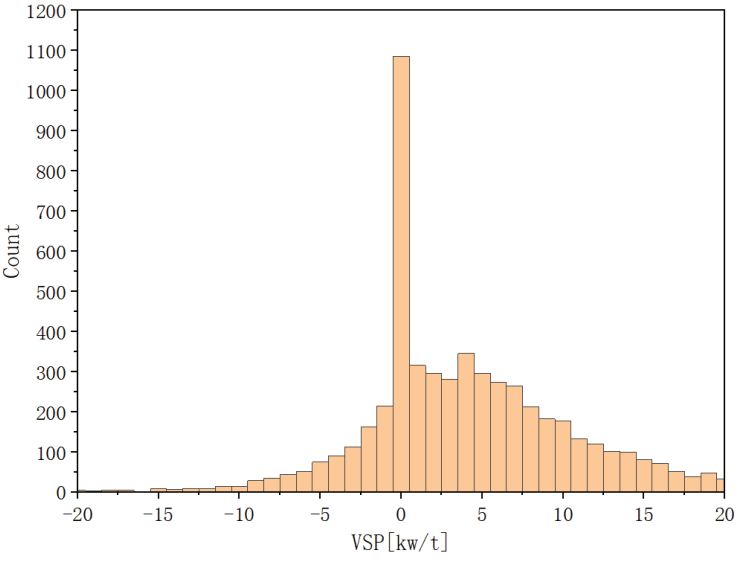

Figure 3. *VSP* bin distribution of the RDE data.

The traffic carbon emission factor generally refers to the carbon emissions generated per unit workload, in order to evaluate carbon emission efficiency. This study applies the speed-specific CO_2 emission factor based on driving distance to characterize the mass of CO_2 emitted by motor vehicles per unit distance (g/km), which can be obtained by Equation (2):

$$EF^k = \frac{\sum ER^k}{\sum v^k} \times 3600 \quad (2)$$

where EF^k, ER^k, and v^k, respectively, represent the CO_2 emission factor (g/km), CO_2 emission rate (g/s), and driving speed (km/h) of the tested vehicle when *VSP* bin = *k*.

2.3. Active Subspace Method

The active subspace is a type of low-dimensional structure in a function of several variables. It can achieve dimensionality reduction through transformations in high-dimensional spaces, which essentially involves important directions with higher sensitivity in high-dimensional spaces through linear space transformations. In the present study, a one-dimensional active subspace is observed to figure out the key contributors to the variability in the emission factor response. The input–output response diagram is approximated by a linear model. This method is applicable when both conditions are satisfied that the activity subspace is one-dimensional and the relationship between the quantity of interest and its input parameters is approximately monotonic. The sufficient summary plot shows the relationship between the linear combination of the quantity of interest and input parameters (i.e., active variables), with the weights of the linear combination being the components of the normalized gradient of the linear model. Each point on the plot represents a set of inputs and corresponding outputs of the model. The specific flowchart of performing the active subspace method for sensitivity analysis is shown in Figure 4. In the current study, speed, acceleration, *VSP*, CO_2 emission rate, and exhaust temperature are selected as input variables, and corresponding CO_2 emission factor as the quantity of interest.

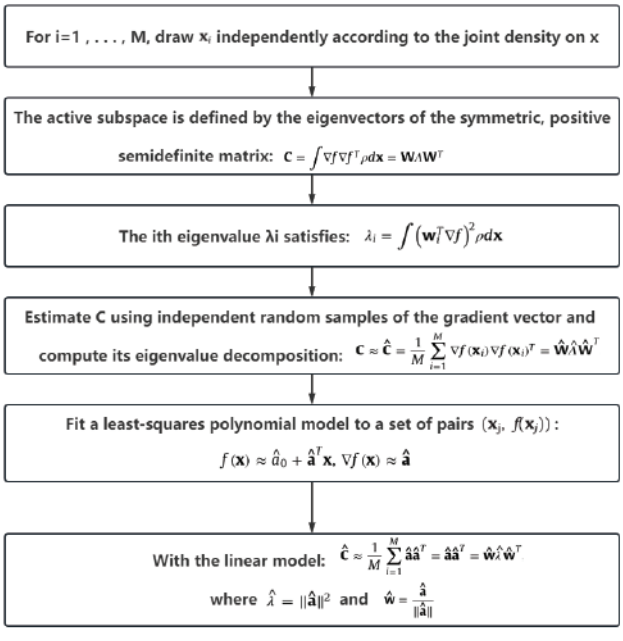

Figure 4. Workflow of active subspace method.

The active subspace is defined by the eigenvectors of a symmetric positive semidefinite matrix:

$$C = \int \nabla \mathrm{f} \nabla \mathrm{f}^{\mathrm{T}} \rho dx = W \Lambda W^T \tag{3}$$

where W is the orthogonal matrix of the eigenvector, and Λ is the diagonal matrix of non-negative eigenvalues arranged in descending order.

To estimate the eigenvectors and eigenvalues, independent random samples of gradient vector are used to estimate C and calculate its eigenvalue decomposition [39]:

$$C \approx \hat{C} = \frac{1}{M} \sum_{i=1}^{M} \nabla f(x_i) \nabla f(x_i)^T = \hat{W} \hat{\Lambda} \hat{W}^T \tag{4}$$

where x_i are based on $\rho(x)$ drawing randomly and independently.

In this study, the gradient of polynomial approximation is worked out and the least-squares polynomial model is fitted to a pair of $\left(x_j, f\left(x_j\right)\right)$. When the polynomial approximation is a linear function of x, the calculation amount of $\hat{W}$ decreases sharply. The gradient of the global linear model is constant for all x:

$$f(x) \approx \hat{a}_0 + \hat{\mathrm{a}}^T x \tag{5}$$

$$\nabla f(x) \approx \hat{\mathrm{a}} \tag{6}$$

Thus, $\hat{C}$ can be expressed as:

$$\hat{C} \approx \frac{1}{M} \sum_{i=1}^{M} \hat{\mathrm{a}} \hat{\mathrm{a}}^T = \hat{\mathrm{a}} \hat{\mathrm{a}}^T = \hat{w} \hat{\lambda} \hat{w}^T \tag{7}$$

where $\hat{w} = \hat{\mathrm{a}} / \|\hat{\mathrm{a}}\|$ is the normalized gradient of the linear model. In a linear model, only one-dimensional active subspace can be identified.

2.4. Bayesian Linear Regression

Bayesian linear regression is a method that uses probability distribution rather than point estimation to construct linear regression. The response variable y is not a single value to be estimated, but a probability distribution assumed to be extracted from a normal distribution. The posterior probability distribution of model parameters $P(\beta \mid y,X)$ is conditional on the inputs and output of the training, as calculated in Equation (8):

$$P(\beta | y, X) = \frac{P(y | \beta, X) P(\beta | X)}{P(y | X)} \tag{8}$$

which is equal to the likelihood $P(y \mid \beta,X)$ multiplied by the prior probability distribution $P(\beta \mid X)$ of the parameter β of the given input and divided by the normalization constant.

In this study, the data with heteroscedastic measurement errors (errors with different variances) in both variables are regression-fitted through Bayesian theory. It is assumed that the independent variable ξ and the dependent variable η follow a Gaussian distribution, and that ξ is a random vector of n data points extracted from a certain probability distribution [40,41]. According to the usual additive model, the dependent variable η depends on ξ:

$$\eta_i = \alpha + \beta \xi_i + \varepsilon_i \tag{9}$$

where ε_i is a random variable which represents the intrinsic scatter in η_i about the regression relationship and (α, β) are the regression coefficients. The mean of ε_i is assumed to be zero and the variance σ^2 is constant. The values (x, y) measured with errors are observed instead

of the actual values of (ξ, η). The measured values are assumed to be related to the actual values as:

$$x_i = \xi_i + \varepsilon_{x,i} \tag{10}$$

$$y_i = \eta_i + \varepsilon_{y,i} \tag{11}$$

where $\varepsilon_{x,i}$ and $\varepsilon_{y,i}$ are, respectively, the random measurement errors on x_i and y_i, which are normally distributed with known variances $\sigma^2_{x,i}$ and $\sigma^2_{y,i}$ and covariance $\sigma_{xy,i}$. The variances and covariance are assumed to be the same for each data point in this study.

Due to the complexity of parameter distribution, the Markov chain Monte Carlo (MCMC) method is introduced to conduct efficient sampling and promote the final convergence to the target distribution. By using MCMC, the mathematical expectation of the posterior distribution inferred by Bayesian inference is obtained as the estimated value of the parameter.

3. Results and Discussion

3.1. Multivariate Sensitivity Analysis of CO_2 Emission Factor

The components of the eigenvector are plotted in Figure 5; the single-column active variable weights quantify the sensitivity of the output to input parameters. The larger the weights, the greater the changes in the CO_2 emission factor caused by the corresponding parameters. The CO_2 emission rate (CO_2/[g/s]) is definitely the most influential input parameter for the CO_2 emission factor, and the *VSP* (vsp/[kw/t]) and speed (v/[km/h]) are coming next, with the *VSP* having a greater weight than speed. In addition, the influence of acceleration (a/[m/s^2]) and exhaust temperature (ExhaustTemp/[degC]) is minimal.

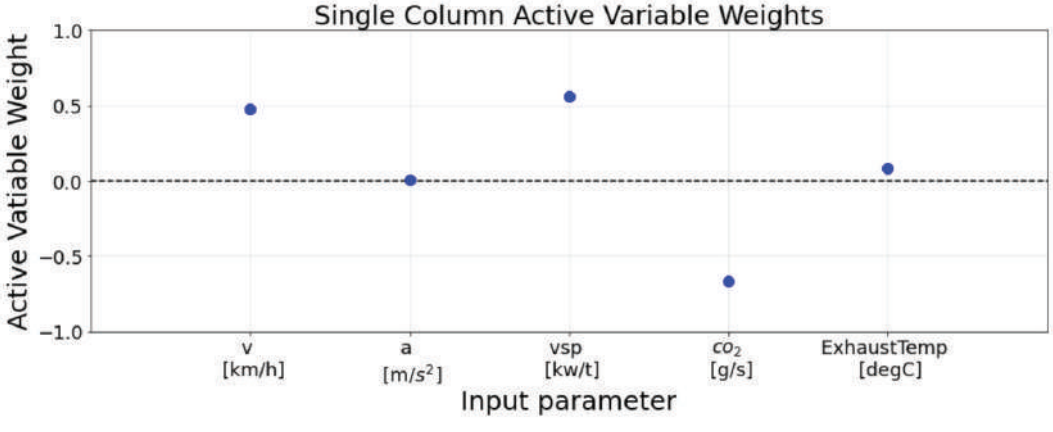

Figure 5. Input parameter weights calculated using all operating points.

The symbol of the input parameter weight can represent the positive and negative ratio relationship between the output parameter and input parameters. Meanwhile, the trend of the change can also be quantitatively described by the quadratic response surface curves and the influence of the eigenvector components on the activity variables (as seen in Figure 6). When all other input parameters suppose fixed values, the CO_2 emission factor decreased by 3.333% when v is increased from 5 to 10, and continually decreased by 3.330% when v reached 15. In general, the CO_2 emission factor will increase with a decrease in speed. This result may be caused by the definition of the emission factor, which is based on the driving distance (Equation (2)). When the speed decreases, $\sum v^k$ decreases, and the amplitude of the $\sum ER^k$ change is much smaller than $\sum v^k$, hence resulting in an increase in EF^k.

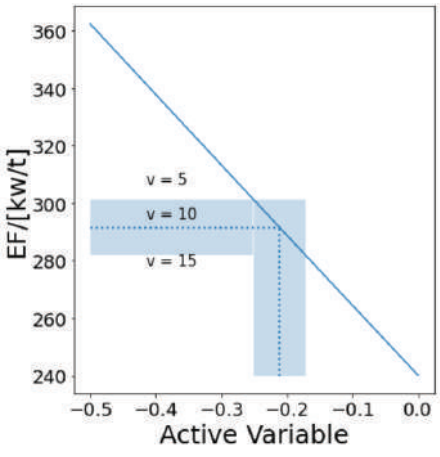

Figure 6. Estimation of output change with respect to input parameter values.

3.2. Inference of CO_2 Emission Factor by Bayesian Regression

The relationship of the CO_2 emission factor with the *VSP* is plotted in Figure 7, with the error bars indicating a 2σ- uncertainty of the data points. The test data are first fitted by the method of ordinary least squares without considering errors, and the fitting function is:

$$\eta = 5.243\,\xi + 142.6 \tag{12}$$

where η is the value of the CO_2 emission factor, and ξ is the *VSP* bin value.

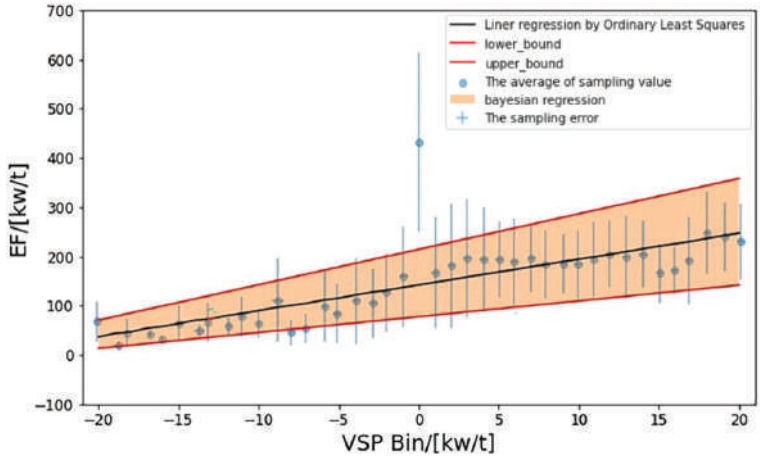

Figure 7. Regression results for *VSP* and CO_2 emission factor.

The test data are not a fixed value but a distribution within a certain range; the CO_2 emission factor should also be taken within a certain range. When considering sampling errors, the uncertainty of the CO_2 emission factor is plotted within the shaded area bounded by the upper and lower 95% confidence interval (95% CI) (in Figure 7). Meanwhile, the posterior probability distributions of parameters α and β are shown in Figure 8, as well as MCMC trace-plotting the samples of α and β under the Bayesian framework. The mean posterior distribution of α is 146.5362, while the mean posterior distribution of β is 5.1986. The progressions of the samples plotted in the trajectories of α and β seem to converge well without significant drift.

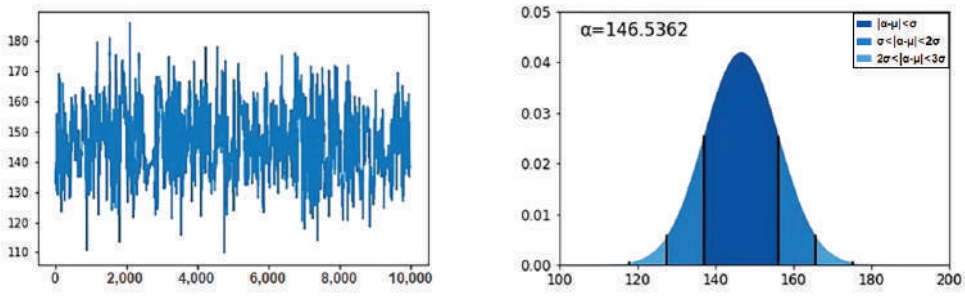

(**a**)

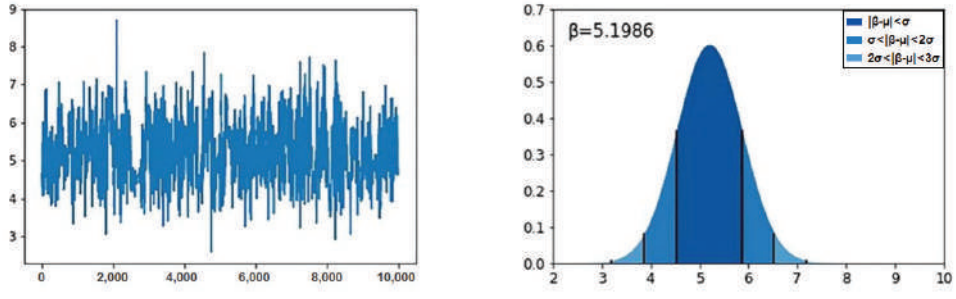

(**b**)

Figure 8. Tracing plots and posterior probability distribution of parameter (α, β) by MCMC under Bayesian inference: (**a**) tracing plots and posterior probability distribution of parameter α by MCMC; (**b**) tracing plots and posterior probability distribution of parameter β by MCMC.

For the surge of the CO_2 emission factor when *VSP* bin = 0 (Figure 7), the reason may be related to the lower vehicle speed. The CO_2 emission factor increases with the decrease in vehicle driving speed [42], and approximately 86.67% of the ultra-low speed operating points (v < 10 km/h) are accumulated in the *VSP* bin = 0 cluster. Meanwhile, the nosedive in vehicle driving speed in the range of *VSP* bin = 0 may result in sustained carbon dioxide emissions without the mileage being increased, causing a rising change shape in the CO_2 emission factor.

3.3. The Influence of Distribution Functions on Multivariate Analysis

Since the surge of the CO_2 emission factor when *VSP* bin = 0 in Section 3.2, only the cases with the *VSP* bin not being equal to zero are considered in this section, to mitigate the accounting uncertainties. The *VSP* distribution is determined to be approximately the Rayleigh distribution using the marginal distribution plot and Q–Q plot (Figure 9), with the corresponding *p*-value being less than 0.05. It can be seen from Figure 9a that, when $VSP > 5$ and $VSP < -5$, the marginal distribution of the *VSP* is in good agreement with the Rayleigh distribution; however, when $-5 < VSP < 5$, there is a certain deviation. For the Q–Q plot (Figure 9b), the quantile of the probability distribution of the *VSP* is basically fit to the Rayleigh distribution.

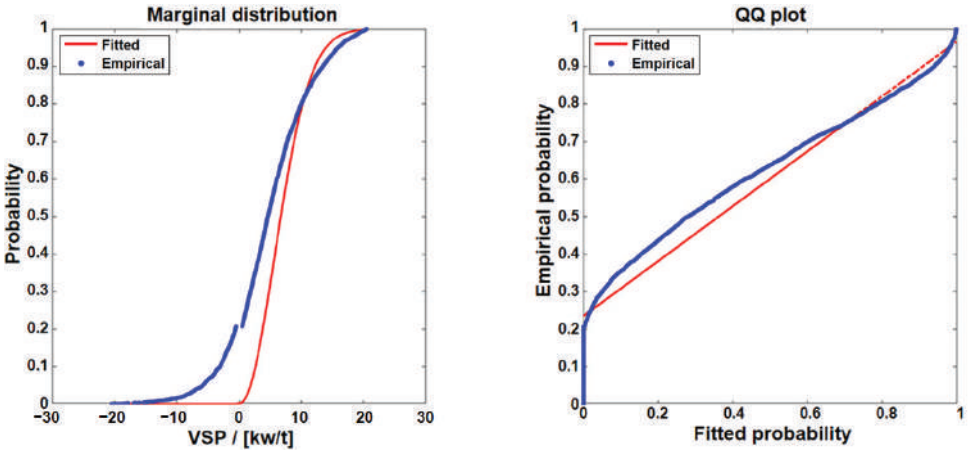

Figure 9. The marginal distribution of input parameters and Rayleigh distribution and the Quantile–Quantile plots: (**a**) the marginal distribution; (**b**) Q–Q plot.

Then, the *VSP* data are set to the uniform distribution and Rayleigh distribution, respectively, when the distribution functions of other input variables remain unchanged. All input variables are normalized and brought into the active subspace for a sensitivity analysis. The linear combinations of the CO_2 emission factor relative to the inputs (i.e., the active variables) exhibit a univariate trend as given in Figure 10, and the relationship between the output and active variables can be represented via a quadratic polynomial:

$$g(y) \approx C_0 + C_1 y + C_2 y^2 \approx C_0 + C_1(\hat{w}^T x) + C_2(\hat{w}^T x)^2 \quad (13)$$

The function $g(y)$ outputs the CO_2 emission factor (g/km) where y represents the active variable, which is the weighted sum of the input parameters after scaling.

The CO_2 emission can be understood through a powerful information combination of the parameter weights and sufficient summary plots. The positive and negative weights of the input parameters can be used to predict the trend of the changes in the active variables affected by the input parameters, thereby further predicting the trend of the changes in the output parameters. For example, as plotted in Figure 10a, since the *VSP* index weight is negative for the EF, a greater *VSP* index decreases the active variable, which results in the decrease in EF. The opposite trend of influence compared to Bayesian fitting is led by the comprehensive influence of other input parameters in multivariate analysis.

It is inferred that the changes in data sampling transform the establishment of subspace matrices, thus affecting the calculation of eigenvector components and the fitting of the final quadratic response surface. As a result, the acceleration and speed, along with the *VSP*, are combined to become the most influenced factor of the CO_2 emission factor when the *VSP* is sampled according to the Rayleigh distribution. The fitting coefficients C_0, C_1, and C_2 in Equation (13) and the corresponding coefficient of determination (R-squared) values for each of the *VSP* distribution functions are tabulated in Table 2. Overall, the result of the R-squared from the *VSP* sampled according to uniform distributions shows a better performance on the goodness of fit. It also suggests that the data shown in Figure 10 are more in line with a quadratic polynomial. Hence, the input parameter distribution function determines the relationship between the combination of inputs and the output of interest to a certain extent.

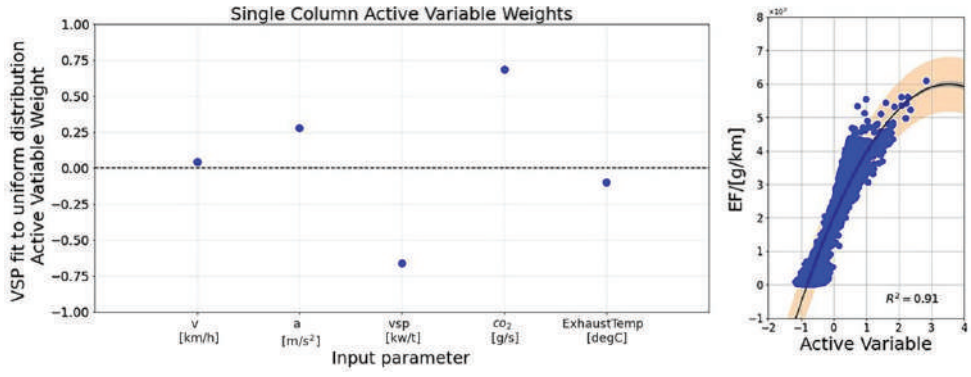

(**a**)

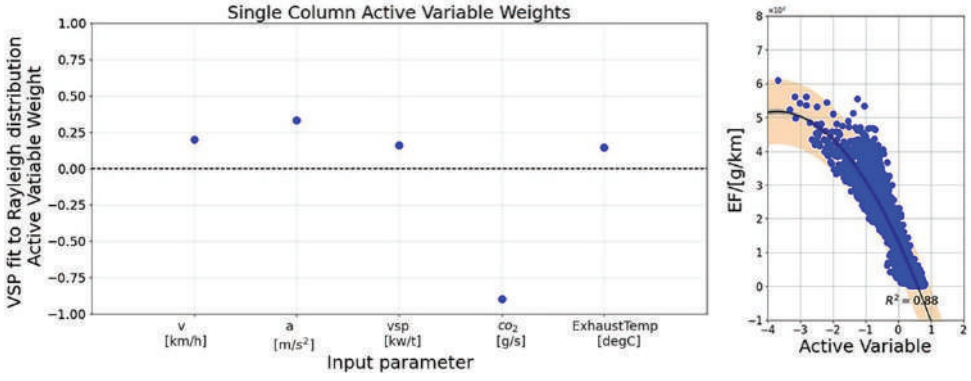

(**b**)

Figure 10. Input parameter weights and sufficient summary plots calculated when *VSP* bin = 0 is excluded from data sampling: (**a**) input parameter weights and sufficient summary plots when *VSP* fit to uniform distribution; (**b**) input parameter weights and sufficient summary plots when *VSP* fit to Rayleigh distribution.

Table 2. Summary of quadratic model coefficients.

Distribution	C_0	C_1	C_2	R^2
Rayleigh	122.59	−124.90	−29.29	0.88
Uniform	202.63	224.32	−31.76	0.91

So far, comprehensive studies on the impact of vehicle driving parameters on emission factors by multivariate sensitivity analysis and uncertainty analysis have been carried out. It is highlighted with high-resolution database processing prepared for the further modelling of the carbon footprint in transportation.

4. Conclusions

In the present study, dynamic vehicle data contributing to traffic carbon emissions are comprehensive studied in the aspects of data sensitivity and uncertainty. The active subspace method can identify which input parameters are the most important through magnitudes of the input parameter weights, while exploring how the combination of inputs is related to the output of interest, without the expense of multiple simulations. It is concluded that the CO_2 emission factor is most sensitive to the *VSP*. The method

has great potential to readily derive the relationship between the combination of inputs and outputs in a complex domain without the expense of multiple simulations. And the relationship between the input parameters (i.e., the active variables) and CO_2 emission factor is able to be formulated using a quadratic function. Moreover, two domains with varied *VSP* data distributions are set up to evaluate the sampling diversity on the emission sensitivity. At the same time, a conclusion similar to that in Section 3.3 can be obtained by changing the distribution function of other vehicle operating parameters. But, due to the study only focusing on the RDE data of one light gasoline vehicle, it cannot be guaranteed that the sensitivity analysis of diesel vehicles or non-light gasoline vehicles is consistent with this study.

Concluded from a sensitivity analysis, the relationship between the *VSP* and CO_2 emission factor is explored via the Bayesian linear regression method with the sampling uncertainties considered. The uncertainty of the CO_2 emission factor within the upper and lower 95% CI is determined when considering the sampling errors. The uncertainty quantifications for the calibrating parameters α and β are well demonstrated by using the heteroscedasticity measurement errors of both variables. In addition, the reason for the surge of the EF in the *VSP* bin = 0 cluster is discussed by combining it with the active subspace method. Compared with traditional linear or nonlinear methods, the proposed method takes into account the uncertainty of the parameter distribution and improves the fitting accuracy.

Generally, this article comprehensively studies the impact of vehicle driving parameters on emission factors via multivariate sensitivity analysis and uncertainty quantification analysis. The input parameters that have a significant impact on emission factors are obtained, and the influence of the error distribution and distribution function of the sampled data on the fitting results is explored. On this basis, a new perspective for modelling traffic carbon emission with a high-resolution database is proposed. And it is conducive to improving the accuracy of carbon counting under varied transportation scenarios, laying the foundation for constructing a high-resolution database of the carbon emission factor.

Author Contributions: Conceptualization, F.Z.; methodology, J.C. and F.Z.; validation, J.C.; formal analysis, J.C.; investigation, J.C., H.Y., H.X., Q.L., Z.Z. and H.C.; data curation, H.Y., H.X., Q.L. and Z.Z.; visualization, H.C.; writing—original draft, J.C.; writing—review and editing, F.Z.; funding acquisition, F.Z. and W.Y.; resources, H.Y., H.X., Q.L. and Z.Z.; supervision, F.Z. and W.Y.; project administration, F.Z. and W.Y. All authors have read and agreed to the published version of the manuscript.

Funding: This research was funded by the Open Funds of Chongqing Key Laboratory of Vehicle Emission and Economizing Energy, grant number No. PFJN-09, and the Shandong Provincial Natural Science Foundation, grant number No. 2022HWYQ-061.

Data Availability Statement: Restrictions apply to the availability of these data. Data were obtained from China Automotive Engineering Research Institute Co., Ltd. and are available Feiyang Zhao with the permission of China Automotive Engineering Research Institute Co., Ltd.

Conflicts of Interest: Authors Hao Yu, Haocheng Xu, Qiang Lv and Zongqiang Zhu were employed by the company China Automotive Engineering Research Institute Co., Ltd. The remaining authors declare that the research was conducted in the absence of any commercial or financial relationships that could be construed as a potential conflict of interest.

References

1. Hu, G.; Zeng, W.; Yao, R.; Xie, Y.; Liang, S. An integrated assessment system for the carrying capacity of the water environment based on system dynamics. *J. Environ. Manag.* **2021**, *295*, 113045. [CrossRef] [PubMed]
2. Chen, Z.; Li, B.; Jia, S.; Ye, X. Modeling and simulation analysis of vehicle pollution and carbon reduction management model based on system dynamics. *Environ. Sci. Pollut. Res. Int.* **2023**, *30*, 14745–14759. [CrossRef] [PubMed]
3. IEA. *CO2 Emissions in 2023*; IEA: Paris, France, 2024. Available online: https://www.iea.org/reports/co2-emissions-in-2023 (accessed on 27 April 2023).
4. Li, Y.; Dong, H.; Lu, S. Research on application of a hybrid heuristic algorithm in transportation carbon emission. *Environ. Sci. Pollut. Res.* **2021**, *28*, 48610–48627. [CrossRef] [PubMed]

5. Wang, L.; Zhao, Y.; Wang, J.; Liu, J. Regional inequality of total factor CO_2 emission performance and its geographical detection in the China's transportation industry. *Environ. Sci. Pollut. Res. Int.* **2022**, *29*, 3037. [CrossRef] [PubMed]
6. IEA. *Energy Technology Perspectives 2015*; OECD Publishing: Paris, France, 2015.
7. Yao, Z.; Cao, H.; Cui, Z.; Wang, Y.; Huang, N. Research on Urban Distribution Routes Considering the Impact of Vehicle Speed on Carbon Emissions. *Sustainability* **2022**, *14*, 15827. [CrossRef]
8. Dong, Y.; Xu, J.; Ni, J. Carbon emission model of vehicles driving at fluctuating speed on highway. *Environ. Sci. Pollut. Res. Int.* **2023**, *30*, 18064–18077. [CrossRef] [PubMed]
9. Rakha, H.; Ahn, K.; Trani, A. Development of VT-Micro model for estimating hot stabilized light duty vehicle and truck emissions. Transportation research. *Part D Transp. Environ.* **2004**, *9*, 49–74. [CrossRef]
10. Kim, W.; Kim, C.; Lee, J.; Kim, J.; Yun, C.; Yook, S. Fine particle emission characteristics of a light-duty diesel vehicle according to vehicle acceleration and road grade. *Transp. Res. Part D Transp. Environ.* **2017**, *53*, 428–439. [CrossRef]
11. Zhao, F.; Liu, F.; Liu, Z.; Hao, H. The correlated impacts of fuel consumption improvements and vehicle electrification on vehicle greenhouse gas emissions in China. *J. Clean. Prod.* **2019**, *207*, 702–716. [CrossRef]
12. Li, X.; Yu, B. Peaking CO_2 emissions for China's urban passenger transport sector. *Energy Policy* **2019**, *133*, 110913. [CrossRef]
13. Pu, X.; Lu, X.; Han, G. An improved optimization algorithm for a multi-depot vehicle routing problem considering carbon emissions. *Environ. Sci. Pollut. Res. Int.* **2022**, *29*, 54940–54955. [CrossRef] [PubMed]
14. Jimenez-Palacios, J.L. *Understanding and Quantifying Motor Vehicle Emissions with Vehicle Specific Power and TILDAS Remote Sensing*; Massachusetts Institute of Technology: Cambridge, MA, USA, 1999.
15. Song, G.; Lei, Y. Characteristics of low-speed vehicle-specific power distributions on urban restricted-access roadways in Beijing. *Transp. Res. Rec.* **2011**, *2233*, 90–98. [CrossRef]
16. Forcetto, A.L.S.; de Salvo Junior, O.; Maciel Filho, F.F.; de Fátima Andrade, M.; de Almeida, F.; Flávio Guilherme, V. Improving the assessment of RDE dynamics through vehicle-specific power analysis. *Environ. Sci. Pollut. Res. Int.* **2022**, *29*, 59561–59574. [CrossRef] [PubMed]
17. Zhang, L.; Zhu, Z.; Zhang, Z.; Song, G.; Zhai, Z.; Yu, L. An improved method for evaluating eco-driving behavior based-on speed-specific vehicle-specific power distributions. *Transp. Res. Part D Transp. Environ.* **2022**, *113*, 103476. [CrossRef]
18. Amoatey, P.; Omidvarborna, H.; Baawain, M.S.; Al-Mamun, A. Evaluation of vehicular pollution levels using line source model for hot spots in Muscat, Oman. *Environ. Sci. Pollut. Res. Int.* **2020**, *27*, 31184–31201. [CrossRef] [PubMed]
19. Smit, R.; Awadallah, M.; Bagheri, S.; Surawski, N.C. Real-world emission factors for SUVs using on-board emission testing and geo-computation. *Transp. Res. Part D Transp. Environ.* **2022**, *107*, 103286. [CrossRef]
20. EPA. *User's Guide to Mobile4 (Mobile Source Emission Factor Model)*; Office of Mobile Sources U.S. Environmental Protection Agency Ann Arbor: Washington, DC, USA, 1989.
21. EPA. User's Guide to MOBILE6.1 and MOBILE6.2: Mobile Source Emission Factor Model [CP/OL]. 2008. Available online: http://www.epa.gov/oms/m6.htm,2008/04/05 (accessed on 27 April 2023).
22. Khazini, L.; Kalajahi, M.J.; Blond, N. An analysis of emission reduction strategy for light and heavy-duty vehicles pollutions in high spatial–temporal resolution and emission. *Environ. Sci. Pollut. Res. Int.* **2022**, *29*, 23419–23435. [CrossRef]
23. Charles, R.; Crawford. *Active Subspaces: Emerging Ideas for Dimension Reduction in Parameter Studies*; SIAM: Philadelphia, PA, USA, 2016.
24. Constantine, P.G.; Emory, M.; Larsson, J.; Iaccarino, G. Exploiting active subspaces to quantify uncertainty in the numerical simulation of the HyShot II scramjet. *J. Comput. Phys.* **2015**, *302*, 1–20. [CrossRef]
25. Constantine, P.G.; Diaz, P. Global sensitivity metrics from active subspaces. *Reliab. Eng. Syst. Saf.* **2017**, *162*, 1–13. [CrossRef]
26. Seshadri, P.; Shahpar, S.; Constantine, P.; Parks, G.; Adams, M. Turbomachinery Active Subspace Performance Maps. *J. Turbomach.* **2018**, *140*, 041003. [CrossRef]
27. Bahamonde, S.; Pini, M.; De Servi, C.; Schiffmann, J.; Colonna, P. Corrigendum to "Active subspaces for the optimal meanline design of unconventional turbomachinery" [*Appl. Therm. Eng.* **2017**, *127*, 1108–1118]. *Appl. Therm. Eng.* **2019**, *150*, 1353–1355. [CrossRef]
28. Ji, W.; Ren, Z.; Marzouk, Y.; Law, C.K. Quantifying kinetic uncertainty in turbulent combustion simulations using active subspaces. *Proc. Combust. Inst.* **2019**, *37*, 2175–2182. [CrossRef]
29. Zhang, L.; Wang, N.; Wei, J.; Ren, Z. Exploring active subspace for neural network prediction of oscillating combustion. *Combust. Theory Model.* **2021**, *25*, 570–587. [CrossRef]
30. Lin, K.; Zhou, Z.; Wang, Y.; Law, C.K.; Yang, B. Using active subspace-based similarity analysis for design of combustion experiments. *Proc. Combust. Inst.* **2023**, *39*, 5177–5186. [CrossRef]
31. Chen, D.; Dahlgren, R.A.; Shen, Y.; Lu, J. A Bayesian approach for calculating variable total maximum daily loads and uncertainty assessment. *Sci. Total Environ.* **2012**, *430*, 59–67. [CrossRef] [PubMed]
32. Rajamand, S.; Caglar, R. Control of voltage and frequency based on uncertainty analysis using Bayesian method and effective power flow control of storage role in electrical vehicle charging station. *Sustain. Energy Grids Netw.* **2022**, *32*, 100837. [CrossRef]
33. Elster, C.; Toman, B. Bayesian uncertainty analysis for a regression model versus application of GUM Supplement 1 to the least-squares estimate. *Metrologia* **2011**, *48*, 233–240. [CrossRef]
34. Lu, D.; Ye, M.; Hill, M.C. Analysis of regression confidence intervals and bayesian credible intervals for uncertainty quantification. *Water Resour. Res.* **2012**, *48*, W09521.1–W09521.20. [CrossRef]

35. Li, X.; Feng, J.; Wellen, C.; Wang, Y. A Bayesian approach of high impaired river reaches identification and total nitrogen load estimation in a sparsely monitored basin. *Environ. Sci. Pollut. Res. Int.* **2017**, *24*, 987–996. [CrossRef]
36. Mudgal, A.; Hallmark, S.; Carriquiry, A.; Gkritza, K. Driving behavior at a roundabout: A hierarchical Bayesian regression analysis. *Transp. Res. Part D Transp. Environ.* **2014**, *26*, 20–26. [CrossRef]
37. Martin, N.P.D.; Bishop, J.D.K.; Choudhary, R.; Boies, A.M. Can UK passenger vehicles be designed to meet 2020 emissions targets? A novel methodology to forecast fuel consumption with uncertainty analysis. *Appl. Energy* **2015**, *157*, 929–939. [CrossRef]
38. EPA. *Methodology for Developing Modal Emission Rates for EPA's Multi-Scale Motor Vehicle and Equipment Emission System*; EPA: Washington, DC, USA, 2002.
39. Jefferson, J.L.; Gilbert, J.M.; Constantine, P.G.; Maxwell, R.M. Active subspaces for sensitivity analysis and dimension reduction of an integrated hydrologic model. *Comput. Geosci.* **2015**, *83*, 127–138. [CrossRef]
40. Yu, W.; Zhao, F.; Yang, W.; Zhu, Q. Uncertainty quantifications of calibrating laser-induced incandescence intensity on sooting propensity in a wick-fed diffusion flame burner. *Fuel* **2021**, *289*, 119921. [CrossRef]
41. Kelly, B.C. Some Aspects of Measurement Error in Linear Regression of Astronomical Data. *Astrophys. J.* **2007**, *665*, 1489–1506. [CrossRef]
42. Shuai, M.; Zhihui, H.; Liang, J.; Haiguang, Z.; Tian, M. CO_2 and NOx emission characteristics from a heavy-duty China VI diesel truck based on portable emission measurement system. *Acta Sci. Circumstantiae* **2022**, *42*, 341–350. [CrossRef]

energies

MDPI

Article

Low-Friction and -Knocking Diesel Engine Cylindrical-Tapered Bore Profile Design

Junhong Zhang [1,2], Ning Wang [1], Jian Wang [1,3,*], Hui Wang [1,3], Xueling Zhang [2], Huwei Dai [1] and Jiewei Lin [1,*]

[1] State Key Laboratory of Engines, Tianjin University, Tianjin 300354, China; zhangjh@tju.edu.cn (J.Z.); 2021201385@tju.edu.cn (N.W.); dhwmail@tju.edu.cn (H.D.)
[2] Department of Mechanical Engineering, Tianjin Renai College, Tianjin 301636, China; zhangxueling0@163.com
[3] Weichai Power Co., Ltd., Weifang 261000, China
* Correspondence: wangjian@weichai.com (J.W.); linjiewei@tju.edu.cn (J.L.); Tel.: +86-13884712670 (J.W.); +86-13752356026 (J.L.)

Abstract: To reduce the friction loss and the piston-knocking noise from the perspective of the design of the cylinder bore profile, the piston-ring cylinder bore (PRCB) dynamic model of an L6 diesel engine was developed using AVL-Excite-Piston & Rings. Based on the full-scale test method, the effects of bore taper, starting height of tapered profile, and ellipticity on the friction power and knocking energy of the PRCB system were investigated, and the optimization of the design of the bore profile was carried out with the objectives of minimizing the system's friction power and the peak knocking kinetic energy. The results showed that the taper of the cylinder bore has the greatest influence on the system's friction power and the peak knocking kinetic energy, followed by the starting height of the conical profile. For the peak knocking kinetic energy of the piston, there was an obvious interaction between the taper and the starting height of the conical profile. When the taper was 35 μm and 45 μm, the peak knocking kinetic energy showed a decreasing and then increasing trend with the increase in the starting height of the profile, and when the taper was 55 μm the peak knocking kinetic energy monotonically was decreased with the increase in the starting height of the conical profile. The optimization results showed that the system's friction power was decreased by 15.05% and the peak knocking kinetic energy was decreased by 21.41% for a taper degree of 55 μm, a tapered profile starting height of 31 mm, and an ellipticity of 50 μm compared to the initial cylindrical cylinder bore.

Keywords: diesel engine; piston-ring cylinder bore; cylinder hole profile; friction power; knocking kinetic energy

Citation: Zhang, J.; Wang, N.; Wang, J.; Wang, H.; Zhang, X.; Dai, H.; Lin, J. Low-Friction and -Knocking Diesel Engine Cylindrical-Tapered Bore Profile Design. *Energies* **2024**, *17*, 2042. https://doi.org/10.3390/en17092042

Academic Editor: Pietro Zunino

Received: 5 March 2024
Revised: 23 April 2024
Accepted: 24 April 2024
Published: 25 April 2024

1. Introduction

With the enhancement of diesel engines, the thermal and mechanical load of their cylinder bore has increased accordingly, and the deformation of the cylinder bore has also increased [1–3]. Studies [4,5] have shown that an increase in the degree of irregular cylinder-bore deformation would lead to an increase in friction loss between the piston and cylinder bore. The friction between the piston assembly and cylinder bore accounts for half of the total friction loss of the engine [6,7]. Research has shown that for every 10% increase in engine friction loss, fuel consumption would increase by 3% to 5%, and the engine's effective output power would also decrease accordingly. The irregular deformation of the cylinder bore will lead to an increase in cylinder clearance, which will cause an increase in piston-knocking noise [8,9]. Therefore, rationalizing the design of the cylinder bore pattern, reducing the friction power and the peak knocking kinetic energy of the PRCB system, is of great significance to improving the economy and NVH performance of diesel engines. Most scholars have chosen to optimize the piston structure [10–12] and rationally design the surface texture of the friction pair [13–15] to reduce the friction loss and the knocking kinetic energy of the PRCB. Few scholars have improved the friction and lubrication

characteristics and knocking characteristics of the PRCB system by rationally designing the macrostructure of the cylinder bore. At present, from the perspective of designing the cylinder bore profile, the use of a non-cylindrical cylinder liner design in the cold state has become another effective method to improve the friction performance of the ring group-cylinder liner system.

The average friction-effective pressure of the piston was reduced [16,17] by expanding the bottom diameter of the cylinder bore of the gasoline engine through the honing process in the experimental test. Numerical calculations were utilized in the literature to compare the deformation of the conical and elliptical cross-section cylinder liner with that of the traditional cylindrical cylinder liner of a certain gasoline engine, and it was found [18,19] that the radial deformation of the elliptical–cone combination cylinder liner was reduced by 70%~80% under the thermal load condition. Alshwawra et al. [20] studied three initial bore shapes of a certain gasoline engine—elliptical, conical–elliptical, and reverse free-form—and found that the reverse free-form bore was closest to a "round" shape at each height after applying thermal and mechanical loads to the bore, and the oil film contact area between the piston ring and the cylinder wall was increased, which provided a new reference for the bore pattern to reduce the friction power of the piston ring group. Halbhuber et al. [21] compared the cumulative friction power of cylindrical bores under the consideration of piston cooling conditions and found that the cumulative friction power of the piston group under cylindrical-tapered compensated bores was 4.4% lower than that using uncompensated bores.

Due to the complexity and high cost of the reverse free-form process, a tapered cylindrical bore is used to improve the geometric performance of the gasoline engine in the cold state, and the tapered bore reduces the friction loss by increasing the distribution of the oil film in the friction gap; however, too large a gap between the piston and the cylinder wall can lead to an increase in the piston-knocking noise, while too small a gap can lead to an increase in the friction power, and the design parameters of the cylinder bore pattern have different degrees of influence on the friction and knocking performance of the piston. Moreover, the design parameters of the cylinder bore pattern have different influences on the piston friction and knocking performance, and there is an interaction between the parameters. At present, there is little literature on the influence of the design parameters of the cylinder bore pattern on the piston friction and knocking characteristics, and there is no systematic design method for the cylinder bore pattern for engineering applications.

Therefore, the influence of the cold design parameters of the cylinder bore pattern on the friction and knocking energy of the piston-ring cylinder bore system in an L6 diesel engine was studied. With the objective function of minimizing the friction power and peak knocking kinetic energy, the parameters of the cylinder bore pattern were optimized, and the optimal design of the cylinder bore pattern was obtained. This provided some theoretical guidance for reducing friction loss and reducing piston-knocking noise from the perspective of cylinder bore design.

2. Numerical Modeling

2.1. The Piston's Dynamic Modeling

In the motion plane of the diesel engine's crank-connecting rod mechanism, the forces on the piston are shown in Figure 1, where F_{rx} and F_{ry} are the normal and tangential forces of the piston ring on the piston, respectively, F_{cx} and F_{cy} are the normal and tangential forces of the cylinder bore on the piston, respectively, F_p is the force on the piston pin, F_{rod} is the force of the linkage system at the con rod's small-end bearing, F_{gc} is the piston gravity, F_{gas} is the gas force, mc is the mass of the piston, M_{gc} is the gravity-induced piston moment around the pin axis, M_{pc} is the friction moment at the piston pin, and β is the crankshaft angle.

After analyzing the force on the piston, the dynamic equations of the piston in the reciprocation, radial motion, and rotation around the pin were expressed as Equations (1)–(3), respectively.

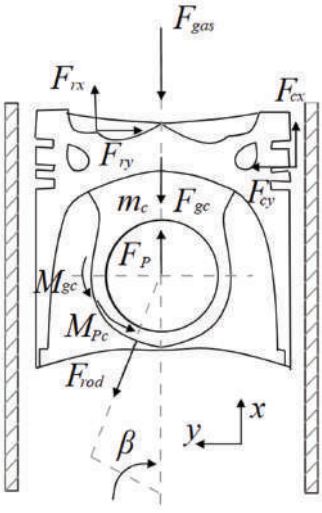

Figure 1. Schematic diagram of piston movement force analysis under calibration conditions.

Forces in the x-direction:

$$m_c \times \ddot{x}_c = F_{cx} + F_{rx} - F_{gcx} - F_{gas} + F_{px} - F_{rodx} \quad (1)$$

Forces in the y-direction:

$$m_c \times \ddot{y}_c = F_{cy} - F_{ry} - F_{gcy} - F_{py} + F_{rody} \quad (2)$$

Rotation around the pin:

$$\Theta_c \times \ddot{w}_c = M_c + M_r + M_{gc} + M_{pc} \quad (3)$$

where $\ddot{x}_c$ and $\ddot{y}_c$ are the acceleration of the piston motion in the x-direction and y-direction, respectively, F_{gcx} and F_{gcy} are the component force of piston gravity along the x-direction and y-direction, respectively, F_{px} and F_{py} are the load on the piston pin along the x-direction and the force in the y-direction, respectively, F_{rodx} and F_{rody} are the force of the linkage system at the con rod's small-end bearing along the x-direction and the force in the y-direction, respectively, Θ_c is the piston's moment of inertia around the pin, $\ddot{w}_c$ is the angular acceleration, Mc is the moment due to piston–liner contact, and M_r is the moment due to ring axial and radial force.

During the working process of the diesel engine, the piston not only reciprocates along the cylinder bore in the height direction, it also includes transverse movement and rotation around the pin, which has a great influence on the piston's knocking on the inner wall of the cylinder bore to produce knocking noise. Therefore, the piston-knocking kinetic energy was used to measure the degree of piston knocking on the inner wall of the cylinder bore; the specific formula is given as follows:

$$E = E_v + E_w = \frac{1}{2} m_c \dot{x}_c^2 + \frac{1}{2} \Psi \dot{w}_c^2 \quad (4)$$

where E_v and E_W are the kinetic energy of radial motion and rotational kinetic energy respectively, m_c is the mass of the piston, $\dot{x}_c$ is the radial velocity, Ψ is the rotational moment of inertia, and $\dot{w}_c$ is the rotational angular velocity.

2.2. The Piston Ring Group Dynamic Model

The force analysis of the piston ring is shown in Figure 2, where m_R is the mass of the piston ring, $\ddot{x}$ is the acceleration of the piston ring in the x-direction, s is the center of gravity, M is the piston ring cross-section center position, P_{above} and P_{below} are the pressure distributions on the upper and lower surfaces of the piston ring, respectively, P_{behind} is the pressure distribution on the inside of the piston ring, $F_{fric,ax}$ is the axial friction between the cylinder bore and piston ring, $F_{gas,ax}$ is the gas axial force, ξ is the piston ring torsion angle, $F_{gas,rad}$ is the gas radial force, $F_{fric,rad}$ is the radial friction between the moving surface of the piston ring and the cylinder bore, and $F_{hydr,ax}$ and $F_{hydr,rad}$ are the axial and radial hydrodynamic friction, respectively.

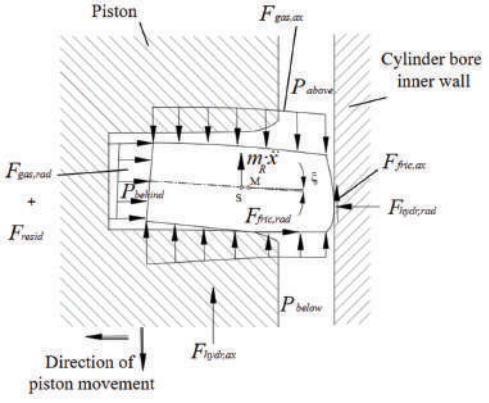

Figure 2. Schematic diagram of piston ring force under calibration conditions.

When the ring is floating (the ring is not in contact with the ring groove), the force equilibrium equations between the ring and the ring groove and the dynamic force equilibrium equations can be expressed as follows:

$$F_{contact} = F_{mass,x} + F_{fric,ax} + F_{gas,ax} + F_{bend} \quad (5)$$

$$m_{ring} \cdot \ddot{x}_{ring} = \Sigma F = F_{damp,ax} + F_{fric,ax} + F_{gas,ax} + F_{bend} \quad (6)$$

where $F_{contact}$ is the contact force between the piston ring and ring groove, $F_{mass,x}$ is the ring's gravity force in the axial direction, F_{bend} is the ring's bending force; m_{ring} is the ring's mass, $\ddot{x}_{ring}$ is the piston ring's axial acceleration, $F_{damp,ax}$ is the axial damping force, and $F_{tension}$ is the tangential elasticity of the piston rings.

The piston ring's radial force equation can be expressed as follows:

$$F_{contact,rad} = F_{fric,rad} + F_{gas,rad} + F_{tension} \quad (7)$$

The equilibrium equation for the bending moment of the ring section around the form center M is given as follows:

$$\sum M = \sum (F_i \cdot h_i) + M_{pre-twist} = M_{elatic} \cdot \xi \quad (8)$$

where F_i is the radial and axial forces on the piston rings, h_i is the distance from each component force to the center of the piston ring's cross-section, $M_{pre\text{-}twist}$ is the moment on the piston ring, and M_{elatic} is the bending moment of the piston ring.

2.3. Friction Force Modeling

The state of the oil film between the piston ring group/skirt and the bore liner has an important influence on the dynamics of the PRCB. The pressure distribution of the oil film can be described by the mean Reynolds equation, which is given as follows:

$$\frac{\partial}{\partial x}\left(\Phi_x h^3 \frac{\partial p_h}{\partial x}\right) + \frac{\partial}{\partial y}\left(\Phi_y h^3 \frac{\partial p_h}{\partial y}\right) = 6\nu U\left(\frac{\partial \overline{h}_T}{\partial y} + \sigma \frac{\partial \Phi_s}{\partial y}\right) + 12\nu \frac{\partial \overline{h}_T}{\partial t} \tag{9}$$

where p_h is the oil film pressure, U is the piston movement speed, h is the nominal oil film thickness, $\overline{h}_T$ is the average value of actual oil film thickness, σ is the combined roughness, ν is the lubricant power viscosity, Φ_x and Φ_y are the pressure flow factors, Φ_s is the shear flow factor, and t is the time.

The calculation assumes that the lubricant film is a Newtonian fluid; the variation in lubricant viscosity with temperature should be described by applying Vogel's formula:

$$\nu(T) = A \times \exp\left(\frac{B}{T + C}\right)$$

where A, B, and C are the coefficients of the viscosity equation related to the type of diesel engine, which in this paper take values of 2.4×10^{-5}, 1641, and 170, respectively, and T is the temperature.

During the reciprocating motion of the piston, the oil film's thickness and pressure are in a state of dynamic change. When the piston moment reaches a certain level, the thickness of the oil film decreases rapidly, which leads to the direct contact of the piston skirt or the piston ring with the micro-convexity on the cylinder bore's surface, and the normal pressure of the contact surface at this time is determined by the contact model of the micro-convexity of the GREENWOOD.

The ratio of the friction pair to the combined roughness of the friction pair is defined as the minimum film thickness ratio, which is calculated as follows:

$$H_{min} = \frac{h_{min}}{\sigma} \tag{10}$$

where h_{min} is the minimum film thickness, H_{min} is the minimum film thickness ratio, and σ is the combined roughness. An H_{min} value of less than 1 indicates boundary lubrication, and H_{min} value of 1 to 4 indicates mixed lubrication, and an H_{min} value greater than 4 indicates hydrodynamic lubrication.

The friction between the piston ring group and the inner wall of the cylinder bore can be derived from Stribeck's formula:

$$F_f = F_n \mu \tag{11}$$

where F_n is the force of pressure between the piston/piston ring and the inner wall of the cylinder bore, and μ is the coefficient of friction.

$$\mu = f\left(\frac{v}{A \cdot v^2 + B \cdot |v| + C} + D \cdot v\right) \tag{12}$$

where f is the overall scaling factor; A, B, C, and D are related to the form of the diesel engine; and v is the dynamic viscosity coefficient.

2.4. Cylinder Bore Deformation Calculation

Firstly, one-dimensional simulation on the working process of an inline six-cylinder diesel engine was carried out by AVL BOOST [22], and the main parameters of the engine were as shown in Table 1. The thermal boundary conditions, such as gas temperature and convective heat transfer coefficient, were obtained from one-dimensional simulations, as shown in Figure 3, which shows the variation in the convective heat transfer coefficient and temperature in the combustion chamber with the crankshaft angle, and it can be seen

that both of them reach their maximum value near the upper stop (90CA), due to the huge heat generated by the gas explosion in the cylinder at this time.

Table 1. Main engine parameters.

Parameters	Value
Maximum power	235 kW
Maximum moment	1300 N·m
Number of cylinders	6
Diameter of a cylinder	107 mm
Stroke	126 mm
Engine capacity	6.8 L
Compression ratio	19.5

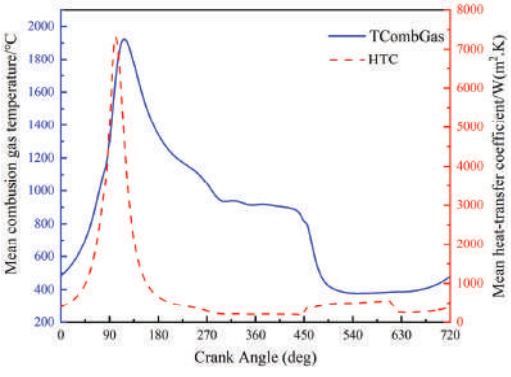

Figure 3. Gas temperature and convective heat transfer coefficient.

In the actual working process of the diesel engine, due to the thermal inertia of the body material, the effect of the heat load of the high-temperature gas on the body is limited to a thin layer on the surface of the material. The temperature of the vast majority of the region is approximate to stabilize; that is, the wall surface of the combustion chamber can be formed without a time-varying steady-state temperature field [23].

The time-averaged convective heat transfer coefficient and temperature of the gas were applied to the finite element model in the form of a third-type boundary condition. In the simulation process, the deformation of the cylinder bore is mainly determined by the inhomogeneous thermal load, and since it is assumed that the thermal load is steady-state and the fuel of each cylinder is consistent in the calculation process, the radial deformation of each cylinder due only to the thermal load is roughly the same, but the deformation of cylinders 2, 3, and 4 is affected by the adjacent two cylinders at the same time, while cylinders 1 and 6 are affected by only one of the neighboring cylinders; thus, in a comprehensive view, the deformation of cylinders 1 and 6 is symmetrically similar, while the deformation of cylinders 2, 3, and 4 is similar, so the calculation process can be simplified to cylinders 1, 2, and 6 in order to ensure the accuracy of the premise, greatly reducing the computing time. The deformation of the engine body was calculated in ABAQUS, and the whole deformation of the engine was as shown in Figure 4. The radial deformation of the bore surface of cylinder 2 was also extracted as a boundary condition for the subsequent dynamic calculations.

Figure 5 shows the radial deformation of the cross-section of the inner wall at different heights in the thermal state of the cylindrical cylinder bore. Since the 0° anti-thrust side (ATS) and 180° thrust side (TS) were subjected to thermal loads in addition to piston-knocking loads, the deformation in the 0° and 180° directions was larger than that in the 90° and 270° directions at different heights, and the overall deformation showed an "oval shape". Figure 6 shows the radial deformation of the cylinder bore surface on the

ATS and TS. Due to the influence of the bolt preload, the deformation at the top of the cylinder bore is small, and the deformation on the ATS and TS is 49.35 μm and 49.45 μm, respectively. Due to the large thermal load on the top half of the cylinder bore, the middle and upper portion of the cylinder bore show more prominent expansion deformation, and the maximum deformation occurs on the TS, with an amplitude of 122.93 μm; the lower part of the cylinder bore shows a smaller expansion deformation relative to the upper part, and the maximum deformation occurs on the TS, with an amplitude of 108.04 μm.

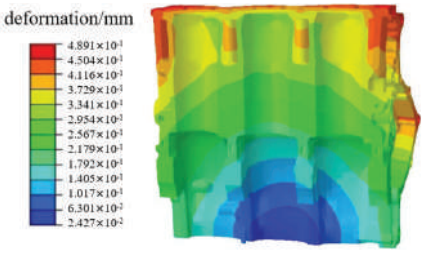

Figure 4. Schematic diagram of cylinder bore deformation.

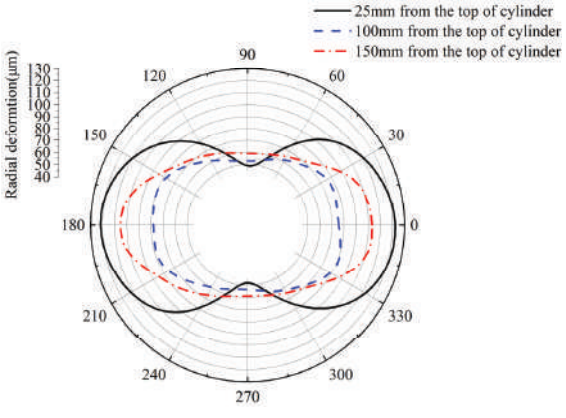

Figure 5. Radial deformation at different heights of the cylinder bore.

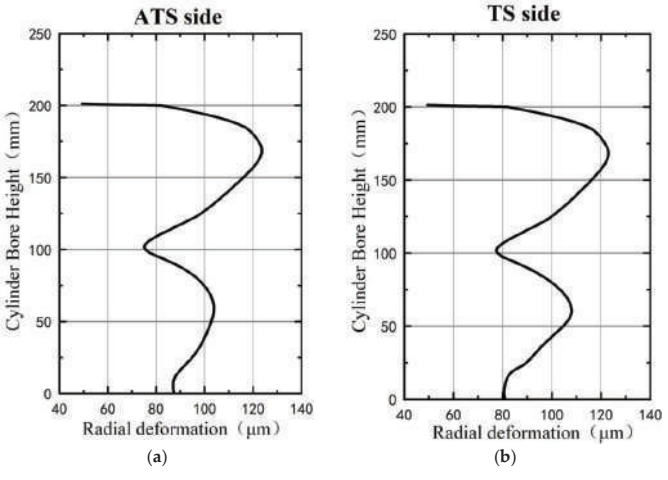

Figure 6. Radial deformation of the ATS and TS: (**a**) ATS radial deformation; (**b**) TS radial deformation.

2.5. The Piston-Ring Cylinder Bore (PRCB) Dynamic Model

The working condition of the engine is complicated; many factors can affect the normal operation of piston friction pairs. The dynamic model of the piston-ring cylinder bore was established by AVL Piston & Rings software R2020.1 [24], which can fully account for the lubrication of the piston group. The modeling process included the following assumptions: (1) Only the motion of the piston in the plane of the TS and ATS was considered. (2) The crankshaft speed was even. (3) The piston was considered to be an elastic body; the cylinder liner, connecting rod, and crankshaft were defined as rigid bodies; and the hinge clearance was zero.

In the modeling process, the cylinder bore deformation profile obtained from the cylinder bore deformation calculation was input as the geometric boundary condition of the calculation.

2.6. Dynamic Model Calibration

The piston leakage is directly affected by the structure of the piston ring group and the deformation of the cylinder bore's inner wall. The accuracy of the PRCB dynamic model established in the previous section was verified by comparing the piston leakage results in the numerical model with that in the experiment. The test process was as follows: block all channels of crankcase interaction with the outside world; keep the crankcase sealing normal (add 0.2 kPa pressure in the crankcase; the amount of air leakage is no more than 5 L/min), after which the throttle is fully open; adjust the engine speed from 1300 r/min to 2100 r/min and record the average leakage of air at each speed point in the process. Figure 7 shows the comparison of the average leakage of a single cylinder in a cycle of the diesel engine (the ratio of total air leakage of the diesel engine to the number of cylinders) in the experiment and the numerical model. It can be seen that the measured and simulated values of piston air leakage under each rotational speed were of the same order of magnitude, and the maximum error was 5.52%, verifying the accuracy of the PRCB dynamic model.

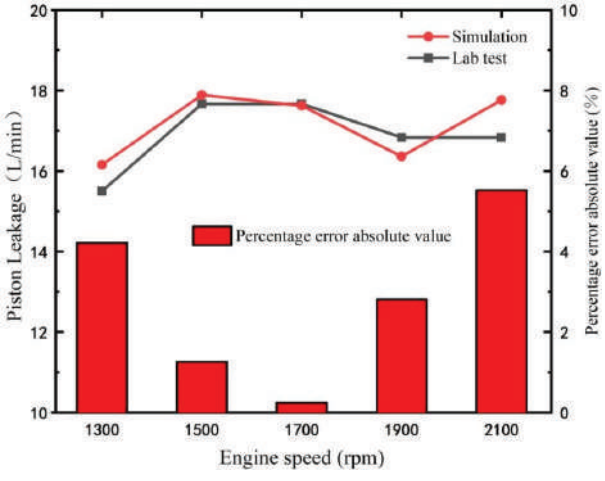

Figure 7. Comparison between measured and simulated average air leakage of a single piston cylinder.

2.7. Design of Cylinder Bore Profiles

A comprehensive experimental method was used to study the influence of the bore pattern parameters on the friction and knocking characteristics of the piston, and the optimal design of the bore pattern was derived to minimize the friction power of the PRCB system and minimize the peak knocking kinetic energy.

A combination of cylindrical taper and elliptical cross-section was adopted for the cylinder bore's cold-state profile, as shown in Figure 8, where A is the taper, and the friction power between the piston and bore was reduced through the optimization of the taper; B is the starting height of the conical profile, and the second-order movement of the piston was improved through the optimization of B; C is the degree of ellipticity, and the ellipse of the difference between the long and short axes of half of the difference between the C is a positive number indicating the different heights that can be attenuated under the cylinder bore's radial deformation to reduce the friction power; and L is the cylinder bore diameter. Subsequent calculations directly superimposed the cold and hot profiles of the cylinder bore as boundary conditions for the dynamic calculations.

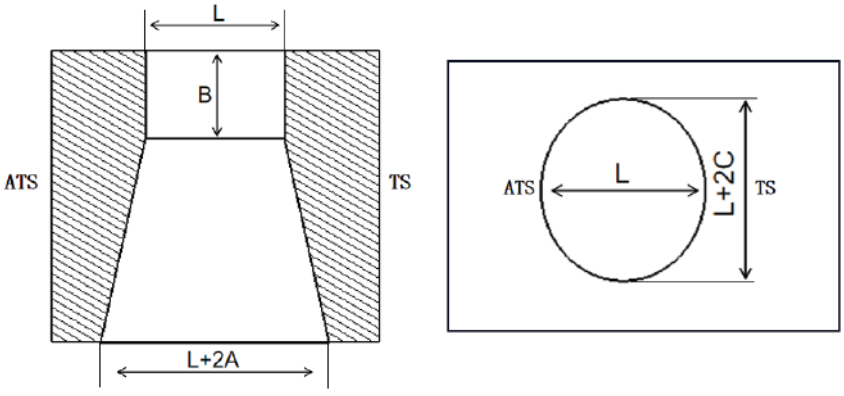

Figure 8. Cold profile of cylinder bore: (**a**) front cutaway view; (**b**) top view.

3. Effect of Cylindrical-Tapered Cylinder Bore Shape Parameters on Friction and Knocking

The control variable method was used to analyze the effects of A, B, and C on the piston friction and knocking characteristics, where the piston friction characteristics were evaluated by the average friction power consumption per cycle, and the knocking characteristics were evaluated by the peak kinetic energy of the piston knocking per cycle.

The effects of the cylindrical-tapered bore profile parameters taper (A), tapered profile start height (B), and ellipticity (C) on the piston skirt friction consumption, piston ring friction consumption, and peak knocking kinetic energy are shown in Figure 9. Overall, the cylindrical-tapered bore has improved friction and knocking characteristics compared to the cylindrical bore.

As shown in Figure 9a, at B = 62 mm, C = 40 μm, and peak kinetic energy was decreased with the increase in taper (A); the skirt friction power was decreased from 232 J to 216 J, the ring group friction power was decreased from 77.87 J to 69.32 J, and the peak kinetic energy was decreased from 256.12 N·mm to 191.97 N·mm. Among them, the rate of decrease in skirt friction power was from fast to slow, while the speed of the decrease in ring group friction power and peak knocking kinetic energy tended to be constant. All three decreased because with the increase in taper (A), the thickness of the oil film between the piston ring's moving surface bore wall and the piston skirt bore wall increases, the area of solid–solid contact between the friction partners decreases, and the dry friction decreases, so the skirt's friction work and the piston ring's friction work are both reduced. At the same time, with the increase in oil film thickness, the viscous shear force of the oil film also increases, and the rotation speed of the piston's knocking moment is reduced, so the peak kinetic energy of the piston knocking is reduced.

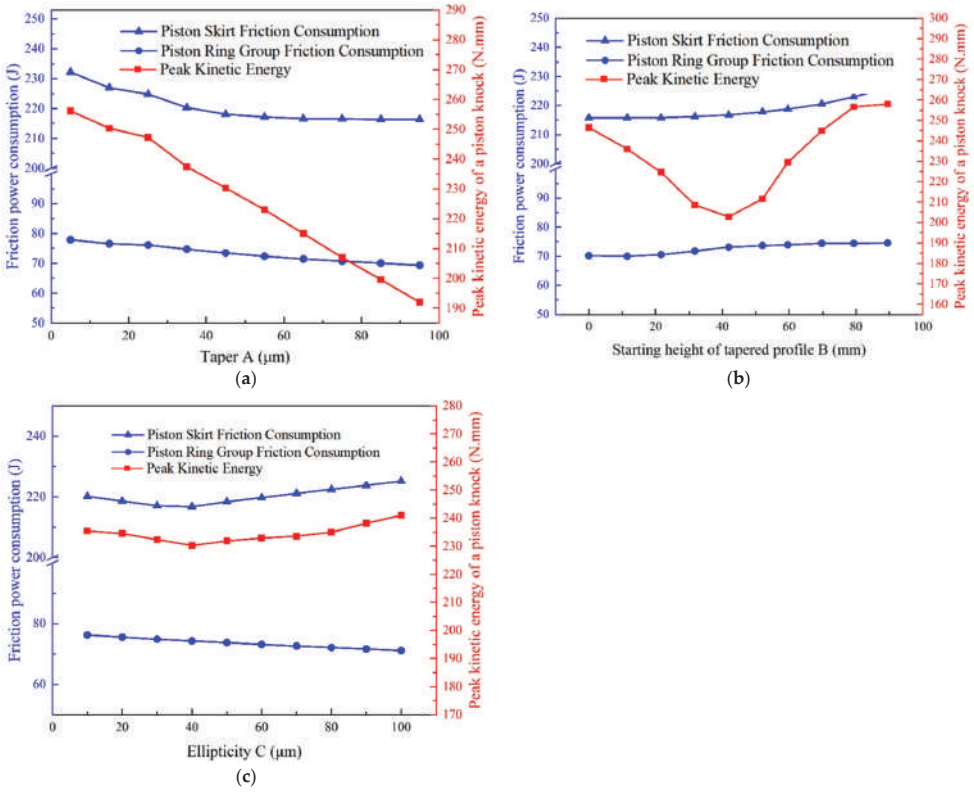

Figure 9. Cylinder bore profile parameters' effects on the piston friction lubrication characteristics and knocking characteristics by (**a**) taper (B = 62 mm, C = 40 μm); (**b**) starting height of tapered profile (A = 45 μm, C = 40 μm); and (**c**) ellipticity (A = 45 μm, B = 62 mm).

As shown in Figure 9b, when B was increased at A = 45 μm and C = 40 μm, the piston skirt friction power and ring set friction power increased from 215 J to 225 J and from 70.15 J to 74.54 J, respectively. The peak piston-knocking kinetic energy decreased and then increased with the increase in B, with a minimum value of 202.79 N at B = 41 mm. The reason for the change in these three parameters is that with the increase in the starting height (B) of the profile, the range of tapered compensation along the height gradually decreases, so the piston skirt and the piston ring moving surface and the cylinder wall in the piston are gradually reduced within a cycle of the average clearance, resulting in a gradual decrease in the average thickness of the lubricant film, and the friction in the solid–solid contact area increases, resulting in an increase in dry friction, so the skirt friction and the friction of the piston ring work increase. The peak knocking kinetic energy is determined by the piston's radial speed and rotation speed. The reduction in the skirt's oil film thickness makes the oil film pressure increase, and the piston's radial speed is weakened, the oil film's viscous shear force decreases, and the piston's angular speed increases, but the piston's radial speed decreases significantly, so the peak knocking kinetic energy as B changes from 0 to 41 mm follows a downward trend, and then as B continues to increase, the angular velocity of the piston's rotation increases more than the radial velocity decreases, so the peak knocking kinetic energy shows an upward trend.

As shown in Figure 9c, at A = 45 μm and B = 62 mm, with the increase in C, both the friction power of the piston skirt and the peak knocking kinetic energy show a decreasing and then increasing trend, achieving minimum values of 216.74 J and 230.27 N·mm at C = 40 μm. The friction power of the piston ring group shows a decreasing trend from

76.25 J to 71.11 J with the increase in C. The reasons for these changes in the three parameters are as follows: with the increase in ellipticity (C), the second-order deformation amplitude of the cylinder bore is gradually weakened, and each cross-section of different heights of the cylinder bore is closer to the "round", while the lubricating oil film around the piston skirt and the piston ring is more uniformly distributed, so the friction power consumption of the piston skirt and the friction power consumption of the piston ring group are gradually reduced. At the same time, because of the increase in ellipticity (C), the gap between the TS and ATS of the piston skirt does not change significantly, so the peak value of knocking kinetic energy does not change significantly.

3.1. Factorial Analysis

The cold-profile parameter factor levels for the cylinder bore under the full-scale test are shown in Table 2. Three parameters related to the design of the cylinder bore's cold profile—namely, taper (A), starting height of tapered profile (B), and ellipticity (C)—were selected as the test factors, and three levels were taken for each factor. The level sizes were selected based on the results of the previous calculations.

Table 2. Factor level values of type line parameters under the full-scale test.

Level	A/μm	B/mm	C/μm
1	35	31	30
2	45	41	40
3	55	51	50

The test scheme and calculation results are shown in Table 3. The effects of the three parameters (A, B, and C) on the piston skirt friction power, the piston ring group friction power, the total friction power (the sum of the ring group friction power and the skirt friction power), and the peak knocking kinetic energy were investigated, where Ai, Bi, and Ci denote the taper, starting height of the tapered profile, and ellipticity at their corresponding i_{th}-level values, respectively.

Table 3. Full-scale test scenarios and calculations.

Programmatic	Skirt Friction Power/J	Ring Group Friction Power/J	Total Friction-Power/J	Peak Knocking Kinetic Energy/(N·mm)
A1B1C1	215.62	71.86	287.48	219
A1B1C2	215.62	71.36	286.98	220
A1B1C3	215.79	70.89	286.68	220
A1B2C1	216.09	72.98	289.04	212
A1B2C2	216.26	72.42	288.69	212
A1B2C3	216.18	71.95	288.13	212
A1B3C1	217.53	73.37	290.90	219
A1B3C2	217.42	72.75	290.19	219
A1B3C3	217.36	72.25	289.60	219
A2B1C1	214.61	69.83	284.41	205
A2B1C2	214.58	69.33	283.91	205
A2B1C3	214.52	68.88	283.41	205
A2B2C1	215.08	71.45	286.53	202
A2B2C2	215.08	70.95	286.03	202
A2B2C3	215.06	70.48	285.56	203
A2B3C1	215.85	72.19	288.04	204
A2B3C2	215.88	71.63	287.48	204
A2B3C3	215.85	71.12	286.98	204
A3B1C1	214.44	68.00	282.43	203
A3B1C2	214.44	67.56	281.99	203
A3B1C3	214.41	67.11	281.55	203
A3B2C1	214.49	70.06	284.56	199
A3B2C2	214.52	69.56	284.11	200
A3B2C3	214.49	69.12	283.61	200
A3B3C1	215.11	71.15	286.30	198
A3B3C2	215.08	70.59	285.71	198
A3B3C3	215.17	70.12	285.29	198

3.2. Analysis of Results

The data obtained from the calculations were analyzed using the range method, and the range results reflected the influence degree of each factor on the calculation results. The factor with the largest range has the highest influence on the results and is the main factor. Range is defined as follows:

$$\text{Range} = \max\left|\overline{K}_i - \overline{K}_j\right| \ (i \neq j) \tag{13}$$

where $K_{i(j)}(i(j) = 1, 2, 3)$ is equal to the sum of certain indicators of level i in the sum column of Table 3, $\overline{K}_{i(j)} = K_{i(j)}/s$ is the arithmetic mean of K_i, and s is the number of factor levels.

The influencing factors are taper (A), taper start height (B), ellipticity (C), and the interaction between the three (A × B, A × C, B × C,), and the calculated indices are the skirt friction power, the piston ring group friction power, the total friction power (the sum of the friction power of the skirt and the friction power of the ring group), and the peak of the kinetic energy of the piston knocking. Tables 4 and 5 show the range method tables.

Table 4. Range method of friction characteristics due to a single parameter.

Parameter Factor Level	Skirt Friction Power/J	Range	Piston Ring Group Friction Power/J	Range	Total Friction Power/J	Range	Peak Knocking Kinetic Energy/N·mm	Range
A1	216.41		72.22		288.628		217	
A2	215.17	1.71	70.65	3.30	285.8255	4.69	203	16
A3	214.70		68.91		283.9375		200	
B1	214.88		69.41		284.321		209	
B2	215.26	1.27	71.01	2.27	286.2385	3.51	204	4
B3	216.15		71.69		287.8315		207	
C1	215.41		71.21		286.622		206	
C2	215.44	0.02	70.68	1.00	286.1205	0.97	207	1
C3	215.41		70.21		285.6485		207	

Table 5. Range method of friction characteristics due to interactions between profile parameters.

Norm	Interactions	Range
Skirt friction power	A × B	0.56
	A × C	0.03
	B × C	0.06
Piston ring friction power	A × B	0.86
	A × C	0.06
	B × C	0.09
Total friction power	A × B	0.38
	A × C	0.06
	B × C	0.12
Peak knocking kinetic energy (physics)	A × B	11.80
	A × C	2.95
	B × C	2.95

3.2.1. Effect of Taper (A) with Respect to Different Values of Ellipticity (C)

The influence of taper (A) on the friction and knocking characteristics under different values of ellipticity (C) is shown in Figure 10. The starting height of the conical profile (B) remained unchanged at 41 mm, the taper (A) was varied from 35 μm to 55 μm, and

different colors indicate different values of ellipticity (C). The dotted lines in Figure 10 represent the values corresponding to the cylindrical cylinder bores (not to be repeated later). For all of the values of C studied in this work, the friction power of the skirt and the ring group, along with the peak knocking kinetic energy, decreased with the increase in A. The optimal parameter set was obtained as A = 55 μm, C = 50 μm, and B = 41 mm; as shown in Figure 10d, under this parameter set, compared to cylindrical cylinder bores, the friction power of the skirt was reduced by 10.63%, the friction power of the ring group was reduced by 24.38%, and the peak knocking kinetic energy was reduced by 22.64%.

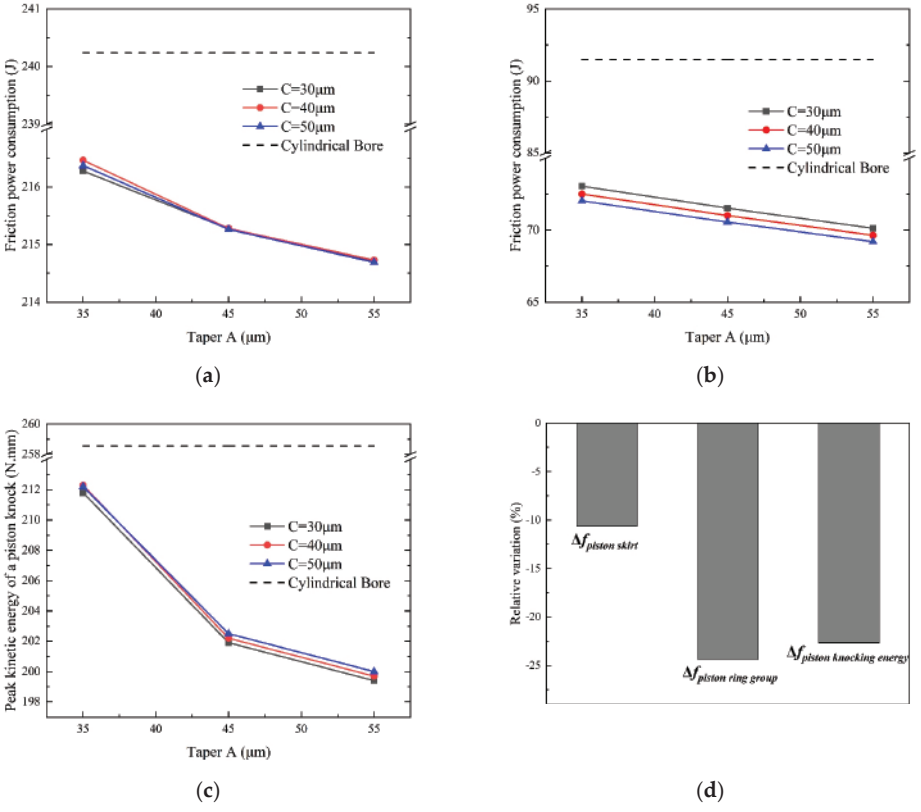

Figure 10. Effect of taper (A) on the piston friction lubrication characteristics and knocking characteristics with different values of ellipticity (C): (**a**) piston skirt friction power; (**b**) piston ring group friction power; (**c**) peak kinetic energy of piston knocking; (**d**) relative changes brought by the optimal parameter group (A = 55 mm, C = 50 μm, B = 41 mm).

3.2.2. Effect of Starting Height of Tapered Profile (B) with Respect to Different Values of Ellipticity (C)

Figure 11 shows the influence of the starting height of the conical profile (B) on the friction and knocking characteristics under different values of ellipticity (C). The taper (A) was kept unchanged at 55 μm, and the starting height of the conical profile (B) was varied from 31 mm to 51 mm. The friction power of the skirt and ring group increased with B regardless of the C value, and the peak knocking kinetic energy decreased with the increase in B. The optimal parameter set was obtained as A = 55 μm and C = 50 μm, and the peak knocking kinetic energy decreased with the increase in B. The optimal parameter set was obtained as A = 55 μm, C = 50 μm, and B = 31 mm; as shown in Figure 11d, under this parameter set, compared to cylindrical cylinder bores, the skirt friction power was reduced

by 10.35%, the ring group friction power was reduced by 23.28%, and the peak knocking kinetic energy was reduced by 23.30%.

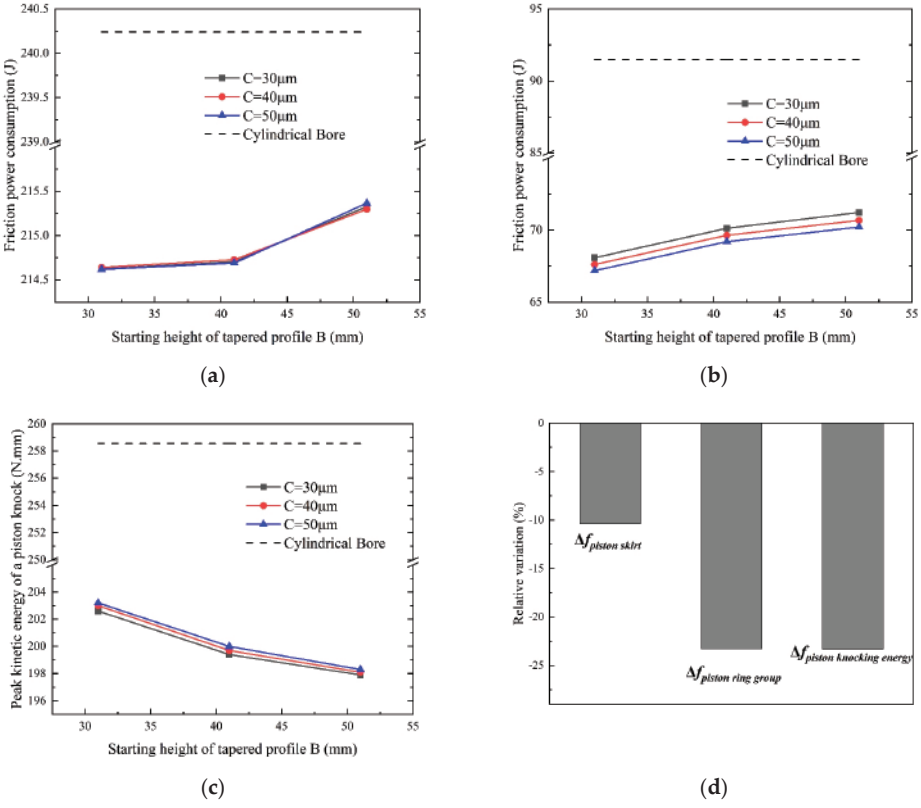

Figure 11. Effect of starting height of tapered profile (B) on the piston friction lubrication characteristics and knocking characteristics with different values of ellipticity (C): (**a**) piston skirt friction power; (**b**) piston ring group friction power; (**c**) peak kinetic energy of piston knocking; (**d**) relative changes brought by the optimal parameter group (B = 31 mm, C = 50 μm, A = 55 μm).

3.2.3. Effect of Starting Height of Tapered Profile (B) with Respect to Different Values of Taper (A)

The influence of the starting height of the conical profile (B) on the friction characteristics and knocking characteristics under different values of taper (A) is shown in Figure 12. The ellipticity (C) remained unchanged at 50 μm, and the starting height of the tapered profile (B) was varied from 31 μm to 51 μm. The friction power of the skirt and the ring group increased with B regardless of the value of A. However, this growth rate was decreased with increasing B. For the peak knocking kinetic energy, there was an interaction between A and B. When A was taken as 35 μm and 45 μm, the peak piston-knocking kinetic energy showed a decreasing and then increasing trend with the increase in B. When the taper (A) was 55 μm, the peak piston-knocking kinetic energy monotonically decreased with the increase in B. The optimal parameter set was taken as A = 55 μm, C = 50 μm, and B = 31 mm. As shown in Figure 12d, under this parameter set, compared to cylindrical cylinder bores, the friction power of the skirt was reduced by 10.66%, the friction power of the ring group was reduced by 26.59%, and the peak knocking kinetic energy was reduced by 21.41%.

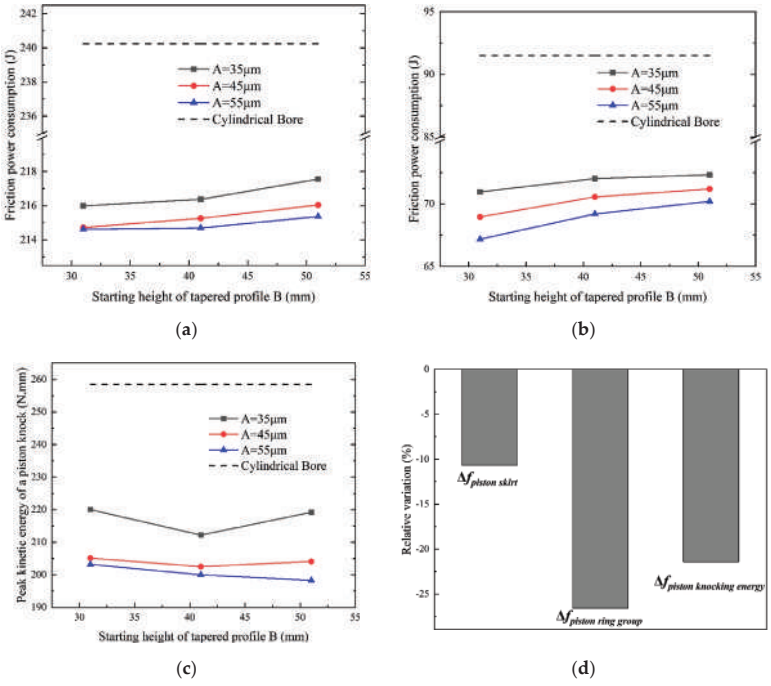

Figure 12. Effect of starting height of tapered profile (B) on the piston friction lubrication characteristics and knocking characteristics with different values of taper (A): (**a**) piston skirt friction power; (**b**) piston ring group friction power; (**c**) peak kinetic energy of piston knocking; (**d**) relative changes brought by the optimal parameter group (A = 55 μm, B = 31 mm, C = 50 μm).

3.3. Comparison between Optimal and Baseline Design

Compared with the peak kinetic energy of the piston knocking, taking the friction consumption of the piston system as the main consideration, A = 55 μm, B = 31 mm, and C = 50 μm were selected as the optimized cylinder bore profile parameter combination; the variation in friction characteristics and knocking characteristics with the crankshaft rotation angle for the cylindrical bore and optimized cylindrical-tapered bore is shown in Figure 13.

After profile parameter optimization, the total friction power of the piston group was reduced by 49.95 J, which mean a decrement of 15.05%. The decrement of friction power was beneficial for reduced fuel consumption. The peak piston knock kinetic energy was reduced by 55.35 N·mm, representing a decrement of 21.41%. The reduction in knocking kinetic energy can reduce the risk of engine cavitation and improve engine NVH performance.

Figure 14 shows the comparison of the minimum film thickness ratio and film pressure on the friction pair. Only the minimum film thickness ratio of the first is shown in Figure 14b, since the first compressor ring accounts for the majority of the friction power in the ring group. Compared with that in the cylindrical bore, the minimum film thickness ratio between the piston skirt and the piston ring moving surface of the cylindrical-tapered bore was improved, as shown in Figure 14a, so the latter resulted in a smaller friction power. The distribution of the oil film pressure on the skirt at the moment of piston knocking is shown in Figure 14c,d. The peak oil film pressure was smaller in the cylindrical-tapered bore and the area of the oil-film-bearing area was larger, which effectively absorbed the kinetic energy of the piston's second-order motion, so the peak knocking kinetic energy was reduced in the latter case.

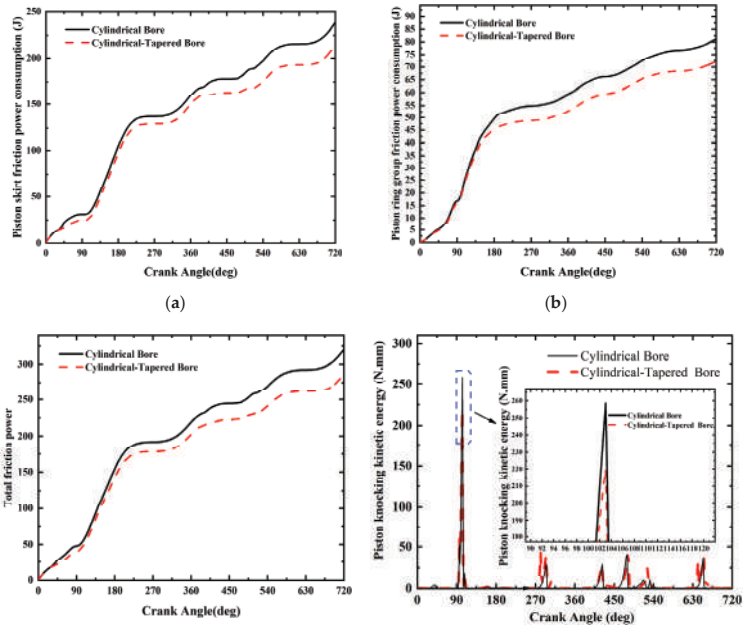

Figure 13. Comparison of piston friction characteristics and knocking characteristics before and after optimization: (**a**) skirt friction power change; (**b**) ring group friction power change; (**c**) total friction power change; (**d**) knocking kinetic energy change.

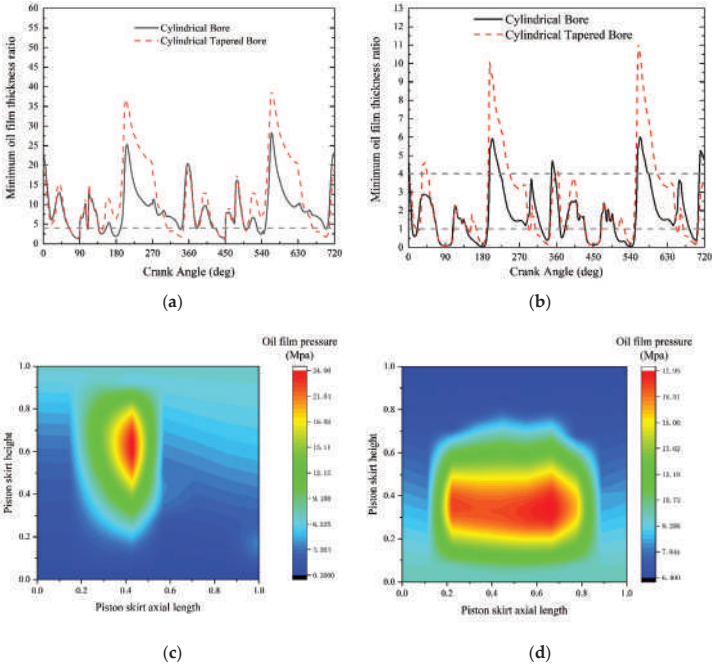

Figure 14. Comparison of oil film thickness and oil film pressure distribution in the cylinder bore before and after optimization: (**a**) minimum oil film thickness ratio change in the skirt; (**b**) minimum

oil film thickness ratio change for the 1st ring; (**c**) oil film pressure distribution in the skirt at the moment of piston knocking (pre-optimization); (**d**) oil film pressure distribution in the skirt at the moment of piston knocking (post-optimization).

4. Conclusions

(1) The taper has the greatest effect on the total friction power and the peak piston-knocking kinetic energy, followed by the starting height of the conical profile, while the ellipticity has the smallest effect; for the peak piston-knocking kinetic energy, there was a significant interaction between the taper and the starting height of the conical profile.

(2) Compared with the cylindrical bore, the optimized skirt friction work of the cylindrical-tapered bore decreased from 240.24 J to 214.62 J, with a decrease of 10.66%; the piston ring friction work decreased from 91.5 J to 67.17 J, with a decrease of 26.59%; and the peak knocking kinetic energy decreased from 258.55 N·mm to 203.2 N·mm, with a decrease of 21.41%.

(3) Compared with the cylindrical bore, the minimum oil film thickness on the moving surface of the piston skirt and the piston ring was increased in the cylindrical-tapered bore, which reduced the contact time of dry friction and increased the contact time of hydrodynamic friction at the piston-knocking moment. The cylindrical-tapered bore provided a larger contact area and oil film thickness, which absorbed some of the energy of the second-order motion of the piston and attenuated the impact.

Author Contributions: Conceptualization, H.D. and N.W.; methodology, J.L.; software, N.W.; validation, N.W., J.W. and X.Z.; formal analysis, N.W.; investigation, H.W.; resources, J.W.; data curation, H.W.; writing—original draft preparation, N.W.; writing—review and editing, H.D.; visualization, X.Z.; supervision, J.L.; project administration, J.Z.; funding acquisition, J.Z. All authors have read and agreed to the published version of the manuscript.

Funding: This research was funded by the National Natural Science Foundation of China (Grant No. 52205166).

Data Availability Statement: The original contributions presented in the study are included in the article, further inquiries can be directed to the corresponding authors.

Conflicts of Interest: Authors Jian Wang and Hui Wang were employed by the Weichai Power Co., Ltd. The remaining authors declare that the research was conducted in the absence of any commercial or financial relationships that could be construed as a potential conflict of interest.

References

1. Bi, Y.; Wang, P.; Luo, L.; Wang, H.; Xin, Q.; Lei, J.; Shen, L. Analysis of out-of-round deformation of a dry cylinder liner of a non-road high-pressure common-rail diesel engine based on multi-field coupling. *J. Braz. Soc. Mech. Sci.* **2021**, *43*, 50. [CrossRef]
2. Bi, Y.; Wang, P.; Xiang, R.; Wen, J.; Lei, J.; Shen, L.; Xin, Q. Numerical investigation on the operating characteristics of the cylinder liners of a turbocharged diesel engine. *Sādhanā* **2021**, *46*, 150. [CrossRef]
3. Li, G.; Gu, F.; Wang, T.; Lu, X.; Zhang, R.; Ball, A. A dynamic deformation based lubrication model between the piston rings and cylinder liner. In Proceedings of the 2017 23rd International Conference on Automation and Computing (ICAC), Huddersfield, UK, 7–8 September 2017; pp. 1–6. [CrossRef]
4. Delprete, C.; Razavykia, A. Piston dynamics, lubrication and tribological performance evaluation: A review. *Int. J. Engine Res.* **2020**, *21*, 725–741. [CrossRef]
5. Sato, K.; Fujii, K.; Ito, M.; Koda, S. *Application to Engine Development of Friction Analysis by Piston Secondary Motion Simulation in Consideration of Cylinder Block Bore Distortion*; 0148-7191; Technical Paper; SAE: Washington, DC, USA, 2006. [CrossRef]
6. Styles, G.; Rahmani, R.; Rahnejat, H.; Fitzsimons, B. In-cycle and life-time friction transience in piston ring–liner conjunction under mixed regime of lubrication. *Int. J. Engine Res.* **2014**, *15*, 862–876. [CrossRef]
7. Wang, Y.; Ma, X.; Li, T.; Lu, X.; Li, W. Influence of thermal effect in piston skirt lubrication considering thermal deformation of piston and cylinder liner. *Int. J. Engine Res.* **2023**, *24*, 14680874231155571. [CrossRef]
8. Li, G.; Gu, F.; Wang, T.; Lu, X.; Zhang, L.; Zhang, C.; Ball, A. An improved lubrication model between piston rings and cylinder liners with consideration of liner dynamic deformations. *Energies* **2017**, *10*, 2122. [CrossRef]

9. Lu, Y.; Li, S.; Wang, P.; Liu, C.; Zhang, Y.; Müller, N. The analysis of secondary motion and lubrication performance of piston considering the piston skirt profile. *Shock. Vib.* **2018**, *2018*, 3240469. [CrossRef]
10. Zhang, J.; Piao, Z.; Liu, S. Influence of skirt profile structure of gasoline engine piston on the friction and wear characteristics under standard conditions. *J. Tribol.* **2018**, *140*, 021703. [CrossRef]
11. Totaro, P.P.; Westerfield, Z.; Tian, T. *Introducing a New Piston Skirt Profile to Reduce Engine Friction*; 0148-7191; Technical Paper; SAE: Washington, DC, USA, 2016. [CrossRef]
12. Pawlus, P.; Reizer, R. Functional importance of honed cylinder liner surface texture: A review. *Tribol. Int.* **2022**, *167*, 107409. [CrossRef]
13. Guo, Z.; Yuan, C.; Liu, P.; Peng, Z.; Yan, X. Study on influence of cylinder liner surface texture on lubrication performance for cylinder liner–piston ring components. *Tribol. Lett.* **2013**, *51*, 9–23. [CrossRef]
14. Grabon, W.; Pawlus, P.; Wos, S.; Koszela, W.; Wieczorowski, M. Evolutions of cylinder liner surface texture and tribological performance of piston ring-liner assembly. *Tribol. Int.* **2018**, *127*, 545–556. [CrossRef]
15. Mezghani, S.; Demirci, I.; Yousfi, M.; El Mansori, M. Mutual influence of crosshatch angle and superficial roughness of honed surfaces on friction in ring-pack tribo-system. *Tribol. Int.* **2013**, *66*, 54–59. [CrossRef]
16. Hu, Y.; Meng, X.; Xie, Y.; Fan, J. Mutual influence of plateau roughness and groove texture of honed surface on frictional performance of piston ring–liner system. *Proc. Inst. Mech. Eng. Part J. J. Eng. Tribol.* **2017**, *231*, 838–859. [CrossRef]
17. Edtmayer, J.; Lösch, S.; Hick, H.; Walch, S. Comparative study on the friction behaviour of piston/bore interface technologies. *Automot. Engine Technol.* **2019**, *4*, 101–109. [CrossRef]
18. Alshwawra, A.; Pohlmann-Tasche, F.; Stelljes, F.; Dinkelacker, F. Enhancing the Geometrical Performance Using Initially Conical Cylinder Liner in Internal Combustion Engines—A Numerical Study. *Appl. Sci.* **2020**, *10*, 3705. [CrossRef]
19. Alshwawra, A.; Pasligh, H.; Hansen, H.; Dinkelacker, F. Increasing the roundness of deformed cylinder liner in internal combustion engines by using a non-circular liner profile. *Int. J. Engine Res.* **2021**, *22*, 1214–1221. [CrossRef]
20. Alshwawra, A.; Pohlmann-Tasche, F.; Stelljes, F.; Dinkelacker, F. Effect of freeform honing on the geometrical performance of the cylinder liner—Numerical study. *SAE Int. J. Engines* **2022**, *16*, 463–486. [CrossRef]
21. Halbhuber, J.; Wachtmeister, G. *Effect of Form Honing on Piston Assembly Friction*; 0148-7191; Technical Paper; SAE: Washington, DC, USA, 2020. [CrossRef]
22. AVL LIST GmbH. *BOOST Rev 2017.1 Users Guide*; AVL LIST GmbH: Steiermark, Austria, 2017.
23. Liang, X.; Wang, Y.; Huang, S.; Yang, G.; Tang, L.; Cui, G. *Investigation on Cylinder Bore Deformation under Static Condition Based on Fourier Decomposition*; 0148-7191; Technical Paper; SAE: Washington, DC, USA, 2017. [CrossRef]
24. AVL LIST GmbH. *Excite Piston & Rings Rev 2017.1 Users Guide*; LIST GmbH: Steiermark, Austria, 2017.

designs

MDPI

Article

An Innovative Mechanical Approach to Mitigating Torque Fluctuations in IC Engines during Idle Operation

Daniel Silva Cardoso [1], Paulo Oliveira Fael [1], Pedro Dinis Gaspar [1,*] and António Espírito-Santo [2]

[1] C-MAST—Center for Mechanical and Aerospace Science and Technologies, Calçada Fonte do Lameiro, 6201-001 Covilhã, Portugal; silva.cardoso@ubi.pt (D.S.C.); pfael@ubi.pt (P.O.F.)
[2] IT—Institute of Telecommunications, Calçada Fonte do Lameiro, 6201-001 Covilhã, Portugal; aes@ubi.pt
* Correspondence: dinis@ubi.pt

Abstract: Internal combustion engines have been a major contributor to air pollution. Replacing these engines with electric propulsion systems presents significant challenges due to different countries' needs and limitations. An active, purely mechanical solution to the problem of irregular torque production in an alternative internal combustion engine is proposed. This solution uses an actuator built on a camshaft and a spring, which stores and returns energy during the engine operating cycle, allowing torque production to be normalized, avoiding heavy flywheels. Designed for control throughout the engine's duty cycle, this system incorporates a cam profile and a spring mechanism. The spring captures energy during the expansion stroke, which is then released to the engine during the intake and compression strokes. Simple, lightweight, and efficient, this system ensures smoother and more consistent engine operations. It presents a viable alternative to the heavy and problematic dual-mass flywheels that were introduced in the 1980s and are still in use. This innovative approach could significantly enhance the performance and reliability of alternative internal combustion engines without notable energy losses.

Keywords: internal combustion engine; driving torque; resistive torque; mass inertia torque; torque fluctuations; energy storage mechanism; camshaft; spring

Citation: Cardoso, D.S.; Fael, P.O.; Gaspar, P.D.; Espírito-Santo, A. An Innovative Mechanical Approach to Mitigating Torque Fluctuations in IC Engines during Idle Operation. *Designs* **2024**, *8*, 47. https://doi.org/10.3390/designs8030047

Academic Editors: Wenbin Yu, Guang Zeng and Junnian Wang

Received: 4 March 2024
Revised: 8 May 2024
Accepted: 15 May 2024
Published: 17 May 2024

1. Introduction

1.1. Background

The internal combustion engine (ICE) exhibits inherent characteristics of torque fluctuations throughout its operational cycle. These fluctuations are a consequence of the engine's mechanism, where the energy from fuel is converted into mechanical energy by discrete combustion events. Each combustion stroke generates a distinct torque impulse, contributing to an uneven torque output over the engine cycle. This phenomenon impacts the smoothness of engine operation and has broader implications for engine efficiency and longevity [1–5].

Historically, the engine industry has continually evolved to address these torque inconsistencies, driven by the pursuit of enhanced engine performance, smoothness, and efficiency. The traditional approach to mitigating torque variations has largely centered on passive mechanical solutions, such as the utilization of conventional flywheels and dual mass flywheels (DMF) [6]. However, while effective in smoothing out rotational speeds, the flywheel adds to the engine's mass and is incapable of adjusting itself to the engine operation variations. On the other hand, the mechanism proposed in this study seeks to offer a relatively lightweight solution that harmonizes the produced torque without affecting the engine's capability for acceleration or deceleration. This initiative is part of a broader research endeavor aimed at studying and developing a mechanism capable of functioning across all engine speed ranges and under various loads. Currently, the focus is on enhancing performance during idle and low-speed operations, where the demand for such systems is most critical [2,7].

Recent advancements employing mechanical, electromechanical, and control strategies have significantly improved torque harmonization and reduced engine vibrations and rotational speed variations. This serves as a clear indication of both the opportunity and the need for further advancements in this domain, emphasizing the shift away from traditional, bulkier, and less efficient solutions towards more accurate and responsive technologies. Moreover, this transition facilitates the integration of engines into hybrid vehicles, range extenders, and microcogeneration systems [8–13].

This study builds upon approaches introduced by Lin et al. [14] and Arakelian et al. [15]. Although the first study focuses on reducing torque variations in the camshaft and the second emphasizes inertia effects in slider-crank mechanisms, both studies commonly utilize a cam to control the mitigating mechanism and a spring to act as energy storage. Another approach, conducted by Cardoso and Fael [16], has demonstrated the feasibility of using switched reluctance machines to replace traditional flywheels, offering a method to correct engine output torque and speed variations, albeit at the cost of a complex system. Despite these advancements, a gap remains in seamlessly integrating these technologies into existing engine designs without complex control systems or significant modifications to the engine architecture. This research aims to fill this gap by developing a mechanically focused solution that maintains engine performance, particularly at low rotational speeds.

1.2. Problem Statement

A series of multifaceted challenges underscore the quest to enhance torque management in internal combustion engines. At the core of these challenges lies the inherent nature of alternative ICE operations, where the intermittent combustion process leads to nonuniform torque output. This irregularity manifests as torque ripple or fluctuations, which not only compromises the smoothness and responsiveness of the engine but also adversely affects overall efficiency and increases vibrations and noise [17,18].

One of the primary issues in contemporary torque management is the limitation of traditional mechanical solutions. While these methods, such as the utilization of flywheels, have been fundamental in maintaining engine operation at low speeds, they fall short of addressing the demands of modern engines. The added mass and inertia of traditional solutions often impede the engine's dynamic response, failing to align with the growing emphasis on lightweight and compact engine designs. Moreover, these approaches do not actively adapt to varying operational conditions, thus limiting their effectiveness in dynamic and diverse operation scenarios [19–21].

Another critical aspect is the evolution of engine technology itself, with advancements in engine design, including the trend towards more compact, lightweight engine designs, different cylinder arrangements, unusual cylinder number engines (this can lead to extreme torque production irregularities), cylinder deactivation technologies, and the advent of hybrid and electric vehicles, highlighting the need for systems that offer greater precision and adaptability [22–27].

1.3. Objectives

Study of Torque Decomposition in a Slider Crank Engine: The objective pretends to study the decomposition of output torque in an alternative engine design. This involves analyzing how different torque types (such as driving torque, resistive torque, and mass inertia torque) contribute to the overall output torque in this kind of engine.

Development of a Camshaft: The main objective of this research is to design and develop a camshaft, which is the main component of the actuator implemented to smooth the torque output. The key challenge is in creating a cam profile that can precisely mimic the torque output profile and can act on the spring, compressing it to store mechanical energy during the expansion stroke and subsequently receiving energy from the spring to return it to the engine during strokes when the engine is not producing positive work.

Development of an Integrated Camshaft-Actuator System: With this objective, an integrated system controlled by the developed cam is intended to be designed and developed. In this process, some considerations must be taken, with some of the most important parts to study and develop being the spring stiffness and preload. The spring needs to be studied to store as much energy as possible without interfering with the engine's natural movement and performance.

Evaluation and Demonstration of System Adaptability and Performance: Lastly, the evaluation of the performance of the developed system during idle operation is aimed at.

1.4. Study Contributions

The major contributions of this work are divided between the development of a mechanical mechanism and advancements in the field of internal combustion engines. The specific contributions of this study are outlined as follows:

Advanced Torque Decomposition Analysis: A comprehensive analysis of torque decomposition in alternative engines is provided. This approach enhances understanding of how different types of torque—driving, resistive, and mass inertia—interact and contribute to overall engine performance. This insight is useful for future work, for example, focusing on studying engine torque output smoothness and examining how geometric and construction parameters influence torque production.

Camshaft Development Methodology: This work includes the design and development of a camshaft that accurately replicates the engine's torque output profile. The design process encounters challenges due to the irregularities of the engine's torque output and the numerous parameters influencing the cam's profile. This paper presents a methodology for cam development.

Development of a Torque Mitigating Mechanism: This study introduces the development of a fully mechanical torque mitigating mechanism. The mechanism is designed to absorb excess energy from the engine system during periods of high output and strategically release it during phases where additional energy is required. This cyclic absorption and redistribution are tailored to operate seamlessly across different periods of time and varying operational conditions.

Integration of a Camshaft-Actuator with a single-cylinder engine: Beyond individual components, this study focuses on integrating the developed mechanism, which includes a camshaft for control and a spring for energy storage, with a single-cylinder engine. This integration aims to enhance torque smoothness and ensure that speed variations during the engine cycle remain closely aligned with the engine's average rotational speed.

2. Engine Torque Analysis

In considering the output torque at the crankshaft of ICEs, as illustrated in Figure 1, torque fluctuation arises mainly from three sources. Firstly, the driving torque generated mostly during the expansion stroke in ICEs leads to irregular driving actuation. This fluctuation is consistent across different crankshaft speeds, depending solely on crankshaft angle (φ) and pressure force ($F_{pressure}$). Secondly, fluctuation occurs due to the inertia force from the acceleration (α) of the imbalanced mass. This type of fluctuation is more pronounced at higher speeds as it is proportional to the square of the engine's angular speed (ω). Lastly, fluctuating resistive loads, such as those in engine valve systems, impart irregular torque to the camshaft, independent of engine angular speed and related to crankshaft angle [14], [28,29].

To mitigate these fluctuations, passive and active techniques have been employed. Flywheels, as referred to previously, for example, can store and release kinetic energy to smooth out speed fluctuations but are less effective at low speeds due to their large inertia. This affects the engine performance and its capacity to change the rotational speed when solicited and the use of this represents an expressive mass increment. Torsional vibration dampers offer a solution across various speeds, but this involves dissipation of energy. Active control techniques, in contrast, counteract torque fluctuations by providing

an opposing force, but at the cost of complex control techniques or input of external energy [30,31].

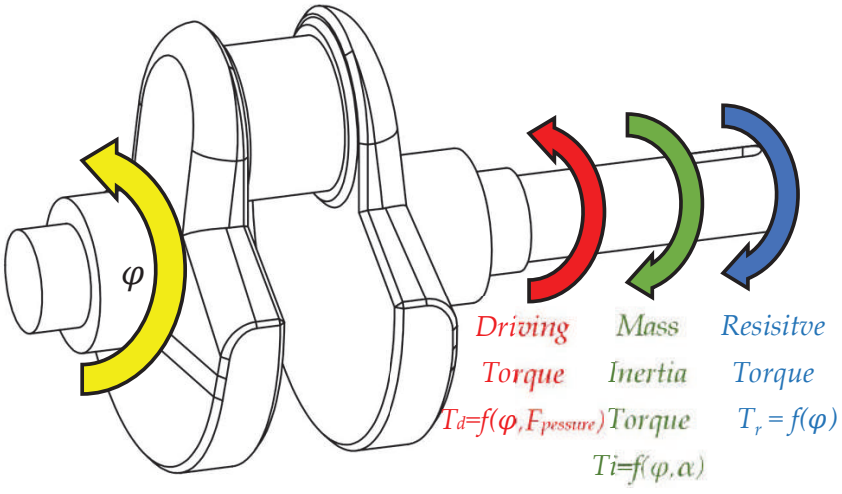

Figure 1. Representation of how the three types of torque mentioned above act on the crankshaft.

For a clearer understanding of the torque production cycle in internal combustion engines, the analysis is often conducted using a single-cylinder engine model. This approach effectively isolates three types of torque fluctuations, which are more difficult to discern in multicylinder engines due to the overlapping of multiple-stroke events.

These events significantly contribute to torque fluctuations and can be categorized into two groups: those that generate positive torque and those that produce negative torque. Only the expansion that represents a quarter (on Otto) of the strokes and is part of the first group is directly useful for the engine's primary purpose. However, the magnitude of this useful stroke at engine full load is about fifteen times greater than the average of the other three strokes. However, despite their negative torque, strokes such as intake, compression, and exhaust are essential for the engine's cycle.

The torque generated by an engine is a composite of the three types of torque previously described, as outlined in Equation (1). The capability of alternative engines to generate torque stems from the slider−crank mechanism, depicted in Figure 2. Through dynamic analysis of this mechanism, both the inertia torque and driving torque of the engine can be accurately determined.

$$T_t = T_d + T_i - T_r \quad (1)$$

T_t—*total engine torque* [Nm]
T_d—*driving torque* [Nm]
T_i—*mass inertia torque* [Nm]
T_r—*resistive torque* [Nm]

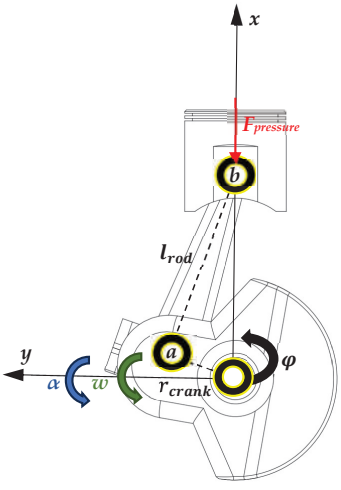

Figure 2. Slider−crank mechanism from a single-cylinder engine.

2.1. Driving Torque

ICEs are volumetric machines designed to convert the chemical energy in fuel into mechanical energy, which is then transferred to the crankshaft. They utilize a slider−crank mechanism to convert pressure variations from fuel combustion in the combustion chamber into mechanical movement. This is due to the design of the alternative engine that only allows the gases in the cylinder to expand in the piston direction.

The force resulting from these pressure variations can be expressed as the product of the cylinder's internal pressure by the piston area, as shown in Equation (2). This equation clearly illustrates the generation of driving force in ICEs due to pressure variation, calculated from Equation (3), determined using the first law of thermodynamics.

For a comparative analysis, Figure 3 demonstrates how the values of pressure exerted in the piston can act in the piston when the engine is running at idle, i.e., when the engine only produces the torque needed to keep it running and when the presence of the flywheel is most necessary to store energy from the expansion stroke for the rest of the strokes. In contrast, Figure 4, derived from an analysis based on Figure 2, culminating in Equation (4), depicts the generation of driving torque throughout a 720° crankshaft rotation in an Otto engine under identical operational conditions to those shown in Figure 3 [32].

$$F_{pressure} = (p_{cyl} - p_{atm})\frac{\pi B^2}{2} \tag{2}$$

$$p_{cyl} = \frac{2\left(\delta Q_f - \delta Q - \delta Q_{vap}\right) + p_{cylprev}\left(\frac{\gamma+1}{\gamma-1}V_{cylprev} - V_{cyl}\right)}{\frac{\gamma+1}{\gamma-1}V_{cyl} - V_{cylprev}} \tag{3}$$

$F_{pressure}$—*pressure force acting on the piston* [N]
B—*bore* [m]
p_{cyl}—*cylinder pressure* [Pa]
p_{atm}—*atmosferic pressure* [Pa]
δQ_f—*energy released by the fuel* [J]
δQ—*nenergy transferred in the form of heat* [J]
δQ_{vap}—*aenergy released by the vaporization of the fuel inside the cylinder* [J]
$p_{cylprev}$—*pressure in the cylinder at the previous iteration* [Pa]
γ—*expansion coefficient*

$V_{cylprev}$—*volume in the cylinder at the previous iteration* $[m^3]$
V_{cyl}—*volume in the cylinder at the current iteration* $[m^3]$

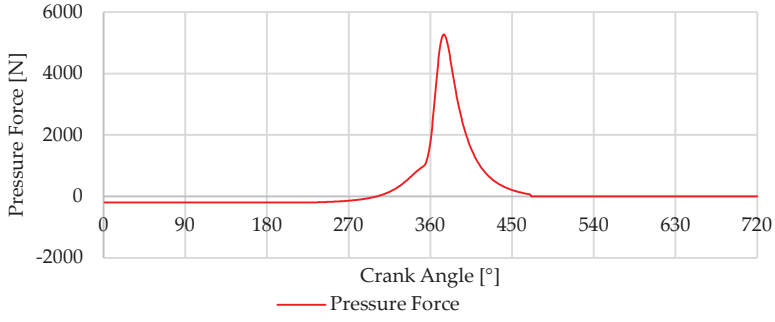

Figure 3. $F_{pressure}$ in the piston from Otto strokes.

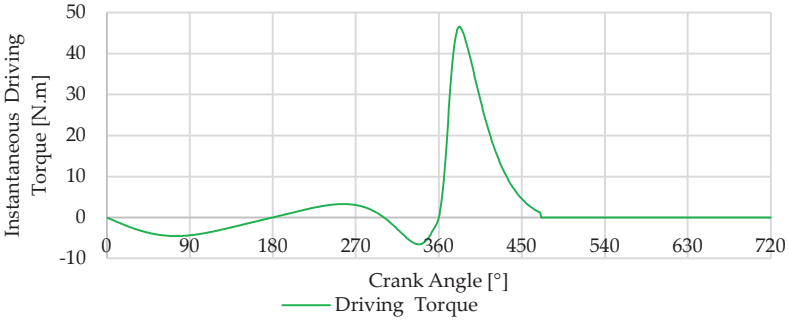

Figure 4. Driving torque from the $F_{pressure}$ on the slider−crank mechanism.

$$T_d = F_{pressure} sin\varphi (1 + \frac{r_{crank}}{l_{rod}} cos\,\varphi) - T_r + T_i \quad (4)$$

T_d—*driving engine torque* [Nm]
r_{crank}—*crank radius* [m]
l_{rod}—*connecting rod length* [m]
φ—*crankshaft rotation angle* [rad]

2.2. Mass Inertia Torque

Mass inertia torque, hereinafter referred to as inertia torque, arises from the moving parts, particularly during changes in their speed. In the context of an ICE, this involves components like the crankshaft, connecting rods, pistons, and other moving parts. The inertia of these components plays a significant role in the engine's responsiveness, vibrations, and overall performance. Inertia torque is influenced by several factors, including the mass and distribution of the engine's moving parts and the speed. The faster the components rotate, the more significant the inertia torque becomes, as it takes more force to change the speed of these rapidly moving parts. This phenomenon is especially noticeable during rapid acceleration or deceleration, where the inertia torque can have a substantial impact on engine performance. The inertia forces can be broken down into components along the piston's movement line (x-axis), which induce forces on the crankshaft and thereby contribute to its torque, presented in Equation (5), and forces acting perpendicularly to the former (y-axis), which do not directly affect the torque generated by the engine, presented in Equation (6). The mass responsible for inducing inertia forces includes the mass of the

piston group and the connecting rod. For simplification purposes, this mass is divided between two distinct points: point a, located on the crankshaft pin (as shown in Figure 2), where, according to literature, we can consider as comprising 2/3 of the connecting rod mass, and point b, located on the piston pin, where the piston group mass and 1/3 of the connecting rod mass are assumed, as outlined in Equations (7) and (8) [33].

$$F_{inertia}^{x} = (m_a + m_b) r_{crank} \omega^2 \cos\varphi + \left(m_b \frac{r_{crank}}{l_{rod}} \right) r_{crank} \omega^2 \cos 2\varphi \quad (5)$$

$$F_{inertia}^{y} = m_a r_{crank} \omega^2 \sin\varphi \quad (6)$$

$$m_a = \frac{2}{3} m_{cr} \quad (7)$$

$$m_b = \frac{1}{3} m_{cr} + m_{pg} \quad (8)$$

$F_{inertia}^{x}$—*inertia forces on* $x-$ *axis* [N]
m_a—*mass considered at point a, crankshaft pin* [kg]
m_b—*mass considered at point b, piston pin* [kg]
ω—*angular speed* [rad/s]
$F_{inertia}^{y}$—*inertia forces on* $y-$ *axis* [N]
m_{pg}—*mass of piston group* [kg]
m_{cr}—*mass of connecting rod* [kg]

To calculate the torque induced by inertia forces on the crankshaft, as detailed in Equation (9), consideration is given only to the masses previously divided and located at point b. This approach is based on the premise that the crankshaft is properly balanced, factoring in the masses on the crankshaft pin and the equivalent connecting rod mass at the point a, ensuring that the rotational balance point of this mass aligns with the crankshaft's center of rotation.

$$T_i = \frac{m_b}{2} {r_{crank}}^2 \omega^2 \left(\frac{r_{crank}}{2 l_{rod}} \sin\varphi - \sin 2\varphi - \frac{3 r_{crank}}{2 l_{rod}} \sin 3\varphi \right) \quad (9)$$

T_i—*mass inertia torque* [Nm]

Figure 5 represents the forces that lead to the torque profile obtained in Figure 6. For clarity, green vertical lines indicate the top dead center and blue vertical lines denote the bottom dead center. Figure 6 illustrates the magnitude of the inertia torque produced by the movement of the internal components in a single-cylinder slider crank engine model at 800 RPM without charge, representing idling operation.

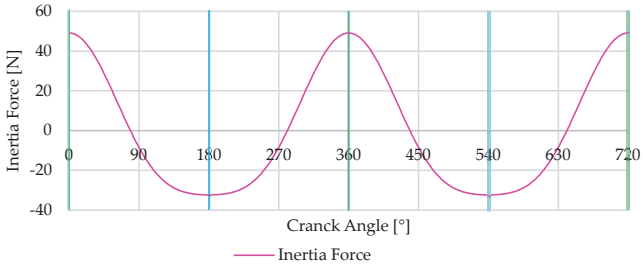

Figure 5. Inertia forces on the crankshaft at 800 RPM from the piston group and connecting rod.

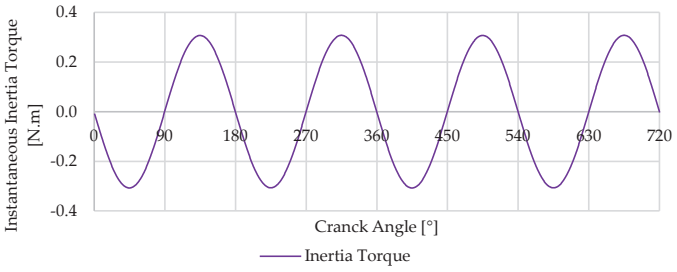

Figure 6. Instantaneous inertia torque on the crankshaft from internal components in a single-cylinder slider−crank engine.

2.3. Resistive Torque

The resistive torque comes essentially from camshafts, oil pumps, or other engine auxiliary elements. This torque type is primarily due to resistive forces that the engine components must overcome during operation. For the purposes of this work, only the resistive torque from camshafts will be considered. In the context of camshafts, this type of torque fluctuates based on the engine cycle, particularly in the valve operation phase, where the opening and closing of valves require varying levels of force. In the camshaft context, the resistive torque is a consequence of the need to compress (negative torque) and then release (resulting in positive torque) the valve springs. The magnitude of this torque fluctuation can vary significantly based on the springs' stiffness and the valve mechanism's design. At lower to medium speeds, the resistive torque fluctuation tends to be more substantial than the inertia torque fluctuation. To quantitatively analyze resistive torque in ICEs, one must consider the spring stiffness, the preload force, the rocker mechanism, and the displacement of valves (see Figures 7 and 8). The spring force from the valve mechanism can be expressed by Equation (10) [34].

$$F = k\delta + P \tag{10}$$

k—*spring stiffness* [N/m]
δ—*valve displacement* [m]
P—*preload of the spring* [N]

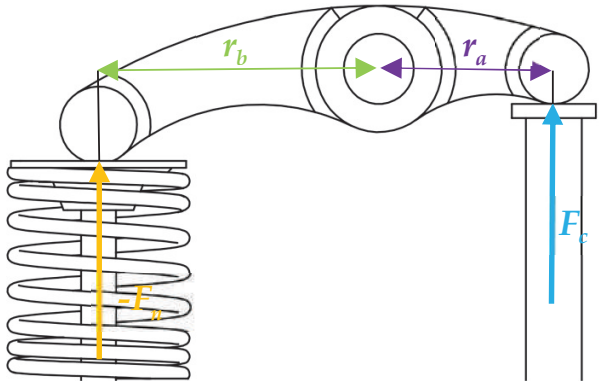

Figure 7. Rocker arm diagram from the valve train.

$$r_a F_c + r_b(-F_n) = 0 \tag{11}$$

r_a—*distance from the push rod to the rocker centre* [m]
r_b—*distance from the valve center to the rocker centre* [m]
F_n—*force from the rocker on the valve* [N]
F_c—*force from the cam on the rocker* [N]

$$\vec{T}_c + \vec{r}_c \times \left(-\vec{F}_c\right) = 0 \tag{12}$$

$\vec{T}_c$—*torque on the camshaft* [Nm]
$\vec{r}_c$—*vector from the center of the cam to the contact point with the follower* [m]

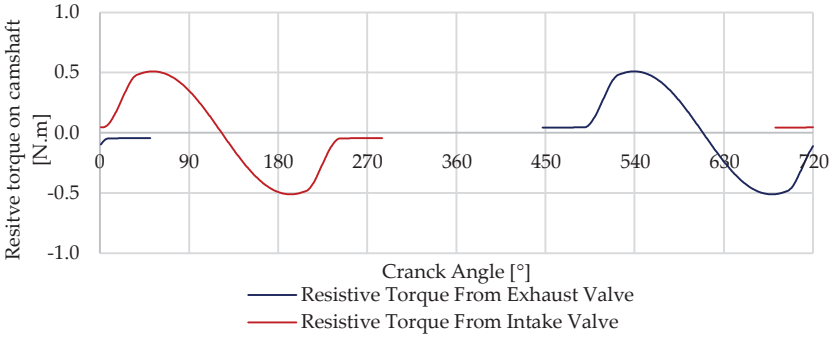

Figure 8. Resistive torque from intake and exhaust valve mechanism.

3. Design of the Torque Correction Mechanism

3.1. Design Concept

To enhance the output torque's smoothness, a specifically engineered mechanism is proposed to create a counteracting torque. This design pretends to minimize fluctuations in the engine's output torque. Key components of this system include a spring for energy storage and a cam tailored to align with the engine's output torque characteristics. A CAD model of this mechanism is shown in Figure 9. The mechanism is structured to generate a counteracting torque at any rotation angle θ, matching the output torque in magnitude but opposite in direction.

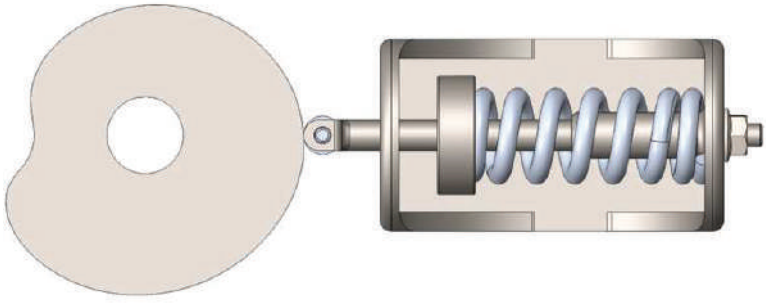

Figure 9. CAD model from the mechanism, with the cam designed to mimic the profile torque desire, the roller follower, and the spring responsible for storing the energy.

To achieve the desired mechanism response, the specially designed cam must replicate the engine's opposing torque. It can be installed on the camshaft or with a 2:1 transmission ratio, similar to the engine's distribution system, which may increase friction and

consequently, resistive torque, leading to a more complex system. This is due to the torque contributing events being dispersed over the 720° crankshaft rotation in a 4-stroke cycle. The direct integration of this mechanism into the crankshaft would simplify implementation but is impractical for addressing resistive and driving torque irregularities, though it would be effective for inertia torque, as shown in Figure 6 with its 360° periodicity. Figures 10–12 illustrate a potential implementation in a single-cylinder engine using the existing distribution system and camshaft to simplify the system and minimize friction. This implementation assumes available space on the camshaft for the cam and that the camshaft shaft and transmission ratio can support the counteracting torque with these premises being valid for a demonstrative implementation in this specific engine construction.

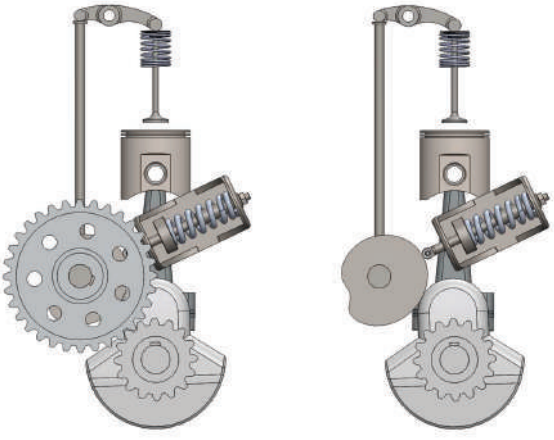

(**a**) (**b**)

Figure 10. Front views of the CAD model from the (**a**) mechanism integrated on the single-cylinder engine, on image (**b**) the camshaft gear was removed to show the positioning of the balancing cam.

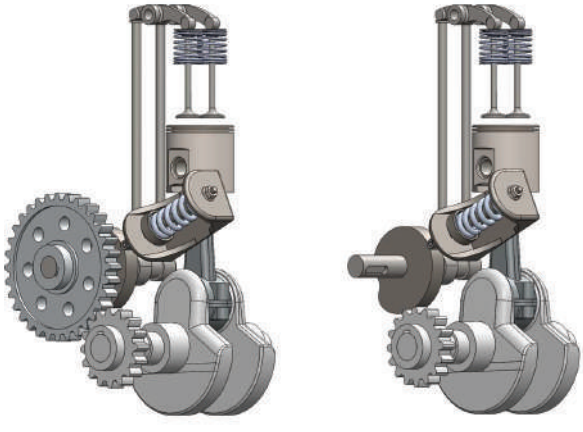

(**a**) (**b**)

Figure 11. Perspective views—left side—of the CAD model from the (**a**) mechanism integrated on the single-cylinder engine, in image (**b**), the camshaft gear was removed to show the positioning of the balancing cam.

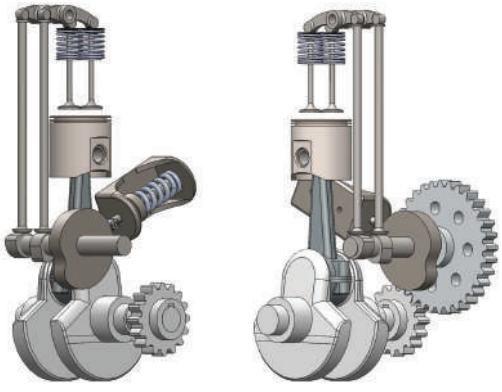

(**a**) (**b**)

Figure 12. Perspective views—right side—of the CAD model from the (**a**) mechanism integrated on the single-cylinder engine, in image (**b**), the camshaft gear was removed to show the positioning of the balancing cam.

3.2. Determination of the Balancing Cam Profile

The cam's profile is essential for controlling the actuator in response to the engine's needs. This cam was developed by considering the torque acting upon it, which is then transformed and stored in the spring. To design the cam profile, it is required to determine the cam radius in the function of the crankshaft rotation angle φ, for a previously defined torque profile. Figure 13 is a diagram of the forces acting on the cam [14,33,34].

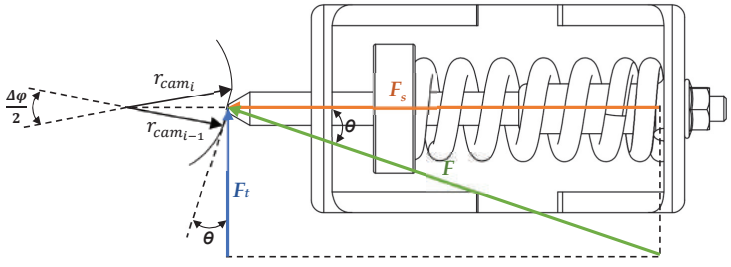

Figure 13. Diagram of the mechanism used to deduce the equations that allow the balancing cam to be obtained that mimics the desired torque profile.

The torque on the mechanism camshaft T_{cam} as the product of the tangential force F_t by cam radius:

$$T_{cam} = F_t r_{cam_i} \tag{13}$$

T_{cam}—*torque on mechanism camshaft* [Nm]
r_{cam_i}—*cam radius* [m]
F_t—*tangential force* [N]

From Figure 13 F_t is the product from the F_s by the $tan\theta$ as presented in Equation (14), and F_t can be directly substituted into Equation (13), which gives the torque as a function of F_s as presented in Equation (15), F_s depends on the spring conditions and the displacement induced by the cam on the spring, as shown by Equation (16).

$$F_t = F_s tan\theta \tag{14}$$

F_s—*spring force* [N]

$$T_{cam} = F_s tan\theta \; r_{cam} \tag{15}$$

$$F_s = k(r_{cam} - r_{initial}) + P \tag{16}$$

$r_{initial}$—*cam initial radius* [m]

Based on the defined torque for the cam T_{cam}, $tan\theta$ can be determined using Equation (17). Then, following Equation (18), which arises from the analysis of the diagram in Figure 13, the radius of the cam can be calculated as a function of the crankshaft angle.

$$tan\theta = \frac{T_{cam}}{r_{cam_i}(k(r_{cam_i} - r_{initial}) + P)} \tag{17}$$

$$r_{cam_i} = r_{cam_{i-1}} + \left(\frac{\Delta\varphi}{2}\right)\left(r_{cam_{i-1}} tan\theta\right) \tag{18}$$

To convert the previously obtained polar coordinates into cartesian coordinates for better visualization and plotting of the cam, Equations (19) and (20) are used.

$$x = r_{cam} cos\left(\frac{\varphi}{2}\right) \tag{19}$$

$$y = r_{cam} sin\left(\frac{\varphi}{2}\right) \tag{20}$$

Finally, when integrating a roller follower, including the roller's radius in the cam profile calculation is necessary. This is done using Equations (21) and (22), ensuring the cam profile meets all specified conditions for the roller follower. This crucial step guarantees that the cam design is effectively customized for the specific follower type in the engine mechanism.

$$x_r = x - r_{roller} cos(\left(\frac{\varphi}{2}\right) - \theta) \tag{21}$$

$$y_r = y - r_{roller} sin\left(\left(\frac{\varphi}{2}\right) - \theta\right) \tag{22}$$

r_{roller}—*roller radius* [m]

4. Modelling of Torque Correction Mechanism

4.1. Engine Modelling and Simulation

The development of the engine simulation, performed using MATLAB® R2024a (MathWorks, Natick, MA, USA), is based on a modeling approach that analyzes the engine's instantaneous torque for each degree of crankshaft rotation. It was specifically constructed to dissect engine torque into three distinct components.

The simulation inputs geometric parameters to model the slider−crank mechanism, iterating through one-degree increments of crankshaft rotation. It spans 720 degrees of rotation to simulate, among other things, torque values and speed variations at each degree, covering a full cycle of the 4-stroke engine under study.

As shown in Section 2 through various graphs, this modeling framework successfully segments engine torque into three main components: the inertia torque driven by mass acceleration, as specified in Equation (9); torque due to pressure differences within the engine cylinder, detailed in Equation (3); and the resistive torque produced by the valve mechanism, outlined in Equation (12).

The engine parameters are outlined in Table 1. The simulation framework is organized around valve timing, divided into four segments that correspond to each stroke of the Otto cycle, thereby covering all necessary conditions to derive operational parameters at each crankshaft angle, as will be analyzed in Section 4.3.

Table 1. Engine parameters used to perform the simulation used to present the idle torque profile.

Slider−Crank	Valve Train
$r = 0.022$ m	$k = 588,000$ N/m
$l = 0.073$ m	$P = 47$ N
$B = 0.06$ m	$r_a = 0.022$ m
$m_{pg} = 0.144$ kg	$r_b = 0.022$ m
$m_{cr} = 0.123$ kg	$IVO = 0°$
	$IVC = 220°$
$\omega = 83.8$ rad/s	$EVO = 470°$
	$EVC = 720°$

This simulation incorporates elements that yield instantaneous torque curves closely resembling those obtained through experimental means. Figure 14 showcases the results from prior experimental work conducted to validate the curves derived from the implemented methodology [3].

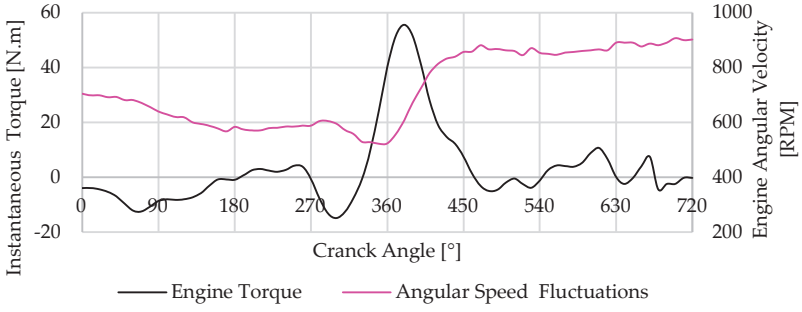

Figure 14. Experimental output torque from the single-cylinder engine at idle, 800 RPM.

4.2. Balancing Cam Mechanism Modelling

For the torque correction mechanism's development, a torque profile established from the process described earlier is used. The mechanism and cam, crafted based on equations detailed in Section 3.2, aim to correct the torque profile illustrated in Figure 15, which represents an engine idle at 800 RPM. In defining the cam profile, in addition to the torque profile, the input parameters are the spring's stiffness k, spring preload P, initial cam radius $r_{initial,}$ and if the mechanism uses a roller follower like the one shown in the CAD representations of the mechanism r_{roller}; These parameters are outlined in Table 2.

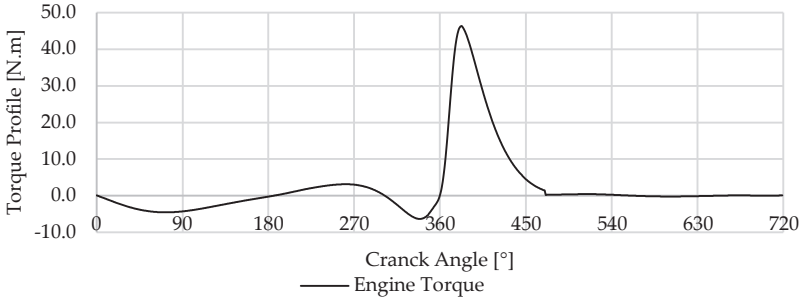

Figure 15. Output torque from single-cylinder engine during idle at 800 RPM, used to design the cam profile.

Table 2. Balancing mechanism parameters.

Cam	Spring
$r_{initial} = 0.05$ m	$k = 100,000$ N/m
$r_{roller} = 0.08$ m	$P = 100$ N

Based on the torque profile outlined, the cam shown in Figure 15 was developed through an iterative process involving the parameters in Table 2 and the torque profile in Figure 15, which shows two cam profiles, one for a follower with and one without a roller. The desired cam profile aimed to maintain a radius not exceeding 50 mm for integration purposes in the specified engine. In Figure 16, the cam analysis shows three distinct zones. Section 1, in the first quadrant, shows the beginning of a cam profile depression, signifying energy release from the spring to the crankshaft, countering the resistive torque during valve opening, and the driving torque of the air-fuel mixture intake. Section 2 highlights a marked decrease in cam radius, associated with compensating the compression process of the air−fuel mixture, with a sharp radius increase towards the end of compression and the start of the expansion. This radius increase continues during the third quadrant, storing energy in the spring from the expansion to utilize during the other strokes. Section 3, located in the fourth quadrant, mirrors the analysis of Section 1, about the exhaust process. Additionally, in Figure 16, a perfect circumference is depicted by a red dotted line, allowing for a comparison between the cam profile variations and a perfect circle profile.

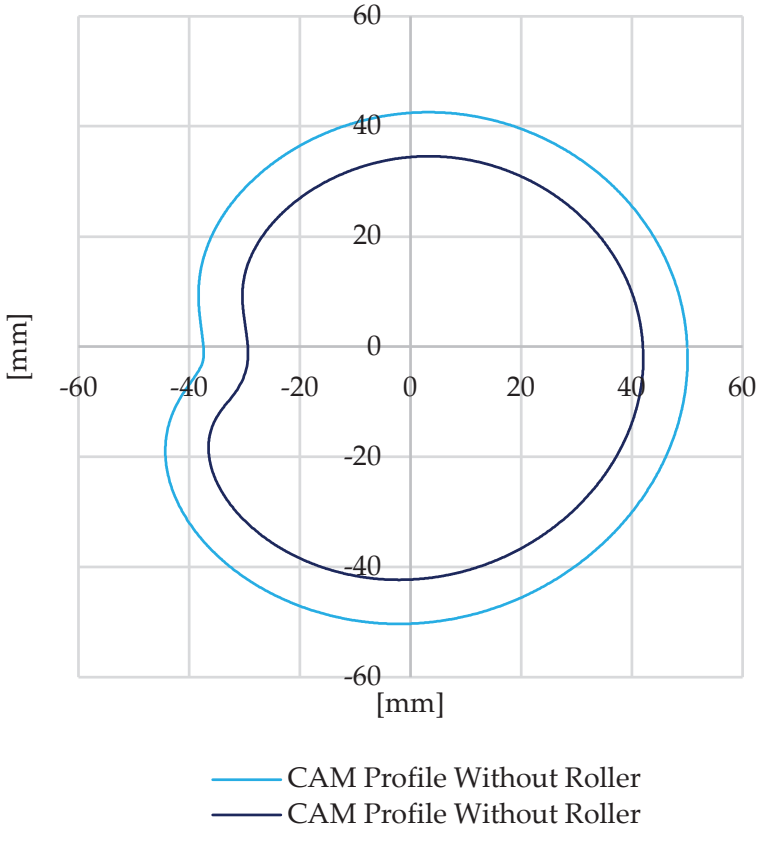

Figure 16. Representation of the determined CAM profile if the follower is with roller or without, considering the torque profile presented previously.

Building upon the previously described cam and maintaining the parameters used for its design, the torque returned by the mechanism to the engine is illustrated in Figure 17. Figure 18 shows the torque delivered from the mechanism into the crankshaft.

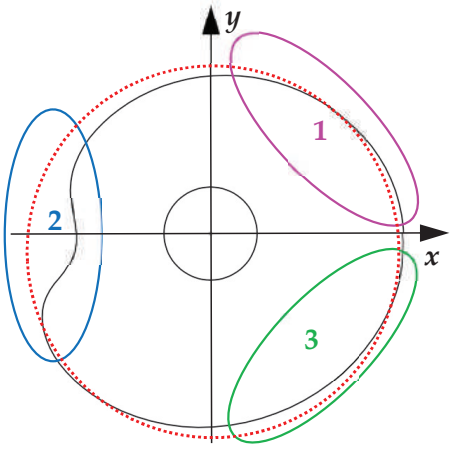

Figure 17. Esquematization of the determined CAM profile, considering the torque profile presented previously.

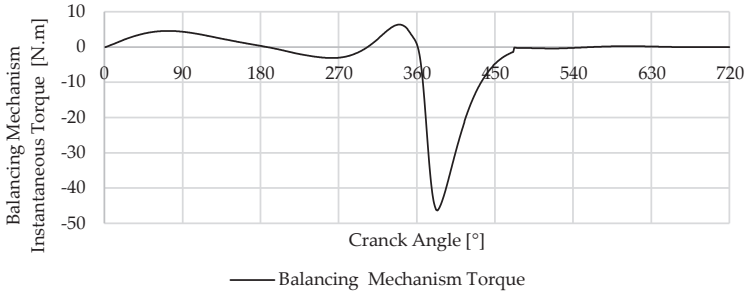

Figure 18. Torque delivered from the mechanism into the crankshaft.

4.3. Balancing Cam Mechanism Integration with the Engine

The integration of the balancing cam mechanism with the engine simulation, as established in Sections 4.1 and 4.2, is detailed in the processes outlined in Figure 19, the flowchart representing the simulation steps. The simulation begins by setting the engine's geometric parameters, initial conditions, and the cam profile for the balancing cam mechanism. The flowchart in Figure 19 tracks the engine cycle through each crank angle φ from 0 to 720 degrees, covering one complete cycle of a four-stroke engine. This encompasses all phases of engine operation: intake, compression, combustion, expansion, and exhaust. During each phase, the simulation calculates various parameters, such as temperatures and pressures within each stroke. These values are crucial for determining the torque and angular speed in each phase. The torque and angular speed calculated by the simulation are then refined by the balancing cam mechanism. This mechanism uses a predefined cam profile and spring parameters to compute the output torque from the mechanism and adjust the engine's simulated torque based on the established initial conditions.

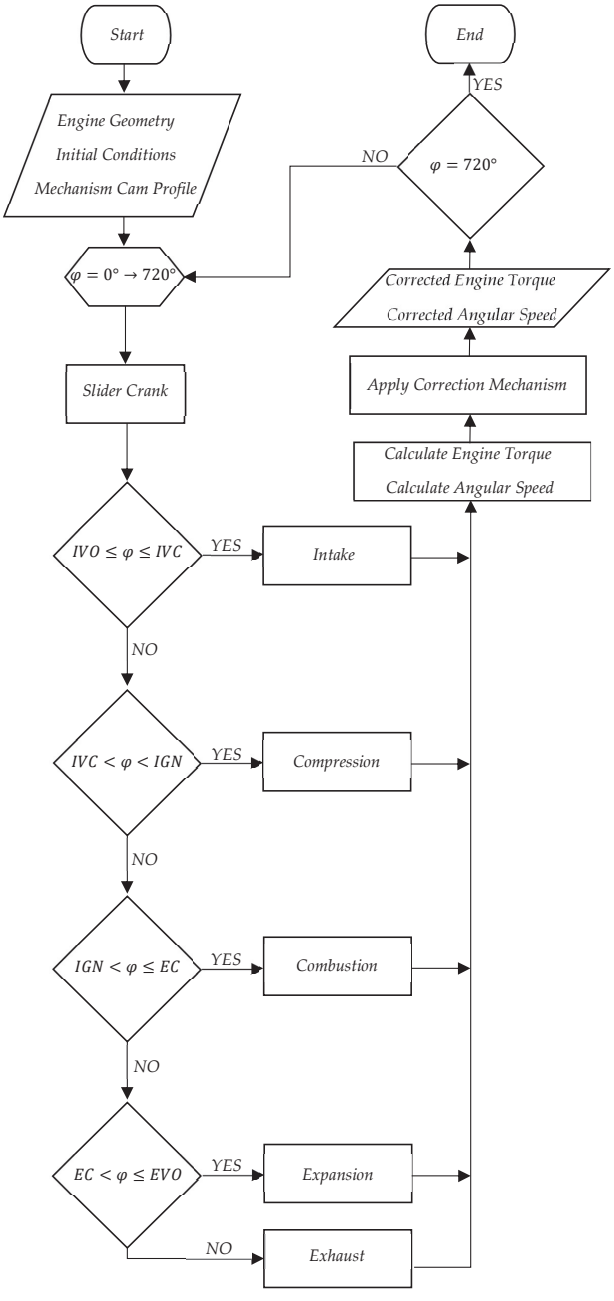

Figure 19. Simulation Flowchart.

The corrections made to the engine torque and angular speed by this integration represent the outputs the simulation aims to achieve. The simulation cycle is documented until the crank angle φ reaches 720 degrees, marking the end of one full engine cycle.

4.4. Simulation Results

The simulations were performed to analyze and determine the distinct characteristics of driving torque, resistive torque, and inertia torque within an internal combustion engine. These types of torque, which have been previously discussed individually, are now collectively examined in Figure 20. This Figure illustrates the engine's output torque profile under the simultaneous influence of driving, resistive, and inertia torque. This comprehensive analysis is crucial as it reveals how the combined effects of these different torques impact the overall performance of the engine. Particularly noteworthy in this idle scenario is that the three types, the torque resulting from the valve mechanism, the inertia of the engine's internal components, and driving torque during intake and exhaust, contribute to the same magnitude for the final engine torque. The variations in engine torque in these conditions are observed during the moments when the piston reaches its extreme positions—the bottom dead center and the top dead center. At these junctures, the piston experiences significant accelerations and decelerations, which in turn influence the directional reversal of its motion. Other variations outcomes from the operation of opening and closing the intake valve approximability from 0 to 180° and the exhaust valve from 540 to 720°, the most pronounced fluctuations from to 180 540° come from the compression and expansion process.

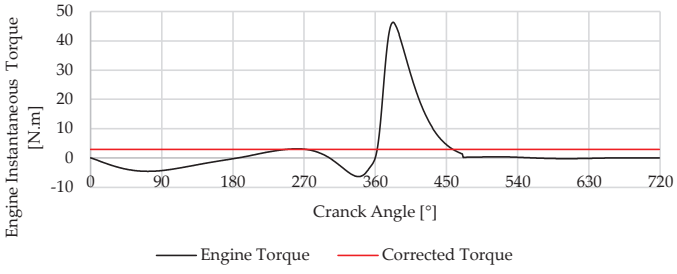

Figure 20. Profile of the engine output torque with the mechanism in red and without the mechanism in black.

In Figure 20, it is possible to observe the overlay of two torque profiles—one from the engine and the other from the mechanism. The computational results assume a loss-free system, indicating that the torque resulting from the system implementation is a consistent profile. This supports the thesis presented, validating the effectiveness of the implemented system in maintaining a stable torque during idle operation.

Torque variations result in corresponding changes in engine speed, which are more noticeable in idle regimes due to the lack of load masking these variations. Figure 21 demonstrates the engine speed variations over a cycle, consistent with the previously analyzed torque variations. As the mechanism suppresses torque fluctuations, it directly impacts reducing speed variations, consequently decreasing vibrations and noise.

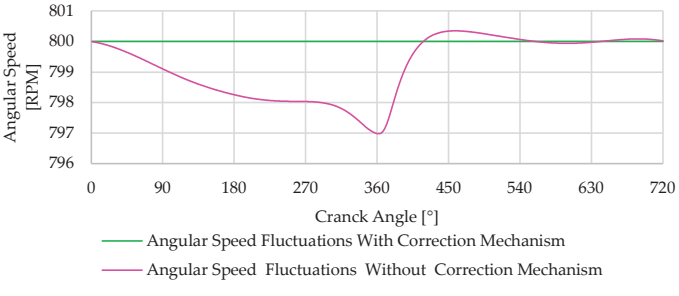

Figure 21. Angular speed variation over the cycle.

4.5. Limitations and Future Work

The need for an energy storage system in ICEs, such as the traditionally used flywheel or the system presented in this work, is more pronounced during low-speed operations or idling. The system developed and designed in this research is specifically tailored to function when the engine is idling. However, as the load imposed on the engine or its rotational speed increases, the influence of this mechanism is lower. To address this limitation, ongoing research efforts are focused on designing a system that can adapt the mechanism to the engine by varying the spring preload based on the engine load and rotation. This adaptation aims to make the system more influential in smoothing the engine's output torque. The development of this system faces several challenges. One significant challenge is that as the engine's rotation speed or load increases, variations primarily occur in the driving torque and inertia torque; consequently, increasing the spring's preload to accommodate these changes can inadvertently amplify the resistive torque correction component from the mechanism, which does not vary under the conditions. This increase in resistive torque, due to the higher preload of the spring, may introduce irregularities in the engine's output torque. Future work will focus on overcoming these challenges by refining the developed cam and the mechanism to balance the varying torque components effectively.

5. Conclusions

This paper introduced a balancing mechanism designed to smooth the output torque of the engine. The torque model proposed for the engine revealed that output torque fluctuations result from a combination of multiple factors, each contributing differently to the final torque produced by the engine. By employing a balancing mechanism with a specifically designed cam profile, the engine operation can be smoothed during idle periods without relying on traditional and heavy flywheels.

The simulations conducted in Section 4 allowed us to study the influence of various factors on engine torque and their actual impact on engine torque. Variations in torque production reflect speed changes throughout the engine cycle, which are responsible for generating vibrations. By developing a system capable of addressing these vibrations, engine operation cannot only be stabilized but also reduce engine mass and the need for energy absorbing dampers.

Although this system does not significantly influence high-speed engine operation, it does not introduce irregularities in the engine's normal functioning. It proves to be an effective solution for correcting engine operation during idling and opens opportunities for developing a system capable of adapting to different engine operating regimes.

Evaluating the performance of our novel mechanism alongside traditional systems like heavy flywheels, we observed notable differences. While flywheels serve well in specific conditions, they do not offer the necessary adaptability and tend to increase the overall weight of the engine system, and inclusively change the engine behavior. On the other hand, our mechanism has the potential to adjust dynamically to meet operational demands and efficiently smooth torque fluctuations with much less impact on engine weight and behavior.

The preliminary results obtained align with those presented in similar studies, albeit for different purposes, such as those by Lin et al. [14] and Arakelian et al. [15], which employ the use of cam-based mechanisms for torque correction. These findings reinforce the validity of our approach and highlight the versatility of cam mechanisms in various engineering applications beyond their traditional uses. By leveraging cam-based designs, we can achieve a consistent correction of torque fluctuations, which is critical for enhancing the operational stability and efficiency of internal combustion engines; this convergence of results across different studies underscores the potential of our proposed mechanism.

This study introduces a unique mechanism for torque harmonization that meets the current and emerging needs of modern engines, emphasizing efficiency and adaptability. Such advancements are instrumental in the development of new technologies, includ-

ing range extenders, microcogeneration systems, and innovative engine configurations, representing a substantial progression in engine technology.

6. Patents

This and subsequent works resulted in a patent application submitted to the Portuguese Institute of Industrial Property (*INPI*) under application number 119346, with the title "Método Implementado por Computador para a Conceção de um Atuador de Equilíbrio para um Motor, Atuador de Equilíbrio, Programa de Computador e Meio de Leitura Associados".

Author Contributions: Conceptualization, D.S.C. and P.O.F.; methodology, D.S.C. and P.O.F.; software, D.S.C. and P.O.F.; validation, P.O.F., P.D.G. and A.E.-S.; formal analysis, P.O.F., P.D.G. and A.E.-S.; investigation, D.S.C. and P.O.F.; data curation, P.O.F.; writing—original draft preparation, D.S.C.; writing—review and editing, D.S.C., P.O.F. and P.D.G.; supervision, P.O.F., P.D.G. and A.E.-S. All authors have read and agreed to the published version of the manuscript.

Funding: This research was funded in part by the Fundação para a Ciência e Tecnologia (FCT) and C-MAST (Centre for Mechanical and Aerospace Science and Technologies) for their support in the form of funding under the project UIDB/00151/2020 (https://doi.org/10.54499/UIDB/00151/2020; https://doi.org/10.54499/UIDP/00151/2020, accessed on 3 January 2024).

Data Availability Statement: Data are contained within the article.

Acknowledgments: We would like to express our gratitude to the Entrepreneurship, Careers, and Alumni Office (GESPA) at the University of Beira Interior for facilitating our collaboration with a company specializing in patent development. We are also thankful to Susana Rodrigues from Inventa, who expertly guided us through the process of writing the patent application.

Conflicts of Interest: The authors declare no conflicts of interest.

References

1. Solmaz, H.; Karabulut, H. A mathematical model to investigate the effects of misfire and cyclic variations on crankshaft speed fluctuations in internal combustion engines. *J. Mech. Sci. Technol.* **2015**, *29*, 1493–1500. [CrossRef]
2. Babagiray, M.; Solmaz, H.; İpci, D.; Aksoy, F. Modeling and validation of crankshaft speed fluctuations of a single-cylinder four-stroke diesel engine. *Proc. Inst. Mech. Eng. Part D J. Automob. Eng.* **2022**, *236*, 553–568. [CrossRef]
3. Cardoso, D.S.; Fael, P.O.; Espírito-Santo, A. Instantaneous angular velocity and torque on Otto single-cylinder engine: A theoretical and experimental analysis. *Energy Rep.* **2020**, *6*, 43–48. [CrossRef]
4. Filipi, Z.S.; Assanis, D.N. A nonlinear, transient, single-cylinder diesel engine simulation for predictions of instantaneous engine speed and torque. *J. Eng. Gas Turbines Power* **2001**, *123*, 951–959. [CrossRef]
5. Antonopoulos, A.K.; Hountalas, D.T. Effect of instantaneous rotational speed on the analysis of measured diesel engine cylinder pressure data. *Energy Convers. Manag.* **2012**, *60*, 87–95. [CrossRef]
6. Munde, K.H.; Mehtre, V.K.; Ware, D.S.; Kamble, D.P. Review on Performance of Dual Mass Flywheel over Conventional Flywheel. *Math. Stat. Eng. Appl.* **2022**, *71*, 496–505. [CrossRef]
7. Dawange, S.V.; Kadlag, V.L. A Review Paper on Vibration Analysis of DI Engine. *Int. J. Sci. Res. IJSR* **2015**, *4*, 759–761.
8. Cardoso, D.; Nunes, D.; Faria, J.; Fael, P.; Gaspar, P.D. Intelligent Micro-Cogeneration Systems for Residential Grids: A Sustainable Solution for Efficient Energy Management. *Energies* **2023**, *16*, 5215. [CrossRef]
9. Mittal, V.; Shah, R.; Przyborowski, A. Analyzing the Usage of Wankel Engine Technology in Future Automotive Powertrains. *SAE Int. J. Sustain. Transp. Energy Environ. Policy* **2023**, *5*, 1–13. [CrossRef]
10. Schaper, U.; Sawodny, O.; Mahl, T.; Blessing, U. Modeling and torque estimation of an automotive Dual Mass Flywheel. In Proceedings of the 2009 American Control Conference, St. Louis, MO, USA, 10–12 June 2009; pp. 1207–1212. [CrossRef]
11. Ayana, E.; Plahn, P.; Wejrzanowski, K.; Mohan, N. Active torque cancellation for transmitted vibration reduction of low cylinder count engines. *IEEE Trans. Veh. Technol.* **2011**, *60*, 2971–2977. [CrossRef]
12. Anjum, R.; Yar, A.; Ahmed, Q.; Bhatti, A. Model-Based Unified Framework for Detection and Mitigation of Cyclic Torque Imbalance in a Gasoline Engine. *J. Eng. Gas Turbines Power* **2021**, *143*, 071013. [CrossRef]
13. Zhang, X.; Liu, H.; Zhan, Z.; Wu, Y.; Zhang, W.; Taha, M.; Yan, P. Modelling and Active Damping of Engine Torque Ripple in a Power-Split Hybrid Electric Vehicle. *Control Eng. Pract.* **2020**, *104*, 104634. [CrossRef]
14. Lin, D.Y.; Hou, B.J.; Lan, C.C. A balancing cam mechanism for minimizing the torque fluctuation of engine camshafts. *Mech. Mach. Theory* **2017**, *108*, 160–175. [CrossRef]
15. Arakelian, V.V.; Briot, S. Simultaneous inertia force/moment balancing and torque compensation of slider-crank mechanisms. *Mech. Res. Commun.* **2010**, *37*, 265–269. [CrossRef]

16. Cardoso, D.S.; Fael, P.O. Simulation and analysis of a switched reluctance machine for flywheel replacement. In *Lecture Notes in Engineering and Computer Science, Proceedings of the World Congress on Engineering 2018, London, UK, 4–6 July 2018*; Springer: Singapore, 2019; pp. 819–823. [CrossRef]
17. Kim, G.W.; Shin, S.C. Research on the torque transmissibility of the passive torsional vibration isolator in an automotive clutch damper. *Proc. Inst. Mech. Eng. Part D J. Automob. Eng.* **2015**, *229*, 1840–1847. [CrossRef]
18. Vehicular Technology Society; Institute of Electrical and Electronics Engineers. Active Torque Ripple Damping in Direct Drive Range Extender Applications: A Comparison and an Original Proposal. In Proceedings of the 2015 IEEE Vehicle Power and Propulsion Conference (VPPC), Montreal, QC, Canada, 19–22 October 2015. [CrossRef]
19. Jianguo, B.; Xudong, L.; Ming, Z.; Kaixiong, L. Design and Optimization for the Main Dimension of Flywheel Motor Based on Torque Density. In Proceedings of the 2018 IEEE 3rd Advanced Information Technology, Electronic and Automation Control Conference (IAEAC), Chongqing, China, 12–14 October 2018; IEEE: New York, NY, USA, 2018; pp. 2156–2162. [CrossRef]
20. Galvagno, E.; Velardocchia, M.; Vigliani, A.; Tota, A. Experimental Analysis and Model Validation of a Dual Mass Flywheel for Passenger Cars. In Proceedings of the SAE 2015 World Congress & Exhibition, Detroit, MI, USA, 21–23 April 2015. [CrossRef]
21. Zhang, Y.; Zhang, X.; Qian, T.; Hu, R. Modeling and simulation of a passive variable inertia flywheel for diesel generator. *Energy Rep.* **2020**, *6*, 58–68. [CrossRef]
22. Fraser, N.; Blaxill, H.; Lumsden, G.; Bassett, M. Challenges for Increased Efficiency through Gasoline Engine Downsizing. *SAE Int. J. Engines* **2009**, *2*, 991–1008. [CrossRef]
23. Hannan, M.A.; Azidin, F.A.; Mohamed, A. Hybrid electric vehicles and their challenges: A review. *Renew. Sustain. Energy Rev.* **2014**, *29*, 135–150. [CrossRef]
24. Cardoso, D.S.; Fael, P.O.; Espírito-Santo, A. A review of micro and mild hybrid systems. *Energy Rep.* **2020**, *6*, 385–390. [CrossRef]
25. Mastrangelo, G.; Micelli, D.; Sacco, D. Extreme Downsizing by the two-cylinder gasoline engine from Fiat. *ATZautotechnology* **2011**, *11*, 18–25. [CrossRef]
26. Omanovic, A.; Zsiga, N.; Soltic, P.; Onder, C. Increased internal combustion engine efficiency with optimized valve timings in extended stroke operation. *Energies* **2021**, *14*, 2750. [CrossRef]
27. Bech, A.; Shayler, P.J.; McGhee, M. The Effects of Cylinder Deactivation on the Thermal Behaviour and Performance of a Three Cylinder Spark Ignition Engine. *SAE Int. J. Engines* **2016**, *9*, 1999–2009. [CrossRef]
28. Kim, C.J.; Kang, Y.J.; Lee, B.H.; Ahn, H.J. Determination of optimal position for both support bearing and unbalance mass of balance shaft. *Mech. Mach. Theory* **2012**, *50*, 150–158. [CrossRef]
29. Guo, J.; Zhang, W.; Zou, D. Investigation of dynamic characteristics of a valve train system. *Mech. Mach. Theory* **2011**, *46*, 1950–1969. [CrossRef]
30. Pfabe, M.; Woernle, C. Reducing torsional vibrations by means of a kinematically driven flywheel—Theory and experiment. *Mech. Mach. Theory* **2016**, *102*, 217–228. [CrossRef]
31. Fan, H.; Jing, M.; Wang, R.; Liu, H.; Zhi, J. New electromagnetic ring balancer for active imbalance compensation of rotating machinery. *J. Sound Vib.* **2014**, *333*, 3837–3858. [CrossRef]
32. Blair, G.P. *Design and Simulation of Four-Stroke Engines*; SAE International: Warrendale, PA, USA, 1999; ISBN 978-0-7680-0440-3.
33. Uicker, J.J., Jr.; Pennock, G.R.; Shigley, J.E. *Theory of Machines and Mechanisms*, 5th ed.; Oxford University Press: New York, NY, USA, 2016; ISBN 9780190264482.
34. Budynas, R.G.; Nisbett, K.J. *Shigley's Mechanical Engineering Design*, 9th ed.; McGraw-Hill: New York, NY, USA, 2010; ISBN 978-0-07-352928-8.

energies

MDPI

Article

Combustion Mechanism of Gasoline Detonation Tube and Coupling of Engine Turbocharging Cycle

Diyun Huang, Jiayong Wang, Minshuo Shi, Puze Yang and Binyang Wu *

State Key Laboratory of Engines, Tianjin University, Tianjin 300072, China; hdytj@tju.edu.cn (D.H.); 1023201121@tju.edu.cn (J.W.); sms_1072@tju.edu.cn (M.S.); yangpz1@tju.edu.cn (P.Y.)
* Correspondence: binyang.wu@tju.edu.cn

Abstract: Traditional exhaust-gas turbocharging exhibits hysteresis under variable working conditions. To achieve rapid-intake supercharging, this study investigates the synergistic coupling process between the detonation and diesel cycles using gasoline as fuel. A numerical simulation model is constructed to analyze the detonation characteristics of a pulse-detonation combustor (PDC), followed by experimental verification. The comprehensive process of the flame's deflagration-to-detonation transition (DDT) and the formation of the detonation wave are discussed in detail. The airflow velocity, DDT time, and peak pressure of detonation tubes with five different blockage ratios (BR) are analyzed, with the results imported into a one-dimensional GT-POWER engine model. The results indicate that the generation of detonation waves is influenced by flame and compression wave interactions. Increasing the airflow does not shorten the DDT time, whereas increasing the BR causes the DDT time to decrease and then increase. Large BRs affect the initiation speed of detonation in the tube, while small BRs impact the DDT distance and peak pressure. Upon connection to the PDC, the transient response rate of the engine is slightly improved. These results can provide useful guidance for improving the transient response characteristics of engines.

Keywords: pulse detonation; deflagration to detonation; blockage ratio; turbine; numerical simulation

Citation: Huang, D.; Wang, J.; Shi, M.; Yang, P.; Wu, B. Combustion Mechanism of Gasoline Detonation Tube and Coupling of Engine Turbocharging Cycle. *Energies* **2024**, *17*, 2466. https://doi.org/10.3390/en17112466

Academic Editors: Wenbin Yu and Guang Zeng

Received: 9 April 2024
Revised: 9 May 2024
Accepted: 18 May 2024
Published: 22 May 2024

1. Introduction

When an engine steps from a low load to a high load, because of the hysteresis of the response to the exhaust gas turbocharger, the intake charge becomes far too low to produce the required acceleration, which seriously worsens the engine's performance and may cause the engine to stall [1]. Therefore, improving the turbocharger's transient response capability is the key to improving the acceleration performance of the engine. Pulse detonation combustion approximates constant volume combustion and is characterized by a fast combustion rate and a small entropy increase [2–4]. It can obtain high-temperature and high-pressure working fluid in an extremely short time, provide additional energy for the exhaust gas turbocharger, promote the rapid rotation of the turbine to supply sufficient fresh air for the engine, and enable the engine to switch to the steady operation mode quickly and smoothly through the valve, injection, and other synergistic control.

The pulse-detonation combustor (PDC) is the core component for generating pulse detonation waves. Optimizing the structure of the combustor can effectively enhance the intensity of detonation combustion, thus improving the transient response rate of the engine. The critical technologies of pulse detonation combustion mainly include air intake, detonation, and gas exchange, wherein the fuel atomization and mixing of fuel, the geometry of the detonation combustor, and the composition of the oxidant and the ignition energy each have an important influence on ignition.

Compared with conventional combustion, the conditions for the formation of detonation combustion are more stringent, especially for the control of the temporal and spatial distribution of the mixture and the initial ignition. Therefore, early research on

detonation mainly focused on gaseous fuels such as hydrogen [5–7], methane [8,9], and ethylene [10,11]. However, liquid fuels are typically used in practical applications because gaseous materials are more difficult to store and transport. The structure of liquid-fueled detonation is more complex and much more difficult to control than that of gas-fueled detonation in terms of aspects including but not limited to the initial state of the mixtures (pressure and temperature), the particle parameters (e.g., particle shape, size, and distribution), the complicated multiphysical processes such as droplet breakup, atomization, and evaporation, as well as incomplete mixing of fuel and air [12,13].

Some studies have shown that the activity of liquid fuels is low; therefore, it is necessary to add a certain percentage of high-activity gaseous fuels to liquid fuels [14,15] or to adopt oxygen-enriched [16–18] and preheating [19–21] methods to accelerate the evaporation and atomization of the liquid fuels. Adopting atomizers [22–24] is another common method to improve fuel atomization and mixing. Frolov et al. [25] fabricated a one-meter-long pre-detonator and an air-assisted atomizer to initiate the detonation in the main detonation tube. Wolanski et al. [26] developed a special liquid fuel atomization system that uses preheated air to assist the early evaporation and mixing of liquid fuel to produce a homogeneous fuel–air mixture. Wu et al. [27] used an ultrasonic acoustic atomizer to finely atomize liquid fuel to increase the pre-evaporation degree of liquid fuel.

The installation of obstacles in the detonation tube also plays a key role in the generation of detonation waves. Common forms of obstacles include orifice plates, Shchelkin spirals, and grooves [28,29]. These obstacles can induce strong disturbances during flame propagation, which can enhance the evaporation and mixing rates of fuel, thereby accelerating combustion and heat release [30]. Research has shown that channel length and height, obstacle spacing, and blockage ratio (BR) all have varying degrees of influence on the deflagration-to-detonation transition (DDT) process. Heilbronn et al. [31] and Goodwin et al. [32] investigated the effects of the BR on the flame acceleration process using experimental and numerical methods, and the results showed that a BR between 0.3 and 0.6 will accelerate the DDT process efficiently, and a BR exceeding this interval will cause the DDT distance to increase drastically. Ciccarelli et al. [33] conducted experimental studies on the effects of obstacle spacing and BR on the DDT process, finding that obstacle spacing has a huge effect on the DDT distance at high BR and acquires the shortest DDT distance when obstacle spacing is roughly equal to the pipe diameter. Saeid et al. [34] studied the spatial height ratio (S/H) of the obstacle spacing to the pipe diameter; they found that in inhomogeneous mixtures, detonation could not be triggered in the tube when the S/H was equal to 10 and that the DDT time was considerably reduced when the S/H was reduced to 2.5. Wang et al. [35] investigated the effect of the number of jet obstacles on the DDT process, speculated that there existed an optimal number of jet obstacles, and concluded that the optimal number of jet obstacles may vary with changes in channel size and obstacle spacing. Coates et al. [36] compared the influences of obstacles of different shapes on flame acceleration and found that rectangular obstacles induced the largest flame acceleration. The aforementioned studies suggest that suitable obstacles would accelerate the combustion reaction rate, which in turn would increase the flame speed and pressure, causing the DDT to occur more easily in the PDC.

Recent studies on pulse detonation combustion mainly focused on aero engines and rocket engines [37–39]; therefore, they have adopted the detonation cycle to replace the Brayton cycle to achieve high thermal efficiency and power performance. The main approach used to optimize the DDT process has been optimizing the ignition and the PDC structure. Most of the research objects have been gaseous fuels, and when liquid fuel has been the research object, it has typically been aviation kerosene [40–42]. A series of complex methods have been devised to accelerate the evaporation and atomization process of fuels [43,44]. In this study, we rely on the engine fuel supply system to inject high-pressure fuel directly into the detonation tube so that the fuel is rapidly broken and atomized into tiny particles (particle size < 8.5 μm), which substantially simplifies the multiphysical process of liquid fuel in the volatilization process. For numerical simulation,

most studies have utilized two-dimensional (2D) simulation to reduce the computation time [45–47]; however, in the study of two-phase detonation, the mixing, atomization, and evaporation process of liquid fuel is the key to the formation of combustible mixtures. Computational fluid dynamics (CFD) can simulate the whole process of fuel from injection to mixing with the oxidant, which can provide a comprehensive understanding of how the three-dimensional (3D) detonation structure evolves so as to better optimize the detonation and combustion process. The idea of this study is to provide additional energy to the diesel engine turbine through the high-temperature and high-pressure working fluid discharged by the PDC so that the turbine can obtain enough power to increase the speed of the compressor and exhibit a fast intake response to improve the transient response performance of the heavy-duty diesel engine. At present, research on the synergistic coupling of the pulse detonation cycle and the diesel cycle to improve the transient response of the turbocharger is still scarce.

In this study, based on relevant literature, a numerical simulation is used to optimize the design of the straight tube detonation combustion process, and an implementation scheme for the detonation combustor is proposed. The numerical simulation results are experimentally verified and then imported into the one-dimensional coupling model of the engine equipped with the detonation afterburning module. The model is intended to serve as a design reference to facilitate the improvement in the transient response performance of heavy-duty diesel engines.

2. Materials and Methods

2.1. Computational Models

Figure 1 presents the configuration and meshing of the computational model, in which the lengths of the injection section, premixing section, ignition section, and main detonation section are 135, 104, 131, and 1030 mm, respectively, and the total length of the tube is 1400 mm. The main detonation section of the tube has a diameter of D = 50 mm, eight groups of symmetrically distributed solid obstacles are arranged inside the tube, the gap between the upper and lower obstacles is d = 34 mm, the spaces between obstacles 1–5 are 80 mm each, and the space between obstacles 6 and 7 is 160 mm; moreover, BR is defined as $BR = 1 - d^2/D^2$. For the suppression of flame and pressure wave back-propagation, a conical thrust wall is arranged behind the premixing section. Because the main detonation section is long, the injectors are placed in two different positions to better organize the distribution of the mixture in the tube. Injector 1 is installed horizontally in the front of the injection section, while injector 2 is installed vertically at around the one-third point along the length of the main detonation section. The two injectors are of the same model, and both use an eight-hole fuel injector with a nozzle orifice diameter of 0.169 mm.

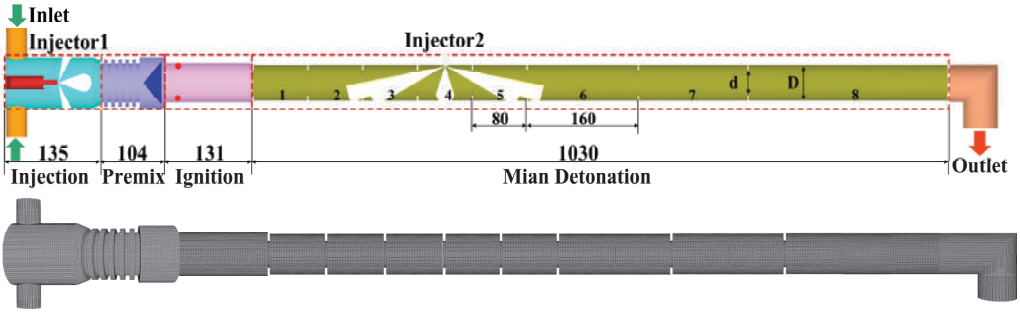

Figure 1. The configuration and meshing of the computational model (unit: mm).

2.2. Computational Numerical Simulation Methods and Boundary Models

The various physical and chemical models used in the computational model are shown in Table 1; the governing equations for all models are solved using CONVERGE. The

characterization fuel of gasoline is isooctane (C_8H_{18}), and the chemical reaction mechanism is a 42-component, 142-step simplified model. In the simulation, the basic grid size is set to 4 mm and is supplemented by an adaptive mesh refinement technique; the minimum grid size is 0.5 mm, and the maximum number of grids is about 1 million.

Table 1. Physical and chemical models of simulation.

Process	Model
Turbulence	RNG k–ε
Spray break	KH-RT
Spray-wall interaction	Rebound/slide
Fuel collision	NTC
Drop evaporation	Frossling
Wall heat transfer	Han and Reitz
Combustion	SAGE chemical reaction solver and simplify chemical reaction mechanism

To ensure that the detonation tube can be filled with fresh air smoothly, the inlet pressure is set to 0.15 MPa, the temperature is 325 K, the outlet pressure is set to 0.1 MPa, and the total temperature is 300 K. Two symmetrically distributed spherical ignition sources, each with a radius of 1 mm, are set up at 26 mm from the left side of the main detonation tube; the ignition energy is 1 J, and the ignition pulse width is 5 ms. The spray cone angle of the injector is 149°, and the injection pressure is 100 MPa.

To make the mixture distribution in the detonation tube more uniform, the fuel quantity of injector 1 is set to 150 mg, that of injector 2 is set to 110 mg, and the injection interval between the two injectors is 6 ms. According to the pulse detonation cycle process, the detonation combustion can be divided into five stages:

1. Intake stage: the intake valve is opened, allowing fresh air to flow into the detonation tube to provide oxidants for subsequent detonation combustion, which is usually carried out at the same time as the purge process.
2. Injection stage: the injector is opened, and fuel mixes with the fresh air in the tube, driven by the airflow and compression wave successively dispatched into the ignition section and the main detonation section.
3. Ignition stage: high-energy igniter discharge instantly ignites the mixture near the spark plug, and a compression wave causes the initial flame to travel into the main detonation section.
4. DDT stage: flames form and propagate, and deflagration gradually transitions to detonation in the tube.
5. Purge stage: the intake valve is reopened, and the exhaust gas in the pipe is discharged by fresh air to prepare for the next detonation.

2.3. Experimental Validation

The experimental setup for the pulse detonation system, detailed in Figure 2, is mainly composed of a control system, an acquisition system, an air intake system, a fuel system, and an ignition system. Among them, the detonation tube used in the experiment is designed in reference to the model parameters in Figure 1, with air flowing vertically into the tube from the side of the injection section and an overall equivalence ratio of about 1.06. The liquid fuel used in the test is gasoline with an octane number of 92, the approximate fuel is C_8H_{16}, and the oxidant is air. The Chapman–Jouguet (CJ) detonation pressure and detonation wave speed are 1.88 MPa and 1796.4 m/s [48], respectively, and the gasoline/air equivalence ratio is 1. According to two-phase detonation research [49], there is a certain loss of detonation wave when using liquid-fueled detonation. Hence, when the peak pressure is up to 80% of the CJ detonation pressure (1.5 MPa), and the detonation wave speed is up to 65% of the CJ detonation wave velocity (1168 m/s), the detonation is considered successful.

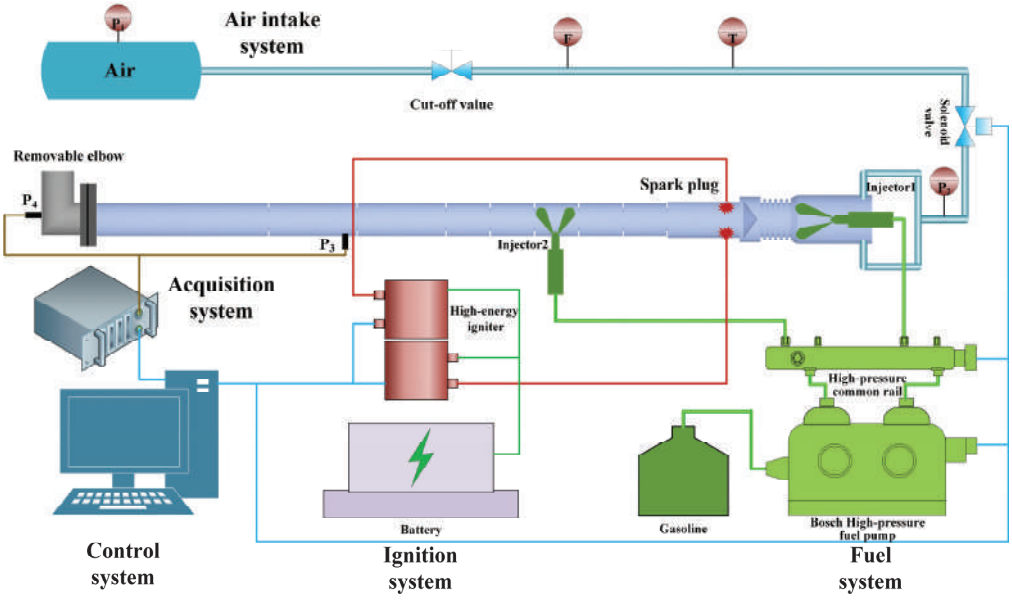

Figure 2. Schematic of the experimental setup for the pulse detonation system.

The control system, developed independently by our research group, can control the whole process of intake, fuel injection, and ignition constantly and accurately. The acquisition system is a self-editing module based on the LabVIEW platform, which allows the number and frequency of acquisition to be freely adjusted according to demand; consequently, the pressure fluctuation in the detonation tube can be accurately collected. To detect whether a detonation wave is generated in the detonation tube, three pressure sensors are set up in the intake section and the main detonation section. A dynamic piezoresistive pressure sensor P_2 with a range of 0–2 MPa is installed at the intake inlet to monitor the intake pressure in the detonation tube. Two Kistler6125C (Kistler, Switzerland) piezoelectric sensors (P_3–P_4), each with a range of 0–30 MPa, are installed on the outer wall of the main detonation section to detect the triggering and development process of the detonation wave in the tube. As shown in Figure 2, P_3 is installed at the head of the seventh section, and the distance to the end of the tube is 450 mm. To measure the total pressure of the detonation tube at the gas outlet, an L-shaped elbow is added to the end of the detonation tube, and the piezoelectric sensor P_4 is placed on the wall facing the burning gases. For the fuel system, the Bosch high-pressure common rail system is utilized to provide high-pressure fuel to both injectors, and the ignition system uses two high-energy igniters driven by 24 V batteries to provide 1 J of ignition energy to each of the spark plugs. All dynamic data of the test are acquired by a NIUSB6259 (National Instruments, Austin, TX, USA) high-speed data acquisition card with thirty-two channels (single channel sampling rate of 1.25 MS/s) and a sampling frequency of 2×10^4 MS/s.

Figure 3 presents a comparison of the trend of detonation pressure curves obtained via a numerical simulation and an experiment under a single detonation with an inlet air pressure of 0.15 MPa. It can be seen from the figure that the peak pressure and change trend of the two curves are basically consistent. The peak pressure of the test is 2.1 MPa, which satisfies the characteristics of detonation. However, there is a certain error in the simulation and test data during the pressure drop stage because the piezoelectric sensor has the inherent characteristics of return hysteresis. In summary, it can be considered that the numerical simulation in this paper can reflect the ignition and detonation process of PDC and can be used to study different parameters.

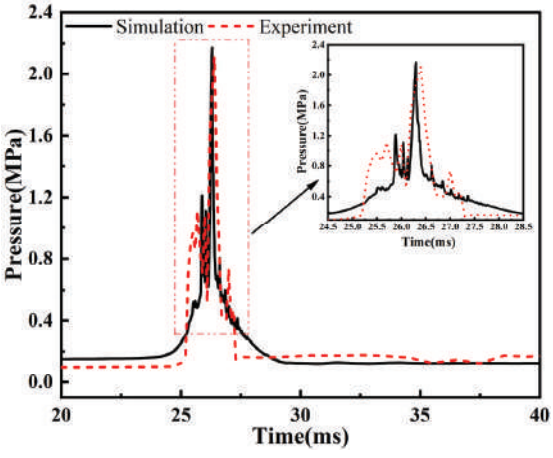

Figure 3. Comparison of detonation pressure between the experiment and numerical simulation.

3. Results

3.1. Process Analysis of the Injection to Ignition Stage

The development process of the mixture is shown in Figure 4. Injector 1 sprays most of the fuel near the wall of the tube. As a result of the impact, a plurality of vortex clusters is formed close to the wall; moreover, the fuel is continuously rolled backward by the airflow and then enters the premixing section. There is weak airflow movement in the small grid near the wall of the premixing section, which can largely prevent the fuel from adhering to the wall. The fuel pauses briefly after contacting the conical body, and the flow of the mixture through the conical body becomes more uniform under the push of the airflow, which can effectively reduce the fuel concentration zone. Subsequently, the mixture quickly passes through the conical body and reaches the ignition point of the spark plug, at which time the mixture exhibits an approximately equivalent distribution.

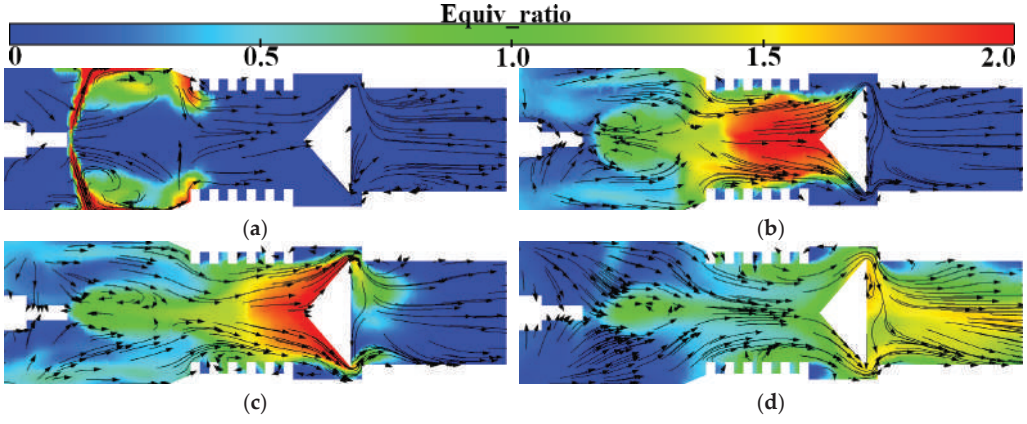

Figure 4. Process of fuel injection and mixing: (**a**) distribution of mixture equivalence ratio and flow field (t = 13 ms); (**b**) distribution of mixture equivalence ratio and flow field (t = 15 ms); (**c**) distribution of mixture equivalence ratio and flow field (t = 18 ms); (**d**) distribution of mixture equivalence ratio and flow field (t = 20 ms).

Figure 5 shows the development of the mixture and flame in the ignition section during the ignition stage (t = 18–23 ms). As shown in Figure 5a, at the initial stage of ignition (t = 18 ms), the mixture in the ignition section exhibits a distribution wherein the middle

is concentrated, and the surroundings are dilute because of the faster flow velocity near the gap between the conical body and the wall. In contrast, it can be seen from Figure 5b,c that the airflow movement is relatively slow at the wall near the spark plug, which can favor the stable formation of the initial flame kernel. The development of the flame front is basically consistent with the contour of the chemical equivalent ratio, and it gradually moves from the periphery to the middle. Afterward, because of the airflow movement of the compression wave, the flame kernel is driven forward continually, passing through the first obstacle at t = 20.4 ms and gradually entering the main detonation tube.

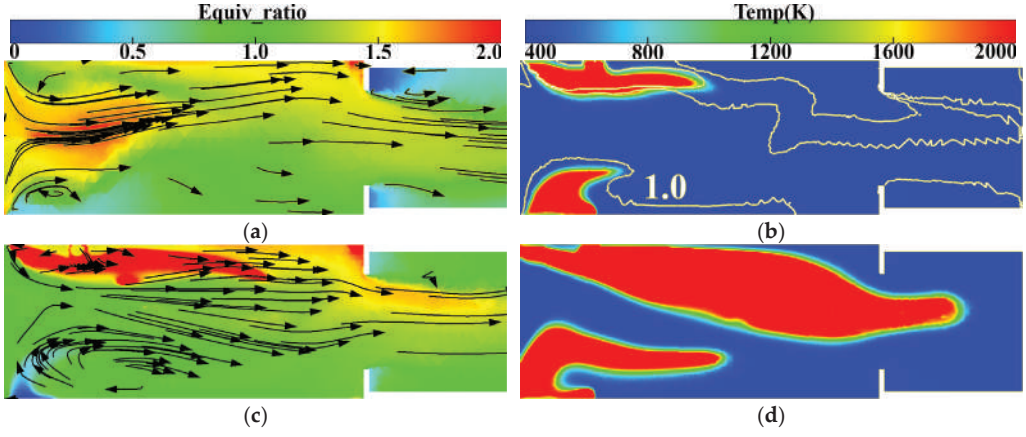

Figure 5. Process of ignition and the initial formation of flame: (**a**) distribution of mixture equivalence ratio and flow field (t = 18 ms); (**b**) distribution of mixture temperature and equivalence ratio contour lines (t = 19 ms); (**c**) distribution of mixture equivalence ratio and flow field (t = 20 ms); (**d**) distribution of mixture temperature (t = 20.4 ms).

3.2. Process Analysis of Flame Acceleration-to-Detonation Transition and Detonation Wave Development

When the flame enters the main explosion section, owing to the presence of obstacles, the high-temperature airflow is often blocked and compressed when it flows around the obstacles, resulting in a sudden rise in the compression wave. As shown in Figure 6a, the initial compression wave is mainly distributed in the tube wall and near the flame front, where the compression wave sweeping through will cause a sudden change in the thermodynamic state of the unburned gas (i.e., the pressure, temperature, and density will all increase), which will intensify the combustion of the flame, increase the heat release, and ultimately enable the flame to propagate at a faster speed. In the meantime, the increase in flame speed will enhance the strength of the compression wave, thus creating a feedback mechanism for flame acceleration. This feedback mechanism makes the distance between the flame front and the compression wave gradually decrease, as shown in Figure 6c, and finally, at t = 24.7 ms, at the end of the sixth section of the main detonation tube, the flame front and the leading shock wave coincide. The state of the compression wave in the tube at this time with the influence of the obstacles is shown in Figure 6e; the trend of airflow in the tube is fast in the middle and slow in the periphery, so its velocity profile is a "bullet" type. The shock wave velocity can reach 718 m/s, which is a form of flame propagation before the detonation wave is triggered. Subsequently, the high-temperature flame surface (T > 2500 K) expands rapidly in the tube, accelerated by the obstacles and coupled with high-temperature, high-pressure reactants. The "detonation wave kernel" is formed at the front end of the obstacle in the seventh section, corresponding to the initial state of detonation wave formation, as depicted in Figure 6d,f. At this point, the velocity of the detonation wave reaches 1283 m/s, with a peak pressure of 0.56 MPa.

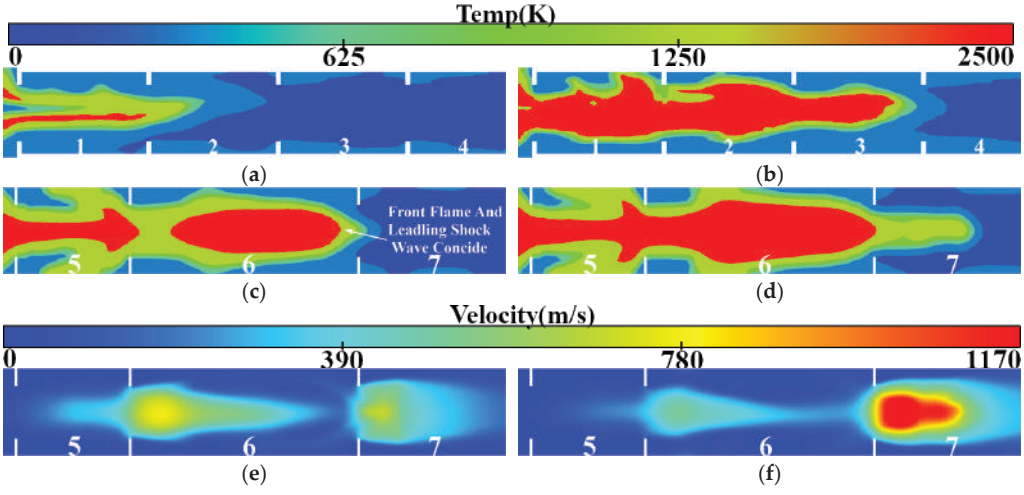

Figure 6. Process of flame acceleration and detonation initiation: (**a**) distribution of mixture temperature (t = 23 ms); (**b**) distribution of mixture temperature (t = 24 ms); (**c**) distribution of mixture temperature (t = 24.7 ms); (**d**) distribution of mixture velocity (t = 24.7 ms); (**e**) distribution of mixture velocity (t = 24.7 ms); (**f**) distribution of mixture velocity (t = 24.8 ms).

Once formed, the detonation shock wave will propagate to both ends. However, owing to the presence of a larger amount of unburned high-temperature and high-pressure mixture downstream, the initial detonation shock wave exhibits a conical shape and expands further downstream. As depicted in Figure 7a, detonation waves are observed in sections 7 and 8 of the tube at t = 25.1 ms. Notably, the trigger mechanisms for these two detonation waves are entirely different. The first detonation wave originates from the progressive acceleration of the flame, leading to the combustion flame's DDT; in contrast, the second detonation wave arises from the direct detonation of high-temperature and high-pressure reactants due to shock wave-wall interactions. Figure 7b shows that the high-temperature and high-pressure reactants at the front end of the eighth section are reignited after touching the leading shock wave near the wall and react rapidly to form a new detonation wave. In comparison to the first shock wave, both the initiation time and distance of the second shock wave are significantly reduced, causing the generation speed of the second detonation wave to be greater than the attenuation speed of the first detonation wave. Consequently, multiple detonations occur within the tube. This phenomenon effectively retards decoupling between shock waves and reaction surfaces during the transmission process while inhibiting downstream back transmission of detonation waves, thereby ensuring stable propagation.

As can be seen from Figure 7c, the decay of the seventh section of the detonation wave results in further augmentation of the velocity and sweep range of the detonation wave in the eighth section, which continues to propagate downstream. Figure 7d demonstrates that at t = 25.3 ms, a high-temperature flame overspreads the detonation tube within the seventh section. At this juncture, the velocity of the detonation wave inside the tube can reach up to 1950 m/s while achieving a maximum burst pressure of 1.98 MPa. Moreover, it is observed that there is a transition in the shape of the detonation wave front from conical to horizontal forward propulsion. The detonation wave reaches the exhaust outlet at t = 25.5 ms, as depicted in Figure 7e. Because of a sharp pressure drop when it reaches the outlet, a smaller range of detonation waves is generated near the outlet of the PDC. This substantial pressure difference leads to a surge of the wave velocity at the outlet, with maximum speeds reaching up to 2033 m/s. Simultaneously, the pressure of the detonation wave in the tube begins to decrease, with a peak pressure of 0.8 MPa. Because there is no

combustible mixture at the leading edge of the PDC, the generation of new detonation waves becomes unattainable. Subsequently, after 0.5 ms, the velocity of the detonation wave drops below 1000 m/s and gradually attenuates until it reaches a stable state.

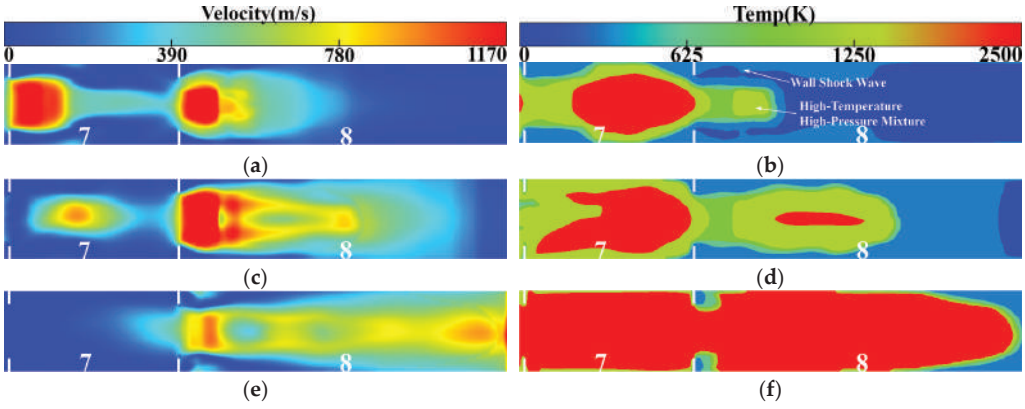

Figure 7. Process of flame and detonation wave propagation: (**a**) distribution of mixture velocity (t = 25.1 ms); (**b**) distribution of mixture temperature (t = 25.1 ms); (**c**) distribution of mixture velocity (t = 25.3 ms); (**d**) distribution of mixture temperature (t = 25.3 ms); (**e**) distribution of mixture velocity (t = 25.5 ms); (**f**) distribution of mixture temperature (t = 25.5 ms).

The aforementioned section provides a comprehensive description of the process involving the formation, ignition, and detonation of the gasoline–air mixture within a tube containing obstacles. To further enhance the optimization of the PDC structure, an analysis is conducted on the BR parameters of the detonation tube based on this foundation.

3.3. Effect of Different BRs on Detonation and Combustion Characteristics of the Detonation Tube

The BR is an important parameter that affects the detonation in the detonation tube. Figure 8 illustrates the gas flow velocities and the DDT times of five different detonation tubes with BRs of 0.3 to 0.7 at the moment of ignition (t = 18 ms). Moreover, this figure clearly demonstrates the considerable impact of BR on gas flow velocity within the detonation tube. A higher value of BR corresponds to a slower gas flow rate in the tube. The gas flow velocity greatly affects the diffusion rate of the fuel particles, thereby influencing the distribution of the mixture throughout the tube.

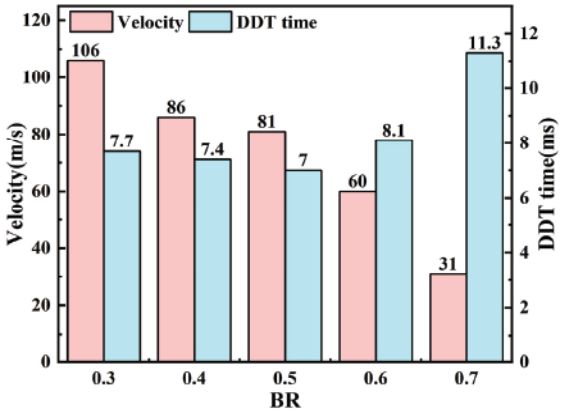

Figure 8. The airflow velocity and DDT time vary with BR.

High BR results in considerable resistance in the tube, which affects the development and step of the compression wave, leading to a substantial increase in the required DDT time. However, the DDT time does not exhibit a monotonic increase as BR decreases; on the contrary, it exhibits a trend of initial decrease and subsequent increase. The minimum DDT time occurs when the BR is approximately 0.5, and the DDT time at BR = 0.7 is 61% higher than that at BR = 0.5. High BR considerably impacts the detonation speed of the detonation tube.

Notably, BR also exerts an influence on the DDT distance of the detonation tube. As depicted in Figure 9a, when the BR ranges from 0.4 to 0.7, the DDT distance remains relatively consistent, with detonation occurring at the onset of the seventh obstacle. Conversely, when BR is 0.3, detonation occurs at the onset of the eighth obstacle and results in the furthest DDT distance, indicating that a low BR has a greater impact on the detonation distance of the DDT.

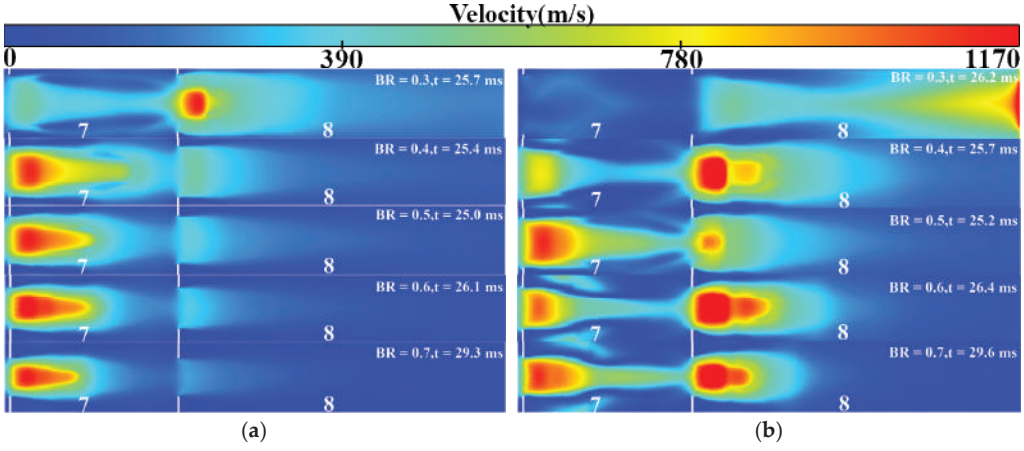

Figure 9. DDT distance and detonation wave distribution vary with BR: (**a**) DDT distance at different BRs; (**b**) distribution of detonation wave at different BRs.

The analysis presented in Figure 9b investigates multiple detonation phenomena in the tube with different BRs. Multiple detonation phenomena are not observed in the tube when the BR ranges from 0.3 to 0.5, and the detonation wave is directly propagated from the beginning of the eighth section to near the outlet when the BR is 0.3. However, for BRs of 0.4 or 0.5, only one detonation wave is generated in the tube; a shock wave is also generated, but its velocity is lower than $0.67V_{CJ}$ (780 m/s), which does not reach the velocity of a detonation wave. When the BR increases to 0.6–0.7, two detonation waves are generated within the tube.

Results demonstrate that the propagation mechanism of detonation waves in the tube with continuous obstacles remains consistent. The detonation wave in the process of traversing obstacles will exhibit attenuation, failure, and re-initiation of the phenomenon. This can be attributed to the fact that the detonation wave is a shock wave coupled with a chemical reaction and that the law of its development through the obstacles is similar to the law of shock wave diffraction in the obstacles. In other words, as airflow passes through the tiny concave corner, compression waves are generated due to the blockage. The magnitude of these compression waves is influenced by both airflow velocity and obstacle shape. Therefore, during the initiation stage of the detonation wave, which involves the interaction between the flame and the shock wave, the turbulence effect does not play a leading role. This also explains why the DDT time does not decrease with the increase in airflow movement. Specifically, the generation and propagation of detonation waves are

jointly determined by interactions among flames, the leading shock wave, obstacles, and local geometric conditions.

The peak pressure and instantaneous heat release rate curves of five different detonation tubes with BRs ranging from 0.3 to 0.7 are depicted in Figures 10a and 10b, respectively. It can be observed from Figure 10a that as BR increases, the peak pressure of the detonation tube exhibits an initial increase followed by a decrease. Notably, the detonation tubes with BRs of 0.5 and 0.6 demonstrate relatively high peak pressures. When the BR is 0.3, the fuel particles disperse rapidly due to the high flow velocity in the tube, which is unfavorable to the formation of a stable initial fire core. Moreover, owing to little obstacle blockage, there is weak disturbance and a small area affected by compression waves, resulting in a negligible impact on the unburned gas state and minimal overall heat release. When the BR is 0.7, although the DDT time is prolonged, the peak pressure of the detonation wave remains high. This can be attributed to low airflow velocity within the tube impeding flame propagation speed and causing slow development of the detonation wave during its formative stage.

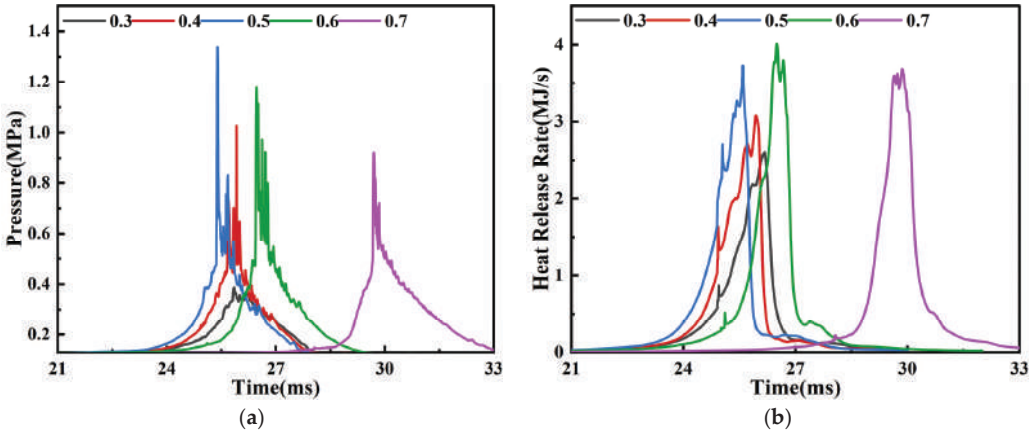

Figure 10. Pressure and heat release rate vary with BR: (**a**) pressure at different BRs; (**b**) heat release rate at different BRs.

The heat release time in the tube becomes longer as the BR decreases, as depicted in Figure 10b. Conversely, as the BR increases, the heat release becomes more concentrated. Although the peak heat release values are higher when BR = 0.6 and 0.7, the maximum pressure is lower than when BR = 0.5. This is because increasing the BR increases the resistance and results in a certain pressure loss within the tube, which emphasizes that detonation wave triggering is a consequence of flame and compression wave interaction. The DDT time is observed to be the shortest and the pressure to be the largest when the BR is 0.5, as depicted in Figure 10a,b. Deviating from this optimal value of BR (in the positive or negative direction) will adversely affect both the fuel particle diffusion speed (making it either excessively slow or fast) and the compression wave magnitude. Even with adjustments made to ignition and injection timing, satisfactory results will not be achieved, and some problems will arise, such as diminished heat release and prolonged detonation cycle time. Through optimization, it has been determined that the optimal DDT time is 6.7 ms, and the peak pressure is 2.2 MPa when the BR of the detonation tube is 0.54.

3.4. Effect of the Detonation Tube Coupled Exhaust Gas Turbine on Diesel Engine Performance

To investigate the impact on the engine performance after accessing the pulse detonation tube, a one-dimensional engine model is constructed based on the GT-POWER platform, which mainly includes cylinders, a supercharging system, an intercooling system,

and a detonation afterburning module. The engine's operating parameters are presented in Table 2.

Table 2. GT-POWER simulation engine parameters.

Item	Value	Unit
Cylinder number	6	-
Bore	126	mm
Stroke	155	mm
Speed	700	r/min
Compression rate	17	-
Displacement	11.6	L
Air intake method	Turbocharged, intercooled	-
Nozzle number × diameter	8 × 0.217	mm

The engine employs a variable-geometry turbocharger. The total outlet pressure and pulse flow from a previous acquisition of the detonation tube are imported at the environmental boundary of the afterburning module e300-2 to drive the turbine and compressor together with the exhaust gas discharged from the engine. The combined cycle arrangement according to GT-POWER is illustrated in Figure 11.

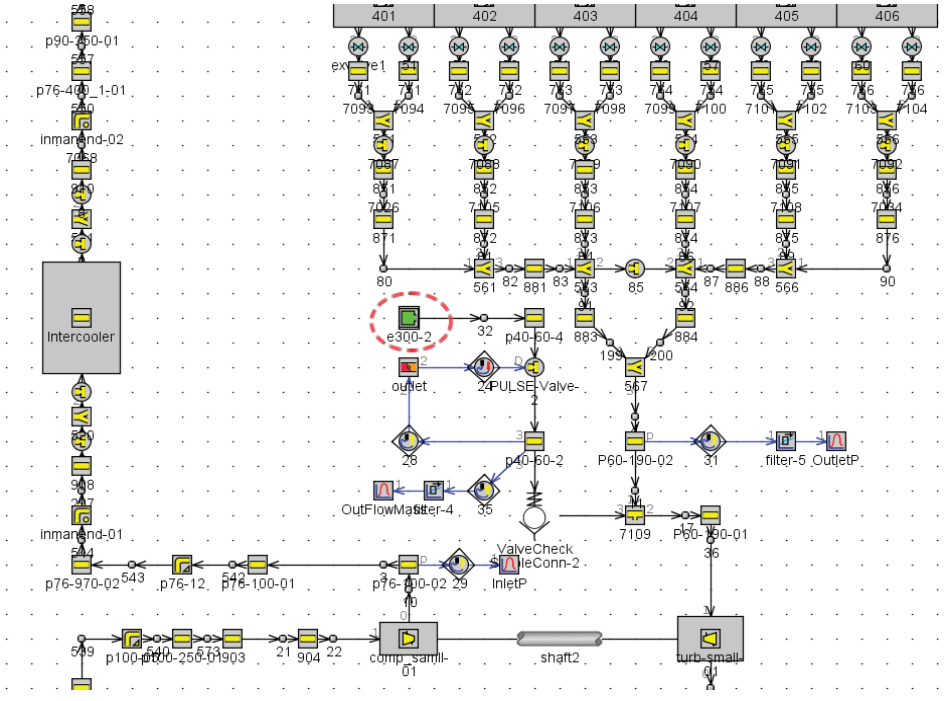

Figure 11. GT-POWER model layout.

The engine's constant speed is set at 700 r/min. From 0 to 5 s, the engine operates in an idle state with a constant fuel quantity of 35 mg. At 5 s, the fuel quantity begins gradually increasing and reaches its maximum value of 212 mg after 0.5 s. At this time, the outlet pressure and pulse flow of the detonation tube at a frequency of 7 Hz are inputted into the e300-2 module of the GT engine model.

Figure 12 presents the transient response abilities of the original engine and the engine connected to the detonation tube, with a variable-geometry turbocharger (VGT) blade

opening of 0.55. As depicted in the figure, it takes 13.3 s for the original diesel engine to achieve an intake pressure of 1.4 bar; however, when the PDC is connected to supply exhaust gas to the turbine, this response time is shortened to 8.2 s, a reduction of 38.3%. This clearly indicates that connecting the PDC significantly improves the compressor supercharging response and yields outstanding supercharging effects.

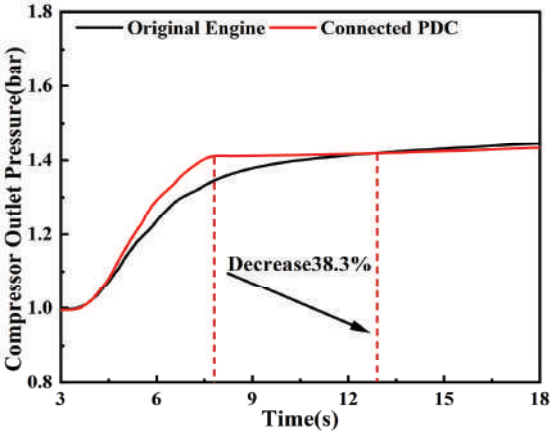

Figure 12. Comparison of compressor outlet pressure between the original engine and connected PDC at a VGT opening of 0.55.

The PDC also demonstrates a certain effect in enhancing the engine's transient response performance. Figure 13 illustrates the impact curve of the PDC outlet's exhaust gas flow on the engine's intake flow and torque at a turbine VGT blade opening of 0.55. It is evident that, under the current VGT setting, connecting the PDC results in a reduction of 1.1 s (approximately 11%) in response time when the intake flow reaches 65 g/s compared to the original engine. Meanwhile, when the engine torque increases to 1600 Nm, it only takes 5.9 s, which is about 11% shorter than the original engine's response time.

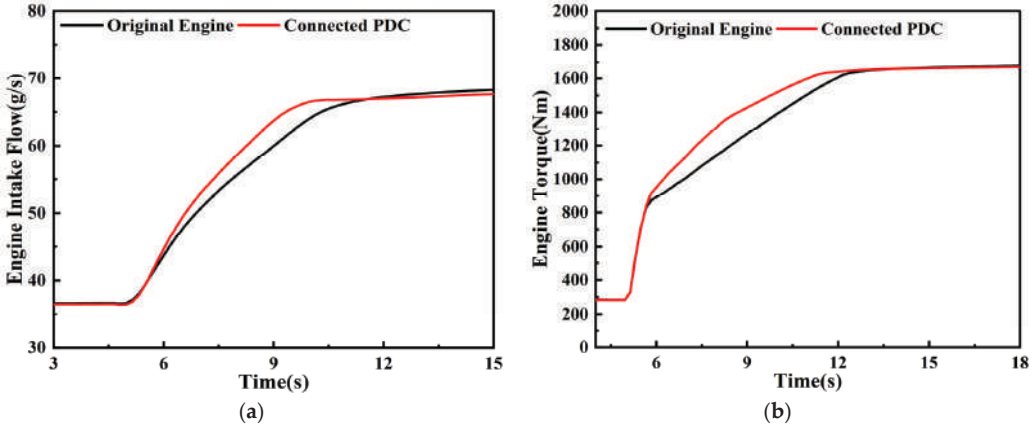

Figure 13. Comparison of transient response performance between the original engine and connected PDC: (**a**) engine intake flow response; (**b**) engine torque response.

From the aforementioned results, it can be concluded that the engine will experience a substantial improvement in the transient response of intake supercharging when the detonation combustion tube is installed. With an appropriate VGT opening, the engine

intake supercharging response time can be effectively shortened, which can meet the transient demand of the engine under special working conditions. These results provide insights and numerical references that will be valuable for improving the transient operating efficiencies of engines.

4. Conclusions

In this study, the detonation characteristics of high-pressure direct-injection gasoline–air mixtures in a long straight detonation tube are investigated using numerical simulations, the effects of different BRs on flame acceleration and the DDT process are determined, and an efficient PDC structure is established. The exhaust gas generated by the PDC is further used to promote turbine operation, effectively compensating for the problem of turbocharging delay and quickly realizing the purpose of pressure boost and intake volume adjustment. This study is intended to serve as a design reference to facilitate the improvement in the transient response performance of heavy-duty diesel engines. The key conclusions are as follows:

1. In the ignition stage, the formation of the initial flame kernel is significantly influenced by the local airflow velocity and the mixture equivalent ratio, while flame development predominantly follows the chemical equivalent ratio contour. In the flame acceleration stage, turbulent flow and compression waves synergistically promote flame propagation, establishing a feedback mechanism for flame acceleration. During the detonation wave development stage, detonation is triggered by one of the following two mechanisms: one involves detonation resulting from the coupling between flames and shock waves, and the other entails direct detonation initiated by collision and reflection of compression waves with the wall.
2. The detonation mechanism of a detonation wave remains fundamentally consistent across varying BRs, but as the BR increases, the airflow in the tube slows, and the DDT time decreases and then increases. DDT time is 61% higher when the BR is 0.7 than when the BR is 0.5, indicating that a high BR seriously impacts detonation velocity and results in substantial pressure loss. When the BR is 0.54, the DDT time is the shortest at 6.7 ms. The BR has less effect on the DDT distance, but a low BR will prolong the DDT distance.
3. When BR $\leq$ 0.5, there are not two types of detonation waves in the detonation tube, indicating that an excessively small BR will affect the strength and range of the compression waves. At this time, the blockage in the tube is small, high-strength leading shock waves cannot be formed, and the interaction between shock waves and the wall surface is insufficient to directly initiate detonation. The flames, compression waves, and local geometric conditions collectively determine the generation and propagation of detonation waves, and re-initiation will occur under appropriate conditions.
4. When the PDC exhaust gas flow is connected to the turbine, the VGT blade opening is 0.55, the intake air is supercharged to 1.4 bar, the response time of the compressor is 5.1 s shorter than that of the original engine, and the response rate is increased by 38.3%. Moreover, the time required for the engine to reach its rated torque of 1600 Nm decreases from 7 s to 5.9 s, indicating that the PDC can effectively improve the transient acceleration response process of the diesel engine and provide sufficient intake air charge for the diesel engine in a short time.

Author Contributions: Writing—original draft preparation, D.H.; writing—review and editing, B.W.; validation, J.W.; investigation, M.S. and P.Y. All authors have read and agreed to the published version of the manuscript.

Funding: This research was funded by the National Defense Science and Technology Key Laboratory Foundation Program, grant number 6142212210205.

Data Availability Statement: The data presented in this study are available on request from the corresponding author. The data are not publicly available due to privacy.

Conflicts of Interest: The authors declare no conflicts of interest.

References

1. Shi, Y.; Zheng, G.; Chen, H.; Wang, L. Transient Behavior Study of HD Diesel Engine and the Effects of Turbochargers. In *Proceedings of the FISITA World Automotive Congress*; Lecture Notes in Electrical Engineering; Springer: Berlin/Heidelberg, Germany, 2013; Volume 190. [CrossRef]
2. Roy, G.D.; Frolov, S.M.; Borisov, A.A.; Netzer, D.W. Pulse detonation propulsion: Challenges, current status, and future perspective. *Prog. Energy Combust. Sci.* **2004**, *30*, 545–672. [CrossRef]
3. Liu, J.Y.; Wang, Z.W.; Zhang, Z.X.; Li, J.L.; Qin, W.F.; Huang, J.J. Reheat effect on the improvement in efficiency of the turbine driven by pulse detonation. *Def. Technol.* **2024**, *31*, 200–210. [CrossRef]
4. Anand, V.; Gutmark, E. Rotating detonation combustors and their similarities to rocket instabilities. *Prog. Energy Combust. Sci.* **2019**, *73*, 182–234. [CrossRef]
5. Jin, S.; Qi, L.; Zhao, N.B.; Zheng, H.T.; Meng, Q.Y.; Yang, J.L. Experimental and numerical research on rotating detonation combustor under non-premixed conditions. *Int. J. Hydrogen Energy* **2020**, *45*, 10176–10188. [CrossRef]
6. Wang, Z.W.; Qin, W.F.; Huang, J.J.; Wei, L.S.; Yang, Y.X.; Wang, Y.Q.; Zhang, Y. Numerical investigation of the effect of jet intensity from internal jet tube on detonation initiation characteristics. *Int. J. Hydrogen Energy* **2022**, *47*, 13732–13745. [CrossRef]
7. Zhao, M.J.; Zhang, H.W. Origin and chaotic propagation of multiple rotating detonation waves in hydrogen/air mixtures. *Fuel* **2020**, *275*, 117986. [CrossRef]
8. Luan, Z.Y.; Huang, Y.; Gao, S.J.; You, Y.C. Formation of multiple detonation waves in rotating detonation engines with inhomogeneous methane/oxygen mixtures under different equivalence ratios. *Combust. Flame* **2022**, *241*, 112091. [CrossRef]
9. Peng, H.Y.; Liu, W.D.; Liu, S.J.; Zhang, H.L.; Jiang, L.X. Hydrogen-air, ethylene-air, and methane-air continuous rotating detonation in the hollow chamber. *Energy* **2020**, *211*, 118598. [CrossRef]
10. Wang, G.Y.; Liu, W.D.; Liu, S.J.; Zhang, H.L.; Peng, H.Y.; Zhou, Y.F. Experimental verification of cylindrical air-breathing continuous rotating detonation engine fueled by non-premixed ethylene (vol 189, pg 722, 2021). *Acta Astronaut.* **2022**, *193*, 795–796. [CrossRef]
11. Wang, Y.; Le, J.; Wang, C.; Zheng, Y. A non-premixed rotating detonation engine using ethylene and air. *Appl. Therm. Eng.* **2018**, *137*, 749–757. [CrossRef]
12. Musick, B.J.; Paudel, M.; Ramaprabhu, P.K.; McFarland, J.A. Numerical simulations of droplet evaporation and breakup effects on heterogeneous detonations. *Combust. Flame* **2023**, *257*, 113035. [CrossRef]
13. Wen, H.C.; Fan, W.Q.; Xu, S.; Wang, B. Numerical study on droplet evaporation and propagation stability in normal-temperature two-phase rotating detonation system. *Aerosp. Sci. Technol.* **2023**, *138*, 108324. [CrossRef]
14. Huang, X.X.; Lin, Z.Y. Analysis of coupled-waves structure and propagation characteristics in hydrogen-assisted kerosene-air two-phase rotating detonation wave. *Int. J. Hydrogen Energy* **2022**, *47*, 4868–4884. [CrossRef]
15. Yao, S.B.; Guo, C.H.; Zhang, W.W. Effects of droplet evaporation on the flow field of hydrogen-enhanced rotating detonation engines with liquid kerosene. *Int. J. Hydrogen Energy* **2023**, *48*, 33335–33345. [CrossRef]
16. Ding, C.W.; Wu, Y.W.; Xu, G.; Xia, Y.Q.; Li, Q.; Weng, C.S. Effects of the oxygen mass fraction on the wave propagation modes in a kerosene-fueled rotating detonation combustor. *Acta Astronaut.* **2022**, *195*, 204–214. [CrossRef]
17. Han, X.P.; Huang, Y.K.; Zheng, Q.; Xiao, Q.; Xu, H.; Wang, F.; Wu, Y.W.; Feng, W.K.; Weng, C.S. Study of the characteristics and combustion efficiency of liquid kerosene/oxygen-enriched air rotating detonation wave with different modes. *Fuel* **2024**, *355*, 18. [CrossRef]
18. Zhang, Q.B.; Qiao, X.Q.; Fan, W.; Wang, K.; Tan, F.G.; Wang, J.G. Study on operation and propulsion features of a pulse detonation rocket engine with secondary oxidizer injection. *Appl. Therm. Eng.* **2020**, *180*, 115661. [CrossRef]
19. Ma, Y.; Zhou, S.B.; Ma, H.; Ge, G.Y.; Yu, D.H.; Zou, G.; Liang, Z.T.; Zhang, T.F. Experimental investigation on propagation characteristics of liquid-fuel/preheated-air rotating detonation wave. *Int. J. Hydrogen Energy* **2022**, *47*, 24080–24092. [CrossRef]
20. Qiu, H.; Bai, Q.D.; Han, J.X.; Huang, B.Y.; Liu, Z.Y.; Weng, C.S. Experimental research on self-initiation process of rotating detonation wave by high-temperature ethylene-rich gas. *Fuel* **2024**, *357*, 129795. [CrossRef]
21. Wang, J.S.; Lin, W.; Huang, W.D.; Shi, Q.; Zhao, J.F. Numerical study on atomization and evaporation characteristics of preheated kerosene jet in a rotating detonation scramjet combustor. *Appl. Therm. Eng.* **2022**, *203*, 117920. [CrossRef]
22. Zhao, J.F.; Ren, Y.J.; Tong, Y.H.; Lin, W.; Nie, W.S. Atomization of a liquid jet in supersonic crossflow in a combustion chamber with an expanded section. *Acta Astronaut.* **2021**, *180*, 35–45. [CrossRef]
23. Malik, V.; Salauddin, S.; Hytovick, R.; Bielawski, R.; Raman, V.; Bennewitz, J.; Burr, J.; Paulson, E.; Hargus, W.; Ahmed, K. Detonation wave driven by aerosolized liquid RP-2 spray. *Proc. Combust. Inst.* **2023**, *39*, 2807–2815. [CrossRef]
24. Xu, G.; Wu, Y.W.; Kang, C.H.; Lei, T.; Qiu, Y.M.; Ding, C.W.; Weng, C.S. Propagation behaviors of kerosene-fueled rotating detonation wave with varied atomizer locations. *Aerosp. Sci. Technol.* **2023**, *142*, 108676. [CrossRef]
25. Frolov, S.M. Liquid-fueled, air-breathing pulse detonation engine demonstrator: Operation principles and performance. *J. Propuls. Power* **2006**, *22*, 1162–1169. [CrossRef]
26. Wolanski, P.; Balicki, W.; Perkowski, W.; Bilar, A. Experimental research of liquid-fueled continuously rotating detonation chamber. *Shock Waves* **2021**, *31*, 807–812. [CrossRef]

27. Wu, Y.W.; Han, Q.X.; Yang, G.Y. Effects of an acoustic atomizer upon liquid-fueled detonation initiations in a detonation tube. *Exp. Therm. Fluid Sci.* **2019**, *109*, 109863. [CrossRef]
28. Zhang, Q.B.; Wang, K.; Dong, R.X.; Fan, W.; Lu, W.; Wang, Y.J. Experimental research on propulsive performance of the pulse detonation rocket engine with a fluidic nozzle. *Energy* **2019**, *166*, 1267–1275. [CrossRef]
29. Zhang, B.; Liu, H.; Wang, C. On the detonation propagation behavior in hydrogen-oxygen mixture under the effect of spiral obstacles. *Int. J. Hydrogen Energy* **2017**, *42*, 21392–21402. [CrossRef]
30. Zheng, K.; Jia, Q.H.; Ma, Z.M.; Xing, Z.X.; Hao, Y.M.; Yu, M.G. Experimental and numerical investigation on the premixed methane/air flame propagation in duct with obstacle gradients. *Process Saf. Environ. Protect.* **2023**, *178*, 893–904. [CrossRef]
31. Heilbronn, D.; Barfuss, C.; Sattelmayer, T. Influence of geometry on flame acceleration and DDT in H₂-CO-air mixtures in a partially obstructed channel. *J. Loss Prev. Process Ind.* **2021**, *71*, 104493. [CrossRef]
32. Goodwin, G.B.; Houim, R.W.; Oran, E.S. Effect of decreasing blockage ratio on DDT in small channels with obstacles. *Combust. Flame* **2016**, *173*, 16–26. [CrossRef]
33. Ciccarelli, G.; Fowler, C.J.; Bardon, M. Effect of obstacle size and spacing on the initial stage of flame acceleration in a rough tube. *Shock Waves* **2005**, *14*, 161–166. [CrossRef]
34. Saeid, M.H.S.; Khadem, J.; Emami, S. Numerical investigation of the mechanism behind the deflagration to detonation transition in homogeneous and inhomogeneous mixtures of H2-air in an obstructed channel. *Int. J. Hydrogen Energy* **2021**, *46*, 21657–21671. [CrossRef]
35. Wang, J.B.; Zhao, X.Y.; Fan, L.Y.; Pan, J.F.; Zhu, Y.J. Effects of the quantity and arrangement of reactive jet obstacles on flame acceleration and transition to detonation: A numerical study. *Aerosp. Sci. Technol.* **2023**, *137*, 108269. [CrossRef]
36. Coates, A.M.; Mathias, D.L.; Cantwell, B.J. Numerical investigation of the effect of obstacle shape on deflagration to detonation transition in a hydrogen-air mixture. *Combust. Flame* **2019**, *209*, 278–290. [CrossRef]
37. Zhou, S.B.; Liu, F.; Ning, H.M.; Hu, N. Experimental investigation on a rotating detonation combustor with the pulse operating frequency of 10 Hz. *Acta Astronaut.* **2024**, *215*, 642–652. [CrossRef]
38. Gray, S.; McLoughlin, M.; Ciccarelli, G. Fuel-oxygen mixing and detonation propagation in a linear rotating detonation rocket engine geometry. *Combust. Flame* **2024**, *260*, 113250. [CrossRef]
39. Luo, S.B.; Sun, Y.H.; Song, J.W.; Liu, J. Performance analysis of a hybrid pulse detonation engine using liquid hydrogen as fuel. *Int. J. Hydrogen Energy* **2022**, *47*, 21537–21551. [CrossRef]
40. Feng, W.K.; Zheng, Q.; Xiao, Q.; Meng, H.L.; Han, X.P.; Cao, Q.; Huang, H.L.; Wu, B.W.; Xu, H.; Weng, C.S. Effects of cavity length on operating characteristics of a ramjet rotating detonation engine fueled by liquid kerosene. *Fuel* **2023**, *332*, 126129. [CrossRef]
41. Xu, S.D.; Song, F.L.; Wu, Y.; Zhou, J.P.; Cheng, P.; Yang, X.K.; Chen, X. Experimental investigation on combustion efficiency of a partially premixed kerosene-air rotating detonation combustor. *Fuel* **2022**, *329*, 125418. [CrossRef]
42. Li, X.F.; Li, J.Z.; Qin, Q.Y.; Jin, W.; Yuan, L. Experimental study on detonation characteristics of liquid kerosene/air rotating detonation engine. *Acta Astronaut.* **2024**, *215*, 124–134. [CrossRef]
43. Tunik, Y.V.; Gerasimov, G.Y.; Levashov, V.Y.; Mayorov, V.O. Busemann diffuser for supersonic ramjet on detonation combustion of kerosene vapor. *Acta Astronaut.* **2022**, *198*, 495–501. [CrossRef]
44. Sato, T.; Chacon, F.; Gamba, M.; Raman, V. Mass flow rate effect on a rotating detonation combustor with an axial air injection. *Shock Waves* **2021**, *31*, 741–751. [CrossRef]
45. Zhao, W.D.; Deiterding, R.; Liang, J.H.; Wang, X.X.; Cai, X.D.; Duell, J. Adaptive simulations of flame acceleration and detonation transition in subsonic and supersonic mixtures. *Aerosp. Sci. Technol.* **2023**, *136*, 108205. [CrossRef]
46. Warimani, M.; Azami, M.H.; Khan, S.A.; Ismail, A.F.; Saharin, S.; Ariffin, A.K. Internal flow dynamics and performance of pulse detonation engine with alternative fuels. *Energy* **2021**, *237*, 121719. [CrossRef]
47. Jiang, C.; Pan, J.; Li, J.; Shi, X.; Quaye, E.K. Numerical simulation of detonation re-initiation in a 90° bifurcated channel filled with n-heptane/air mixture. *Acta Astronaut.* **2023**, *202*, 497–510. [CrossRef]
48. Wang, Z.W.; Wang, Y.Q.; Peng, C.X.; Zheng, L.X. Experimental study of pressure back-propagation in a valveless air-breathing pulse detonation engine. *Appl. Therm. Eng.* **2017**, *110*, 62–69. [CrossRef]
49. Qiu, H.; Su, Z.; Xiong, C. Experimental investigation on multi-cycle two-phase spiral pulse detonation tube of two configurations. *Proc. Inst. Mech. Eng. Part G-J. Aerosp. Eng.* **2019**, *233*, 4166–4175. [CrossRef]

energies

MDPI

Article

The Influence of Injector Nozzle Diameter on High-Density and Lean Mixture Combustion in Heavy-Duty Diesel Engines

Yize Liu * and Wanhua Su

State Key Laboratory of Engines, Tianjin University, Tianjin 300072, China
* Correspondence: liuyize@tju.edu.cn

Abstract: In order to improve the fuel economy of heavy-duty diesel engines under high-load conditions, based on the combustion pathway model, it is proposed that the proportion of lean mixture with $0 < \Phi < 1$ is the most important spray characteristic affecting the overall diesel combustion process. Answering the question of how to increase the proportion of lean mixture inside the spray is the key to achieving the efficient and clean combustion of diesel engines. This paper investigated the mechanism of injector nozzle diameter on the in-cylinder air–fuel mixture and combustion process based on a high-density and lean mixture characteristic combustion strategy. The experimental results show that with an increase in nozzle diameter, the peak pressure and instantaneous heat release rate significantly increase, the combustion duration is shortened by about 20%, and the heat release becomes more concentrated. At 1200 rpm and IMEPg~2.3 MPa conditions, the indicated thermal efficiency increases by 1.3%, reaching a maximum of 51.5%. The numerical simulation results show that with the increase in nozzle diameter from 0.169 mm to 0.218 mm, the spray ejection momentum per unit time increases by 30%, the momentum transferred to the air by the spray increases, the oxygen transport process becomes more intense, and the air entrainment mass during the spray free development stage increases by 42%. The proportion of lean mixture inside the spray throughout the entire spray development process increases, resulting in an increase in the heat release rate of the lean mixture, making the overall combustion more intense and concentrated.

Keywords: heavy-duty diesel engine; injector nozzle diameter; lean mixture; spray characteristic; air entrainment; fuel–air mixing; thermal efficiency

Citation: Liu, Y.; Su, W. The Influence of Injector Nozzle Diameter on High-Density and Lean Mixture Combustion in Heavy-Duty Diesel Engines. *Energies* **2024**, *17*, 2549. https://doi.org/10.3390/en17112549

Academic Editor: Dimitrios C. Rakopoulos

Received: 24 April 2024
Revised: 17 May 2024
Accepted: 22 May 2024
Published: 24 May 2024

1. Introduction

In order to address the environmental issues brought about by global climate change, the Paris Agreement aims to reduce greenhouse gas emissions to near zero by the end of this century [1]. Road transport accounts for 72.06% of greenhouse gas emissions from the transport sector as a whole, and the diesel engine is still the most widely used means of road transportation [2,3]. The intensification of energy consumption and the urgent need for environmental protection have prompted the upgrading of traditional diesel engine technology to meet the requirements of efficient and clean combustion.

In order to further improve the thermal efficiency of diesel engines, extensive research has been carried out on combustion modes and various innovations have been made. In terms of combustion theory, the pursuit of in-cylinder homogeneous charge combustion became a key research direction for internal combustion engines following the proposal of the homogeneous charge compression ignition combustion mode [4]. However, this combustion mode still had some difficulties, such as high pressure rise rate and limited operating load [5]. Under heavy-load conditions, diesel engines predominantly use diffusion combustion. The large cycle fuel injection mass and slow heat release rate limit the improvement of thermal efficiency.

Researchers have made significant progress in the development of high mixing rate combustion technology for diesel engines [6,7]. The parameters of the fuel injection system

determine the initial fuel injection momentum and the subsequent fragmentation and entrainment process. Zhai [8] et al. investigated the effect of injector nozzle diameter on injection characteristics under different injection pressure conditions. As the injection pressure increases and the injector nozzle diameter decreases, the time for the liquid length to reach a stable stage is shortened, and strong oxidation reactions are simultaneously distributed in both the upstream and downstream regions of the flame. Compared to using a micro-hole diameter (D = 0.07 mm, Pinj = 100 MPa), increasing the injection pressure to 300 MPa (D = 0.133 mm, Pinj = 300 MPa) can more effectively reduce the soot produced per unit of fuel mass and improve the thermal efficiency of diesel engines. The increase in fuel injection pressure enhances the speed of radial air entrainment at the initial stage of fuel injection, which increases the spray angle and significantly improves the fuel–air mixing rate [9,10]. Shi [11] et al. studied the effect of injection pressure on the combustion characteristics of diesel engine low-temperature wall-impinging ignition, finding that increasing the injection pressure is beneficial for optimizing high-temperature combustion but may lead to unstable low-temperature ignition. With an increase in the injection pressure from 40 MPa to 100 MPa, the ignition delay at 840 K ambient temperature initially shortened and then prolonged, with the combustion condition being best at 80 MPa. Reducing the fuel injection mass is detrimental to low-temperature ignition, as the ignition transitions from stable to unstable, and then to misfire, as the injection mass decreases from 35–50 mg to 20–30 mg, and further to 15 mg. Comprehensive analysis reveals that the minimum fuel mass required for stable wall-impinging ignition approximately increases linearly with injection pressure increasing, thus reducing injection pressure and increasing fuel mass help to improve combustion quality and enhance environmental adaptability. Xia [12] et al. conducted experimental analysis on the spray characteristics under different nozzle diameters (100, 300, 350 μm) and injection pressures (60, 100, 140, 180 MPa) within a constant volume bomb to elucidate the effects of key factors such as nozzle diameter, injection pressure, and thermodynamic boundary conditions on fuel spray characteristics and critical characteristics. The 350 μm nozzle, due to its higher injection flow rate, results in a significantly larger spray volume compared to other nozzles, while the spray generated by the 100 μm nozzle is easily affected by the ambient air entrainment movement, thereby enhancing the radial expansion process of the spray. The effect of injection pressure on the liquid-phase fuel length, volume, and spray cone angle is not significant, but it significantly affects the fuel–air mixture process. Even under supercritical conditions, increasing the injection pressure still significantly improves the mixing quality in the downstream region of the spray. In summary, the influence of the injector nozzle diameter on in-cylinder fuel–air mixture and combustion process is not clear, and a universal rule has not yet been summarized. The optimization scheme of injector nozzle diameter needs further improvement. Addressing the above issues, this paper adopts a combined approach of bench experiments and numerical simulation to investigate the mechanism of the injector nozzle diameter on the in-cylinder fuel–air mixture and combustion process, based on high-density and lean mixture characteristic combustion strategy, aiming to provide guidance and suggestions for the selection of injector nozzle diameter in the development of diesel engine combustion systems.

2. Spray Characteristics of High-Efficiency Clean Combustion in Diesel Engines

Traditional diesel engine combustion is a highly complex physicochemical process, where liquid diesel undergoes processes such as droplet formation, collision, breakup, atomization, evaporation diffusion, air entrainment, and mixing after leaving the injector before ignition and combustion can occur. John Dec et al. used the two-dimensional laser Rayleigh scattering (LRS) technique to quantitatively study the concentration fields of gas and liquid phase sprays and the generation of soot in an optical engine, and based on quantitative experimental results, proposed a modern diesel engine combustion process model [13] (Figure 1). After the fuel jet leaves the nozzle, it rapidly atomizes as the spray progresses forward, and high-temperature ambient gas is entrained into the spray,

causing the temperature rise and phase change in the liquid-phase fuel, leading to chemical reactions. A high equivalence ratio premixed flame (Φ~4, T = 825 K) appears at the head of the spray, generating heat to heat up the fuel–air mixture to about 1600 K, contributing to approximately 10–15% of the total heat release. In the mid–late stage of spray development, a high-temperature diffusion flame envelope of 2700 K appears around the entire fuel jet, and combustion products rich in fuel from the spray interior such as CO, UHC, PM are continuously transported to this envelope, where they undergo diffusion combustion (including the generation of CO_2 and H_2O, NOx generation, and oxidation of soot). It can be seen that traditional diesel engine combustion is a predictable combustion, closely related to fuel injection, which is easier to control and more suitable for high-load conditions. However, the inherent nature of heterogeneous combustion inevitably results in NOx and soot emissions. Under the flame lift height downstream, the diesel spray forms a premixed reaction zone with an equivalence ratio close to four, and the premixed combustion products will become the "fuel" for the downstream diffusion combustion process of the spray, including the precursor of soot generation. In other words, the distribution characteristics of equivalence ratio inside the spray at the moment of ignition will affect the total amount of harmful emissions such as soot and the heat release rate of the diffusion combustion process.

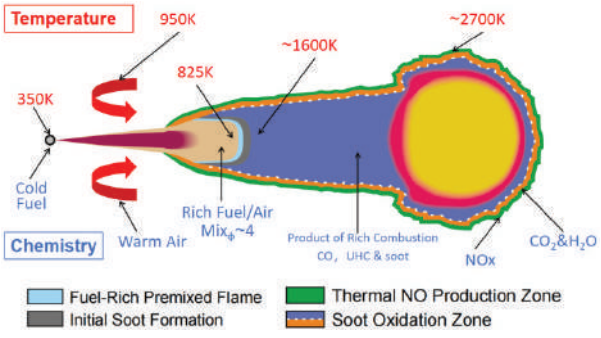

Figure 1. The combustion and emission generation model of traditional diesel engine.

Pickett and Siebers from Sandia National Laboratories in the United States first proposed the concept of leaner lifted flame combustion (LLFC) [14]. By enhancing the air entrainment process within the flame lift height, the equivalence ratio of the mixture in the premixed reaction zone is kept below or equal to 2 (Figure 2), achieving a completely smokeless and relatively low-temperature combustion strategy. The key to achieving the LLFC strategy is to increase the flame lift height and strengthen the spray air entrainment capability. Pickett et al. [14,15] conducted experimental studies in optical constant volume chambers and found that diesel LLFC combustion could be achieved when the ambient temperature and pressure were below specific values. Additionally, reducing the injector nozzle diameter or using oxygen-containing fuels can broaden the operating range of LLFC, as shown in Figure 3. Polonowski et al. [16] found that achieving a continuous smokeless LLFC mode in actual engines is challenging. It requires injection pressures as high as 240 MPa, moderate exhaust gas recirculation rates, and lower intake air temperatures to achieve completely smokeless LLFC with a two-hole injector equipped diesel engine. For injectors with six or more holes, the secondary entrainment of combustion products and the interactions between sprays, making LLFC combustion unsustainable. It is worth noting that the above experimental results were obtained under moderate-load conditions. Achieving LLFC under high-load conditions requires the use of oxygen-containing fuels [17,18], as shown in Figure 4.

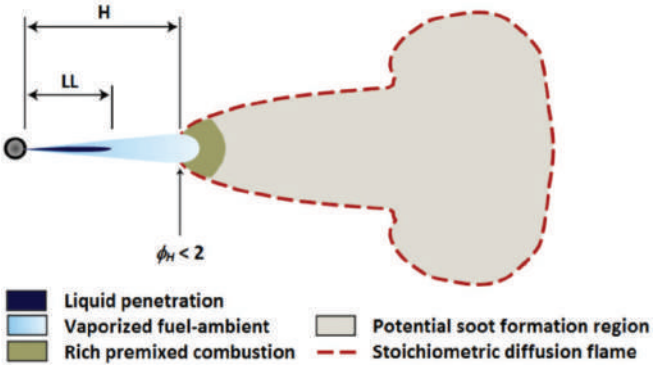

Figure 2. Conceptual model of LLFC combustion strategy.

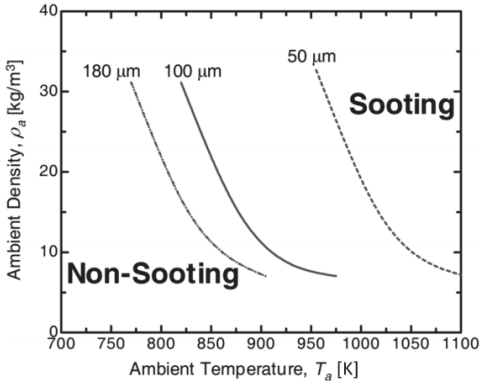

Figure 3. Relationship between soot formation status and injector nozzle diameter in constant volume combustion chamber.

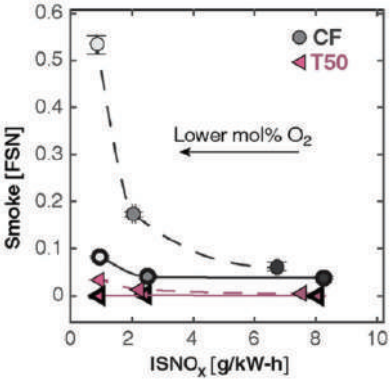

Figure 4. Influence of oxygen-containing fuels on soot and NOx emissions.

In the combustion process of diesel engines, the final amount of soot generated is the result of the combined effects of its formation and oxidation processes. Pursuing combustion processes with zero soot generation is not the only way to address soot emissions. However, in many LLFC test results, excessively low intake air temperatures and oxygen concentrations are used to extend flame lift height, affecting the overall fuel–air mixing process and leading to prolonged combustion duration, sharp increases in HC and CO

emissions levels, and significant reductions in combustion efficiency and engine thermal efficiency. Therefore, simply pursuing combustion modes with flame lift height positions where the mixture equivalence ratio is below two does not meet the requirements of current high-efficiency, clean, low-carbon diesel engines. The inherent uneven mixing of diesel spray leads to a complex distribution of equivalence ratios inside the spray. To determine the relevant reaction pathways, the mixture is divided into different regions based on local fuel–oxygen equivalence ratios: $0 < \Phi < 1$, $1 < \Phi < 2$, and $\Phi > 2$. Different mixtures in different equivalence ratio regions follow specific reaction pathways, as shown in Figure 5. In high-temperature environments above 1400 K, lean mixtures with $0 < \Phi < 1$ directly oxidize to CO_2, releasing a large amount of heat instantly. Rich mixtures with $1 < \Phi < 2$ first generate intermediate product CO, which then reacts with oxygen to form CO_2, with the rate of heat release controlled by the fuel–air mixing rate. Overly rich mixtures with $\Phi > 2$ exceed the equivalence ratio boundary for soot generation. Therefore, lean mixtures with $0 < \Phi < 1$ can complete the combustion heat release process in the shortest time scale, while mixtures with $\Phi > 1$ inevitably undergo the mixing processes, with the mixing time scale far exceeding the chemical reaction time scale, resulting in combustion rates limited by the mixing rate.

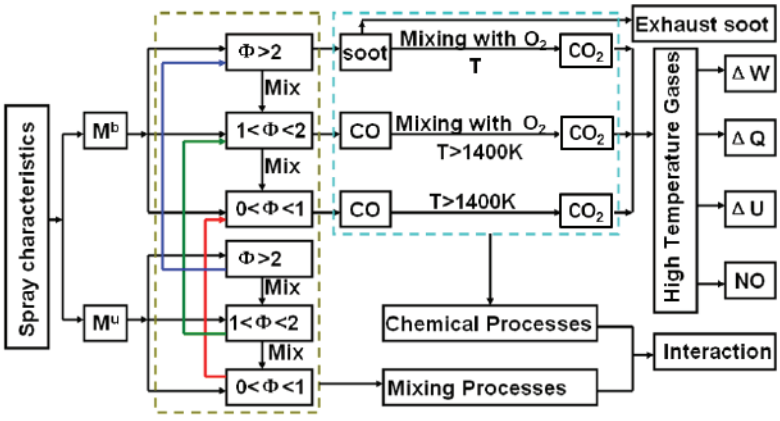

Figure 5. The schematic diagram of spray combustion path of heavy-duty diesel engine.

Diesel spray will form a premixed reaction zone downstream of the flame lift height, where the combustion products in this zone are mainly composed of over-rich mixtures with $\Phi \geq 2$, serving as "fuel" for the downstream diffusion combustion process of the spray. From the analysis of the combustion path, achieving complete combustion of the rich mixture in the premixed reaction zone unavoidably requires a relatively long time scale for the mixing process. It is only through the incomplete combustion product and unburned fuel transport during the fuel–air mixing process that contact with oxygen can achieve complete combustion. At this point, the combustion becomes a mixed-dominated, staged process with a large amount of intermediate product generation. Introducing the Φ–T diagram of CO generation [19] to characterize the combustion efficiency of the diffusion combustion process, it can be seen from Figure 6 that the combustion path curves of diffusion combustion differ significantly at different mixing rates. The smaller the mixing time, that is, the faster the mixing rate, and the further the combustion path is from the CO generation area, indicating that more fuel develops along the lean mixture path throughout the combustion process. At the time scale level that cannot be characterized by the Φ–T diagram, the mixing rate largely affects the duration of diffusion combustion, thereby influencing combustion phase and piston work capacity.

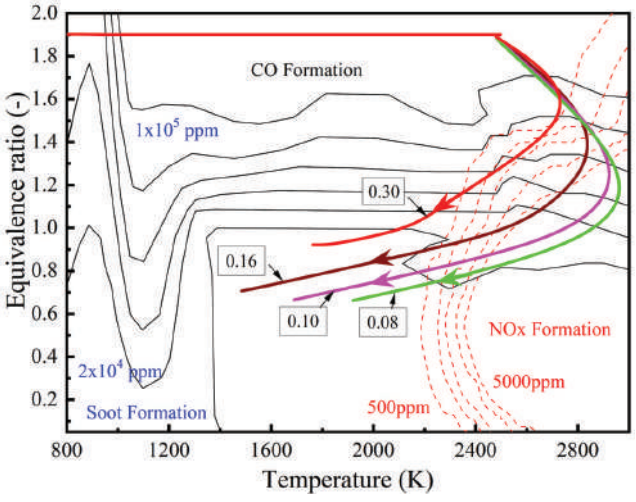

Figure 6. Influence of different mixing rates on the diesel diffusion combustion process.

In summary, the proportion of lean mixtures with $0 < \Phi < 1$ is the most important spray characteristic affecting the overall diesel combustion process. Increasing the proportion of lean mixtures with $0 < \Phi < 1$ inside the spray can enhance the heat release during the premixed combustion stage, and on the other hand, significantly reduce the dependence of the diffusion combustion stage on the mixing rate, making the overall heat release process more concentrated. Ultra-high proportions of lean mixtures are an ideal spray characteristic for efficient and clean combustion. Therefore, increasing the proportion of lean mixtures throughout the ignition timing and the entire spray development process is the key to achieving high-efficiency clean diesel combustion.

3. Test Platform and 3-D Simulation Model

3.1. Single-Cylinder Engine Test Platform

In this study, experiments were conducted on a single-cylinder engine test platform. The original engine parameters are listed in Table 1, and the schematic diagram of a single-cylinder engine test platform is shown in Figure 7. During the experiment, the first cylinder of the original engine was used as the test cylinder. The intake system of the test cylinder used external pressurization combined with intake heating and an independent exhaust gas recirculation system, allowing flexible control of intake pressure, temperature, and EGR rate. In this study, three different injector nozzle diameters were used, with nozzle diameters of 0.169/0.203/0.218 mm. Table 2 shows the parameter settings for the experimental conditions. Table 3 provides specific information on the measurement instruments and their error rates. Single-cylinder exhaust components were detected using a Horiba 7100 exhaust gas analyzer made in Japan, and soot emissions were measured with an AVL 415 smoke meter made in Austria. Cylinder pressure signals were collected using a 6125C cylinder pressure sensor and 5165A charge amplifier by the Kistler company made in Switzerland. The uncertainty of the single-cylinder engine test platform was calculated as follows: Total uncertainty = Square root of {(uncertainty of soot)^2 + (uncertainty of load)^2 + (uncertainty of speed)^2 + (uncertainty of temperature)^2 + (uncertainty of air flow)^2 + (uncertainty of diesel measurement)^2 + (uncertainty of pressure acquisition)^2 + (uncertainty of angle encoder)^2}, and after calculation, the total uncertainty was confirmed to be 1.47%. In addition, cylinder pressure data were measured every 0.5 crank angle degree and the average was taken from 100 consecutive engine cycles. The gaseous emissions and the particulate mass emission were continuously measured for 5 min and the average results

were calculated. The steady-state tests were repeated twice to ensure that the results were repeatable, within the experimental uncertainties of the measurements.

Table 1. Main technical parameters of heavy-duty diesel engine.

Parameter	Value
Cylinder Diameter/mm	116
Stroke/mm	150
Displacement/L	9.5
Compression Ratio	18.5
Intake Swirl Ratio	1.1
Combustion Chamber Shape	Stepped-lip type
Intake Mode	Turbocharged and Intercooled
Rated Power (kW)	294 (at 1900 r/min)
Maximum Torque (N·m)	1800 (1000–1400 r/min)
Maximum Cylinder Pressure (MPa)	24

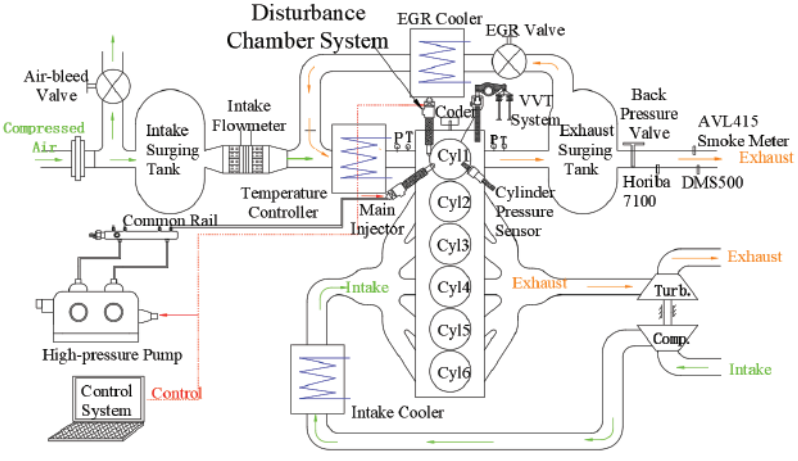

Figure 7. Schematic diagram of single-cylinder engine test platform.

Table 2. Experimental operating conditions parameter.

Parameter	Value	Note
Speed	1200 r/min	Constant
Total Cycle Fuel Mass	180 mg	90% load, constant
Common Rail Pressure	180 MPa	Constant
Fuel Injection Timing	−2~8 deg. ATDC	Variable
Nozzle Diameter	0.169 mm; 0.203 mm; 0.218 mm	Variable
Intake Valve Closing Timing	−100 deg. ATDC (Using RIVCT structure, original engine −150 deg. ATDC)	Constant
Intake Pressure	2.7~4.15 bar	Variable
Intake Temperature	330 ± 3 K	Constant

Table 3. Measuring instruments and error rates.

	Instruments Type	Error
Cylinder pressure sensor	KISTLER 6125C 0–30 MPa	±0.01%F·S
Charge amplifier	5165A	±0.05%F·S
Emission collection equipment	Horiba 7100	±0.1%F·S
Smoke detector	AVL 415	±0.05%F·S
Temperature sensor	PT100 0–700 K	±0.1%F·S
Pressure sensor	0–1 MPa	±0.25%F·S

3.2. Injector Hydraulic System Simulation Model

To simplify the simulation model of the injector hydraulic system, the following basic assumptions are proposed [20]: (1) the rail pressure remains uniformly constant during the injection process; (2) the fuel temperature remains constant during the injection process; (3) the viscosity, density, and elastic modulus of the fuel are considered constant; (4) elastic deformation of the components in the system is not considered; (5) leakage caused by machining issues in flat and conical seals and its effect on chamber pressures are not considered. The following equations form the mathematical model describing the dynamic process of the hydraulic system [21]:

(1) The internal pipes of the injector are treated as concentrated volumes, and fuel flow follows the law of mass conservation

$$Q_{gi} = Q_{go} + \frac{V_g}{E} * \frac{dp_g}{dt}, \tag{1}$$

where Q_{gi} is the flow into the pipe, Q_{go} is the flow out of the pipe, V_g is the pipe volume, E is the elastic modulus of the fuel, p_g is the fuel pressure inside the pipe, and t is time.

(2) The influence of the shape of the control chamber and pressure-bearing groove on the operation of the injector can be neglected, and the volume is the main influencing factor. It can be expressed as a volume chamber model, and fuel flow follows the law of mass conservation

$$\sum Q_i = \frac{V_i}{E} * \frac{dp_i}{dt} + \frac{dV_i}{dt}, \tag{2}$$

where Q_i is the change in flow rate in the i volume chamber, V_i is the volume of the i volume chamber, p_i is the pressure inside the i volume chamber, and t is time.

(3) Treating the control rod and needle valve as a whole, according to Newton's second law, the motion equation of the needle valve is

$$m\frac{^2x}{t} = F_C + F_y + F_z - F_k - k(xo + x), \tag{3}$$

where x is the lift of the needle valve, m is the total mass of the control rod and needle valve, F_c is the force of the fuel on the needle valve at the pressure-bearing groove, F_y is the force of the fuel on the needle valve at the pressure chamber, F_z is the supporting force at the needle valve seat, F_k is the force of the control chamber on the control rod, k is the stiffness of the needle valve spring, and x_0 is the preload of the needle valve spring.

Based on the above mathematical model, a simulation model of the injector hydraulic system is built in the AMESim 2020 simulation platform, as shown in Figure 8. To verify the accuracy of the simulation model, the actual fuel injection rate is measured using the EFS high-pressure common rail test bench. The test was carried out under the conditions of 180 MPa common rail pressure and 1.5 ms pulse width. After filtering and shaping, the measured fuel injection rate matches well with the simulated fuel injection rate under the same conditions, as shown in Figure 9. This indicates that the simulation results can reflect the actual fuel injection pattern, and the simulation model of the high-pressure common rail injector hydraulic system is reliable.

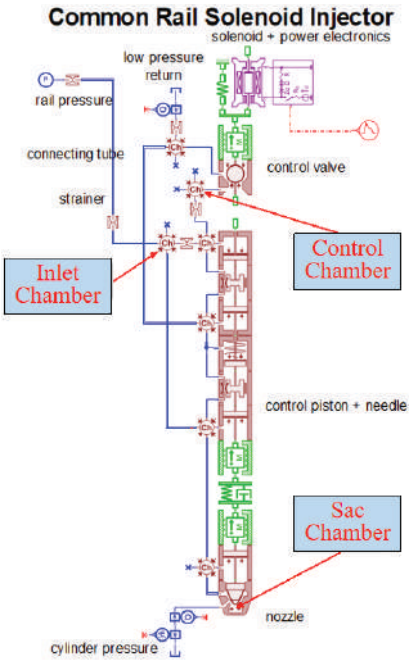

Figure 8. Simulation model of high-pressure common rail injector hydraulic system.

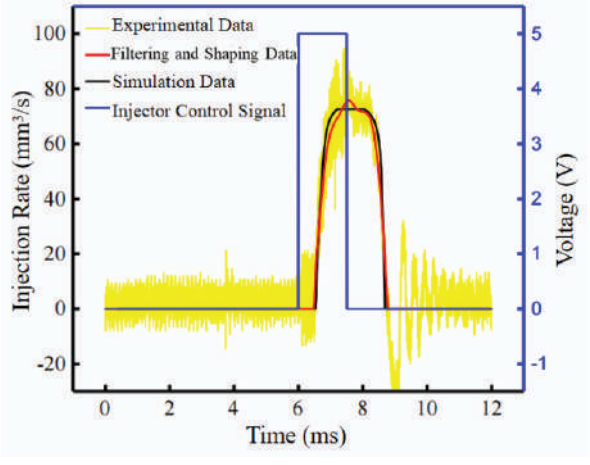

Figure 9. Comparison of fuel injection rate experimental results and simulation results.

3.3. 3-D Combustion Simulation Model

Based on the geometric parameters of the combustion chamber, modeling will be carried out using Solidworks 2023. Since the original engine combustion chamber is a rotationally symmetric regular revolving body, and the eight injector nozzles are evenly distributed circumferentially, a one-eighth combustion chamber will be used for simulation to improve computational speed. Three-dimensional simulation models were established based on the computational fluid dynamics software CONVERGE 2.3 (Figure 10), with a base grid size of 4.0 mm. The important mathematical models used in the simulation calculations are shown in Table 4.

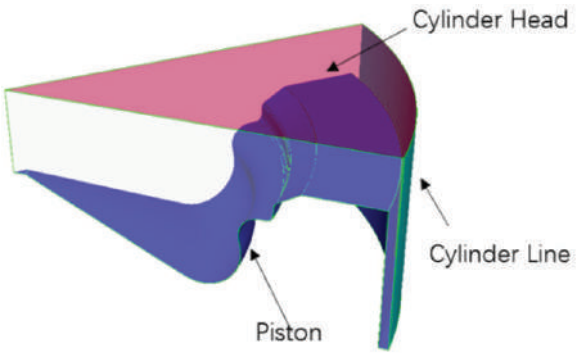

Figure 10. Geometric model of the combustion chamber.

Table 4. Models used in simulation calculations.

Parameter	Value
Turbulence Model	RNG k-ε
Combustion Model	SAGE Chemical Reaction Solver + Simplified Chemical Reaction Kinetics Mechanism
Heat Transfer Model	Han and Reitz
Spray Breakup Model	KH-RT
Spray Wall Impact Model	O'Rourke and Amsden
Droplet Collision Model	NTC collision
Spray Evaporation Model	Frossling
Base Grid Size/mm	4

Based on the obtained experimental data, the simulation model was calibrated and validated. The calibration condition had an intake pressure of 4.15 bar and an injection timing of −2 deg. ATDC, with other test conditions referenced from Table 2. The simulation results for injectors with different nozzle diameters were compared with actual experimental results, as shown in Figure 11. Comparing the simulation results with the experimental results, the peak cylinder pressure error was less than 0.1%, the crank angle error corresponding to the peak cylinder pressure was less than 0.5 deg, and the peak heat release rate error was less than 2%. It can be considered that the simulated data closely matches the experimental data, and the established simulation model can be used to accurately describe the combustion process of the diesel engine.

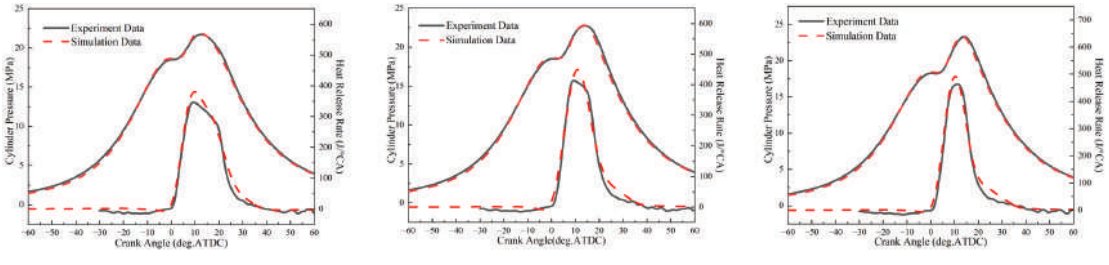

(**a**) (**b**) (**c**)

Figure 11. Comparison of cylinder pressure and heat release rate between simulation and experiment: (**a**) 0.169 mm; (**b**) 0.203 mm; (**c**) 0.218 mm.

4. Results and Discussion

4.1. Experimental Study on the Influence of Injector Nozzle Diameter on Combustion Process

Experimental research on the influence of the injector nozzle diameter on combustion and emissions was conducted based on the aforementioned test platform. Figure 12 presents experimental data including cylinder pressure, instantaneous heat release rate, and average in-cylinder temperature for three injector nozzle diameters at an intake pressure of 4.15 bar and a rail pressure of 180 MPa. The injection strategy was single injection, and the injection start time was −2 deg. ATDC. As the injector nozzle diameter increases from 0.169 mm to 0.218 mm, the maximum cylinder pressure increases, and the combustion heat release process becomes more intense and concentrated. The peak heat release rate increases by 33.9%, and the combustion duration shortens from 26.3 deg to 20.8 deg. Additionally, both the combustion center CA50 and the combustion end CA90 move closer to the top dead center. Furthermore, observation of the average in-cylinder temperature reveals that increasing the injector nozzle diameter leads to a greater temperature rise during the combustion process, with the timing of the temperature peak significantly advancing.

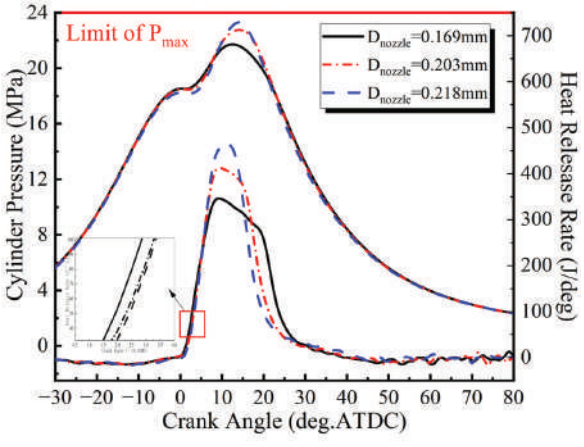

(**a**)

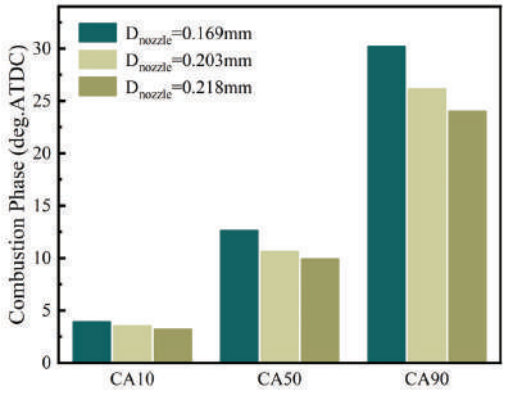

(**b**)

Figure 12. *Cont.*

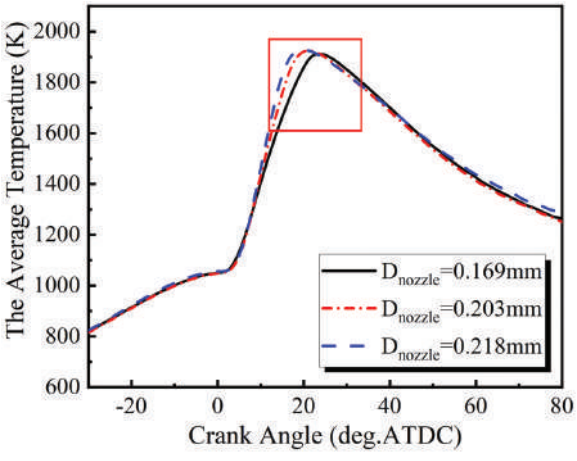

(**c**)

Figure 12. Combustion characteristic parameters corresponding to three injector nozzle diameters: (**a**) cylinder pressure and heat release rate; (**b**) combustion phase; and (**c**) average temperature.

Figure 13 illustrates the impact of injector nozzle diameter on major harmful emissions. Experimental results indicate that there is little difference in the emissions of CO, soot, and UHC for different nozzle diameters. The original emissions of CO and soot from the engine are much lower than the emission limits corresponding to the WHSC test cycle in the Euro VI emission standard. The original emission of UHC is close to the aforementioned emission limit. When the nozzle diameter increases from 0.169 mm to 0.218 mm, the NOx emissions exhibit a trend of first increasing and then decreasing. This is because increasing the nozzle diameter leads to a greater temperature rise in the cylinder during diesel combustion, resulting in an increase in NOx production. However, when the nozzle diameter increases to 0.218 mm, the overall combustion duration shortens by 20%, and the duration of high-temperature NOx generation elements also decreases accordingly, leading to a reduction in NOx emissions.

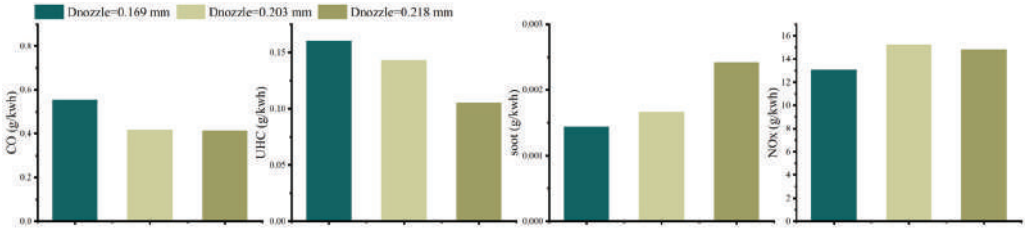

Figure 13. Influence of injector nozzle diameter on major harmful emissions.

Figure 14 shows the influence of the injector nozzle diameter on energy loss distribution. As the nozzle diameter increases, the heat transfer loss initially increases and then decreases. This is mainly due to the increase in the nozzle diameter, which significantly increases the cylinder temperature and average pressure during diesel combustion, affecting the temperature difference and heat transfer coefficient in the wall heat transfer process, resulting in an increase in wall heat transfer rate. However, on the other hand, the 20% reduction in combustion duration reduces the duration of high-temperature in-cylinder, so under the interplay of these two factors, heat transfer loss exhibits a trend of initially increasing and then decreasing with the increase in nozzle diameter. The increase in nozzle diameter increases the proportion of constant volume combustion, allowing for a more

thorough expansion of the working fluid and reducing exhaust temperature. Consequently, exhaust loss decreases monotonically with the increase in nozzle diameter. Benefiting from the simultaneous reduction in heat transfer loss and exhaust loss, indicated thermal efficiency increases with the increase in nozzle diameter. Under the condition of 1200 rpm and IMEPg of 2.3 MPa, using a nozzle diameter of 0.218 mm, the indicated thermal efficiency reaches as high as 51.5%.

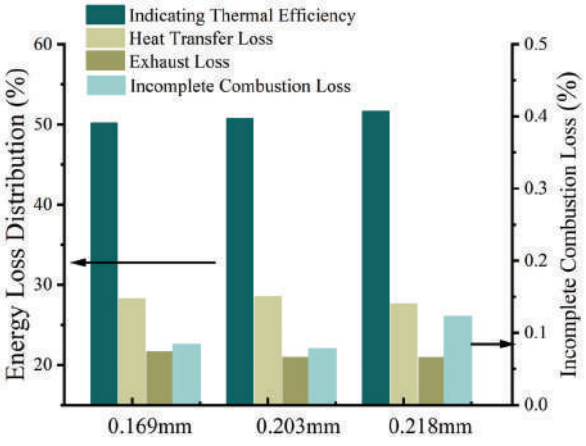

Figure 14. Influence of injector nozzle diameter on energy loss distribution.

Based on the comprehensive analysis of the test results, under the thermodynamic boundary conditions in this study, as the nozzle diameter increases from 0.169 mm to 0.218 mm, the combustion process of diesel becomes more rapid, with a 20% reduction in the duration of combustion. Furthermore, the combustion is sustained for a shorter period, and the proportion of constant volume combustion increases. Indicated thermal efficiency at high-load conditions also rises from 49.8% to 51.5%. While the experimental results provide insights at a macroscopic level into the impact of nozzle diameter on heat release rate, thermal efficiency, and emissions, a microscopic understanding of the variation in nozzle diameter on in-cylinder fuel–air mixture and combustion processes is lacking. The following sections will utilize numerical simulation methods to analyze in-cylinder spray air entrainment motion and the distribution of mixed gas within the spray, aiming to elucidate the influence mechanism of nozzle diameter on the combustion process from the perspective of fuel–air mixture.

4.2. Influence of Nozzle Diameter on Spray Internal Mixing Quality

Changes in nozzle diameter affect the pressure fluctuation characteristics inside the injector, but the range of pressure fluctuation is mainly influenced by the effective injection pressure. Therefore, it is necessary to focus on the impact of nozzle diameter on the pressure loss characteristics inside the injector. Three injectors used in the experiments were simulated in the AMESim model to analyze the effects of nozzle diameter on effective injection pressure and actual fuel injection rate. It should be noted that the three injectors used in this study are all conical hole nozzles, with a nozzle coefficient K of 0.5. The coefficient K is defined as $(D_{inlet} - D_{outlet})/10$. Previous studies [22] have shown that when $K > 0$, it indicates that the nozzle along the flow direction is contracting, which will significantly inhibit the geometrically induced cavitation process inside the nozzle. Therefore, this study does not consider the influence of cavitation process inside the nozzle.

Friction in the internal pipeline, pipeline diameter switching, connection points, and the opening position of the needle valve of the fuel injection system all contribute to fuel pressure loss, ultimately leading to an actual fuel injection pressure much lower than the pressure inside the common rail. Figure 15a shows the pressure distribution and the form

of pressure loss at various positions inside the injector when the needle valve is fully open. Along-the-way loss refers to the energy loss caused by fuel flow friction with the pipe wall in a straight pipe, mainly occurring in the external high-pressure fuel pipe and the internal high-pressure fuel passage. There are also local pressure losses inside the injector, including sudden expansion and sudden contraction of the pipeline, especially at the needle valve. Changes in the nozzle diameter affect the local resistance coefficient between the sac chamber and the nozzle, but the greater influence on effective injection pressure is its effect on the flow rate of the entire high-pressure fuel passage. The flow velocity of fuel in the entire fuel injection system increases, and both the along-the-way loss and local loss in the internal fuel injection system significantly increase, leading to a significant decrease in effective injection pressure, as shown in Figure 15. For the three nozzle diameter injectors, under the common rail pressure of 180 MPa and the cycle fuel mass quantity of 180 mg, the average injection pressure within a single injection cycle is 131, 105, and 94 MPa (0.169 mm/0.203 mm/0.218 mm), respectively.

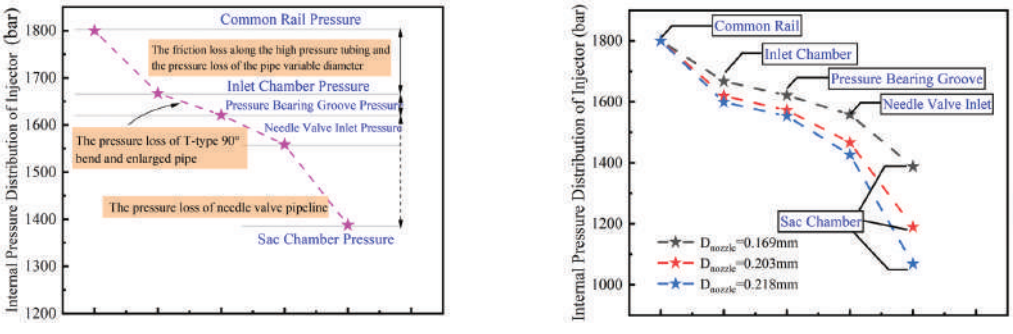

(**a**) (**b**)

Figure 15. Pressure loss characteristics inside the injector: (**a**) pressure loss forms at various positions inside the injector; (**b**) pressure distribution at various positions inside different diameter injectors.

The change in the nozzle diameter from 0.169 mm to 0.218 mm will result in alterations in both the internal pressure loss of the injector and the cross-sectional area at the nozzle outlet, inevitably affecting the actual fuel injection rate. According to the Bernoulli equation, the fuel flow rate through the nozzle can be expressed as follows:

$$\dot{m}_f = \int Au \cdot \rho dA = A\sqrt{2\Delta p(t)\rho} = \frac{\pi}{4} d^2 \sqrt{2\Delta p(t)\rho}, \quad (4)$$

where $\Delta p(t)$ is the pressure difference between the inlet and outlet of the nozzle; A is the cross-sectional area at the nozzle outlet; ρ is for the density of the diesel used in the experiment; and $\dot{m}_f$ is the mass flow rate at the nozzle outlet. Figure 16 illustrates the fuel injection rate corresponding to different nozzle diameters under a fixed injection pulse width. The fuel injection rate curves exhibit a trapezoidal pattern, which is quite similar to the lift curve of the needle valve. This resemblance is primarily due to the influence of the constrained area formed between the needle valve and its seat on the fuel injection rate. When the needle valve reaches its maximum lift, the fuel injection rate peaks. After 0.003 s from the start of injection, the fuel injection rate stabilizes relatively. At this point, the fuel injection rates corresponding to the three nozzle diameters, from smallest to largest, are 5.28 L/min, 6.70 L/min, and 7.23 L/min, respectively. Under the condition of 180 MPa common rail pressure and a cycle fuel mass of 180 mg, the durations of fuel injection for the respective nozzle diameters are 2950 ms, 2370 ms, and 2180 ms.

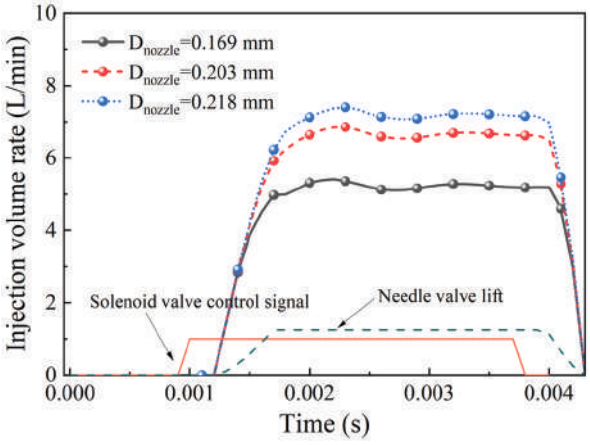

Figure 16. Influence of injector nozzle diameter on actual fuel injection rate.

The momentum of spray ejected will affect the subsequent evaporation and mixing quality of the spray in-cylinder, thereby influencing the final combustion process and emissions. The momentum of the spray at the nozzle outlet can be defined as follows:

$$\dot{M}_f = \int Au^2 \cdot \rho dt = 2A \cdot \int \Delta p(t) dt = \frac{\pi}{2} d^2 \int \Delta p(t) dt, \quad (5)$$

where $\dot{M}_f$ is the momentum of spray at the nozzle outlet within a fixed time step. To calculate the momentum of spray ejection, it is necessary to determine the statistical time step. In this study, a unit time step of 1×10^{-5} s was chosen. Increasing the injector nozzle diameter results in a decrease in actual injection pressure and fuel ejection velocity. However, increasing the injector nozzle diameter significantly improves the fuel injection rate. These two factors combined result in an increase in the average momentum of spray ejection per unit time from 3.25 kg·m/s to 4.21 kg·m/s as nozzle diameter increases when the needle valve is fully open, as shown in Figure 17. However, when cumulative momentum of spray ejection is calculated for a fixed total cycle fuel injection mass, it is found that due to differences in the duration of fuel injection, the cumulative momentum of spray ejection for smaller nozzle diameters actually increases.

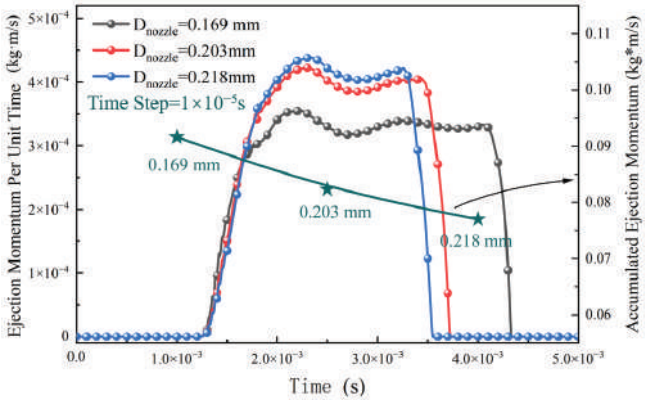

Figure 17. Influence of injector nozzle diameter on fuel ejection momentum.

The phenomenon of air entrainment during the development of fuel spray is a crucial physical process. The high-temperature air entrained into the spray promotes the evapora-

tion of liquid fuel by exchanging energy with the fragmented liquid droplets. Additionally, the motion of air entrainment determines the mixing quality between fuel and fresh air during spray development. Therefore, the quantity and velocity of air entrainment during spray development are important factors affecting the overall combustion performance of diesel engines. The strength of air entrainment during the free development of the spray depends on the rate of momentum exchange between the spray and the ambient gas. Within the range of injector diameters studied, the momentum of spray ejected per unit time increases with the increase in nozzle diameter, and the momentum entering the cylinder space per unit time should also increase synchronously. After high-speed spray enters the cylinder, its momentum density distribution exhibits a spindle-shaped layered structure, with the spray core area near the nozzle outlet having the highest momentum density, as shown in Figure 18. With the increase in nozzle diameter, the axial penetration speed of the spray increases, and the axial range of the high momentum density region expands. While the spray develops axially, the spray edges experience frictional shearing with the air, resulting in intense momentum exchange at the spray edges. To quantify the radial momentum transfer of the spray, the kinetic energy of the core and non-core regions at various axial positions of the spray was statistically analyzed, where the core region is defined as a cylinder with the nozzle axis as the axis and the nozzle diameter as the bottom diameter. As shown in Figure 19, increasing the nozzle diameter significantly increases the total kinetic energy at various axial positions of the spray, enhances the spray penetration rate, intensifies the frictional shearing between the spray and ambient air, improves the momentum exchange capability, and increases the proportion of kinetic energy transferred from the upstream region of the spray to the non-core region from 53% to 59%. As a result, the radial expansion of the spray increases.

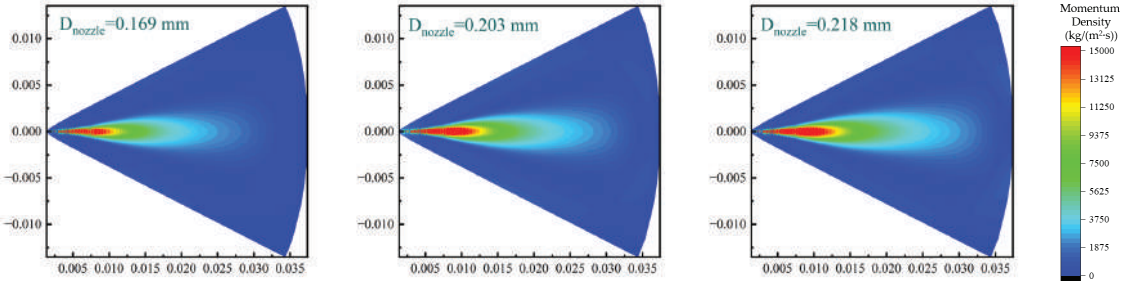

Figure 18. Momentum density distribution contour under three nozzle diameters.

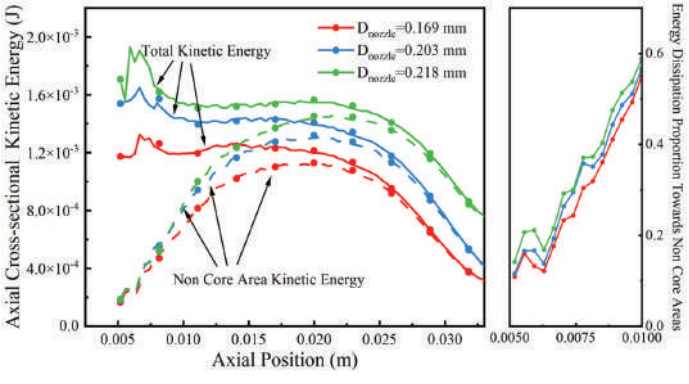

Figure 19. Axial cross-sectional kinetic energy and energy dissipation ratio at various positions under three nozzle diameters.

Figure 20 illustrates the characteristics of flow field distribution in the near and far fields of the spray under different nozzle diameters before spray/wall impingement (5.5 deg. ATDC). From the figure, it can be observed that while diesel spray develops axially, its front end pushes fresh air to both sides of the spray, and under the action of pressure difference, air from the sides enters the interior of the spray. The process of air entrainment by the spray mainly occurs at the middle and upper positions of the spray, and the air entrainment effect at the middle position of the diesel spray is most significant. As the spray develops axially forward, the momentum transferred to the radial air gradually increases, while the corresponding penetrating momentum gradually decreases. Ultimately, under the combined action of upstream spray and ambient gas, the mixture of spray far from the axis stops forward penetration and undergoes lateral movement, and under the action of pressure difference, flows backward upstream, defining this region as the "recirculation zone" where the outflow of fresh charge equals the inflow. Analyzing the velocity field near the edges of the spray under different nozzle diameters, both in the near and far fields, the airflow velocity increases with the increase in nozzle diameter. Statistically, the average air velocities near the spray edges corresponding to nozzle diameters from small to large are 7.67 m/s, 9.69 m/s, and 9.85 m/s in the near field, and 9.75 m/s, 11.71 m/s, and 11.93 m/s in the far field. The airflow velocity of the spray depends on the momentum flux transferred from the spray to the air radially. From the above study, it can be inferred that increasing the injector nozzle diameter increases the momentum ejected per unit time by the spray, increases the total momentum transferred to the surrounding gas, intensifies the mass transfer entrainment process at the spray edge, and increases the lateral airflow velocity near the spray edges.

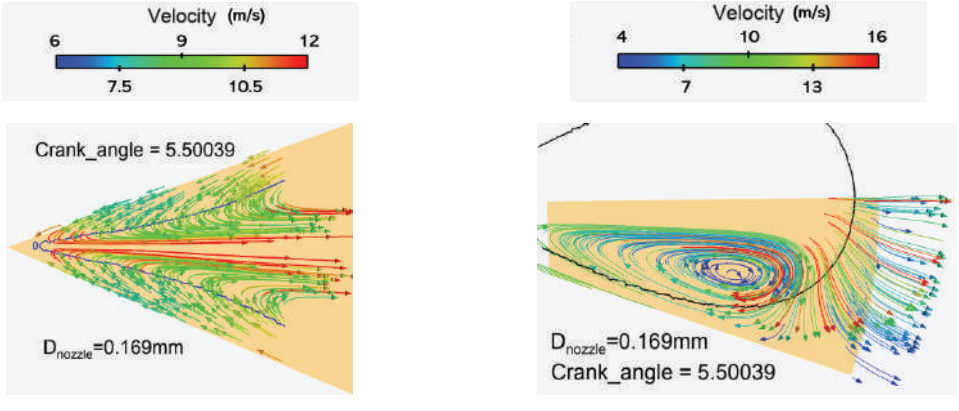

(**a**)

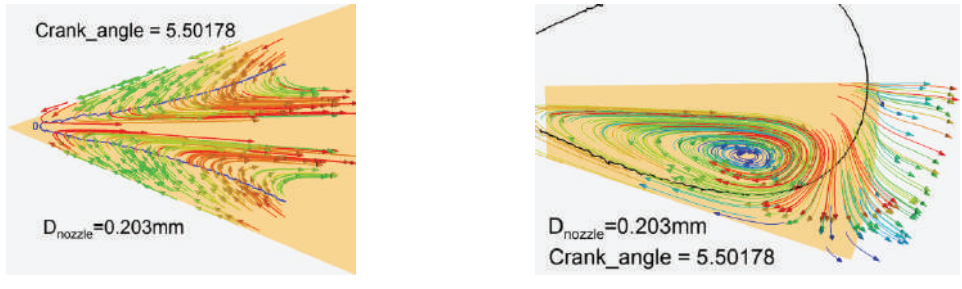

(**b**)

Figure 20. *Cont.*

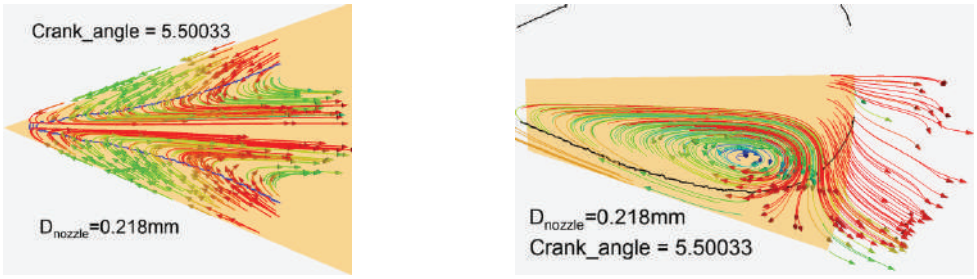

(**c**)

Figure 20. Distribution flow fields in the near and far fields of the sprays under three injector nozzle diameters (5.5 deg. ATDC): (**a**) 0.169 mm; (**b**) 0.203 mm; (**c**) 0.218 mm.

High airflow velocity does not necessarily imply more efficient oxygen transport. It is also necessary to consider the relationship between flow direction and spray, as well as the concentration gradient of input substances. Therefore, Dr. Zhang from Tianjin University proposed the oxygen transport rate α to measure the strength of oxygen transport during the free development process of the spray [23]. This parameter comprehensively considers the direction of airflow and the concentration gradient of input substances. It is defined as follows:

$$\alpha = \vec{V} \cdot \nabla O_2 = \left|\vec{V}\right| |\nabla O_2| cos\theta, \tag{6}$$

That is a detailed explanation of the oxygen transport rate α, defined as the dot product between the flow direction and the gradient of oxygen mass fraction. θ is the angle between the velocity vector and the gradient vector of oxygen mass fraction. When the angle θ is less than 90° (approximately indicating the same direction), $\alpha > 0$; when the angle is greater than 90°, $\alpha < 0$.

Figure 21 presents the distribution of oxygen transport rate in the cylinder under three different nozzle diameters at 5.5 deg. ATDC. It can be observed from the figure that during the free development process of the spray, oxygen is primarily transported along the concentration gradient into the spray, with a large amount of oxygen entering the interior of the spray. The oxygen transport rate is high in the region near the nozzle outlet, and as the spray moves away from the nozzle outlet, the concentration gradient between the spray edge and the surrounding environment as well as within the spray decreases significantly, leading to a decrease in transport rate. Meanwhile, the distribution of high transport rate regions also changes. Unlike the upstream where the entire spray has globally high transport rates, the oxygen transport in the middle region of the spray mainly occurs between the spray edge and the spray core region due to the large oxygen concentration gradient in that area. The spray core region closer to the axis does not have effective oxygen transport due to low oxygen concentration gradients and high axial penetration speeds. Figure 22 shows the distribution of transport rates at various positions on two radial sections, X = 0.1 m and X = 0.2 m, representing the upstream and midstream of the spray, respectively. The oxygen transport in the upstream of the spray is undergoing intense motion with a bimodal distribution, while the oxygen transport distribution in the midstream differs significantly from the upstream. Although it also shows a bimodal distribution, there is no effective oxygen transport near the nozzle axis. With increasing nozzle diameter, the oxygen transport rate in the upstream and midstream of the spray significantly increases, intensifying the entrainment motion of ambient air into the spray and promoting the mixing and combustion processes.

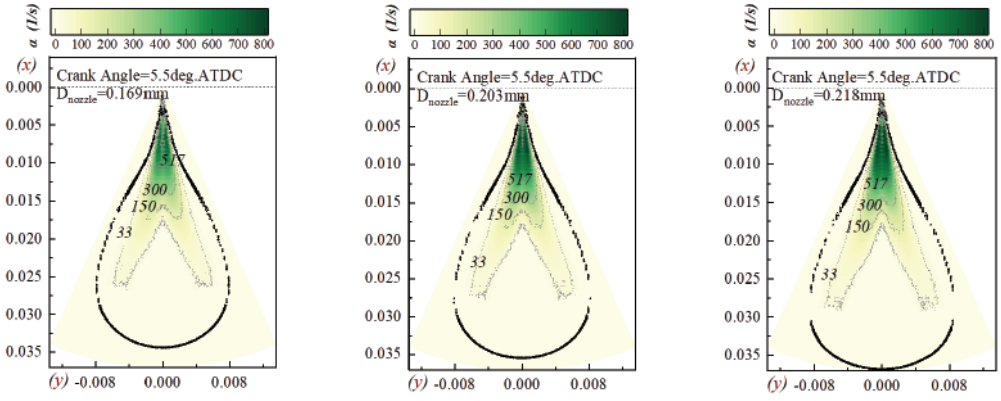

Figure 21. Distribution of oxygen transport rate under three injector nozzle diameters (5.5 deg. ATDC).

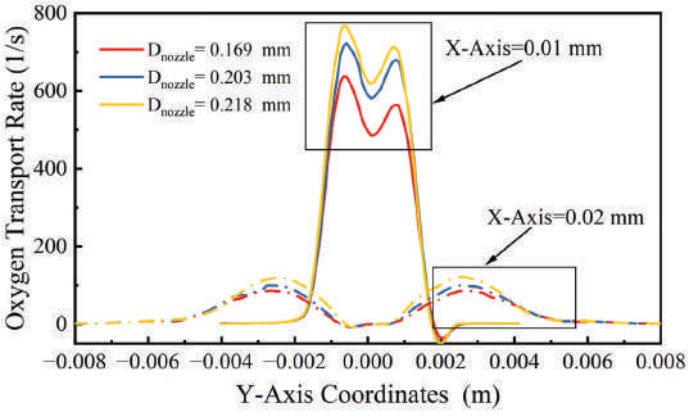

Figure 22. Distribution of oxygen transport rates at various positions on two radial sections of spray under three injector nozzle diameters (5.5 deg. ATDC), X = 0.1 m and X = 0.2 m.

Coupled time series statistically analyzed the cumulative air entrainment mass by the spray at different times, as shown in Figure 23. The air entrainment mass by the spray monotonically increases with the injection time, and the rate of increase continues to rise until the spray/wall impingement. When the spray develops to the piston wall, the effective entrainment area of the spray during the free development stage will no longer increase. Additionally, the fuel impinging on the wall will be guided by the wall to move in the opposite direction from both sides of the spray, which will have a negative effect on the air entrainment during the free development stage. Therefore, the impingement of the spray on the wall is the turning point of the rate of change of air entrainment mass, and its peak appears near the moment of spray/wall impingement. As the nozzle diameter increases from 0.169 mm to 0.218 mm, the air entrainment mass by the spray significantly increases in the same spray development time. Although increasing the nozzle diameter may lead to an earlier spray/wall impingement time, from the perspective of air entrainment mass at the impingement time, the larger nozzle diameter still has advantages. The air entrainment mass at the impingement time corresponding to a nozzle diameter of 0.218 mm is 1.42 times that of 0.169 mm.

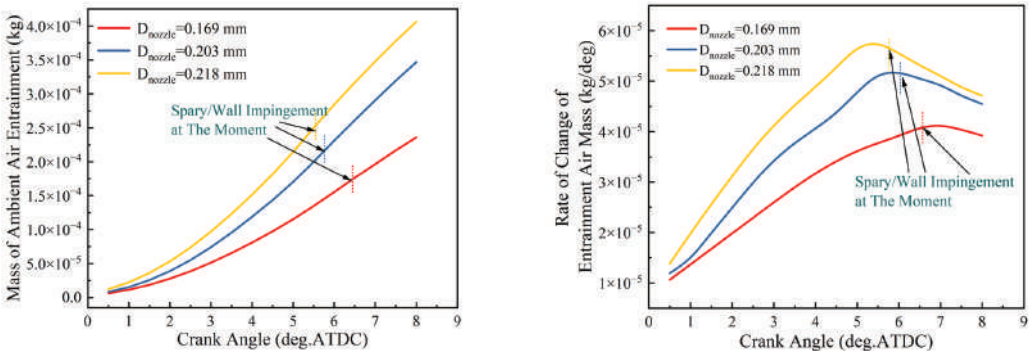

Figure 23. The variation of entrained air mass and its rate of change with injection time under different nozzle diameters: (**a**) air entrainment mass; (**b**) rate of change of air entrainment mass.

Earlier analysis of the combustion path of diesel engines revealed that the proportion of lean mixtures ($0 < \Phi < 1$) plays a crucial role in the overall diesel combustion process, with an ultra-high lean mixture ratio being ideal for efficient and clean combustion. However, the concentration field distribution inside the spray is non-uniform, and different regions within the spray exhibit different mixing characteristics. Taking a nozzle diameter of 0.169 mm as an example (Figure 24), in the region from the nozzle outlet to the ignition boundary (0–0.005 m), the high-temperature air entrained into the spray exchanges energy with the fragmented liquid droplets, thereby promoting droplet evaporation. In this region, the evaporation rate of liquid-phase fuel is significantly higher than the air entrainment rate. Consequently, the phenomenon of $\Phi > 1$ mixtures reaching peak values in ascending order of equivalence ratio intervals is observed. Wherein, the mass fraction of mixtures with $\Phi > 4$ continuously increases and eventually reaches 50%. In the region from the ignition boundary to the maximum liquid length (0.005–0.015 m), air entrainment gradually reaches a balance with fuel evaporation and even dominates. The mass fraction of mixtures with $\Phi > 4$ first stabilizes and then rapidly decreases. Notably, the decrease in mixtures with $\Phi > 4$ does not lead to a significant increase in mixtures with $1 < \Phi < 3$; instead, there is a substantial increase in the proportion of lean mixtures with $\Phi < 1$. In the region from the maximum liquid length to the spray head (>0.015 mm), the liquid-phase fuel has completely evaporated, while air entrainment continues. The equivalence ratio in the core region of the spray gradually decreases. Coupled time series comparison of the mass fractions of lean mixtures with $\Phi < 1$ and rich mixtures with $\Phi > 1$ under different injector nozzle diameters (Figure 25) reveals that in the early stage of injection, the mass fraction of rich mixtures corresponding to larger nozzle diameters is higher, indicating more liquid-phase fuel has evaporated, which is beneficial for subsequent fuel–air mixing. As the injection progresses, the proportion of liquid fuel that has evaporated inside the spray continuously increases, leading to an increase in the mass fraction of lean mixtures. At the moment of ignition, the mass fractions of lean mixtures corresponding to the three nozzle diameters are comparable, with approximately 52%. Larger nozzle diameters change the fuel injection rate, leading to an increase in the total amount of fuel entering the cylinder at the moment of ignition, thereby synchronously increasing the mass fraction of lean mixtures with $\Phi < 1$. The mass fraction of lean mixtures inside the spray reaches its peak value at the moment of impingement. The mass fractions of lean mixtures corresponding to the three nozzle diameters, from smallest to largest, are 60.2%, 62.7%, and 64.0%, respectively. Hence, increasing the nozzle diameter can increase the proportion of lean mixtures inside the spray during the free development stage, thereby enhancing the rate of heat release during the free development stage.

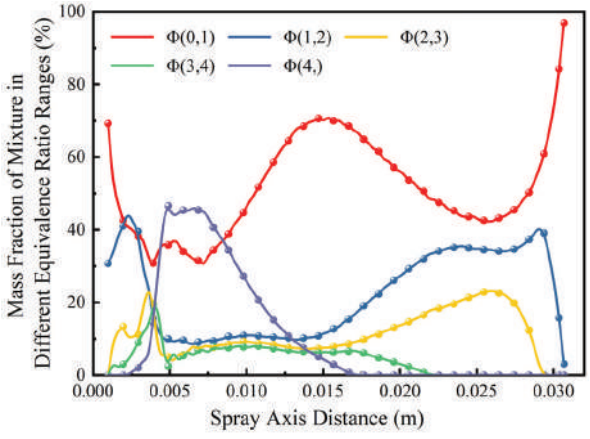

Figure 24. Mass fraction of mixture in different equivalence ratio range (0.169 mm 5.5 deg. ATDC).

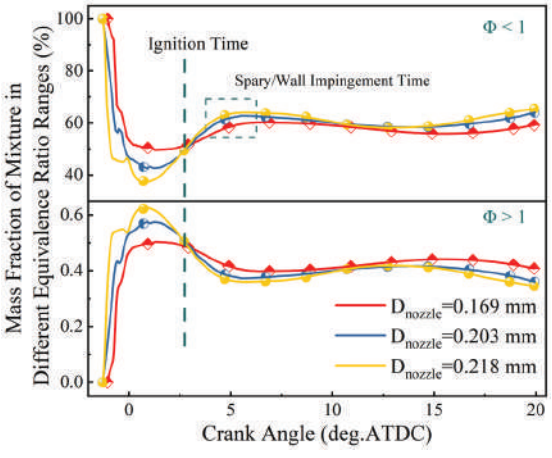

Figure 25. Mass fraction of mixture in different equivalence ratio ranges under three injector nozzle diameters.

Owing to the increase in spray momentum at the nozzle outlet, the friction and shear effects between the spray and fresh air become more pronounced during the axial penetration development process. As the injector nozzle diameter increases, the proportion of momentum transferred radially in the core region of the spray upstream becomes higher. The increase in the total momentum coupled with the increase in the dissipation ratio, results in an increase in the momentum transferred to the fresh air by the spray radially. Consequently, the overall oxygen transport process within the spray becomes more intense, the air entrainment rate significantly increases, and the accumulated air entrainment mass during the free development stage increases. This leads to an improvement in the mixture quality inside the spray, an increase in the proportion of lean mixtures, and an acceleration of the heat release during the free development stage of the spray combustion. However, it is noteworthy that, under the operating conditions considered in this study, over 70% of the combustion process is accompanied by spray/wall impingement. After spray/wall impingement, the mixing rate between the spray and air is significantly reduced due to momentum loss, and the limited fuel–air contact area slows down the fuel heat release rate, affecting the overall combustion quality. Therefore, it is necessary to discuss the influence of the wall-attached fuel mixing rate. In this study, a stepped-lip combustion chamber was used, which replaces the protruding lip of the traditional reentrant ω-shaped combustion

chamber with a recessed annular lip. As shown in Figure 26, under conventional injection strategies, spray/wall impingement occurs near the lip, and under the guidance of the combustion chamber wall, the spray is divided into two parts: the majority enters the bottom of the piston and forms a clockwise vortex core, while a minority develops upwards, crosses the step, enters the squish region, and forms a counterclockwise vortex core. Both vortex cores continue to grow over time and form large-scale vortex structures with strong air entrainment capabilities at the leading edge of the wall-attached fuel, especially structure A at the bottom of the piston. With increasing nozzle diameter, the scale and intensity of the vortices at the bottom of the piston increase, while the intensity of the vortices in the squish region decreases. This phenomenon is particularly evident 15 degrees after spray/wall impingement, as the larger nozzle diameter causes the spray/wall impingement point at the end of injection to be closer to the bottom of the piston, resulting in more fuel entering the piston and less fuel entering the squish region. Furthermore, the residual momentum of wall-attached fuel is relatively high, leading to larger scale and intensity of vortices at the bottom of the piston. Although increasing the nozzle diameter weakens the vortices in the squish region, comparing the oxygen concentration in the squish region under different nozzle diameters reveals that even with strong vortex structures in the squish region, it is difficult to entrain air between the piston and cylinder liner gaps. However, the strengthened vortices at the bottom of the piston can entrain a large amount of surrounding air into the vortex structure, facilitating the mixing of air and unburnt fuel within the vortex structure and improving the air utilization rate in the piston center region. Benefiting from the higher mixture quality inside the spray during the free development stage and the larger and stronger vortices induced after spray/wall impingement, the mixing of wall-attached fuel is enhanced, leading to an increase in the mixing quality after the spray/wall impingement stage.

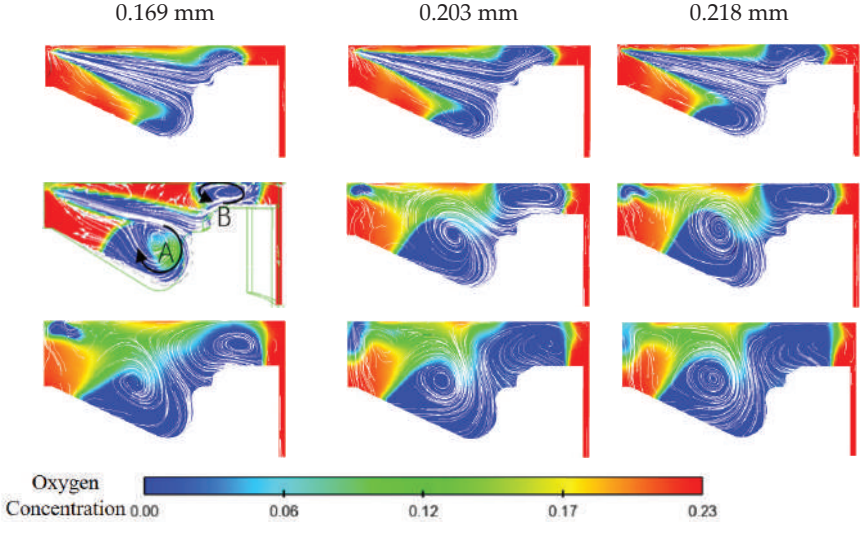

Figure 26. Distribution of in-cylinder flow field and oxygen concentration after spray/wall impingement for three nozzle diameters.

There are significant differences in the reaction pathways corresponding to different equivalence ratio ranges of the mixture, which inevitably lead to significant differences in the contribution to combustion heat release. Instantaneous heat release rates of mixture in different equivalence ratio ranges were statistically analyzed, as shown in Figure 27. When the nozzle diameter increases from 0.169 mm to 0.218 mm, due to the increase in the mass of fuel entering the cylinder per unit time, the heat release rates of mixture in different equivalence ratio ranges during the injector duration all show varying degrees

of improvement. The heat release contribution of lean mixtures with Φ < 1 is the highest, and the corresponding increase in heat release rate is most significant. This is also the key reason why increasing the nozzle diameter leads to the most significant increase in heat release rate.

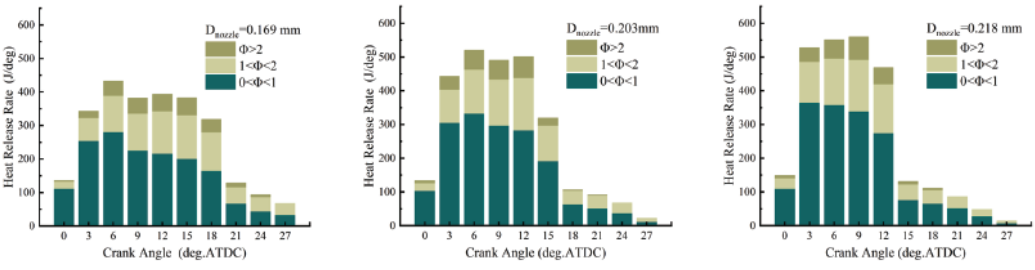

Figure 27. The instantaneous heat release rates of mixture in different equivalence ratio ranges for three injector nozzle diameters: (**a**) 0.169 mm; (**b**) 0.203 mm; (**c**) 0.218 mm.

In summary, the research results show that in a high charge density environment, increasing the nozzle diameter from 0.169 mm to 0.218 mm not only increases the mass of fuel entering the cylinder per unit time but also improves the overall mixture quality during the entire spray development process. The proportion of lean mixtures inside the spray increases, resulting in more combustible mixture being produced per unit time. As a result, the combustion heat release rate significantly increases, the combustion duration is notably shortened, and the proportion of constant volume combustion increases, allowing for more complete expansion of the working fluid, leading to an indicated thermal efficiency increase to 51.5%.

The above research was conducted within the range of experimental fuel injectors (0.169 mm to 0.218 mm). Given the limitations of the experimental fuel injector nozzle diameter range, numerical simulation methods were employed to expand the research scope of the fuel injector nozzle diameter in order to verify the applicability of the conclusions obtained within a wider range of nozzle diameters. Figure 28 shows the simulation results of the hydraulic system model of the fuel injector. With the increase in nozzle diameter, the actual fuel injection pressure shows a linear decreasing trend, the fuel injection rate continuously increases and the duration of fuel injection continuously shorten. However, when the nozzle diameter exceeds 0.2 mm, the rate of decrease in the duration of fuel injection significantly slows down. This means that the benefits of increasing the fuel injection rate decrease as the nozzle diameter increases, mainly because increasing the nozzle diameter will increases the pressure loss inside the fuel injector, resulting in an excessive decrease in the actual fuel injection pressure. In addition, expanding the research scope of the fuel injector nozzle diameter reveals that the spray momentum at the nozzle outlet per unit time shows a trend of initially increasing and then decreasing with increasing nozzle diameter. This is the result of the interplay between the nozzle flow area and the actual fuel injection pressure. Excessive enlargement of the nozzle diameter will lead to a significant decrease in spray momentum, thereby affecting subsequent droplet atomization, fuel–air mixture, and combustion processes. In this study, the nozzle diameter corresponding to the peak spray momentum at the nozzle outlet was within the range of 0.218 mm to 0.25 mm.

Figure 29 shows the numerical simulation results of the in-cylinder combustion process. When the nozzle diameter exceeds 0.25 mm, the decrease in spray momentum entering the cylinder per unit time leads to a reduction in the air entrainment rate, and the duration of free spray development is significantly shortened, resulting in deterioration of the mixture quality inside the spray at the spray/wall impingement moment. From the perspective of heat release rate, within the range of nozzle diameters from 0.13 mm to 0.25 mm, the combustion duration gradually shortens and the thermal efficiency significantly improves

as the nozzle diameter increases. Within the range of nozzle diameters from 0.25 mm to 0.37 mm, the combustion duration remains around 23 degrees and the thermal efficiency shows a slow decreasing trend as the nozzle diameter increases. Therefore, under the engine operating parameters and thermodynamic boundary conditions considered in this study, the optimal nozzle diameter should be within the range of 0.218 mm to 0.25 mm.

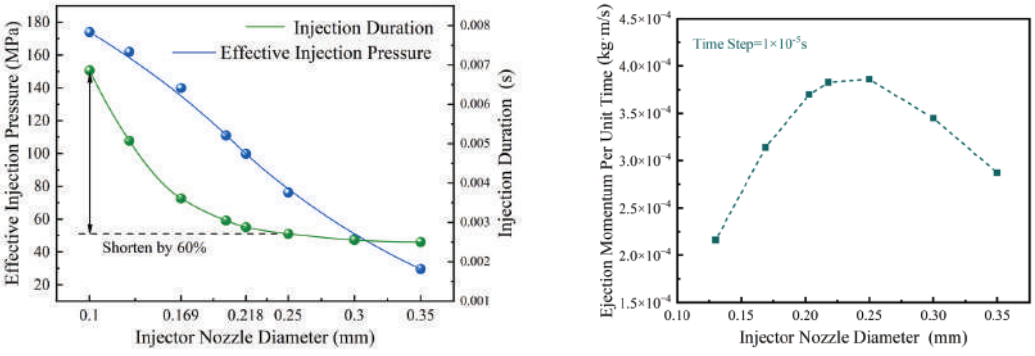

(**a**) (**b**)

Figure 28. Simulation results obtained from expanding the research scope of nozzle diameters: (**a**) effective injection pressure and fuel injection duration; (**b**) spray momentum at nozzle outlet.

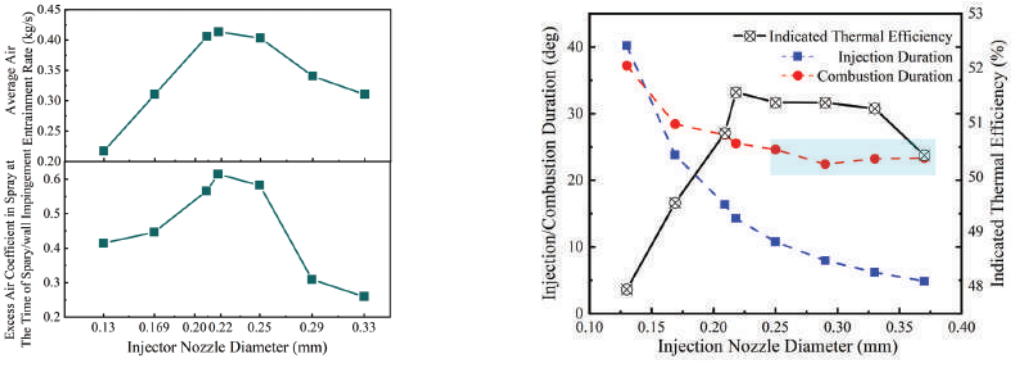

(**a**) (**b**)

Figure 29. Numerical simulation results obtained from expanding the fuel injector nozzle diameter range: (**a**) spray mixture quality; (**b**) combustion duration and indicated thermal efficiency.

5. Conclusions

In order to improve the fuel economy of heavy-duty diesel engines under high-load conditions, based on the combustion pathway model, it is proposed that the proportion of lean mixture with $0 < \Phi < 1$ is the most important spray characteristic affecting the overall diesel combustion process. Answering the question of how to increase the proportion of lean mixture inside the spray is the key to achieving efficient and clean combustion of diesel engines. Through experiment and numerical simulation methods, the following conclusions are drawn regarding the impact mechanism of fuel injector nozzle diameter on spray lean mixture characteristics, fuel–air mixture, and combustion process under high charge density conditions, as well as the potential to improve thermal efficiency:

In a high charge density environment, increasing the nozzle diameter from 0.169 mm to 0.218 mm can improve the overall mixture quality throughout the spray development process. The experimental results show that with the increase in nozzle diameter, the peak

pressure and instantaneous heat release rate significantly increase, the combustion duration is shortened by about 20%, the heat release becomes more concentrated, and the proportion of constant volume combustion increase. At 1200 rpm and IMEPg~2.3 MPa conditions, the indicated thermal efficiency increases by 1.3%, reaching a maximum of 51.5%.

With the increase in nozzle diameter, the spray ejection momentum per unit time also increases significantly. The increase in spray penetration velocity strengthens the friction and shear effects between the spray and fresh air, resulting in faster energy dissipation rates and a higher proportion of energy dissipation in the radial direction of the spray core, especially in the upstream region where the penetration velocity is highest. The higher spray momentum combined with the increased dissipation proportion means that larger nozzle diameter fuel injectors transfer more momentum to the fresh air radially, resulting in a wider radial distribution range of high-momentum regions in the middle region of the spray, intensifying the mass transfer and entrainment process at the spray edge.

Introducing the oxygen mass transport rate to evaluate the strength of air entrainment motion at various positions of the spray: during the free development process of the spray, oxygen forward transport is dominant; i.e., the oxygen transport rate parameter is greater than 0. During this process, a large amount of oxygen enters the interior of the spray, and the most intense oxygen transport occurs at the inner boundary of the gas phase spray with obvious oxygen concentration stratification. With the increase in nozzle diameter, the higher spray momentum during the free development stage leads to more intense oxygen transport motion, and the radial range of effective oxygen transport in the middle region of the spray increases significantly.

In the region near the spray outlet where liquid-phase fuel evaporation is dominant, high air entrainment leads to a significant increase in the amount of gas-phase fuel generated, which is beneficial for subsequent fuel–air mixing. The proportion of rich mixture increases rapidly, the mass fraction of lean mixture inside the spray reaches its peak until the spray/wall impingement moment. Increasing the nozzle diameter increases the air entrainment by 42% during the free development stage of the spray, and the proportion of lean mixture inside the spray increases from 60.2% to 64.0%. Benefit from the higher mixture quality during the free development stage of the spray and the larger and stronger vortex generated at the front of the spray after spray/wall impingement, increasing the nozzle diameter intensifies the mixing process between the wall-attached fuel and air, leading to an improvement in the mixture quality after the spray/wall impingement stage. Overall, increasing the nozzle diameter from 0.169 mm to 0.218 mm increases the mass of fuel entering the cylinder per unit time, while also increasing the proportion of lean mixture throughout the entire spray development process, resulting in an increase in the heat release rate of the lean mixture, making the overall combustion more intense and concentrated.

By using numerical simulation methods to expand the research scope of fuel injector nozzle diameters, the applicability of the conclusions obtained within a wider range of nozzle diameters is verified. It is found that a nozzle diameter that is too small sacrifices fuel injection duration, leading to a large amount of fuel combustion during the piston descent process, while a nozzle diameter that is too large leads to an excessive reduction in effective injection pressure, affecting spray momentum and subsequent fuel–air mixture processes, with no further reduction in combustion duration but a slow decrease in thermal efficiency. Under the engine operating parameters and thermodynamic boundary conditions considered in this study, the optimal nozzle diameter should be in the range of 0.218 mm to 0.25 mm.

Author Contributions: Conceptualization, W.S. and Y.L.; methodology, Y.L.; software, Y.L.; validation, Y.L.; formal analysis, Y.L.; data curation, Y.L.; writing—original draft preparation, Y.L.; writing—review and editing, W.S.; funding acquisition, W.S. All authors have read and agreed to the published version of the manuscript.

Funding: This research was funded by the National Key Research and Development Program of China (No. 2022YFE0100100).

Data Availability Statement: The data presented in this study are available on request from the corresponding author. The data are not publicly available due to privacy.

Conflicts of Interest: The authors declare no conflicts of interest.

Nomenclature

Item	Definition
NOx	Nitrogen Oxide
UHC	Unburnt Hydrocarbon
ATDC	After Top Dead Center
CA	Crank Angle
ECU	Electronic Control Unit
EGR	Exhaust Gas Recirculation
Φ	Fuel–oxygen Equivalence Ratio
CA10	10% Heat Release Point
Ca50	50% Heat Release Point
Ca90	90% Heat Release Point
HRR	Heat Release Rate
IMEP	Indicated Mean Effective Pressure
ITEg	Gross Indicated Thermal Efficiency

References

1. Huang, M.; Zhai, P. Achieving Paris Agreement temperature goals requires carbon neutrality by middle century with far-reaching transitions in the whole society. *Adv. Clim. Chang. Res.* **2021**, *12*, 281–286. [CrossRef]
2. Gunfaus, M.T.; Waisman, H. Assessing the adequacy of the global response to the Paris Agreement: Toward a full appraisal of climate ambition and action. *Earth Syst. Gov.* **2021**, *8*, 100102. [CrossRef]
3. Senecal, P.; Leach, F. Diversity in transportation: Why a mix of propulsion technologies is the way forward for the future fleet. *Results Eng.* **2019**, *4*, 100060. [CrossRef]
4. Kumano, K.; Iida, N. Analysis of the effect of charge inhomogeneity on HCCI combustion by chemiluminescence measurement. *J. Fuels Lubr.* **2004**, *113*, 974–986.
5. Verma, S.K.; Gaur, S.; Akram, T.; Gautam, S.; Kumar, A. Emissions from homogeneous charge compression ignition (HCCI) engine using different fuels: A review. *Green Energy Environ. Sustain.* **2022**, *29*, 50960–50969. [CrossRef] [PubMed]
6. Liu, Y.; Su, W.; Wu, B.; Wang, J. The Research and Development of a Jet Disturbance Combustion System for Heavy-Duty Diesel Engines. *Energies* **2024**, *17*, 1065. [CrossRef]
7. Zhang, Z.; Liu, Y.; Wu, B.; Nie, J.; Su, W. Effect of Nozzle Diameter on Combustion and Emissions of a Heavy Duty Diesel Engine. *Trans. CSICE* **2022**, *40*, 97–105.
8. Zhai, C.; Jin, Y.; Nishida, K.; Ogata, Y. Diesel spray and combustion of multi-hole injectors with micro-hole under ultra-high injection pressure–non-evaporating spray characteristics. *Fuel* **2021**, *283*, 119322. [CrossRef]
9. Zhao, J.; Grekhov, L.; Yue, P. Limit of fuel injection rate in the common rail system under ultra-high pressures. *Int. J. Automot. Technol.* **2020**, *21*, 649–656. [CrossRef]
10. Wang, L.; Lowrie, J.; Ngaile, G.; Fang, T. High injection pressure diesel sprays from a piezoelectric fuel injector. *Appl. Therm. Eng.* **2019**, *152*, 807–824. [CrossRef]
11. Shi, Z.; Wu, H.; Li, H.; Zhang, L.; Lee, C. Effect of injection pressure and fuel mass on wall-impinging ignition and combustion characteristics of heavy-duty diesel engine at low temperatures. *Fuel* **2021**, *299*, 120904. [CrossRef]
12. Xia, J.; Zhang, Q.; Huang, Z.; Ju, D.; Lu, X. Experimental study of injection characteristics under diesel's sub/trans/supercritical conditions with various nozzle diameters and injection pressures. *Energy Convers. Manag.* **2020**, *215*, 112949. [CrossRef]
13. Dec, J. *A Conceptual Model of DI Diesel Combustion Based on Laser-Sheet Imaging*; SAE Technical Paper 970873; JSTOR: New York, NY, USA, 1997.
14. Pickett, L.M.; Siebers, D.L. Non-sooting, low flame temperature mixing-controlled DI diesel combustion. *SAE Trans.* **2004**, *113*, 614–630.
15. Kook, S.; Bae, C.; Miles, P.C.; Choi, D.; Pickett, L.M. The influence of charge dilution and injection timing on low-temperature diesel combustion and emissions. *SAE Trans.* **2005**, *114*, 1575–1595.
16. Polonowski, C.J.; Mueller, C.J.; Gehrke, C.R.; Bazyn, T.; Martin, G.C.; Lillo, P.M. An experimental investigation of low-soot and soot-free combustion strategies in a heavy-duty, single-cylinder, direct-injection, optical diesel engine. *SAE Int. J. Fuels Lubr.* **2012**, *5*, 51–77. [CrossRef]

17. Manin, J.; Skeen, S.; Pickett, L.M.; Kurtz, E.; Anderson, J.E. Effects of oxygenated fuels on combustion and soot formation/oxidation processes. *SAE Int. J. Fuels Lubr.* **2014**, *7*, 704–717. [CrossRef]
18. Dumitrescu, C.E.; Mueller, C.J.; Kurtz, E. Investigation of a tripropylene-glycol monomethyl ether and diesel blend for soot-free combustion in an optical direct-injection diesel engine. *Appl. Therm. Eng.* **2016**, *101*, 639–646. [CrossRef]
19. Huang, H. Numerical and Experimental Study on the Combustion Process of Diesel HCCI Engines. Ph.D. Dissertation, Tianjin University, Tianjin, China, 2007.
20. Wang, H.; Zheng, D.; Tian, Y. High pressure common rail injection system modeling and control. *ISA Trans.* **2016**, *63*, 265–273. [CrossRef] [PubMed]
21. Kim, J.; Lee, J.; Kim, K. Numerical study on the effects of fuel viscosity and density on the injection rate performance of a solenoid diesel injector based on AMESim. *Fuel* **2019**, *256*, 115912. [CrossRef]
22. Blessing, M.; König, G.; Krüger, C.; Michels, U.; Schwarz, V. Analysis of flow and cavitation phenomena in diesel injection nozzles and its effects on spray and mixture formation. *SAE Trans.* **2003**, *112*, 1694–1706.
23. Zhang, X. Research on Interaction of Physical and Chemical Factors in MULIN-BUMP Compound Combustion. Ph.D. Dissertation, Tianjin University, Tianjin, China, 2007.

MDPI AG
Grosspeteranlage 5
4052 Basel
Switzerland
Tel.: +41 61 683 77 34

MDPI Books Editorial Office
E-mail: books@mdpi.com
www.mdpi.com/books

Academic Open
Access Publishing

mdpi.com

ISBN 978-3-7258-1944-7